REPORT DOCUMENTATION PAGE

Form Approved OMB NO. 0704-0188

1. REPORT DATE (DD-MM-YYYY)	2. REPORT TYPE	3. DATES COVERED (From - To)
20-06-2018	Final Report	1-Jun-2016 - 31-May-2017

4. TITLE AND SUBTITLE
Final Report: Conference and Symposia grants for The U.S. Workshop on the Physics and Chemistry of II-VI Materials - ARO Research Area 9: Materials Science - Physical Properties of Materials

5a. CONTRACT NUMBER
W911NF-16-1-0346

5b. GRANT NUMBER

5c. PROGRAM ELEMENT NUMBER
611102

6. AUTHORS

5d. PROJECT NUMBER

5e. TASK NUMBER

5f. WORK UNIT NUMBER

7. PERFORMING ORGANIZATION NAMES AND ADDRESSES
Rensselaer Polytechnic Institute
110 8th Street

Troy, NY 12180 -3522

8. PERFORMING ORGANIZATION REPORT NUMBER

9. SPONSORING/MONITORING AGENCY NAME(S) AND ADDRESS (ES)
U.S. Army Research Office
P.O. Box 12211
Research Triangle Park, NC 27709-2211

10. SPONSOR/MONITOR'S ACRONYM(S)
ARO

11. SPONSOR/MONITOR'S REPORT NUMBER(S)
68804-MS-CF.1

12. DISTRIBUTION AVAILIBILITY STATEMENT
Approved for public release; distribution is unlimited.

13. SUPPLEMENTARY NOTES
The views, opinions and/or findings contained in this report are those of the author(s) and should not contrued as an official Department of the Army position, policy or decision, unless so designated by other documentation.

14. ABSTRACT

15. SUBJECT TERMS

16. SECURITY CLASSIFICATION OF:			17. LIMITATION OF ABSTRACT	15. NUMBER OF PAGES	19a. NAME OF RESPONSIBLE PERSON
a. REPORT	b. ABSTRACT	c. THIS PAGE			Ishwara Bhat
UU	UU	UU	UU		19b. TELEPHONE NUMBER: 518-276-2786

RPPR Final Report
as of 17-Sep-2018

Agency Code:

Proposal Number: 68804MSCF **Agreement Number: W911NF-16-1-0346**
INVESTIGATOR(S):

Name: Ishwara B. Bhat
Email: bhati@rpi.edu
Phone Number: 5182762786
Principal: Y

Organization: **Rensselaer Polytechnic Institute**
Address: 110 8th Street, Troy, NY 121803522
Country: USA

DUNS Number: 002430742 EIN: 141340095
Report Date: 31-Aug-2017 Date Received: 20-Jun-2018
Final Report for Period Beginning 01-Jun-2016 and Ending 31-May-2017
Title: Conference and Symposia grants for The U.S. Workshop on the Physics and Chemistry of II-VI Materials - ARO Research Area 9: Materials Science - Physical Properties of Materials
Begin Performance Period: 01-Jun-2016 **End Performance Period:** 31-May-2017
Report Term: 0-Other

Submitted By: Ishwara Bhat Email: bhati@rpi.edu
Phone: (518) 276-2786

Distribution Statement: 1-Approved for public release; distribution is unlimited.

STEM Degrees: 0 **STEM Participants:** 0

Major Goals: The goal of this program is to support a conference and symposia title “The U.S. Workshop on the Physics and Chemistry of II-VI Materials” that will be of interest to the Army. As stated in the proposal, we will organize a Workshop in October 2016 as a part of the annual workshop that will bring together the industrial, governmental, and academic communities that work with II-VI materials. These II-VI materials are critical in a wide range of detector technologies operating in the infrared, ultraviolet, x-ray, and gamma-ray regions of the spectrum, as well as broad-band devices such as solar cells. They include HgCdTe, ZnSe, ZnO, ZnS, and CdTe, as well as other II-VI semiconductors and alloys. Spectrometers, imagers, and other sophisticated systems exploiting various properties of these materials are finding applications in many fields, including national security, homeland security, medicine, industrial process monitoring, basic science, astronomy, energy production, and more. The Workshop aims at advancing the understanding of the basic physics and chemistry of these materials, and thereby contributes to the continual improvement of these system capabilities.

The topics to be covered:

International in scope, these annual workshops bring together university, government and industrial participants in an interactive three-day setting to address fundamental issues in the science and technology of II-VI materials and devices. Areas covered include a broad range of disciplines and materials properties. Included are materials growth and characterization, materials engineering, intrinsic and extrinsic defects and dopants, surface chemistry, fabrication processes, electrical properties and modeling, charge transport, noise sources, optical properties, photorefraction, electro-optical and magneto-optical properties, as well as the interaction among all these.

The scope of the Workshop includes the basic physics and chemistry of all II-VI materials and their applications. Materials of interest include HgCdTe, HgCdSe, ZnSe, ZnO, ZnS, CdTe, and CdZnTe. Issues in the following critical areas are of interest:

- X-Ray & Gamma-Ray Radiation Detectors
- Radiation Effects in HgCdTe
- II-VI–Based Solar Cells
- Materials Growth and Characterization
  - Control of composition, carrier concentration, and lifetime
  - Modeling of growth and processing
  - Equilibrium and non-equilibrium growth

- Defects and Doping
- Physics of Failure
- Characterization, particularly non-destructive
- Effect on electrical and optical properties
- P-doping issues in HgCdTe
- Impurities
- Diffusion
- Activation and segregation
- Dislocations: generation mechanisms, properties, kinetics, characterization, mitigation
- Surfaces and Interfaces
- Etching, passivation, and metallization
- Modeling and Simulation
- Material properties
- Growth and processing
- Device physics
- Characterization of Materials
- Electrical, optical, and microstructural characterization
- ZnO and ZnS Materials and Devices
- Magnetic semiconductors
- 2D Materials
- Quantum Dots

Accomplishments: The workshop was organized in 2016. The details are:

- The 2016 U.S. WORKSHOP on the PHYSICS and CHEMISTRY of II–VI MATERIALS, Sheraton Inner Harbor Hotel, October 17–20, 2016, Baltimore, Maryland, USA

- A total of 106 research scientists from US and abroad have attended the workshop during the 3-day workshop with about 62 contributed and invited presentations. The details on the paper list and attendees list are attached to this report.

- Two tutorials were presented during the evening on October 16, 2016. The tutorials are for the benefit of graduate students and post-doctoral scientists.

- The final workshop program is attached to this final report. It has the full schedule of the workshop.
- A workshop abstract proceedings is also prepared as attached. The proceedings has the detailed abstracts of all the presented papers.
- In addition to these, most of the presenters are encouraged to write full-length papers of their talks. These manuscripts are peer reviewed and published as a special issue of Journal of Electronic Materials, Volume 46, Issue 9, 2017. The foreword of the proceedings is attached here and the full issue of the workshop is available from the Journal of Electronic materials, 46, 2017.

Training Opportunities: The II-VI Workshop featured two tutorials on Monday evening, October 17.
Roger DeWames, MTEQ, and Jonanthan Schuster, Army Research Laboratory, presented and discussed "Hetereojunctions for Everything" for 1 hour and 15 minutes.
Dr. Herbert S. Schaake, EPIR Technologies, discussed "Modeling the Role of Point-Defect Diffusion in Diode Formation, Impurity Activation, and Tellurium Precipitation in HgCdTe." for another 1 hour and 15 minutes.
The tutorials were well attended and welcomed all interested and registered II-VI
Workshop participants.

Results Dissemination: The abstracts of all the papers presented are formed as a proceeding book and disseminated to all attendees. In addition, a special of Journal of Electronic Materials was published last year that contained most of the papers presented at the workshop. These papers were peer reviewed and forms an archival publications of the workshop.

Honors and Awards: Nothing to Report

Protocol Activity Status:

RPPR Final Report
as of 17-Sep-2018

Technology Transfer: Nothing to Report

PARTICIPANTS:

Participant Type: PD/PI
Participant: Ishwara Bhat
Person Months Worked: 12.00 **Funding Support:**
Project Contribution:
International Collaboration:
International Travel:
National Academy Member: N
Other Collaborators:

Rensselaer Polytechnic Institute
Final Report for the Conference Grant Award

Conference and Symposia grants for the U.S. Workshop on the Physics and Chemistry of II-VI Materials

Final Report for the Conference Grant Award
W911NF-16-1-0346

Prepared by: Ishwara Bhat
Department of Electrical Computer and Systems Engineering
Rensselaer Polytechnic Institute
110 8th St.
Troy, NY 12180
bhati@rpi.edu

Submitted to:

Us Army ACC-APG-RTP W911nf
800 Park Office Drive
Suite 4229
Research Triangle Park Nc 27709
Attention: Dr. Chakrapani Varanasi, 919-549-4325
e-mail: Chakrapani.v.varanasi.civ@mail.mil

Period of Performance: 1 June 2016 – 31 May 2017

June 20, 2018

1. Program Goal

The goal of this program is to support a conference and symposia title "The U.S. Workshop on the Physics and Chemistry of II-VI Materials" that will be of interest to the Army.

2. Accomplishments

The workshop was organized in 2016. The details are:

- The 2016 U.S. WORKSHOP on the PHYSICS and CHEMISTRY of II–VI MATERIALS, Sheraton Inner Harbor Hotel, October 17–20, 2016, Baltimore, Maryland, USA

- A total of 106 research scientists from US and abroad have attended the workshop during the 3-day workshop with about 62 contributed and invited presentations. The details on the paper list and attendees list are attached to this report.

- Two tutorials were presented during the evening on October 16, 2016. The tutorials are for the benefit of graduate students and post-doctoral scientists.

- The final workshop program is attached to this final report. It has the full schedule of the workshop.
- A workshop abstract proceedings is also prepared as attached. The proceedings has the detailed abstracts of all the presented papers.
- In addition to these, most of the presenters are encouraged to write full-length papers of their talks. These manuscripts are peer reviewed and published as a special issue of Journal of Electronic Materials, Volume 46, Issue 9, 2017. The foreword of the proceedings is attached here and the full issue of the workshop is available from the Journal of Electronic materials, 46, 2017.

LAST_NAME	FIRST_NAME	COMPANY	COUNTRY
Affouda	Chaffra	Naval Research Laboratory	USA
Almeida	Leo	US Army NVESD	USA
Altun	Oguz	ASELSAN	Turkey
Aqariden	Fikri	EPIR Technologies, Inc.	USA
Ari	Ozan	IZTEK A.S.	Turkey
Arkun	Erdem	Teledyne Imaging Sensors	USA
BAIER	Nicolas	CEA - Commissariat L'Energie Atomique	France
Bajaj	Jagmohan	Army Research Laboratory	USA
Baker	Joshua	JX Nippon Mining & Metals USA Inc.	USA
Ballet	Philippe	CEA-LETI	France
Becla	Piotr	CAPESYM Inc.	USA
Bellotti	Enrico	Boston University	USA
Benson	J. David	US Army NVESD	USA
Berthoz	Jocelyn	Sofradir	France
Bhat	Ishwara	Rensselaer Polytechnic Institute	USA
Bornfreund	Richard	FLIR Systems, Inc.	USA
Brown	Alexander	US Army NVESD	USA
Burns	Joseph	Air Force Research Laboratory	USA
Caicedo	Paola	University of Illinois At Chicago	USA
Carmody	Michael	Teledyne Imaging Sensors	USA
Chaix Wagom	Catherine	RIBER	France
Ciani	Anthony	Sivananthan Laboratories	USA
Clark	William	U.S. Army Research Office	USA
DeCuir	Eric	Army Research Laboratory	USA
Delacourt	Bruno	CEA	France
Destefanis	Gerard	Consultant	France
DeWames	Roger	MTEQ/NVESD	USA
Dhar	Nibir	US Army NVESD	USA
Douglas	Sheri	Teledyne Imaging Sensors	USA
D'Souza	Arvind	DRS Technologies	USA
Easley	Justin	University of Michigan	USA
Egarievwe	Stephen	University of Tennessee	USA
Eich	Detlef	AIM INFRAROT-MODULE GmbH	Germany
Eker	Suleyman	ASELSAN	Turkey
Faraone	Lorenzo	The University of Western Australia	Australia
Figgemeier	Heinrich	AIM Infrarot-Module GmbH	Germany
Flint	James	Galaxy Compound Semiconductors, Inc.	USA
Fulk	Chad	Raytheon Vision Systems	USA
Furlong	Mark	IQE	United Kingdom
Gessert	Timothy	EPIR Inc.	USA
Glasmann	Andreu	Boston University	USA
Grein	Christoph	University of Illinois At Chicago	USA
Grenouilloux	Thomas	Sofradir	France

Hoffman	Craig	Naval Research Laboratory	USA
Jackson	Eric	Naval Research Laboratory	USA
Jacobs	Randolph	NVESD	USA
Jaime-Vasquez	Marvin	US Army NVESD	USA
Johnson	Scott	Raytheon Vision Systems	USA
Jozwikowski	Krzysztof	Military University of Technology	Poland
Kan	Steven	Pulse Instruments	USA
Kawahira	Keita	Jx Nippon Mining and Metals	Japan
Kaya	Yasin	Princeton University	USA
Klipstein	Philip	Semiconductor Devices Ltd.	Israel
Kobayashi	Masakazu	Waseda University	Japan
Kohler	Ken	Veeco	USA
Krishnamurthy	Srini	SRI International	USA
Kujofsa	Tedi	University of Connecticut	USA
LeBlanc	Elizabeth	Texas State University	USA
Lee	Donald	Teledyne Imaging Sensors	USA
Lennon	Craig	U.S. Army NVESD	USA
Liao	Pok-Kai	Intelligent Epitaxy Technology	USA
Madni	Imtiaz	University of Western Australia	Australia
Mahendranathan	Nimalan	EPIR Technologies Inc.	USA
Marmon	Jason	UNC Charlotte	USA
McLaren	Robert	NNSA/NA-22	USA
Mitra	Pradip	DRS Technologies	USA
Miura	Hiroshi	Jx Nippon Mining and Metals	Japan
Mohanty	Dibyajyoti	Rensselaer Polytechnic Institute	USA
Morath	Christian	Air Force Research Laboratory	USA
Motakef	Shariar	CapeSym, Inc.	USA
Myers	Thomas	Texas State University	USA
Niraula	Madan	Nagoya Insitute of Technology	Japan
Ociepa	Jozef	CSi2D Inc.	USA
Ogedengbe	Olanrewaju	Texas State University	USA
Palosz	Witold	Brimrose Corporation of America	USA
Pethuraja	Gopal	Magnolia Optical Technologies Inc.	USA
Phillips	Jamie	University of Michigan	USA
Pinkie	Benjamin	NVESD	USA
Piquette	Eric	Teledyne Imaging Sensors	USA
Rab	Sadia	Texas State University	USA
Reed	Meredith	Army Research Laboratory	USA
Reine	Marion	Consultant, Infrared Detectors	USA
Robinson	Ernest	DRS Technologies	USA
Sbrockey	Nick	Structured Materials Industries, Inc.	USA
Schaake	Herbert	EPIR Technologies Inc.	USA
Schuette	Larry	Office of Naval Research	USA
Schuster	Jonathan	Army Research Laboratory	USA
Sivananthan	Sivalingam	University of Illinois At Chicago	USA
Sohal	Sandeep	Texas State University	USA

Stoltz	Andrew	US Army NVESD	USA
Sullivan	William	DRS Technologies	USA
Sun	Xiaoli	NASA Goddard Space Flight Center	USA
Tamargo	Maria	City College, CUNY	USA
Timmerman	Andrew	Fairfield Crystal Technology	USA
Tuaz	Aymeric	CEA-LETI	France
Uruno	Aya	Waseda University	Japan
Vallone	Marco	Politecnico Di Torino	Italy
Wang	Alice	EAG Laboratories	USA
Wijewarnasuriya	Priyalal	U.S. Army Research Laboratory	USA
Wilson	James	Leonardo	United Kingdom
Xiong	Gang	First Solar	USA
Yasuda	Kazuhito	Nagoya Institute of Technology	Japan
Zandian	Majid	Teledyne Imaging Sensors	USA
Zeller	John	Magnolia Optical Technologies Inc.	USA
Zhang	Yong	UNC - Charlotte	USA
Zhang	Yong-Hang	Arizona State University	USA

PROGRAM

The 2016 U.S. WORKSHOP on the PHYSICS and CHEMISTRY of II–VI MATERIALS

Sheraton Inner Harbor Hotel
October 17–20, 2016
Baltimore, Maryland, USA

II-VI Detector Materials

- **IR**
- **UV**
- **Gamma-Ray**
- **X-Ray**
- **Photovoltaic**
- **CdZnTe**
- **HgCdTe**
- **ZnO**
- **ZnS**
- **History of IR Detectors**

Special Sessions

- **Superlattices: II-VI and III-As/Sb**
- **II-VI Based Solar Cells**
- **Alternatives to CdZnTe Substrates**
- **HgCdTe Avalanche Photodiodes**
- **X-Ray and Gamma-Ray Detectors**
- **Surfaces and Interfaces**
- **ZnO Materials and Devices**
- **Defects and Doping**
- **Surface Passivation**

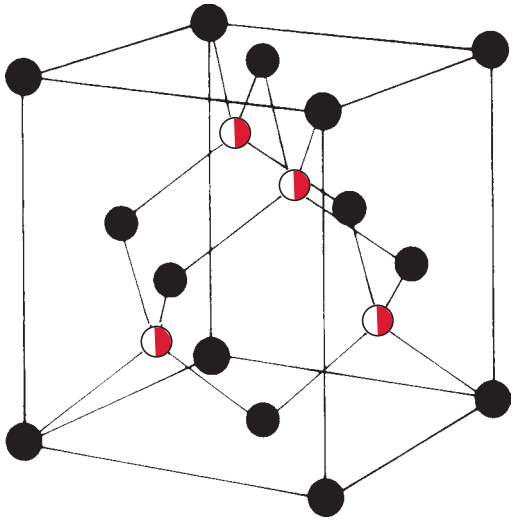

Participating Organizations

U.S. Army RDECOM CERDEC Night Vision & Electronic Sensors Directorate
U.S. Army Research Laboratory
U.S. Army SMDC
U.S. Navy Electro-Optics Center
Penn State University
Office of Naval Research
Air Force Research Laboratory
The Minerals, Metals & Materials Society

Endorsed by

The American Physical Society

Promotional Partners

The 2016 II-VI Workshop would like to express sincere thanks to our supporting organizations and for the contributions from our very generous corporate sponsors.

Gold Partners

Tabletop Exhibitors

Evans Analytical Group (EAG)

JX Nippon Mining & Metals

Pulse Instruments

2016 II-VI WORKSHOP

In the 35 years since the first MCT Workshop was held in 1981, the technology of HgCdTe and related devices has significantly matured and broadened.

The Workshop plays a vital role in this technological evolution. It provides the principal open forum for the exchange of information relative to theory and experiment, synthesis, and analysis. It brings together university, governmental, and industrial research in a highly interactive manner.

- To encourage in-depth discussion and audience participation, the Workshop combines solicited and invited presentations with sufficient time allocated for questions and answers.
- To broaden exposure without sacrificing depth, invited speakers offer insight into areas relevant to II-VI materials.
- To ensure dissemination of results, submitted peer-reviewed full-length papers will appear in the *Journal of Electronic Materials.*

The Workshop will focus on fundamental research on the major scientific problems in II-VI materials. Its primary goal is to promote an understanding of the relationship among the physical and chemical properties and leverage this understanding into manufacturing and performance improvements.

This year, the II-VI Workshop will feature two tutorials on Monday evening, October 17. Roger DeWames, MTEQ, and Jonanthan Schuster, Army Research Laboratory, will discuss *"Hetereojunctions for Everything"* and Herbert S. Schaake, EPIR Technologies, will discuss *"Modeling the Role of Point-Defect Diffusion in Diode Formation, Impurity Activation, and Tellurium Precipitation in HgCdTe."* The tutorials welcome all interested and registered II-VI Workshop participants. The Workshop committee particularly encourages graduate students, post-docs, and junior researchers to attend the tutorials and explore the topics in detail and tap into the experience of and network with well-established researchers.

Informal discussions among participants are strongly encouraged and ample time for paper discussion and individual interactions has been scheduled. To foster these interactions, lunch will be provided on all three days of the Workshop, while a Wine and Cheese Reception along with Tabletop displays has been scheduled for Tuesday evening.

WORKSHOP CO-CHAIRS

Ishwara Bhat, *Rensselaer Polytechnic Institute*
Pradip Mitra, *DRS-RSTA, Inc.*

PROGRAM COMMITTEE

Tony Almeida, *U.S. Army NVESD*
Jose M. Arias, *Rand Corp./U.S. Army NVESD*
Enrico Belotti, *Boston University*
Arnold Burger, *Fisk University*
Joseph Burns, *Air Force Research Laboratory*
William Clark, *Army Research Office*
Roger DeWames, *U.S. Army NVESD*
Nibir Dhar,*+ *U.S. Army NVESD*
Tim Gessert, *EPIR Technologies*
Craig Hoffman, *Naval Research Laboratory*
Ralph James, *Brookhaven National Laboratory*
Scott Johnson, *Raytheon Vision Systems*
Thomas Myers, *Texas State University – San Marcos*
Joe Pellegrino, *U. S. Army NVESD*
Eric Piquette, *Teledyne Imaging Sensors*
Marion Reine, *Consultant, Infrared Detectors*
Siva Sivananthan,* *University of Illinois at Chicago*
Herbert Schaake, *EPIR Technologies, Inc.*
Honnavalli Vydyanath, *IRDT Solutions, Inc.*
Priyalal Wijewarnasuriya, *Army Research Laboratory*

*Proceedings Co-Editor
+Web Site Manager

WORKSHOP COORDINATOR

Samantha Tola
Palisades Convention Management, Inc.
212/460-8090 x 203
212/460-5460 (fax)
e-mail: stola@pcm411.com

SPECIAL ISSUE EDITORIAL COORDINATOR

Yesim Anter
Project Coordinator
EPIR Technologies
e-mail: yanter@epir.com

WORKSHOP PARTICIPATING ORGANIZATIONS

U.S. Army RDECOM CERDEC Night Vision & Electronic Sensors Directorate

U.S. Army Research Laboratory

U.S. Army SMDC

U.S. Navy Electro-Optics Center
Penn State University

Office of Naval Research

Air Force Research Laboratory

The Minerals, Metals & Materials Society

Endorsed by
The American Physical Society

WORKSHOP PARTICULARS

LOCATION AND DATE

The 2016 II-VI Workshop will be held from October 17–20, 2016, at the Sheraton Inner Harbor Hotel, Baltimore, Maryland.

TRAVEL ARRANGEMENTS

The Sheraton Inner Harbor Hotel is located about 9 miles from the Baltimore-Washington International Airport.

Getting to and from the Airport:

- ***Supershuttle*** *– $15 one way per person*
- ***Taxi*** *– Typically $35 (one person)*
- ***Rental Car*** *– The distance from hotel is approximately 9 miles and the average drive time is 20 minutes*

For additional map and direction information visit:
https://www.starwoodmeeting.com/events/start.action?id=1512088777&key=2868FB37

WORKSHOP CHECK-IN

Attendees arriving on Monday, October 17, will be able to pick up their Workshop material at the II-VI Registration Desk located in the Cheseapeake Gallery between 4:00 and 8:00 pm. Attendees will also be able to pick up their Workshop material at the II-VI Registration Desk beginning at 7:00 am each day.

REGISTRATION/INFORMATION DESK

The Registration/Information Desk will be located in the Chesapeake Gallery. For incoming messages, call the hotel at (410) 962-8300 and ask to be transferred to the II-VI Workshop Registration Desk.

LUNCHES

Lunches will be served on all three days of the Workshop in the Chesapeake Ballroom III. To keep the Workshop on schedule, attendees are encouraged to participate.

WINE AND CHEESE/TABLETOP DISPLAYS

Following the presentations on Tuesday afternoon, a Wine and Cheese Reception has been scheduled to help promote informal discussion and attendee interaction. The Wine and Cheese Reception will be accompanied by several tabletop displays from commercial vendors displaying products of interest to the II-VI community. The tabletops will be on view during the Tuesday evening Reception as well as during the day on Wednesday and Thursday in the Chesapeake Gallery.

WORKSHOP MEETING ROOMS

The Workshop tutorials and presentations will be held in the Chesapeake Ballroom I & II. The Wine and Cheese Reception, tabletop displays, and refreshment breaks will all take place in the Chesapeake Gallery.

BOOK OF EXTENDED ABSTRACTS

A copy of the *Book of Extended Abstracts* will be distributed to all attendees at the Workshop. The Extended Abstracts will contain summaries of all oral and poster papers presented at the Workshop. An electronic version can be purchased for an additional $5 for CDs and $10 for USBs.

WORKSHOP PROCEEDINGS

The II-VI Workshop papers will be published in a special issue of the *Journal of Electronic Materials*. The Proceedings will contain full-length refereed versions of papers presented at the Workshop. The cost of a copy of the electronic Proceedings is included in the fee. Login instructions to access the Workshop Proceedings will be e-mailed to all attendees when available.

INSTRUCTIONS TO AUTHORS PLANNING TO SUBMIT FULL-LENGTH MANUSCRIPTS

We are asking all authors to submit their manuscripts to II-VI workshop for online peer review using the link provided by *Journal of Electronic Materials (JEM)* http://www.editorialmanager.com/jems/. Please click on "submit manuscript" at the top of the page. The online manuscript submission will close on October 30, 2016.

II-VI Paper Submission

- Authors who presented their work at the Workshop can submit their manuscripts either by going to the JEM's editorial web page at http://www.editorial manager.com/ jems/ or via the II-VI workshop's website, http://www.ii-viworkshop.org/. The link to the manuscript submission can be accessed by clicking on the Author's Info link located under *"About Workshop"* link on the navigation banner on top of the II-VI Workshop's website. Submissions via e-mail will not be accepted.
- New users will need to create an account. During the submission process, authors will be asked to enter additional information.
- The type of paper is "Special Issue" and the category is "2016 U.S. II-VI Workshop".
- All submissions require an abstract of 200 words or less, a keywords line, a transfer of copyright form, and an electronic file. Papers are reviewed by two qualified referees to determine suitability. The editors' decision to accept or reject a paper, based on referees' comments, is final. Please employ the following guidelines when submitting a paper for review:
- Manuscripts, written in English, should be in a single column and formatted to fit on a 22 x 28-cm sheet. Should

manuscripts contain too many grammatical errors or awkward passages, the papers will be returned without review. Assistance of a professional proofreader (such as www.journalexperts.com) or qualified native speaker of English is recommended under these circumstances and may not only accelerate the review process but also allow for an early publication date.

- The title of the article and abstract should be separate from the text. References, figure captions, and tables should also be on separate pages.
- The works' significance and its relation to the work of others should be detailed in the Introduction. Major assumptions should be stated and procedures adequately outlined.
- References should be cited by Arabic numbers as superscripts. Include the names of all authors, standard abbreviated name of journal (see, for example, http://library.caltech.edu/reference/abbreviations/) the volume number, initial page number, and year of publication in parenthesis. For books, include city of publication and publisher.
- Measurements should be given in metric units, including common abbreviations for time such as h, min, and s.
- Figures may be published online in color with no charge, but color figures in the print version of the *Journal* carry a mandatory fee.

To avoid delays, please:

1. Define all acronyms upon first use, including in the abstract, in this style: scanning electron microscopy (SEM).
2. All micrographs must have scale markers. All plots must have both axes labeled with the variable name (units).
3. Contact author e-mail address and keywords must be included on the abstract page.

For detailed guidelines on artwork and the copyright issue please visit: http://www.springer.com/materials/optical+ %26+ electronic+materials/journal/11664#

WORKSHOP CONTACT

Anyone requiring additional information should contact the Workshop Coordinator, Samantha Tola, at 212/460-8090 x203, fax 212/460-5460, e-mail: stola@pcm411.com.

PROGRAM

MONDAY, OCTOBER 17, 2016

4:00– 8:00 pm	Pre-Workshop Registration
5:00– 7:45 pm	Tutorials

TUESDAY, OCTOBER 18, 2016

7:00– 6:00 pm	Registration
7:00– 8:00 am	Continental Breakfast
8:00– 8:15 am	Welcoming Remarks
8:15– 8:45 am	Keynote Address
8:45–10:30 am	1: Devices I
10:30–10:45 am	**BREAK**
10:45–12:00 pm	2: Modeling I
12:00– 1:30 pm	**LUNCH**
1:30– 3:15 pm	3: Growth I
3:15– 3:30 pm	**BREAK**
3:30– 5:00 pm	4: Solar I
5:00– 6:30 pm	**TABLETOPS / WINE & CHEESE RECEPTION**

WEDNESDAY, OCTOBER 19, 2016

7:30– 5:00 pm	Registration
7:30– 8:45 am	Continental Breakfast
8:45–10:15 am	5: Growth II
10:15–10:30 am	**BREAK**
10:30–12:15 pm	6: Solar II
12:15– 1:45 pm	**LUNCH**
1:45– 3:15 pm	7: Modeling II
3:15– 3:45 pm	**BREAK**
3:45– 5:30 pm	8: Devices II

THURSDAY, OCTOBER 20, 2016

7:30– 2:00 pm	Registration
7:30– 8:00 am	Continental Breakfast
8:00–10:15 am	9: Characterization & Processing
10:15–10:30 am	**BREAK**
10:30–12:00 pm	10: Characterization & Processing II
12:00– 1:30 pm	**LUNCH**
1:30– 2:45 pm	11: DEVICES III
2:45– 3:00 pm	**WILLIAM E. SPICER AND THOMAS N. CASSELMAN BEST STUDENT PAPER AWARD PRESENTATION**
3:00– 3:15 pm	Closing Remarks & Adjourn

MONDAY, OCTOBER 17, 2016
Chesapeake Ballroom
(4:00 – 8:00 pm)

Workshop Pre-Registration **(4:00–8:00)**

Tutorials **(5:00–7:45)**

"Heterojunctions for Everything" **(5:00–6:15)**

Roger DeWames, *MTEQ, Lorton, VA, USA*

Jonathan Schuster, *Army Reasearch Laboratory, Adelphi, MD, USA*

During the early days of the development of $Hg_{1-x}Cd_xTe$ p^+n double layer heterojunction (DLH) for infrared imaging, numerical and analytical simulations tools were used to explore effects on dark currents and quantum efficiency associated, for example, with the placement of the junction relative to the position of the metallurgical heterointerface and energy band offsets. Today, photodiode designs in use in various applications are mostly shallow p^+n homojunctions; this choice was made to ensure photovoltaic behavior, high quantum efficiency, and short-circuit photocurrent. However, for low-illumination conditions, when cooling is required to maintain photon shot noise performance near-mid-gap Shockley-Read Hall flaws can be limiting in achieving the required condition that the dominant current is the photocurrent. Such limitations are encountered for example in SWIR sensors for astronomical instrumentation and imaging under nightglow illumination. In this tutorial, a SWIR photodiode is studied to illustrate the heterojunction design optimization method and to define conditions that significantly reduce the temperature onset of G-R dominated dark current observed in the homojunction detector and maintain photon shot noise performance at a temperature limited by intrinsic radiative recombination diffusion dark currents. Achieving this condition provides the highest operating temperature for low-and high-illumination conditions.

BREAK **(6:15–6:30)**

"Modeling the Role of Point-Defect Diffusion in Diode Formation, Impurity Activation, and Tellurium Precipitation in HgCdTe" **(6:30–7:45)**

Herbert S. Schaake, *EPIR Technologies, Chicago, IL, USA*

TUESDAY, OCTOBER 18, 2016
Chesapeake Ballroom
(7:00 am – 6:30 pm)

Registration **(7:00–6:00)**

Continental Breakfast **(7:00–8:00)**

Welcoming Remarks **(8:00–8:15)**

Ishwara Bhat, *Workshop Co-Chair*
Rensselaer Polytechnic Institute, Troy, NY, USA

Pradip Mitra, *Workshop Co-Chair*
DRS Technologies, Inc., Dallas, TX, USA

KEYNOTE ADDRESS
8:15 – 8:45 am

Dr. Larry Schuette
Director of Research, Office of Naval Research, Washington, DC, USA
"Naval S&T: The Innovation Engine"

This presentation will define the participants, processes, and goals of Naval Science and Technology. The talk will give examples of the various levels of exploration from the most basic research performed by academia and the service labs to applied field tests and experimentation that take advantage of the unique features of navy platforms and naval environments. The emphasis will be on the ways in which Naval S&T fosters innovation in support of the Navy and the nation.

1: DEVICES I
(8:45 – 10:30 am)

Chair: **S. Johnson**
Raytheon Vision Systems, Goleta, CA, USA

Co-Chair: **M. Reine**
Consultant, Infrared Detectors, Cambridge, MA, USA

1.1:
Invited Paper: **HgCdTe: A Vision for the Near Future** **(8:45)**

D. Lee, M. Carmody, E. Piquette, P. Dreiske, A. Chen, A. Yulius, D. Edwall, S. Bhargava, M. Zandian
Teledyne Imaging Sensors, Camarillo, CA, USA

W. E. Tennant
Tennant Electro Optics Consulting, Inc., Thousand Oaks, CA, USA

1.2:
Progress of MCT Detector Technology at AIM towards Smaller Pitch and Lower Dark Current **(9:15)**

D. Eich, W. Schirmacher, S. Hanna, K. M. Mahlein, P. Fries, H. Figgemeier
AIM INFRAROT-MODULE GmbH, Heilbronn, Germany

1.3:
Short-Wavelength Infrared (SWIR) N^+/p $Hg_{1-x}Cd_xTe$ Diodes for LADAR Applications **(9:30)**

E. A. DeCuir, Jr., K. Olver, J. Pattisson, P. S. Wijewarnasuriya
Army Research Laboratory, Adelphi, MD, USA

P. Boieriu
EPIR Technologies, Bolingbrook, IL, USA

1.4:
Absolute-Temperature Sensing by a Two-Color ZnCdSe/ZnCdMgSe Detector **(9:45)**

Y. Kaya, C. Gmachl
Princeton University, Princeton, NJ, USA

A. Ravikumar
Princeton University, Princeton, NJ, USA
and
Stanford University, Stanford, CA, USA

G. Chen, A. Shen, M. C. Tamargo
The City College of New York, NY, USA

1.5:

HgCdTe Avalanche Photodiodes for UV-to-IR Photon Counting **(10:00)**

W. Sullivan III, J. Beck, M. Skokan, C. Schaake, R. Scritchfield, P. Mitra
DRS Technologies, Dallas, TX, USA

D. Carpenter, B. Lane
A/DIC, Inc., Longwood, FL, USA

1.6:

Linear-Mode Photon-Counting HgCdTe Avalanche Photodiode Array in an Integrated Detector Cooler Assembly (IDCA) for a CubeSat Demonstration **(10:15)**

X. Sun, J. B. Abshire, M. A. Krainak, G. Yang, W. Lu
NASA Goddard Space Flight Center, Greenbelt, MD, USA

R. A. Fields, D. A. Hinkley
Aerospace Corp., El Segundo, CA, USA

J. D. Beck, R. M. Rawlings, W. W. Sullivan III
DRS Network & Imaging Systems, LLC, Dallas, TX, USA

BREAK **(10:30–10:45)**

2: MODELING I
(10:45 am – 12:00 pm)

Chair: **P. Wijewarnasuriya**
Army Research Laboratory, Adelphi, MD, USA

Co-Chair: **E. Bellotti**
Boston University, Boston, MA, USA

2.1:
Invited Paper: **Center for Semiconductor Materials and Device Modeling: Advancing Sensor Technology through the Understanding of Materials Synthesis, Device Operation, and Design Controllable Parameters** **(10:45)**

M. Reed, J. Bajaj, J. Schuster, P. Wijewarnasuriya, G. Brill, P. Uppal, G. Wood, P. Perconti
Army Research Laboratory, Adelphi, MD, USA

2.2:
The Numerical Experimental Enhanced Analysis of Hot MCT Barrier Infrared Detectors **(11:15)**

K. Jóźwikowski, M. Kopytko, P. Martyniuk, P. Madejczyk, A. Kowalewski, O. Markowska, A. Martyniuk, A. Rogalski
Military University of Technology, Warsaw, Poland

A. Jóźwikowska
University of Life Science, Warsaw, Poland

W. Gawron
Vigo System S.A. Poznańska, Mazowiecki, Poland

2.3:
Simulation of Small-Pitch HgCdTe Photodetectors **(11:30)**

M. Vallone, M. Goano, F. Bertazzi, G. Ghione
Politecnico di Torino, Torino, Italy

W. Schirmacher, S. Hanna, H. Figgemeier
AIM Infrarot Module GmbH, Heilbronn, Germany

2.4:
Numerical Modeling of Dark-Current Suppression in IR Photodetectors **(11:45)**

A. Glasmann, B. Pinkie, T. Hubbard, E. Bellotti
Boston University, Boston, MA, USA

LUNCH **(12:00–1:30)**

3: GROWTH I
(1:30 – 3:00 pm)

Chair: **T. Almeida**
U.S. Army NVESD, Ft. Belvoir, VA, USA

Co-Chair: **J. Arias**
CACI/NVESD, Ft. Belvoir, VA, USA

3.1:
Invited Paper: **CdZnTe Substrate's Impact on MBE HgCdTe Deposition** **(1:30)**

J. D. Benson, L. O. Bubulac, M. Jaime-Vasquez, J. M. Arias, P. J. Smith, R. N. Jacobs, J. K. Markunas, L. A. Almeida, A. Stoltz
U. S. Army RDECOM, CERDEC Night Vision and Electronic Sensors Directorate, Ft. Belvoir, VA, USA

P. S. Wijewarnasuriya
Army Research Laboratory, Adelphi, MD, USA

M. Reddy, J. Peterson, S. M. Johnson, B. Hanyaloglu, J. Bangs, D. D. Lofgreen
Raytheon Vision Systems, Goleta, CA, USA

3.2:
Characterization of HgCdTe Films on Large-Area CdZnTe Substrates Grown by MBE **(2:00)**

F. E. Arkun, D. D. Edwall, S. Douglas, M. Zandian, M. Carmody, D. Lee
Teledyne Imaging Sensors, Camarillo, CA, USA

3.3:
Effect of Cyclic Annealing on Electronic and Optic Properties of MBE-Grown CdTe Layers **(2:15)**

O. Ari, E. Ozceri, E. Bilgilisoy, Y. Selamet
Izmir Institute of Technology, Izmir, Turkey

3.4:
Strain Relaxation and Misfit Dislocations in HgCdTe on Alternative Substrates **(2:30)**

I. Madni, W. Lei, J. Antoszewski, R. Gu, L. Faraone
University of Western Australia, Crawley, Australia

3.5: (Formerly Late-News Paper 12.1)
Characterization of *n*-Type and *p*-Type Long-Wave InAs/InAsSb Superlattices **(2:45)**

A. E. Brown, N. Baril, L. A. Almeida, S. Bandara
U. S. Army RDECOM, CERDEC, Night Vision and Electronic Sensors Directorate, F. Belvoir, VA, USA

J. Arias
U. S. Army RDECOM, CERDEC, Night Vision and Electronic Sensors Directorate, Fort Belvoir, VA, USA and
CACI Technologies, Arlington, VA, USA

3.6: (Formerly Late-News Paper 12.2)
Effect of Photonic Annealing on the Reduction of Surface Defects on Si(111) and Si(112) Measured by Changes in the Effective Surface Debye Temperature Using LEED **(3:00)**

S. Kroll
CSi2D, Inc., Chicago, IL, USA

BREAK **(3:15-3:30)**

4: SOLAR I
(3:30 – 5:00 pm)

Chair: **S. Sivananthan**
University of Illinois at Chicago, Chicago, IL, USA

Co-Chair: **C. Hoffman**
Naval Research Laboratory, Washington, DC, USA

4.1:
Invited Paper: **Advances and Opportunities in High-Efficiency CdTe Solar Cells** **(3:30)**

G. Xiong
First Solar, Inc., Santa Clara, CA, USA

4.2:
Importance of Target Preparation on the Electrical and Optical Properties of ZnTe:Cu Contact Interface Layers **(4:00)**

T. A. Gessert
EPIR Inc., Bolingbrook, IL, USA

B R. Faulkner
Colorado School of Mines, Golden, CO, USA

J. M. Burst, J. N. Duenow, C. L. Perkins, B. To
National Renewable Energy Laboratory, Golden, CO, USA

4.3:
High-Quality $AgGaTe_2$ Layers Formed from Ga_2Te_3/Ag_2Te Two-Layer Structures **(4:15)**

A. Uruno, Y. Sakurakawa, M. Kobayashi
Waseda University, Tokyo, Japan

4.4:
Iodine Doping of CdTe and CdMgTe for Photovoltaic Applications **(4:30)**

O. S. Ogedengbe, P. A. R. D. Jayathilaka, J. E. Petersen, S. Sohal, E. G. LeBlanc, M. Edirisooriya, C. H. Swartz, T. H. Myers
Texas State University at San Marcos, San Marcos, TX, USA

K. N. Zaunbrecher, T. M. Barnes
National Renewable Energy Laboratory, Golden, CO, USA

A. Wang
EAG, Inc. (Evans Analytical Group), Sunnyvale, CA, USA

4.5:

Preparation and Photoelectric Properties of n-TiO_2/p-$Cd_{1-x}Zn_xTe$ Heterojunction Films **(4:45)**

K. Xu, Y. Shen, Z. Zhang, J. Huang, M. Cao, F. Gu, L. Wang
Shanghai University, Shanghai, P. R. China

RECEPTION / TABLETOPS (5:00-6:30)

WEDNESDAY, OCTOBER 19, 2016
Chesapeake Ballroom
(7:30 am – 5:30 pm)

Registration **(7:30–6:00)**

Continental Breakfast **(7:30–8:45)**

5: GROWTH II
(8:45 – 10:15 am)

Chair: **N. Dhar**
U.S. Army NVESD, Ft. Belvoir, VA, USA

Co-Chair: **H. Schaake**
EPIR Technologies, Inc., Bolingbrook, IL, USA

5.1:
Invited Paper: **MOVPE-Grown HgCdTe Heterostructure Development at Leonardo (formally Selex-ES)** **(8:45)**
C. D. Maxey, J. W. Wilson, I. Baker, L. Hipwood
Leonardo, Southampton, UK

5.2:
Geometrical Characteristic of Cd-Rich Inclusion Defects in CdZnTe Materials **(9:15)**
C. Xu, F. Sheng, J. Yang
Shanghai institute of Technical Physics, Chinese Academy of Sciences, Shanghai, P. R. China

5.3:
Characterization of (211) and (100) CdTe Layers Grown on Si Substrates by Metalorganic Vapor-Phase Epitaxy **(9:30)**
K. Yasuda, M. Niraula, M. Kojima, S. Kitagawa, S. Tsubota, T. Yamaguchi, J. Ozawa, Y. Agata
Nagoya Institute of Technology, Nagoya, Japan

5.4:
Invited Paper: **Simulation of Molecular-Beam Epitaxy Semiconductor Film Growth** **(9:45)**
C. H. Grein, A. Ciani
University of Illinois at Chicago, Chicago, IL, USA

BREAK **(10:15–10:30)**

6: SOLAR II
(10:30 am – 12:15 pm)

Chair: **T. Gessert**
EPIR, Inc., Bolingbrook, IL, USA

Co-Chair: **T. Myers**
Texas State University at San Marcos, San Marcos, TX, USA

6.1:
Invited Paper: **Chalcogenide Perovskites as Ionic Semiconductors for Photovoltaics** **(10:30)**

Y.-Y. Sun, M. L. Agiorgousis, S. B. Zhang
Rensselaer Polytechnic Institute, Troy, NY, USA

P. Zhang, H. Zeng
University at Buffalo, State University of New York, Buffalo, NY, USA

6.2:
Carrier-Lifetime Study of Undoped and Iodine-Doped CdMgTe/CdSeTe Double Heterostructures Grown by Molecular-Beam Epitaxy **(11:00)**

S. Sohal, M. Edirisooriya, O. S. Ogedengbe, J. E. Petersen, C. H. Swartz, E. G. LeBlanc, T. H. Myers, J. V. Li, M. Holtz,
Texas State University at San Marcos, San Marcos, TX, USA

6.3:
Controlling the Magnesium Composition in CdTe/CdMgTe Heterostructures **(11:15)**

E. G. LeBlanc, M. Edirisooriya, O. S. Ogedengbe, O. C. Noriega, P. A. R. D. Jayathilaka, S. Rab, C. H. Swartz, T. H. Myers
Texas State University at San Marcos, San Marcos, TX, USA

D. Diercks, G. Burton, B. Gorman
Colorado School of Mines, Golden, CO, USA

A. Wang
EAG Laboratories (Evans Analytical Group), Sunnyvale, CA, USA

T. M. Barnes
National Renewable Energy Laboratory, Golden, CO, USA

6.4:
van der Waals Epitaxy of CdTe Thin Film Using Graphene as the Buffer Layer **(11:30)**

D. Mohanty, W. Xie, Y. Wang, Z. Lu, J. Shi, S. Zhang, G.-C. Wang, T.-M. Lu, I. B. Bhat
Rensselaer Polytechnic Institute, Troy, NY, USA

6.5:
Invited Paper: **Monocrystalline CdTe/MgCdTe Double-Heterostructure Solar Cells with a V_{oc} over 1.1 V and an Efficiency over 18%** **(11:45)**

Y-H. Zhang
Arizona State University, Tempe, AZ, USA

LUNCH **(12:15-1:45)**

7: MODELING II
(1:45 – 3:30 pm)

Chair: **E. Piquette**
Teledyne, Camarillo, CA, USA

Co-Chair: **J. Pellegrino**
U.S. Army RDECOM, CERDEC, NVESD, Aberdeen, MD, USA

7.1:
Analytical and Numerical Analysis of Depletion-Region Currents in Extrinsic and Intrinsic VLWIR HgCdTe Detectors **(1:45)**

J. Schuster, P. S. Wijewarnasuriya
Army Research Laboratory, Adelphi, MD, USA
R. E. DeWames
Manufacturing Techniques, MTEQ, Lorton, VA, USA

7.2:
Auger and Radiative Lifetimes in ESWIR Materials: HgCdTe, InGaAs, and GeSn **(2:00)**

A. Glasmann, S. Dominici, H. Wen, E. Bellotti
Boston University, Boston, MA, USA

7.3:
Native Point-Defect Levels in Strained-Layer Superlattices **(2:15)**

S. Krishnamurthy
SRI International, Menlo Park, CA, USA
Z-G. Yu
Washington State University, Spokane, WA, USA

7.4:
The Evolution of Kinetically-Limited Lattice Relaxation and Threading Dislocation in Temperature-Graded ZnSe/GaAs (001) Metamorphic Heterostructures **(2:30)**

T. Kujofsa, J. E. Ayers
University of Connecticut, Storrs, CT, USA

7.5:
Scattering in HgCdTe nBn Detector with Superlattice Barrier **(2:45)**

N. D. Akhavan, G. Umana-Membreno, J. Antoszewski, L. Faraone
University of Western Australia, Crawley, Australia

7.6:
Invited Paper: **Development and Production of Array Barrier Detectors at SCD** **(3:00)**

P. Klipstein
Semiconductor Devices, Haifa, Israel

BREAK **(3:30–3:45)**

8: DEVICES II
(3:45 – 5:30 pm)

Chair: **C. Hoffman**
Naval Research Laboratory, Washington, DC, USA

Co-Chair: **R. DeWames**
U.S. Army NVESD, Ft. Belvoir, VA

8.1:
Invited Paper: **Variations around p-on-n HgCdTe with Liquid-Phase Epitaxy** **(3:45)**
N. Baier, O. Gravrand, C. Cervera, C. Lobre, F. Rochette
CEA-LETI, Grenoble, France

8.2:
HgTe Quantum Dots for Near-, Mid-, and Long-Wavelength IR Devices **(4:15)**
W. Palosz, S. Trivedi, D. Zhang
Brimrose Corporation of America, Sparks, MD, USA
G. Meissner, K. Olver, E. DeCuir, P. S. Wijewarnasuriya
Army Research Laboratory, Adelphi, MD, USA
J. L. Jensen
Edgewood Chemical Biological Center, Aberdeen Proving Ground, MD, USA

8.3:
Advances in HgTe Colloidal Quantum Dots for Infrared Detectors **(4:30)**
A. J. Ciani, R. E. Pimpinella, C. H. Grein
Sivananthan Laboratories, Bolingbrook, IL, USA
P. Guyot-Sionnest
James Franck Institute, Chicago, IL, USA

8.4:
Optical Amplification in a Single CdSe–Nanowire Based Light-Effect Transistor (LET) for High Sensitivity and Responsivity Photodetection **(4:45)**
J. K. Marmon, Y. Zhang
University of North Carolina at Charlotte, Charlotte, NC, USA
S. C. Rai, K. Wang, W. Zhou
University of New Orleans, New Orleans, LA, USA

8.5:

Performance of Science-Grade HgCdTe H4RG-15 Image Sensors **(5:00)**

M. Zandian, M. Farris, W. McLevige, D. Edwall, E. Arkun, E. Holland, M. Carmody, J. Auyeung, J. W. Beletic
Teledyne Imaging Sensors, Camarillo, CA, USA
J. E. Gunn
Princeton University, Princeton, NJ, USA
S. Smee
John Hopkins University, Baltimore, MD, USA
D. N. B. Hall, K. W. Hodapp
University of Hawaii, Hilo, HI, USA
A. Shimon, N. Tamura
Kavli Institute for the Physics and Mathematics of the Universe, Kashiwa, Japan

8.6:

An Empirical Study of the Disparity in Radiation Tolerance of the Minority-Carrier Lifetime between II-VI and III-V Space Detector Technologies in the MWIR **(5:15)**

G. D. Jenkins, C. P. Morath, V. M. Cowan
Air Force Research Laboratory, Albuquerque, NM, USA

THURSDAY, OCTOBER 20, 2016
Chesapeake Ballroom
(7:30 am – 3:00 pm)

Registration **(7:30–2:00)**

Continental Breakfast **(7:30–8:00)**

9: CHARACTERIZATION AND PROCESSING I
(8:00 – 10:15 am)

Chair: **J. Burns**
AFRL, Wright-Patterson AFB, OH, USA

Co-Chair: **R. James**
Brookhaven National Laboratory, Upton, NY, USA

9.1:
Invited Paper: **Novel Applications and New Physical Phenomena Based on Heterovalent and Heterocrystalline Nanostructures** **(8:00)**

M. Tamargo
The City College of New York, New York, NY, USA

9.2:
Chemical Etching and Chemomechanical Polishing of CdZnTe X-Rays and Gamma-Ray Detectors **(8:30)**

S. U. Egarievwe
Alabama A&M University, Normal, AL, USA
and
University of Tennessee, Knoxville, TN, USA
and
Brookhaven National Laboratory, Upton, NY, USA

E. D. Lukosi
University of Tennessee, Knoxville, TN, USA

E. O. Agbalagba
Federal University of Petroleum Resources, Effurun, Delta State, Nigeria

A. Hossain, U. N. Roy, A. E. Bolotnikov
Brookhaven National Laboratory, Upton, NY, USA

R. Gul
Alabama A&M University, Normal, AL, USA
and
Brookhaven National Laboratory, Upton, NY, USA

R. B. James
Savannah River National Laboratory, Science & Technology, Aiken, SC, USA

9.3:
Effects of Electrode Contacts on the Performance of CdZnTe Film UV Detectors **(8:45)**

L. Wang, J. Huang, K. Tang, Y. Shen
Shanghai University, Shanghai, P. R. China

9.4:
Dry-Etching Characteristics of MOVPE-Grown CdTe Epilayers in CH_4, H_2, Ar ECR Plasmas **(9:00)**

K. Yasuda, M. Niraula, N. Araki, M. Miyata, S. Kitagawa, M. Kojima, J. Ozawa, S, Tsubota, T. Yamaguchi, Y. Agata
Nagoya Insitute of Technology, Nagoya, Japan

9.5:
Overcoming Etch Challenges on a 6-in. MBE $Hg_{1-x}Cd_xTe$/Si Wafer **(9:15)**

P. Apte, E. Norton, S. Robinson
Raytheon Vision Systems, Goleta, CA, USA

9.6:
Defect- and Chemical-Induced Tuning of Exciton–Phonon Coupling in Bulk and Thin-Film ZnTe for Optically Driven Sensor Applications **(9:30)**

J. K. Marmon, T. Sheng, H. Zhang, Y. Zhang
University of North Carolina at Charlotte, Charlotte, NC, USA

Y. Chen, P. S. Wijewarnasuriya
Army Research Laboratory, Adelphi, MD, USA

9.7:
Optical, Structural, and Electrical Characterization of $Cd_{1-x}Zn_xTe$ Thin Films Deposited by Thermal Evaporation **(9:45)**

Z. Ali, M. Ashraf
Optics Laboratories, Islamabad, Pakistan

M. Ali, A. Syed
International Islamic University, Islamabad, Pakistan

9.8: (Formerly Late-News Paper 12.3)
Characterization of Thermally Treated MgZnO Nanowire Alloys Synthesized by the Vapor-Transport Technique for Deep UV Detection **(10:00)**

E. A. Azhar, J. Vanjaria, S. Ahn, T. Salagaj, N. Sbrockey, G. Tompa, H. Yu
Arizona State University, Tempe, AZ, USA

BREAK **(10:15-10:30)**

10: CHARACTERIZATION & PROCESSING II
(10:30 am – 12:00 pm)

Chair: **A. Burger**
Fisk University, Nashville, TN, USA

Co-Chair: **I. Bhat**
Rensselaer Polytechnic Institute, Troy, NY, USA

10.1:
Micro-Diffraction Investigation of Localized Strain in Mesa-Etched HgCdTe Photodiodes **(10:30)**

A. Tuaz, P. Ballet
Universitié Grenoble Alpes, CEA-LETI, Grenoble, France

X. Biquard, F. Rieutord
Universitié Grenoble Alpes, CEA, INAC-SP2M, NRS, Grenoble, France

10.2:
Temperature and Injection Dependence of Photoluminescence Decay in MWIR HgCdTe **(10:45)**

B. Delacourt, P. Ballet, F. Boulard, A. Ferron, L. Bonnefond, T. Pellerin, J. Rothman
Universitié Grenoble Alpes, CEA-LETI, Grenoble, France

A. Kerlain, V. Destefanis
SOFRADIR – Development and Production Center, Veurey-Voroize, France

10.3:
Diffusion Mechanism for Arsenic in Intrinsic and Extrinsic HgCdTe **(11:00)**

T. Grenouilloux
SOFRADIR, Palaiseau, France
and
Université de Strasbourg and CNRS, Strasbourg, France

A. Ferron
Universitié Grenoble Alpes, CEA-LETI, Grenoble, France

N. Péré-Laperne
SOFRADIR, Palaiseau, France

D. Mathiot
Université de Strasbourg and CNRS, Strasbourg, France

10.4:

Effect of Buffer Layer on the Properties of Boron and Gallium Co-Doped ZnO Films **(11:15)**

J. Huang, J. Yang, L. Yuanxi, K. Tang, F. Gu, Y. Lu, L. Wang
Shanghai University, Shanghai, P.R. China

10.5:

Characterization of Evolution of Implant-Induced Defects in Arsenic-Implanted and Annealed HgCdTe Epilayers **(11:30)**

C. Shi, C. Lin, Y. Wei, L. Chen
Shanghai Institute of Technical Physics, Chinese Academy of Sciences, Shanghai, P.R. China

10.6:

Variable-Field Hall-Effect Analysis of HgCdTe Epilayers with Very Low Doping Density **(11:45)**

J. Easley, J. Phillips
University of Michigan, Ann Arbor, MI, USA
E. Arkun, M. Carmody
Teledyne Imaging Sensors, Camarillo, CA, USA

LUNCH **(12:00-1:30)**

11: DEVICES III
(1:30 – 2:45 pm)

Chair: **W. Clark**
Army Research Office, Durham, NC, USA

Co-Chair: **P. Mitra**
DRS Technologies, Dallas,TX, USA

11.1:
Metamorphic Buffers for High-Absorption Long-Wave-Infrared Superlattices and Bulk Materials **(1:30)**

C. A. Affouda, S. Tomasulo, N. Mahadik, M. Twigg, J. A. Nolde, E. M. Jackson, E. R. Cleveland, E. H. Aifer
Naval Research Laboratory, Washington, DC, USA

11.2:
Plasmonic Grating Design and Optimization for Increased Operating Temperature of MWIR nBn Detectors **(1:45)**

E. M. Jackson, J. A. Nolde, M. Kim, C. S. Kim, C. T. Ellis, E. R. Cleveland, C. A. Affouda, C. L. Canedy, J. G. Tischler, O. J. Glembocki, I. Vurgaftman, J. R. Meyer, E. H. Aifer
Naval Research Laboratory, Washington, DC, USA

11.3:
Development of Nanostructured Antireflection Coatings for Infrared Sensors and Optical Applications **(2:00)**

G. G. Pethuraja, R. E. Welser, A. K. Sood, Y. R. Puri
Magnolia Optical Technologies, Inc., Woburn, MA and Albany, NY, USA

H. Efstathiadis, P. Haldar
CNSE, SUNY Polytechnic Institute, Albany, NY, USA

N. K. Dhar
U.S. Army NVESD, Ft. Belvoir, VA, USA

E. A. DeCuir, P. S. Wijewarnasuriya
Army Research Laboratory, Adelphi, MD, USA

11.4:
Invited Paper: **Epitaxial HgCdTe on Silicon and CdZnTe Substrates: A Performance Comparison** **(2:15)**

C. Fulk
Raytheon Vision Systems, Goleta, CA, USA

WILLIAM E. SPICER
and
THOMAS N. CASSELMAN
Best Student Paper Award
(2:45 – 3:00)

CLOSING REMARKS **(3:00–3:15)**

NOTES

NOTES

NOTES

Journal of ELECTRONIC MATERIALS, Vol. 46, No. 9, 2017
DOI: 10.1007/s11664-017-5661-z

Foreword

The 2016 U.S. Workshop on the Physics and Chemistry of II–VI Materials (a.k.a. U.S. II–VI Workshop) was held at the Sheraton Inner Harbor Hotel, in Baltimore, Maryland, USA, on October 17–20, 2016. This workshop was the 35th in the series, which began in October 1981 in Minneapolis, Minnesota, USA. The first meeting was dedicated to the scientific and generic technological issues of importance to mercury cadmium telluride and its applications in infrared imaging. The workshop interest has now evolved to include all II–VI materials having application in a variety of emitters and detectors. Since 1989, the workshop expanded its scope to include related II–VI materials such as CdTe and CdZnTe which are used as substrates for epitaxial HgCdTe growth, as well as for gamma ray detectors and solar cells, and for other electro-optical II–VI materials such as ZnO and ZnMgO.

The 2016 U.S. II–VI workshop offered a venue for discussions for 3 days, bringing together 41 contributed and 12 invited talks along with a keynote speaker. Nearly half of these presentations are published in this volume of *Journal of Electronic Materials* (JEM), all of which have been carefully peer-reviewed. The 2016 workshop co-chairs were Dr. Ishwara Bhat of the Rensselaer Polytechnic Institute and Dr. Pradip Mitra of DRS Technologies, Inc. Alicia Waldron and Samantha Tola of the Palisades Convention Management, Inc. and Paola Caicedo of the University of Illinois at Chicago coordinated the workshop arrangements and on-site activities, while Yesim Anter of the EPIR Technologies, Inc.* coordinated the editorial arrangements and proceedings.

Dr. Larry Schuette of the Office of the Naval Research gave the keynote speech on “Naval S&T: The Innovation Engine”. Several interesting papers were presented in subject areas of solar cells, CdZnTe substrates, gamma ray detectors, type-II strained layer superlattices, devices, processing, characterization, impurity doping and defects in II–VI materials.

In 2016, the “William E. Spicer-Thomas N. Casselman Award” for best student paper was presented to Elizabeth LeBlanc of the Texas State University for her presentation on “Controlling the Magnesium Composition in CdTe/CdMgTe Heterostructures”. She is advised by Professor Tom Meyers. The award acknowledges excellence in student paper presentations. For more information about the award and previous recipients, please visit our website: www.ii-viworkshop.org.

The U.S. II–VI Workshop Committee would like to thank the following organizations for their continued sponsorship:

- U.S. Army RDECOM CERDEC Night Vision & Electronic Sensors Directorate.
- U.S. Army Research Laboratory.
- U.S. Army SMDC.
- U.S. Navy Electro-Optics Center, Penn State University.
- Office of Naval Research.
- Air Force Research Laboratory.
- Army Research Office.
- The Minerals, Metal & Materials Society.

The American Physical Society has endorsed this workshop.

The proceedings of the original workshops (from 1981 to 1991) have been published in the *Journal of Vacuum Science and Technology*. Papers from the workshop from 1992 onward appear in special issues of the *JEM*.

*Now with Sivananthan Laboratories Inc.

(Published online July 13, 2017)

TABLE OF CONTENTS

Session 1: Devices I

Session 2: Modeling I

Session 3: Growth I

Session 4: Solar I

Session 5: Growth II

Session 6: Solar II

Session 7: Modeling II

Session 8: Devices II

Session 9: Characterization and Processing I

Session 10: Characterization & Processing II

Session 11: Devices III

STUDENT PAPERS

HgCdTe - A Vision for the Near Future

D. Lee, [1,3] M. Carmody, [1] E. Piquette, [1] P. Dreiske,[1] A. Chen, [1] A. Yulius, [1] D. Edwall, [1] S. Bhargava, [1] M. Zandian [1] and W. E. Tennant [2]

1. –Teledyne Imaging Sensors, 5212 Verdugo Way, Camarillo, CA 93012. 2. – Tennant Electro Optics Consulting, Inc., 1579 Calle Yucca, Thousand Oaks, CA 91360. 3. – E-mail: donald.lee@teledyne.com

ABSTRACT

In this paper we review recent advances in the HgCdTe material quality and detector performance achieved at Teledyne using MBE growth and the Double Layer Planar Hetero-junction (DLPH) detector architecture.[1]

By using an un-doped, fully depleted absorber[2], Teledyne's DLPH architecture can be extended for use in High Operating Temperature (HOT) and other applications.

We assess the potential achievable performance for LWIR hetero-junction PIN detectors based on recently reported results for 10.7µm cutoff 1Kx1K FPAs tested at temperatures down to 30K. [3] Variable temperature dark current measurements show that any Shockley-Read-Hall currents in the depletion region of these devices have lifetimes that are reproducibly greater than 100ms. This lifetime predicts that fully-depleted radiatively-limited performance can be expected for 10µm cutoff detectors from room temperature to well below liquid nitrogen temperatures, with room temperature dark current nearly 400 times lower than predicted by Rule 07.[4,5]

The hetero-junction PIN diode is shown to have numerous other significant potential advantages including minimal or no passivation requirements for pBn-like processing[6], low 1/f noise, compatibility with small pixel pitch while maintaining high MTF, low crosstalk and good QE.

By appropriate design of the FPA dewar shielding, analysis shows that dark current can theoretically be further reduced below the thermal equilibrium radiative limit.

Modeling shows that radiatively-limited LWIR HgCdTe operating with f/1 optics has the potential to operate within √2 of BLIP at 215K. By reducing the background radiation by 2/3 using novel shielding methods, operation with a single-stage TE-cooler may be possible. If the background radiation can be reduced by 90%, then room temperature operation is possible.

Key words: HgCdTe, HOT detectors, LWIR, Radiative-limit, Auger-suppressed, PIN detector

[1] J.M. Arias, et. al, Appl. Phys. Lett., V.62, 976 (1993).
[2] US Patent 7368762 B2 Heterojunction Photodiode
[3] D. Lee et. al, 2014 Parallel meetings of the MSS Symposia Specialty Groups on Passive Sensors, Battlefield Survivability & Discrimination; Materials and Detectors
[4] W. Tennant et. al, J. Electronic Materials, V.37, 1406 (2008)
[5] W. E. Tennant, J. Electron. Mater. 39, 1030 (2010)
[6] A. Rogalsi, P. Martyniuk, J. Electronic Materials, V.43, 2963 (2014)

Progress of MCT detector technology at AIM towards smaller pitch and lower dark current

D. Eich*, W. Schirmacher, S. Hanna, K.M. Mahlein, P. Fries, and H. Figgemeier

AIM INFRAROT-MODULE GmbH, Heilbronn, Germany

In recent years, the IR-detector community has worked hard on raising the operating temperature of cooled detectors and on decreasing the pixel pitch[1,2,3,4]. AIM as a leading supplier of cooled MCT-based detectors devoted its research efforts besides an ongoing improvement of standard n-on-p technology to the development of a p-on-n detector technology while shrinking the pixel size at the same time[5,6,7]. Here we present the most recent results of this development. Detectors based on the p-on-n technology developed at AIM now span the spectrum from MWIR to VLWIR (cut-off wavelengths from 5µm to 13.5 µm).

AIM's technology for n-on-p and p-on-n MCT detector manufacturing is based on the liquid phase epitaxial (LPE) growth of MCT from a Te-rich melt on lattice-matched in-house grown CdZnTe substrates using a vertical dipping method. The photodiode array technology for p-on-n is realized by a p-type implant of As into an n-type absorber and subsequent activation of the As dopant. The development of the p-on-n technology for the (V)LWIR as well as for the MWIR is mainly made in a planar photodiode detector design with 640x512 pixels and a 20 µm pixel pitch. We compare the performance of these devices by looking at important figures of merit such as noise equivalent temperature difference (NETD) (Figure 1), defective pixel count (Figure 2), dark current and noise characteristics. The focus of this comparison is on the high temperature performance of these devices. The results show the considerable improvements recently made compared to earlier technology approaches. To illustrate the achieved technology level, IR-pictures at various operating temperatures are displayed (Figure 3).

*Corresp. author: detlef.eich@aim-ir.com, Phone: +49-7131-6212-171, Fax: +49-7131-6212-199

Furthermore, the results of recent developments of small pixel pitch devices are presented. Concerning the pixel pitch reduction, AIM provides FPAs with 1280x720 pixels on a 12µm pitch and with 1024x768 pixels on a 10µm pitch. This 10 µm pitch detector is best suited to upgrade the standard MWIR 640x512 pixel, 15µm pitch detector, mainly for HOT and, e.g., hand-held applications. Recent results (Figure 4) of several 10µm pitch detectors produced by different technological approaches are shown and discussed.

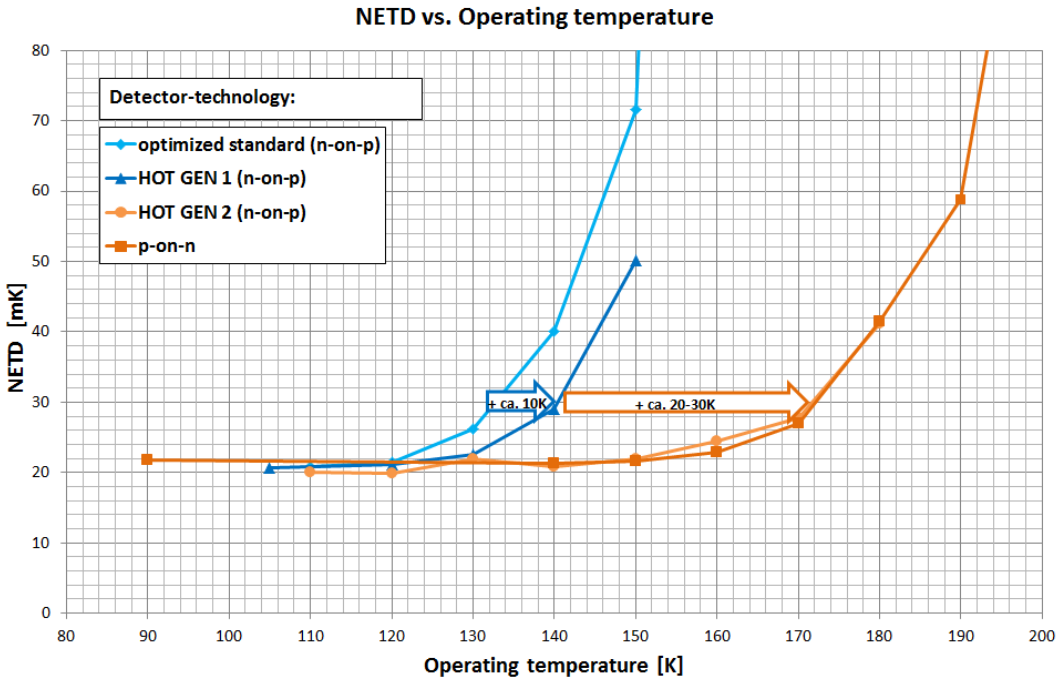

Figure 1: NETD as a function of FPA operating temperature made from three different n-on-p and one p-on-n MWIR detectors with a (5.2 ± 0.1) µm cut-off wavelength at 80K.

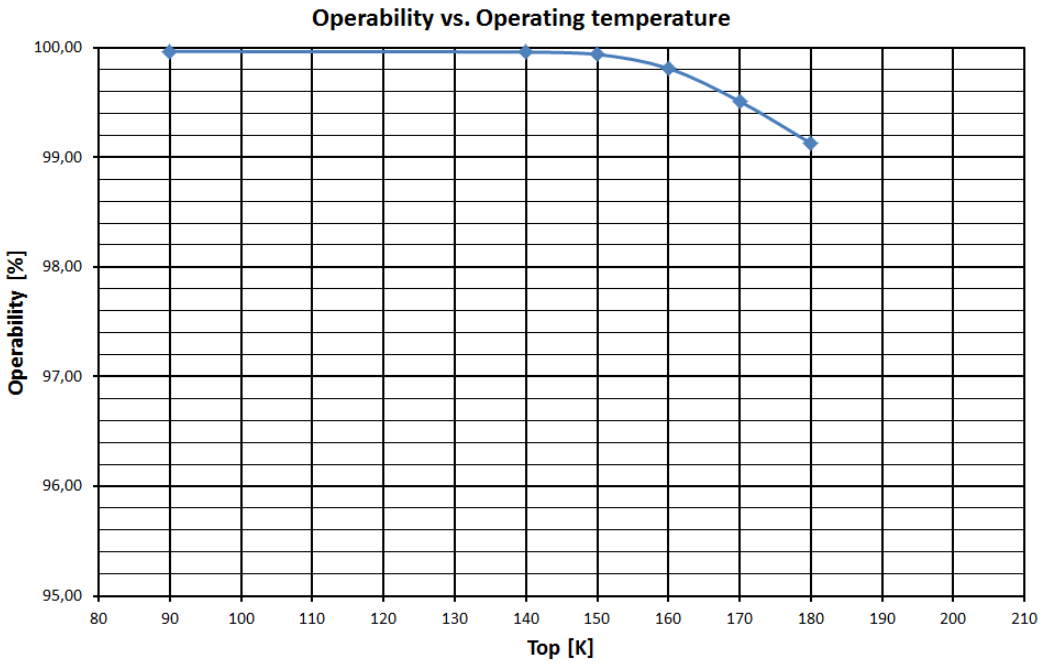

Figure 2: Operability as a function of FPA operating temperature of an AIM p-on-n MWIR detector (640x512, 20 µm pitch, F# 2,1; Defect pixel criterion: [0,2] x NETD mean, [0.5,2] x gain mean, [0,5] x noise median).

Figure 3: Infrared images taken with an AIM p-on-n MWIR MCT FPA of a person (2-point corrected, with bad pixel replacement) for detector operating temperatures between 120K and 220K. The detector's cut-off wavelength is 5.25 µm at 80K.

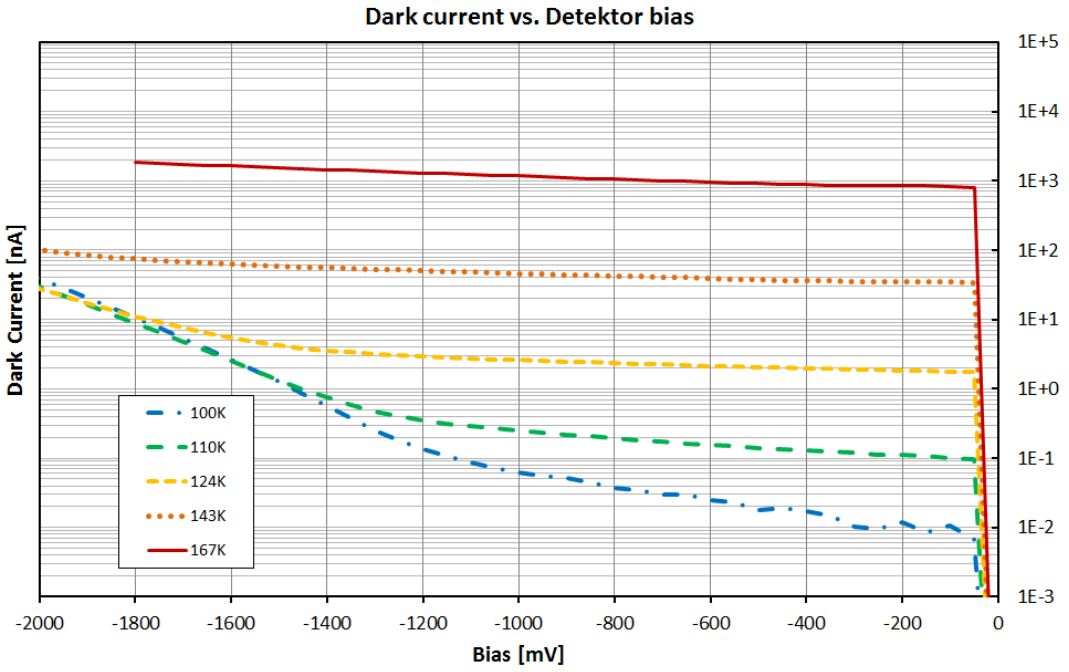

Figure 4: Dark current as a function of detector bias voltage of a 100x100 p-on-n planar photodiode pixel array with a 10 µm pixel pitch for different operating temperatures; applied guard-bias: -250 mV (cut-off wavelength: 5.25 µm at 80K).

References

[1]Pillans, L., Baker, I., McEwen, R.K., "Ultra-low power HOT MCT grown by MOVPE for handheld applications“, Proc. SPIE 9070, 90701E (2014).

[2]Karni, Y., Klipstein, P., Avnon, E., Berkowitz, E., Cohen, O., Cohen, Y., Dobromislin, R., Hirsh, I., Klin, O., Lukomsky, I., Pivnik, I., Rozenberg, O., Shtrichman, I., Singer, M., Sulimani, S., Weiss, E., “Large format 15µm pitch XBn detector”, Proc. SPIE 9070, 90701F (2014).

[3]Reibel, Y., Taalat, R., Brunner, A., Rubaldo, L., Augey, A., Kerlain, A., Péré-Laperne, N., Manissadjian, A., Gravrand, O., Castelein, P., Destéfanis, G., "Infrared SWAP Detectors: pushing the limits“, Proc. SPIE 9451, 945110 (2015).

[4]Ramirez, D., Plis, E., Myers, S., Morath, C., Cowan, V., Krishna, S., “High-operating temperature MWIR unipolar barrier photodetectors based on strained layer superlattices”, Proc. SPIE 9451, 945113 (2015).

[5]Hanna, S., Eich, D., Mahlein, K.-M., Fick. W., Schirmacher,. W., Thöt. R., Wendler, J., Figgemeier, H., “MCT-Based LWIR and VLWIR 2D Focal Plane Detector Arrays for Low Dark Current Applications at AIM”, J. of ELECTR. MAT., Vol. 45, No. 9, (2016).

[6]Wollrab, R., Schirmacher, W., Schallenberg, T., Lutz, H., Wendler, J., Ziegler, J., „Recent Progress in the Development of HOT MWIR-Detectors”, Paris OPTRO-2014-2967621

[7]Lutz, H., Breiter, R., Eich, D., Figgemeier, H., Fries, P., Rutzinger, S., Wendler, J., „Small pixel pitch MCT IR-modules“, Proc. SPIE 9819, 98191Y (2016).

Short Wavelength Infrared (SWIR) N+/p $Hg_{1-x}Cd_xTe$ diodes for LADAR Applications

Eric A. DeCuir Jr., Kimberley Olver, James Pattison, Priyalal S. Wijewarnasuriya
U.S. Army Research Laboratory, 2800 Powder Mill Rd., Adelphi, MD, USA 20783-1138
Paul Boieriu
EPIR Technologies, 590 Territorial Drive, Suite B, Bolingbrook, IL 60440

ABSTRACT

The Army Research Laboratory has ongoing efforts to push the performance of Laser Detection and Ranging (LADAR) systems for eye-safe laser ranging efforts on small unmanned ground vehicles (UGVs) and unmanned aerial vehicles (UAVs). Improved LADAR performance drives the need for large area, low capacitance photodiodes for improved range sensitivity and speed, respectively. In an effort to improve the performance of these systems, recent efforts have focused on investigating the suitability and performance of SWIR N+/p HgCdTe photodiode architecture in lieu of commercial $In_{0.53}Ga_{0.47}$ as diodes currently used in this system. Specifically, an N+/p HgCdTe double planar heterostructure diode architecture was adopted to provide access to high mobility minority carriers (electrons) in the absorber region in order to achieve high frequency responses above the 250 MHz range. The SWIR structure consists of an $Hg_{1-x}Cd_xTe$ heterostructure grown by Molecular Beam Epitaxy (MBE). The grown layer was extrinsically doped with indium as n-type and then converted to p-type utilizing a Hg vacancy anneal which resulted in a p-type layer. A cadmium fraction (x) of 0.592 was selected for the absorber layer which yielded a 1.71 um 50% cut-off at T=300K. A lateral collection device architecture is utilized to minimize the diode capacitance by adopting a hexagonal arrangement of N+ pocket boron implants [1-2] which are spaced not to exceed a minimum of twice the diffusion length. The overall capacitance of the lateral collection architecture, like its full implant analogue, is also related to the area and width of the depletion region which is also bias dependent. Additionally, since the application of this work mandated the fabrication of large area diodes ($1mm^2$ or greater), the lateral collection architecture provides higher yield/operability over the full implant analogue due to the reduced probability of intersecting defects[1-2].

Previous studies on P+/n PV devices revealed diminished response at frequencies greater than 400 MHz and 5 MHz when illuminated from the p-side or n-side, respectively. An intuitive understanding of this behavior is attributed to the disparity of minority carrier mobilities in n-side (holes) and p-side (electrons). Hence the rationale for adopting a HgCdTe architecture which gives access to high mobility minority carriers (electrons) in a p-type absorber. In this work, we present current vs. voltage, QE vs. wavelength, capacitance vs. voltage/frequency, and response vs. frequency to better understand the suitability of this device architecture for high speed LADAR applications. In addition to device studies, the material was further characterized with Photoconductive decay (PCD) spectroscopy to determine the minority carrier lifetime in the vacancy doped absorber layer.

Keywords: LADAR, SWIR, HgCdTe, PCD, detector, lateral collection, vacancy

[1] H. Holloway, “Theory of lateral-collection photodiodes.” J. Appl. Phys. 49, 4264 (1978)

[2] Wijewarnasuriya, P.S. et.al., “Advances in large area Hg1-xCdxTe Photovoltaic Detectors for Remote Sensing Applications,” *Proc. SPIE Materials for Infrared Detectors*, Vol. 4454, (2001)

Absolute Temperature Sensing by a Two-color ZnCdSe/ZnCdMgSe Detector

Yasin Kaya[1], Arvind Ravikumar[1,2], Guopeng Chen[3], Maria C. Tamargo[4], Aidong Shen[3], and Claire Gmachl[1]
[1]*Department of Electrical Engineering, Princeton University, Princeton, NJ 08544, USA*
[2]*Current Address: Department of Energy Resources Engineering, Stanford University, Stanford CA 94305, USA*
[3]*Department of Electrical Engineering, The City College of New York, NY 10031, USA*
[4]*Department of Chemistry, The City College of New York, NY 10031, USA*
Author e-mail address: ykaya@princeton.edu

Multi-color detection plays a key role in target recognition applications. The idea is to eliminate the object depended parameters to obtain the absolute temperature. There are optical system approaches of implementing multi-color detection such as using separate single-color detectors in company with filter wheels, beam splitters and mirrors. However, additional optical elements introduce a delay to the collection of the signal from different optical bands as well as requiring more space and being more vulnerable to mechanical noise. Our alternative approach is growing two detectors on top of each other by using a single material system which can cover two optical bands. ZnCdSe/ZnCdMgSe is a favorable material system since the quantum wells formed by a large conduction band offset (up to ~1.2 eV) support both mid wavelength (MWIR) and long wavelength (LWIR). The quantum wells structure is grown lattice matched to the InP substrate.

After the growth, the wafer was processed by using conventional photolithography and wet etching techniques into two step structure (Fig. 1) which makes possible to control each detector independently and simultaneously. One facet of the sample was polished at 45° to have strong light coupling. The peak wavelength response of MWIR and LWIR detectors were measured at 4.8 μm and 7.6 μm. The spectral responses of the detectors were mostly preserved for high temperatures as shown in Fig. 2. The maximum signal to noise ratio, detectivity, versus the applied bias on the detectors was characterized by using a calibrated black body source. After finishing the characterization of the detectors, the absolute temperature measurement was performed by taking the ratio of the integrated current signals from both detectors. Fig. 3 shows the good consistency between theoretical calculations and the experimental results for the absolute temperature sensing application. The experimental results show that ZnCdSe/ZnCdMgSe two color detectors have comparable performance with commercially available multi-color QWIP detectors and they can also be used for the absolute temperature detection application.

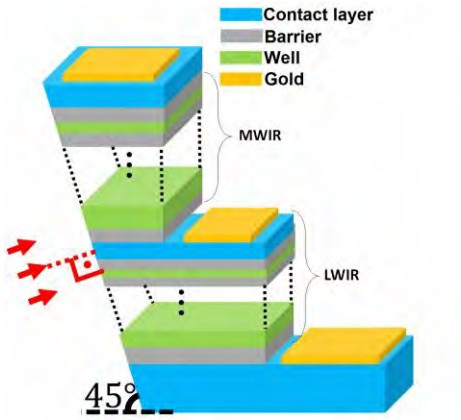

Figure 1: The schematic representation of two-color ZnCdSe/ZnMgCdSe quantum well infrared detector after fabrication

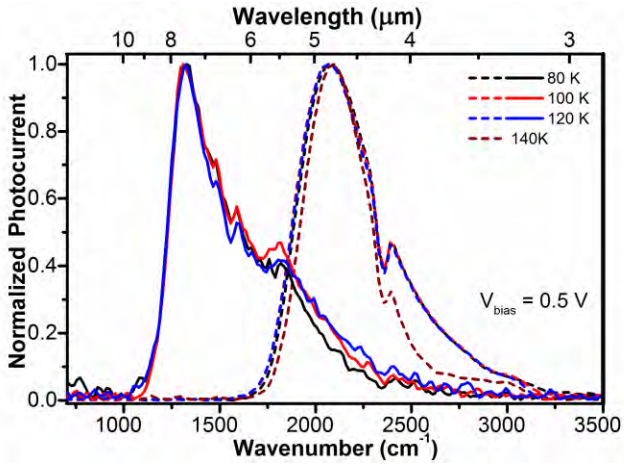

Figure 2: Independently measured normalized photocurrent spectrum of MWIR (solid lines) and LWIR (dashed lines) detectors at 0.5 V applied bias. Different colors corresponds measurement at different temperatures

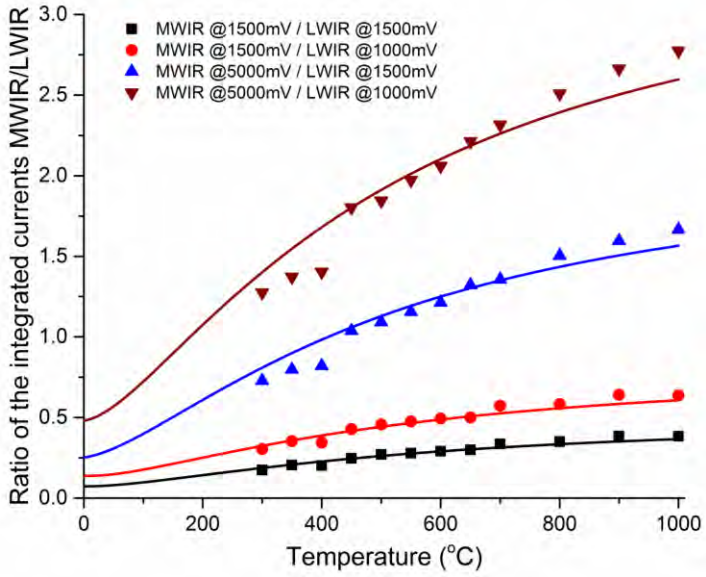

Figure 3: Solid lines and scattered points represent theoretical calculations and experimental results for the current ratio between MWIR and LWIR detectors, respectively. Different colors corresponds to different applied biases on the detectors.

HgCdTe Avalanche Photodiodes for UV to IR Photon Counting*

William Sullivan III, Jeff Beck, Mark Skokan, Chris Schaake, Richard Scritchfield, Pradip Mitra

DRS Technologies, Dallas, TX

Darren Carpenter and Barry Lane

A/DIC Inc., Longwood, FL

Abstract: Linear mode HgCdTe electron avalanche photodiodes (APDs) with photon counting sensitivity from ultraviolet to infrared were fabricated using DRS' High Density Vertically Integrated Photodiode (HDVIP™) cylindrical diode format in a 2x8 array with 64 µm pixel pitch. Previously, DRS demonstrated photon counting APD arrays using 4.4 µm cutoff HgCdTe with false event rates (FERs) of approximately 200 kHz at over 60% flooded field photon detection efficiencies (PDEs). Adding microlens arrays (MLAs) to these 4.4 µm cutoff devices increased the PDEs to over 80% by providing 100% fill factor. Shortening the cutoff to 3.7 µm reduced the overall system false event rate (FER) by a factor of 5 to approximately 40 kHz while still simultaneously achieving flooded field PDEs of greater than 60%. Stable gains of over 2000 on the 3.7 µm cutoff arrays were achieved at bias voltages of only 15 V by reducing the diode pn-junction diameters to 19 µm. These front-side illuminated arrays exhibit a wide spectral response from 350 nm to 3.7 µm. Array level test data will be presented and other improvements implemented will be discussed.

Keywords: HgCdTe, avalanche photodiode, photon counting, photon detection efficiency, infrared, ultraviolet

1. Introduction

Recently, DRS has developed a 3rd generation of its 2x8 format HgCdTe electron avalanche photodiode focal plane array (FPA) detectors. These detectors feature continuous single photon counting sensitivity across the UV, visible, and IR spectral bands and exhibit sub-10 ns minimum time between single photon

*Supported by DRS internal funds, NASA Goddard Space Flight Center and NASA Jet Propulsion Lab

events. All 3 generations were fabricated on a 64 µm pitch pixel using DRS' High Density Vertically Integrated Photodiode (HDVIP™) top-illuminated diode architecture. Each pixel is comprised of 4 parallel APDs in a 2x2 configuration. In 2015 DRS reported on its 2nd generation FPAs which made performance improvements to the 1st generation FPAs including reducing the dark count rate (also referred to herein as the false event rate (FER)), increasing the PDE, and optimizing the pixel's geometry [1]. To reduce the FER, an opaque metal layer was added under the APD array to block photons emitted from the readout integrated circuit (ROIC) from reaching the APDs, and the ROIC's biases were optimized to reduce the amount of ROIC emitted photons. To increase the PDE, the APDs' junction diameters were optimized to increase APD gain, and a more efficient anti-reflection (AR) coating was developed and implemented. Good photon counting performance was measured with PDEs of over 60% reached at FERs of 200 kHz [1,2]. Both the 1st and 2nd generation 2x8 FPAs were fabricated from 4.4 µm cutoff HgCdTe. All measurements were performed using a pour-fill liquid nitrogen lab Dewar operating at 82 K.

2. Third Generation 2x8 FPAs

In the recent 3rd generation FPA lots, FERs were reduced to below 40 kHz while still maintaining PDEs over 60% by shortening the HgCdTe cutoff wavelength to from 4.4 µm to 3.7 µm. At 50% PDE a FER of 30 kHz was measured on a 3.7 µm cutoff FPA, as shown in Figure 1, which is 5x lower than the best 2nd generation 4.4 µm cutoff FPA's measured FER of 150 kHz. This is also closer to the dark current of the bare diodes when they are measured on a passive Si fanout. The shortened cutoff doesn't affect the detection of signal photons in the 1.0-2.1 µm range, as shown in Figure 2, however, it does reduce the APDs' sensitivity to room temperature blackbody radiation in the 3.7-4.4 µm band. To counter the expected reduction in gain from the shortened HgCdTe cutoff, DRS also reduced the multiplication region's width by decreasing the APD's pn-junction diameter. This allowed stable gains of over 2000, c.f. Figure 3, to be achieved at ROIC-tolerant APD bias voltages of only 15 V to ensure the mean single photon signal to noise ratio of over 15 was maintained. The drawback of reducing the junction diameter without also decreasing diode pitch is photoelectron (PE) diffusion jitter increases because the PE has a farther distance to diffuse

before being collected. Additionally, the electron mobility in p-type 3.7 µm cutoff material is approximately 75% of what it is in p-type 4.4 µm cutoff material. Lower mobility coupled with longer diffusion distance increased the jitter measured on 3.7 µm cutoff APDs with 19 µm diameter junctions to 3908 ps, compared to 2370 ps in 4.4 µm cutoff APDs with 21 µm diameter junctions. Due to the increase in jitter, DRS is planning to place the diodes on a closer diode pitch within the same 64 µm pixel to reduce the diffusion distance and therefore the jitter. DRS expects to reduce the jitter to the 1500 ps range, consistent with what was measured on the 2nd generation FPAs.

As part of the improvements to the 2nd generation FPAs, DRS also integrated microlens arrays to the 4.4 µm cutoff FPAs which increased the flooded field PDEs to over 80% at the same FERs. The microlens arrays provided a 100% detector fill factor and were AR coated for optimum performance across 1.0-2.1 µm.

3. Conclusions

DRS has improved performance of its single photon sensitivity 2x8 HgCdTe electron avalanche photodiode focal plane arrays by integrating microlens arrays as well as reducing the cutoff to 3.7 µm allowing sub-30 kHz false event rates to be achieved at over 50% photon detection efficiencies.

4. Figures

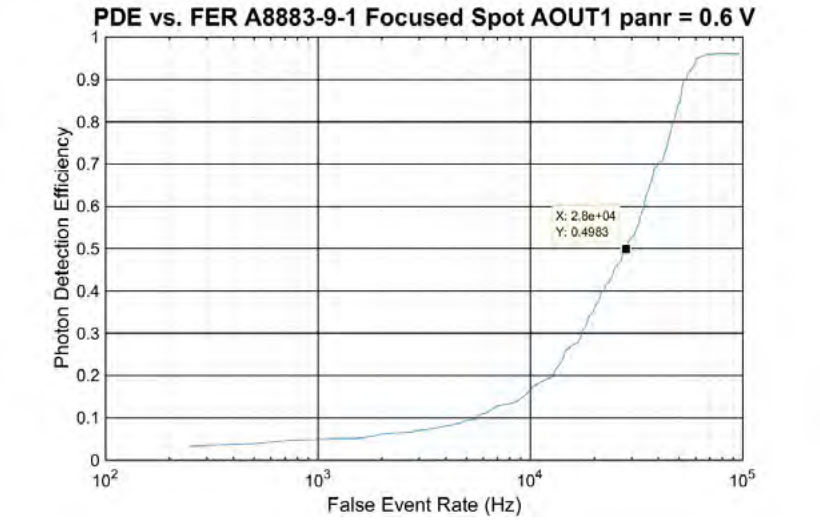

Figure 1: Third generation 3.7 µm cutoff APD showing 50% PDE at 28 kHz FER.

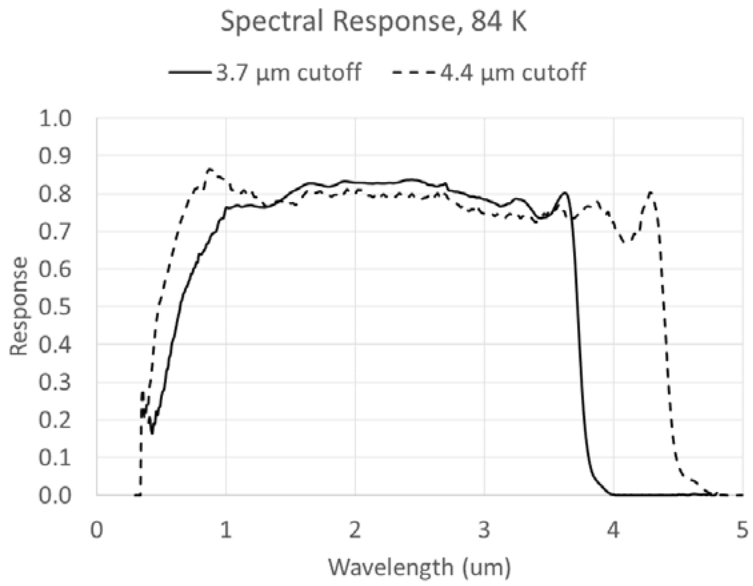

Figure 2: Comparison of spectral response vs. wavelength of 3.7 µm and 4.4 µm cutoff APDs

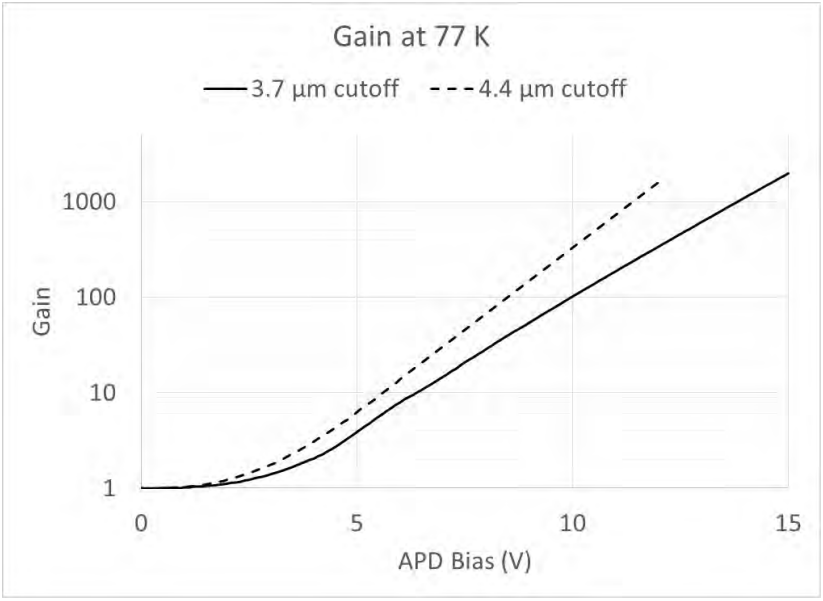

Figure 3: Comparison of gain vs. voltage on 3.7 µm and 4.4 µm cutoff APDs

5. References

[1] Sullivan III, William, et al. "Linear-Mode HgCdTe Avalanche Photodiodes for Photon-Counting Applications." Journal of Electronic Materials 44.9 (2015): 3092-3101. doi:10.1007/s11664-015-3824-3

[2] Sullivan III, William, et al. "Linear mode photon counting from visible to MWIR with HgCdTe avalanche photodiode focal plane arrays." Proc. SPIE 9492, Advanced Photon Counting Techniques IX, (2015): 94920T. doi:10.1117/12.2180394

Linear Mode Photon Counting HgCdTe Avalanche Photodiode Array in an Integrated Detector Cooler Assembly (IDCA) for a CubeSat Demonstration

Xiaoli Sun[1], James B. Abshire[1], Michael A. Krainak[1], Guangning Yang[1], Wei Lu[1]
Renny A. Fields[2], David A. Hinkley[2]
Jeffrey D. Beck[3], Richard M. Rawlings[3], and William W. Sullivan III[3]

[1]NASA Goddard Space Flight Center, Greenbelt, MD 20771
[2]The Aerospace Corporation, El Segundo, CA 90245
DRS Network & Imaging Systems, LLC, Dallas, TX 75243

Contact: xiaoli.sun-1@nasa.gov, (301) 614-6732

Abstract: We report on progress in integrating and testing of a linear mode photon counting (LMPC) 2x8 pixel HgCdTe avalanche photodiode (APD) array into an integrated detector-cooler assembly (IDCA) for an in-space technology demonstration on a CubeSat.

1. INTRODUCTION

DRS has developed an integrated detector-cooler assembly (IDCA) to accommodate a linear mode photon counting (LMPC) HgCdTe avalanche photodiode (APD) focal plane array. The IDCA is designed for a CubeSat demonstration in space for the Aerospace Corporation under the NASA Earth Science Technology Office (ESTO) In-space Validation of Earth Science Technology (InVEST-12) program[1]. The new detector array will enable near quantum limited receiver performance in future space lidar for topography, atmospheric gas absorption, and surface spectral absorption measurements over the 400 to 4000 nm wavelength region[2,3].

2. THE FOCAL PLANE ARRAYS

The focal plane array (FPA) consists of an LMPC HgCdTe APD array mounted on top of a read-out integrated circuit (ROIC) substrate[4]. The 16 element APD array was fabricated in a 2x8 format with a 64 μm pixel pitch from $Hg_{1-x}Cd_xTe$ grown by use of liquid phase epitaxy (LPE)[4] with a cut-off wavelength of 4.3 μm at 77K. Each pixel is composed of four parallel diodes in a

2x2 configuration. The active area of the detector has a diameter of about 22 μm at the center of the four diodes. The arrays used DRS's high-density vertically integrated photodiode (HDVIP®) architecture: a front-face-illuminated p-around-n cylindrical homojunction diode structure that features low capacitance for high bandwidth, low defect density, and interdiffused CdTe surface passivation on both array surfaces for low dark current[5]. The ROIC consists of a set of custom high gain-bandwidth silicon transimpedance amplifiers provided by the Analog Digital Integrated Circuits Inc. The combination of high APD gain, low excess noise, and low ROIC noise enables single photon detection., The output of the ROIC is the linear sum of the individual photon signals, allowing the detection of multi-photon events, like an analog photodetector but at a sub-photon noise floor[6]. For this work a micro-lens array was also integrated with the HgCdTe APD array to improve the detector fill factor.

3. THE COOLER

The cryo-cooler used here is a 1/5 watt linear drive Stirling cooler previously developed by DRS for infrared detectors. It consists of a compressor and an expander connected to the Dewar assembly[7]. These coolers are designed to survive rocket launch and have demonstrated multi-year lifetime. The cooler is designed to cool the detector to 80K but can also operate at a higher setpoint temperature.

4. THE INTEGRATED COOLER DETECTOR ASSEMBLY

Two identical IDCA's were successfully assembled and tested for a CubeSat experiment under the NASA InVEST program[1]. The entire IDCA fits into an 8x8x20 cm^3 volume and weight about 1 kg with the support structure and a magnet shield around the compressor. The test results showed the cryo-cooler cooled the detector from room temperature to 80K in about 5 minutes.

The cryo-cooler is capable of operating at a heat sink temperature from -24 to 60°C. Our tests showed the detector arrays operate from 80K to 110K with nearly identical performance. The cooler consumes about 7.6 and 4.4 W electrical power for a detector array temperatures of 80K and 110K, respectively, with the cooler heat sink held at room temperature. The support electronics consume about 1.4 W. Tests showed that the micro-lens array to improved the detector fill factor to nearly 100%, which was consistent with the design. The gain of the HgCdTe APD array was measured to be >1000 at a bias voltage of 13 V, which allows detecting single photon events with some margin. The photon counting efficiency was measured to be >50%. The noise equivalent power (NEP), of the IDCA was well below 1 fW/√Hz. For these assemblies a large portion of this noise was found to originate from an unshielded ambient thermal emission. This thermal leakage will be minimized in the next iteration of the Dewar assembly design. The IDCA assembly has passed vibration, thermal shock, and thermal cycle testing for a CubeSat launch and planned operation in low Earth orbit.

5. FIGURES

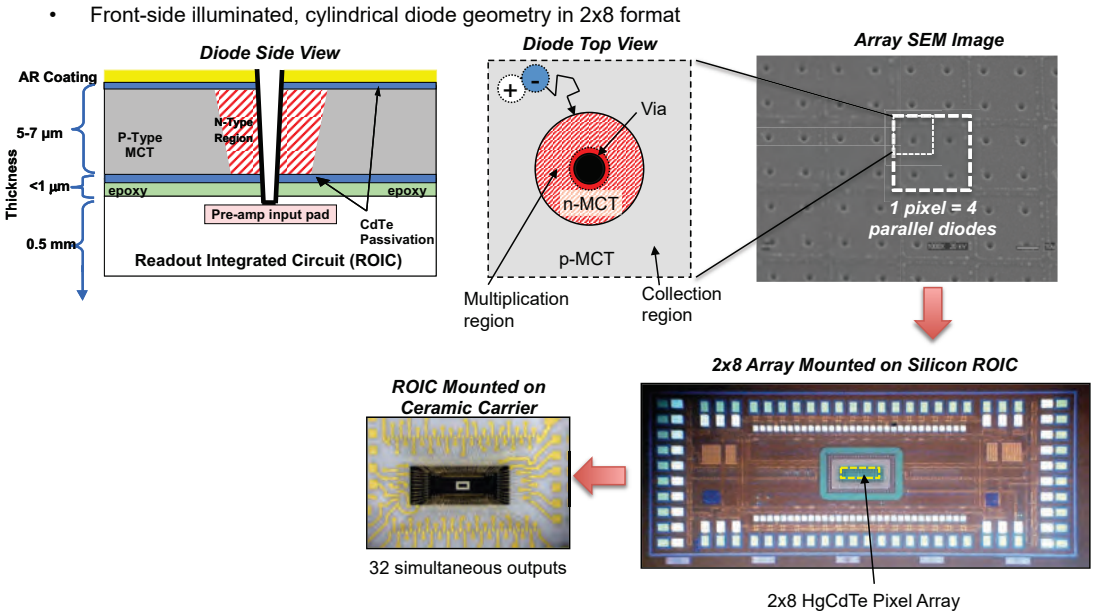

Figure 1. DRS HDVIP™ HgCdTe APD architecture and 2x8 array configuration.

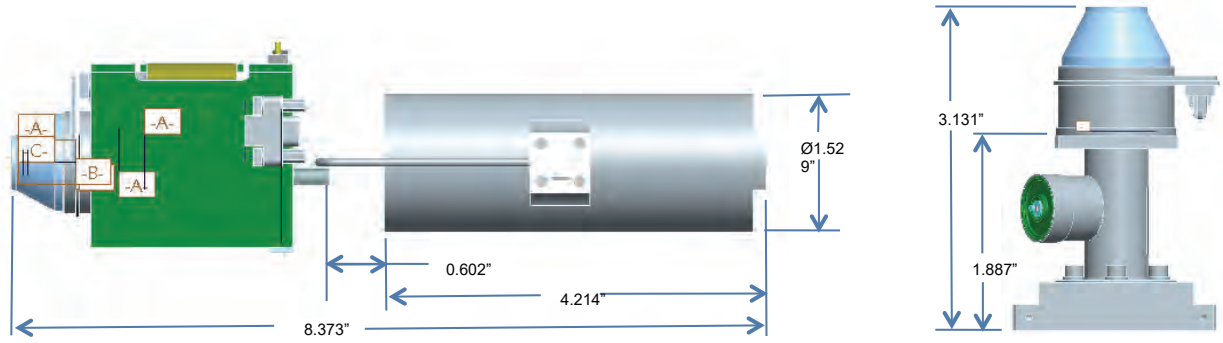

Figure 2. Mechanical drawing of the integrated detector cooler assembly (IDCA) The dimensions are in inches.

Figure 3. Photograph of the IDCA. The total mass is <1kg including the bracket and magnet shield. The total electrical power is <6W with detector chip temperature set at 110K and the heat sink (the bracket) at room temperature.

6. REFERENCES

[1] R. Fields *et al*., "A linear mode photon-counting (LMPC) detector array in a CubeSat to enable earth science lidar measurements," *IEEE International Geoscience and Remote Sensing Symposium (IGARSS)*, Paper FR2.B1.5, 2015.

[2] J. Beck *et al*., "A highly sensitive multi-element HgCdTe e-APD detector for IPDA lidar applications," *J. Electron. Mater.*, Vol. 43, pp. 2970-2977, 2014.

[3] X. Sun, J. B. Abshire, and J. D. Beck, 'Using HgCdTe e-APD detector arrays with single photon sensitivity for space lidar,' *SPIE 9114,* Paper number 91140K, 2014.

[4] W. Sullivan III *et al*., "Linear mode HgCdTe avalanche photodidoes for photon counting applications," *J. Electron. Mater.*, Vol. 44, pp. 3092-3101, 2015.

[5] J. Beck *et al*., "The HgCdTe Electron Avalanche Photodiode," *J. Electron. Mater*., Vol. 6, pp. 1166-1173, 2006.

[6] J. D. Beck *et al*., "Linear mode photon counting with the noiseless gain HgCdTe e-avalanche photodiode," *Optical Engineering*, Vol. 53, pp. 081905-1 to -10, 2014.

[7] D. Rawlings and G. Averitt, "A linear driver cryocooler for ultra-small infrared sensor systems," SPIE 9070, Paper 90702R, 2014.

Center for Semiconductor Materials and Device Modeling: Advancing Sensor Technology through Understanding of Materials Synthesis, Device Operation and Design Controllable Parameters

Meredith Reed, Jagmohan Bajaj, Jonathan Schuster, Priyalal Wijewarnasuriya, Greg Brill, Parvez Uppal, Gary Wood, and Phil Perconti

U.S. Army Research Laboratory, 2800 Powder Mill Road, Adelphi, MD 20783

As the Army progresses in its need for the most capable, most efficient devices built from semiconductor materials, the need for fundamental research and understanding will increase in order to assure a timely transition of technology from demonstration to system deployment with reduced risk. This understanding comes from a robust process of multi-scale modeling and its validation through materials growth and device performance. Since many of the semiconductor technologies of Army relevance have no commercial market, the Army must work with industry and academia to advance the understanding of fundamental properties that impact design of a given application. The US Army Research Laboratory proposed Center for Semiconductor Materials and Device Modeling has been devised to address this problem by bringing together government, academia, and industry in a collaborative fashion to continuously push semiconductor research forward so that the ultimate customer, the Soldier, always has the best possible equipment to accomplish the mission. The leveraged attributes of the Center include combined broad knowledge base in semiconductor modeling; combined modeling, materials and device expertise and availability; sharing of computational resources; project continuity; and extension of the bench. The US Army has chosen to start with Infrared Semiconductor Materials and Devices and will later broaden the scope to other material systems. The intent of this paper is to introduce the Modeling Center, outline the motivation, present a general framework, discuss initial problems the modeling center will address, and present a roadmap of the subsequent steps in establishing the Center.

The numerical-experimental enhanced analysis of hot MCT barrier infrared detectors

K. Jóźwikowski[1,4], A. Jóźwikowska[2], M. Kopytko[1], P. Martyniuk[1], W. Gawron[3], P. Madejczyk[1], A. Kowalewski[1], O. Markowska[1], A. Martyniuk[1] and A. Rogalski[1]
1.-Institute of Applied Physics, Military University of Technology, 2 Kaliskiego Str., 00-908 Warsaw, Poland.
2.-Faculty of Applied Informatics and Mathematics, University of Life Science,166 Nowoursynowska Str.,02-787, Warsaw, Poland.
3- Vigo System S.A. Poznańska 129/133, 05-850 Ożarów Mazowiecki, Poland
4- email: krzysztof.jozwikowski@wat.edu.pl, tel.48-261-83-90-14

In this paper we present the hot MCT barrier detectors manufactured by the metal-organic chemical vapor deposition (MOCVD) growth method in the joint laboratory of Vigo-System SA and Military University of Technology It is shown that MOCVD technology is an excellent tool for HgCdTe barrier architecture growth with a wide range of composition, donor/acceptor doping and without post grown annealing. The device concept of a specific barrier bandgap architecture integrated with Auger-suppression is as a good solution for high-temperature operating infrared detectors. MWIR and LWIR detector structures were simulated with our original computer program. A detailed analysis of the detector performance was made taking into account SRH, Auger and tunneling currents as well as the influence of dislocations. We have also simulated the fluctuation phenomena by using our original Langevine-like numerical method. It enables the analysis of the influence of different noise sources on the noise current: shot noise, diffusion noise, generation-recombination (G-R) noise and 1/f noise caused by fluctuations of G-R and scattering processes. We have also determined the distributions of noise power density caused by fluctuations of Joule power. They enable determination of the influence of different noise sources on the total noise current and finding the areas where the noise power is mainly generated. Both the photoelectrical parameters as well as the spectrum of noise current determined numerically were compared with the performance of the manufactured detectors. An example of detectors' architecture and some theoretical and experimental results are presented below. For manufactured detectors we have obtained a satisfactory accordance of the theory and experiment.

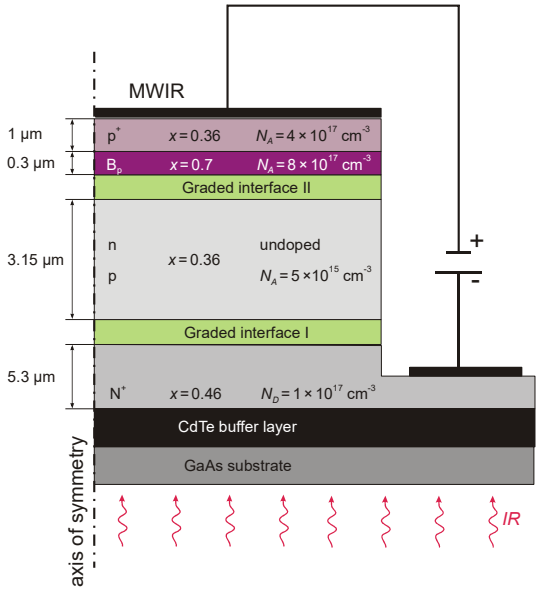

Fig.1a

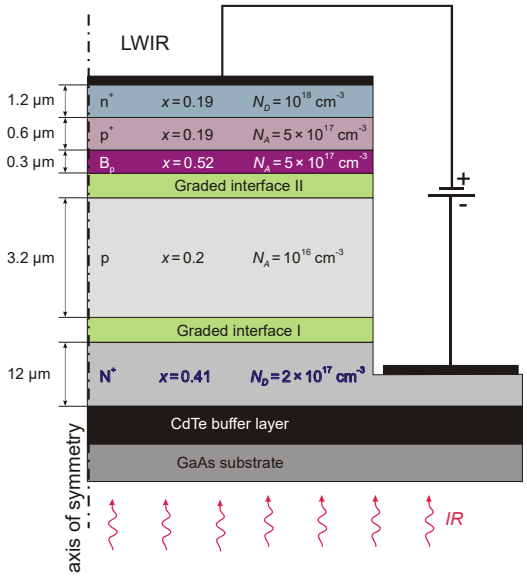

Fig.1b

Fig.1.The architecture of the half cross-section of cylindrical barrier mesa structures. (Fig1a MWIR detector, Fig1b LWIR detector)

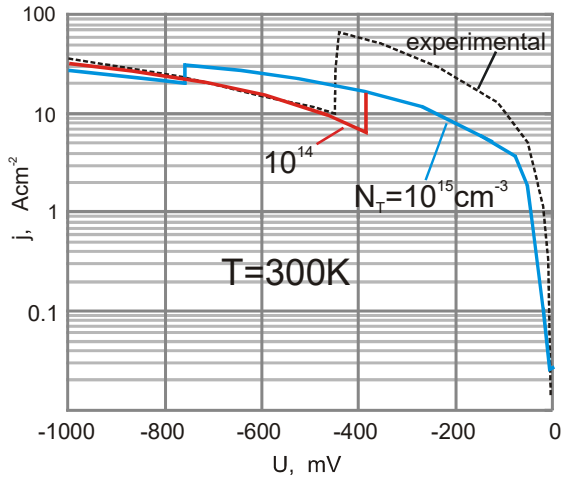

Fig.3

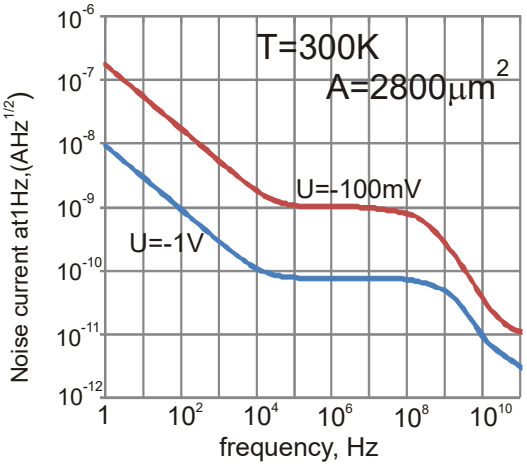

Fig.4

Fig.3. Current density as a function of bias voltage for LWIR detector at 300K. Dashed line shows experimental result. Calculated results (solid lines) are carried out under assumption that the concentration of metal vacancies is equal to 10^{15} cm^{-3} (blue line) and 10^{14} cm^{-3} (red line)

Fig.4.Calculated spectral density of the noise current for mesa LWIR structure with surface area 2800 μm2 at 300K. U denotes the bias voltage.

Simulation of small-pitch HgCdTe photodetectors

Marco Vallone*, Michele Goano*, Francesco Bertazzi*, Giovanni Ghione*
Wilhelm Schirmacher†, Stefan Hanna†, Heinrich Figgemeier†

*Politecnico di Torino, Dipartimento di Elettronica e Telecomunicazioni, Torino, Italy
†AIM Infrarot Module GmbH, Heilbronn, Germany
E-mail: michele.goano@polito.it

Current technologies have enabled the production of high quality Focal Plane Arrays (FPA) infrared (IR) detectors with pixel sizes in the order of 10-15 μm. High-performance FPAs with pixel dimensions approaching the wavelength scale (Nyquist limit) are under intense investigation [1-4]. Recent research indicate that an *F*/1 system with 5-μm-pitch pixels has identical performance of a more conventional *F*/4 system with 20 μm pixels, with the advantage of an overall smaller volume, lower weight and potentially cheaper imaging sensor. Here we present combined three-dimensional (3D) optical Finite Differences Time Domain (FDTD) and electrical drift-diffusion simulations of a 5-μm-pitch long-wavelength infrared (LWIR) HgCdTe FPA, with cutoff wavelength λ_c = 10 μm, each pixel having a $p-n^{-}-n^{+}$ photodiode architecture (Fig. 1). Our simulations, performed on a 5×5 pixel array, predict interesting cavity effects triggered by contact metallizations [5-8]. In a first group of simulations, we illuminated the entire FPA with monochromatic plane waves, whereas in a second group we illuminated only the FPA's central pixel with a Gaussian beam, focused by an *F*/1 optical system. Fig. 2 reports the absorbed photon density distribution A_{abs}, where cavity effects are clearly visible at λ = 9.5 μm and produce resonances in the quantum efficiency (QE) spectra, shown in Figs. 3-4 for the case of uniform illumination and in Fig. 5 for Gaussian beam illumination (in both cases for two values of W_{met}). In addition, the wavelength-dependent inter-pixel crosstalk is evaluated (Fig. 6), separating the role of optical crosstalk (due to light diffusion in the neighboring pixels) and electrical crosstalk (due to both light *and* photogenerated carrier diffusion in the neighboring pixels).

References

[1] R. G. Driggers, R. Vollmerhausen, P. Reynolds, J. Fanning, and G. C. Holst, "Infrared detector size: how low should you go?", *Opt. Eng.* 51(6), 063202 (2012)

[2] G. C. Holst and R. G. Driggers,"Small detectors in infrared system design", *Opt. Eng.* 51(9), 096401 (2012)

[3] W.E. Tennant, D.J. Gulbransen, A. Roll, M. Carmody, D. Edwall, A. Julius, P. Drieske, A. Chen, W. McLevige, S. Freeman, D. Lee, D.E. Cooper, and E. Piquette, "Small-pitch HgCdTe photodetectors", *J. Electron. Mater.* 43(8), 3041 (2014)

[4] A. Rogalski, P. Martyniuk and M. Kopytko, "Challenges of small-pixel infrared detectors: a review", *Rep. Prog. Phys.* 79, 046501 (2016)

[5] O. Gravrand and G. Destefanis, "Recent progress for HgCdTe quantum detection in France", *Infrared Phys. Tech.* 59, 163 (2013).

[6] C. Keasler, E. Bellotti, "Three-dimensional electromagnetic and electrical simulation of HgCdTe pixel arrays", *J. Electron. Mater.* 40 (8) 1795 (2011).

[7] B. Pinkie, E. Bellotti, "Numerical simulation of spatial and spectral crosstalk in two-color MWIR/LWIR HgCdTe Infrared detector arrays", *J. Electron. Mater.* 42, 3080 (2013).

[8] M. Vallone, M. Goano, F. Bertazzi, G. Ghione, W. Schirmacher, S. Hanna, H. Figgemeier, "Comparing FDTD and ray-tracing models in numerical simulation of HgCdTe LWIR Photodetectors", *J. Electron. Mater.* (2016), doi: 10.1007/s11664-016-4481-x.

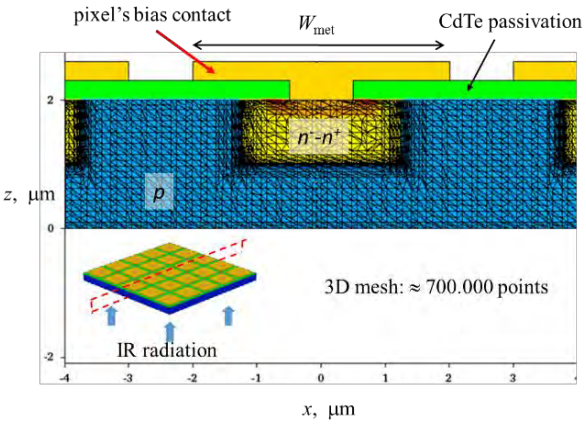

Figure 1: 3D view and two-dimensional (2D) cross section of the simulated LWIR 5x5 FPA with pixel pitch of 5 μm.

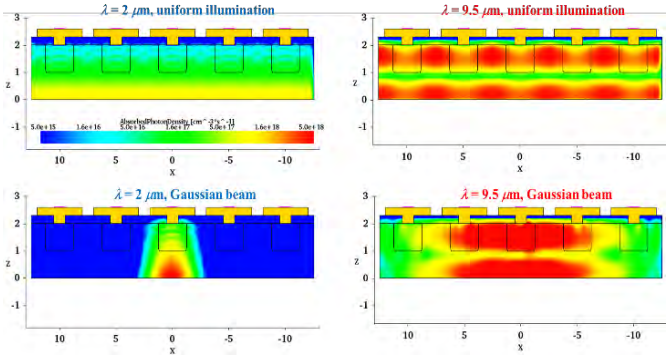

Figure 2: 2D distribution of A_{abs} for $W_{met} = 4\,\mu m$ under illumination with plane waves (above) or with a Gaussian beam focused on the central pixel (below). (Lengths are in μm.)

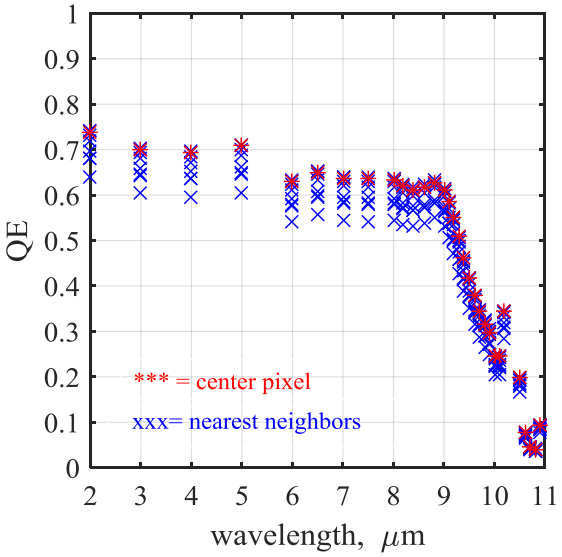

Figure 3: Simulated QE spectra for W_{met} = 2 μm.

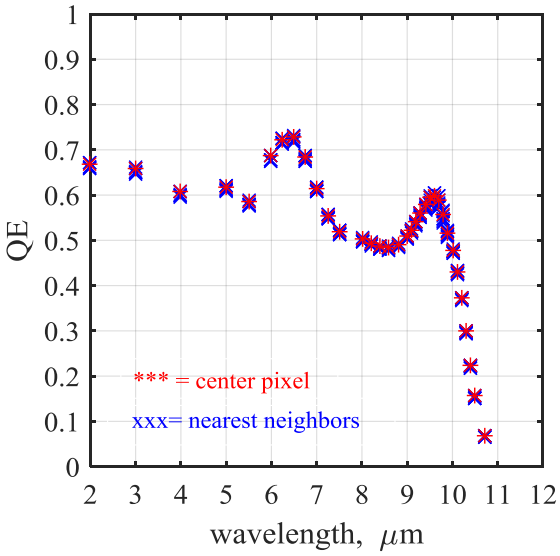

Figure 4: Simulated QE spectra for W_{met} = 4 μm.

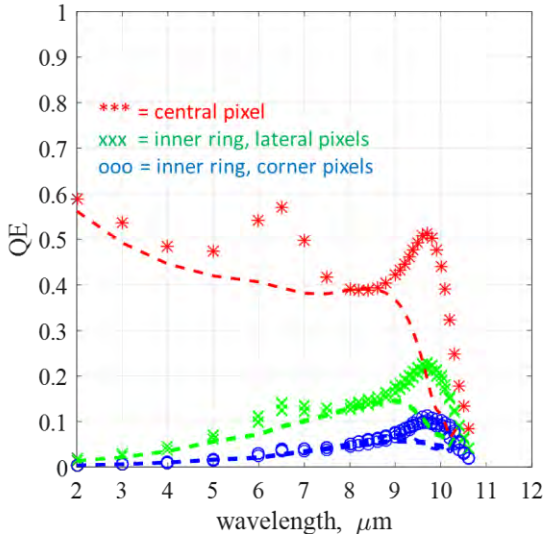

Figure 5: Simulated QE spectra for Gaussian beam illumination, for the 5x5 FPA described in Fig. 1. Symbols: W_{met} = 4 μm; lines: W_{met} = 2 μm

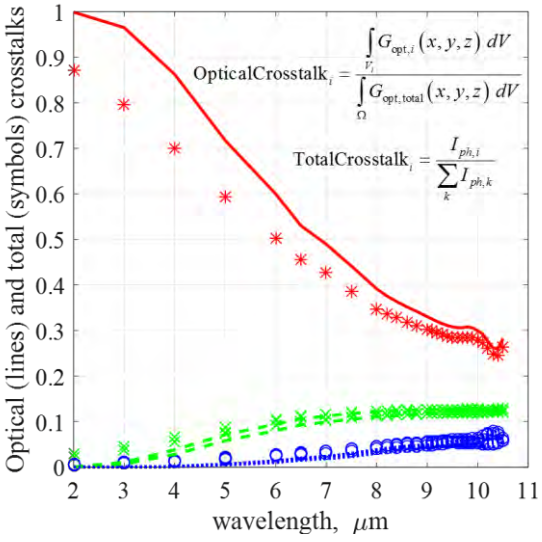

Figure 6: Simulated *total* and *optical* crosstalk, defined as in [7], for W_{met} = 4 μm. In the formulas, $I_{ph,i}$ is the photocurrent in the *i*-th pixel, $G_{opt,i}$ and $G_{opt,total}$ are the optical photogeneration density in the *i*-th pixel and in the entire array.

Numerical Modeling of Dark Current Suppression in IR Photodetectors

Andreu Glasmann[1], Benjamin Pinkie[1], Taylor Hubbard[1], Enrico Bellotti[1]
Electrical and Computer Engineering, Boston University[1]

Presenter: Enrico Bellotti – Mail: Boston University, Department of Electrical and Computer Engineering, 8 Saint Mary's Street Boston, MA 02215. Email: bellotti@bu.edu Phone: (617) 358-1576 Fax: (617) 353-7337

Dark current, resulting from generation of charge carriers across the semiconductor band gap, is one of the primary factors that defines infrared photodetector performance. Here we report numerical simulation results demonstrating the efficacy of a novel dark current suppression mechanism in dense photodiode arrays. As inter-diode spacing decreases below minority carrier diffusion lengths, it is possible to reduce the gradient of excess minority carriers between sensing diodes in the array. To control this effect, we simulate the presence of additional non-sensing diodes among an array of sensing diodes. These non-sensing diodes, which we term Diffusion Control Junctions (DCJs), may be individually biased, which allows for the control of diffusion currents. The result is reduced dark current at higher temperatures. This phenomenon has promising applications in SWIR, E-SWIR, and MWIR photodetector arrays operating in the diffusion limited regime.

Optimal use of this dense array effect requires the balance of dark current reduction in sensing diodes with the loss of photocurrent to DCJs. To this end we investigate the effects of varying bias, pixel pitch, and array geometry. Our simulations show an order of magnitude reduction in HgCdTe FPA dark current operating at 250K, as compared to the same array without the incorporation of DCJs. Similar reductions in dark current have been observed in Silicon and InGaAs FPAs.

Figure 1: A simulated FPA with DCJ's in place

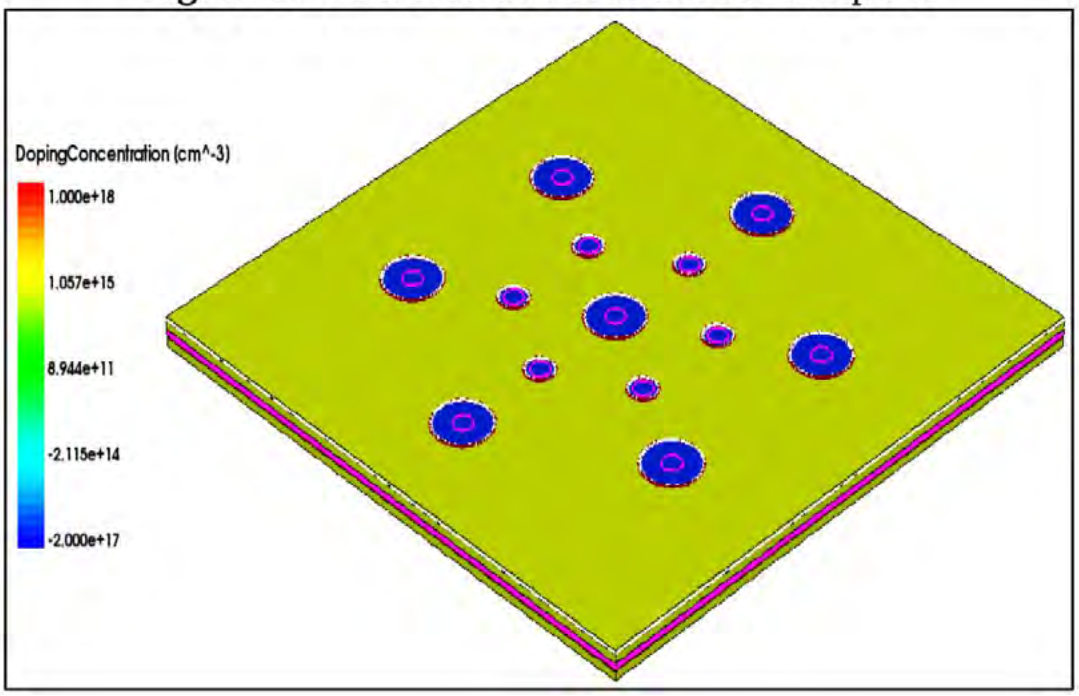

The larger diffusions are the "sensing" diodes, and the smaller diffusions are the DCJs used to suppress the minority carrier density at critical locations.

Figure 2: Arrhenius dark current vs. 1000/T for a conventional FPA and a FPA with DCJs

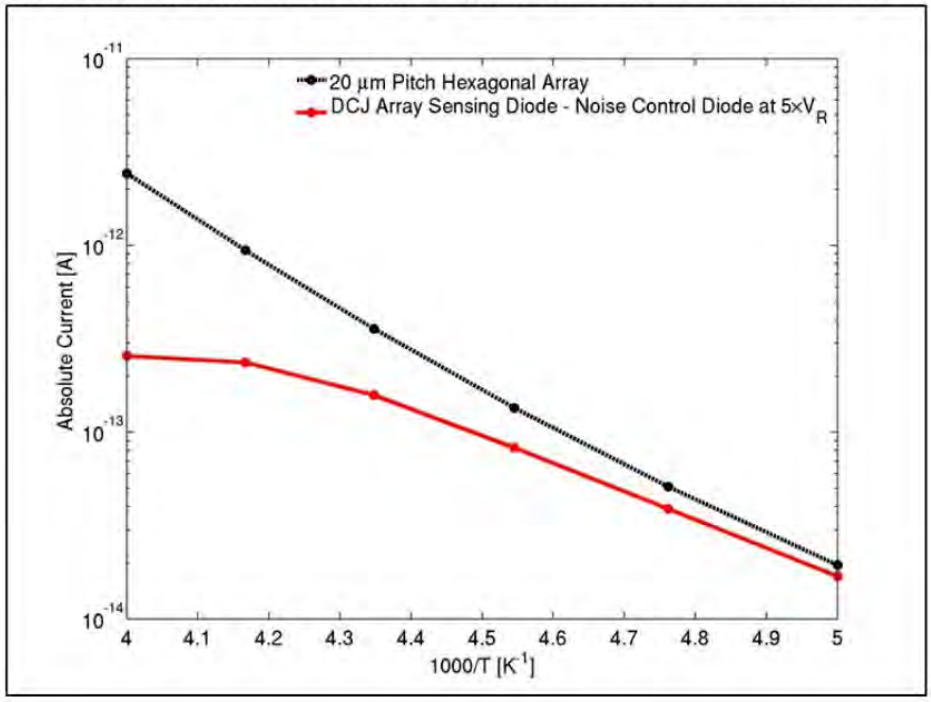

Simulated demonstration of the dark current reduction in a HgCdTe array when the device is operated at higher temperature to remain diffusion-limited. The temperature range is 200K – 250K. At 250K we see a reduction from 2.5E-12 A to approximately 2.5E-13 A. The curve appears flat at this high temperature; can we operate at even greater temperatures?

CdZnTe Substrate's Impact on MBE HgCdTe Deposition

J. D. Benson, L. O. Bubulac, M. Jaime-Vasquez, J. M. Arias, P. J. Smith, R. N. Jacobs, J. K. Markunas, L. A. Almeida, A. Stoltz, P. S. Wijewarnasuriya*, M. Reddy**, J. Peterson**, S. M. Johnson**, B. Hanyaloglu**, J. Bangs**, and D. D. Lofgreen**
U. S. Army RDECOM, CERDEC Night Vision and Electronic Sensors Directorate
*U. S. Army Research Laboratory
**Raytheon Vision Systems

The highest sensitivity, lowest dark current infrared focal plane arrays (IRFPAs) are produced using HgCdTe on CdZnTe substrates. As-received CdZnTe wafers were characterized for polishing residue and impurity contamination. 4×4, 6×6, and 7×7.5 cm (112)B state-of-the-art, as-received CdZnTe wafers were analyzed. High surface impurity contamination of Al, Si, Cl, S, P, Fe, Br, and Cu was observed on the as-received 4×4 and 6×6 cm CdZnTe wafers. Wide lateral variation (either coefficient of variation >1 or skew >2) in surface contamination for the as-received wafers was observed for many of the above elements.

As-received wafers were further characterized for polishing residue. The final polishing step leaves residual polishing grit, CdZnTe particles, and large organic residue droplets. We found a factor of 7 variation of residual polishing grit/CdZnTe particle density across a 6×6 cm wafer. SEM/EDS profiles showed the polishing grit on the (112)B surface is composed of SiO_2. Figure 1 shows Nomarski microscopy and Dektak profilometer images of a large organic residue droplet on a 6×6 cm (112)B as-received CdZnTe wafer. This residue droplet was ~ 0.8 cm from the center of the 6×6 cm as-received wafer. SEM/EDS analysis of the edge of the 6×6 cm as-received CdZnTe wafer

shows residual SiO_2 and possibly Al_2O_3 polishing grit, Cd(Zn)Te particles, as well as residual mounting wax.

As-received wafers are not epi-ready 'out of the box'. The wafers' surface damage and impurity levels dictate that an MBE preparation etch is required. The ultimate goal for the MBE preparation etch is to provide a clean, stoichiometric, atomically smooth, and well-ordered surface to minimize growth defects. The current Br:methanol-based MBE preparation etch does not significantly reduce the contamination level of impurities on the surface. High maximum surface impurity contamination of Al, Si, Cl, S, P, Fe, Br, and Cu was observed on MBE preparation etched CdZnTe wafers. Wide lateral variation (either coefficient of variation >1 or skew >2) in surface contamination for many impurities was observed. Additionally, we observed Cu contaminated 'hot spots' revealed by the MBE preparation etch as defects on the CdZnTe wafer. Figure 2 shows 2 SIMS profiles from the same MBE prep etched CdZnTe wafer. The first image shows the typical profile of below SIMS detection limit Cu in a CdZnTe wafer. The second SIMS profile is from a Cu 'hot spot' in the CdZnTe wafer. We have further observed these Cu 'hot spots' in HgCdTe epilayers deposited on CdZnTe substrates.

The MBE preparation etched surface contamination consists of Cd(Zn)Te particles, and large organic residue droplets. No residual SiO_2 polishing grit was observed on the (112)B surface by SEM/EDS analysis. SEM/EDS analysis of the edge of the 6×6 cm MBE preparation etched CdZnTe wafer demonstrates that the residual SiO_2 polishing grit, as well as the residual mounting wax, have been removed from the wafer edge by the MBE preparation etch.

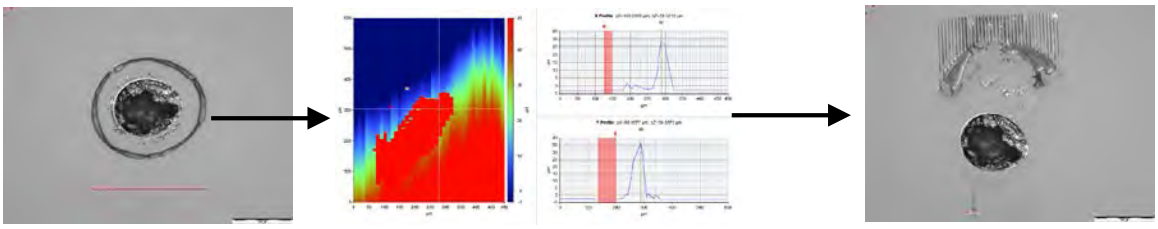

Figure 1. A large organic residue droplet near the center of an as-received 6×6 cm CdZnTe substrate. The residue's outer diameter is ~ 410 µm with a maximum height ~ 40 µm. The Dektak measurement dislodged the contaminant and smeared the outer ring of organic material.

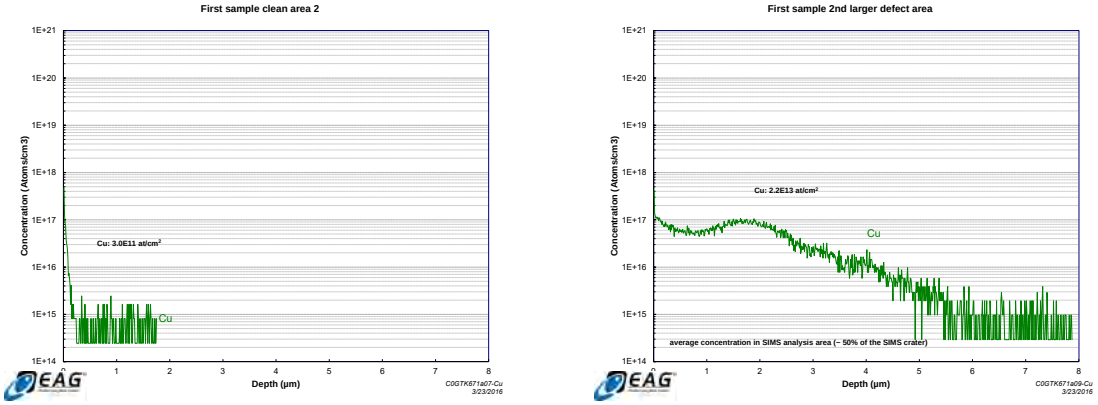

Figure 2. Two SIMS Cu profiles measured on the same MBE prep etched wafer. The profile on the left shows a typical below background level Cu profile for a CdZnTe substrate. The SIMS profile on the right is from a Cu 'hot spot' on a defect on the same CdZnTe wafer.

Characterization of HgCdTe films on Large Area CdZnTe substrates Grown by Molecular Beam Epitaxy

F. Erdem Arkun*, Dennis D. Edwall, Sheri Douglas, Majid Zandian, Michael Carmody, Donald Lee

Teledyne Imaging Sensors, 5212 Verdugo Way, Camarillo, CA, 93012
*erdem.arkun@teledyne.com ~ Phone: +1 805 373 4664

Recent advances in the growth of HgCdTe films on large area (7cm x 7.5cm) CdZnTe (CZT) substrates is presented. Growth of HgCdTe on large area wafers with good uniformity is achieved in a Riber 412 MBE tool designed for growth of HgCdTe compounds. We report on the growth of HgCdTe thin films on (211)B oriented CZT substrates by molecular beam epitaxy. The reactor is equipped with conventional CdTe, Te and Hg sources for achieving uniform exposure of the wafer during growth. The composition of the HgCdTe compound is controlled *in situ* by employing a closed loop spectral ellipsometry technique to achieve a cut off wavelength ($\boldsymbol{\lambda}$co) of 14µm at 78K. We will present data on the thickness and composition uniformity of grown films for large format focal plane array applications. The composition and thickness non-uniformity has been determined to be <1% over the area of a 7x7.5cm wafer. The films are further characterized by FTIR spectroscopy, optical microscopy and hall measurements. Additionally defect maps show the spatial distribution of defects generated during the epitaxial growth of the HgCdTe films. Microdefect densities are in the low $10^3/cm^2$ range and void defects are less than $500/cm^2$. Dislocation densities less than $5x10^4/cm^2$ are routinely achieved for HgCdTe films grown on CZT substrates. HAWAII H4RG 4kx4k FPAs with 15µm pitch have been produced using the recently developed growth process by MBE at Teledyne Imaging Sensors (TIS).

Effect of Cyclic Annealing on Electronic and Optic Properties of MBE Grown CdTe Layers

Ozan Arı[1,2], Elif Ozceri[1], Elif Bilgilisoy[1], Yusuf Selamet[1]

[1] Department of Physics and Infrared and Micro-electronic Material Research Laboratory (IRMAM) Izmir Institute of Technology, Izmir, Turkey

[2] e-mail: ozanari@gmail.com; ozanari@iyte.edu.tr

Introduction

More than several decades, CdTe layers are extensively investigated for buffer layer to HgCdTe (MCT), photo-detectors and solar cell applications. GaAs, Si, Ge, and GaSb are widely used substrates for CdTe growth. The large lattice mismatch between CdTe and substrate materials introduces dislocations in the interface region between CdTe and substrate[1]. These dislocations may extend to the CdTe surface which reduce CdTe overall crystal and surface quality. Extended defects such as dislocations in CdTe will affect the epitaxial growth of MCT or other layers when CdTe serve as buffer layer. In situ thermal cyclic annealing by interrupting growth of CdTe has been shown to reduce dislocation density[2,3].

In this study, we have employed molecular beam epitaxy (MBE) to grow CdTe layers on 3" GaAs(211)B and GaAs(211)A substrates with different in situ cyclic annealing conditions in order to understand cyclic annealing effects on structural, electronic and optic properties of CdTe layers.

Experimental Details

GaAs substrates were thermally deoxidized prior to CdTe growth and CdTe growth was initiated with low temperature nucleation. CdTe growth was interrupted for cyclic thermal annealing process. Firstly, growth of CdTe layers on GaAs(211)A and GaAs(211)B substrates were optimized for optimum CdTe layer quality. Three CdTe layers grown on GaAs(211)A substrates were annealed after every 1.8±0.1 μm of growth. Three different annealing process were applied for final layer of CdTe layers grown on GaAs(211)A substrate; (1) no annealing, (2) extended duration annealing, (3) standard flash annealing. Similarly, three CdTe layers grown on GaAs(211)B substrates were annealed after every 1.4±0.1 μm of growth. Annealing temperature effect of cyclic annealing to CdTe layers grown on GaAs(211)B substrates was investigated. We have examined effects of annealing conditions to CdTe layer crystal quality, electrical and optic properties with high resolution X-ray diffraction (HRXRD), spectroscopic ellipsometry (SE), photoluminescence (PL), and etch pit density (EPD) methods.

Results & Discussion

HRXRD CdTe(422) rocking curve (RC) measurements were performed from both [0-11] and [-111] azimuths with four-crystal HRXRD system. Anisotropy in RC FWHM values were calculated with;

$$RC\ FWHM\ Anisotropy = \frac{(RC\ FWHM\ from\ [0-11]) - (RC\ FWHM\ from\ [-111])}{RC\ FWHM\ from\ [0-11]} \times 100.$$

PL measurements were taken at 80 K with S&I Tri Vista Raman system with Princeton Ins. Acton SP-2750 monochromator and ProEM EMCCD camera. SE measurements were carried out following CdTe growth at 25±2°C surface temperature in MBE chamber. CdTe oscillator model with surface roughness and GaAs substrate was used to analyze SE measurements. Everson type wet etching was used to reveal structural defects of CdTe layers grown on GaAs(211)B substrates. Representative SE measurement and fit with CdTe oscillator model, PL (80K) spectrum, and HRXRD RC measurement from [-111] and [0-11] azimuths are given in Figure 1 and Figure 2. Critical points (CP) E1 and E1+Δ1 were calculated from CdTe oscillator model optical constants. PL spectrum of samples exhibit a near band gap emission and extended defects (dislocations etc.) and point defects (Frenkel) related Y-emission peak[4]. EPD values were calculated after Everson type etching applied to CdTe samples using post etch scanning electron microscopy images.

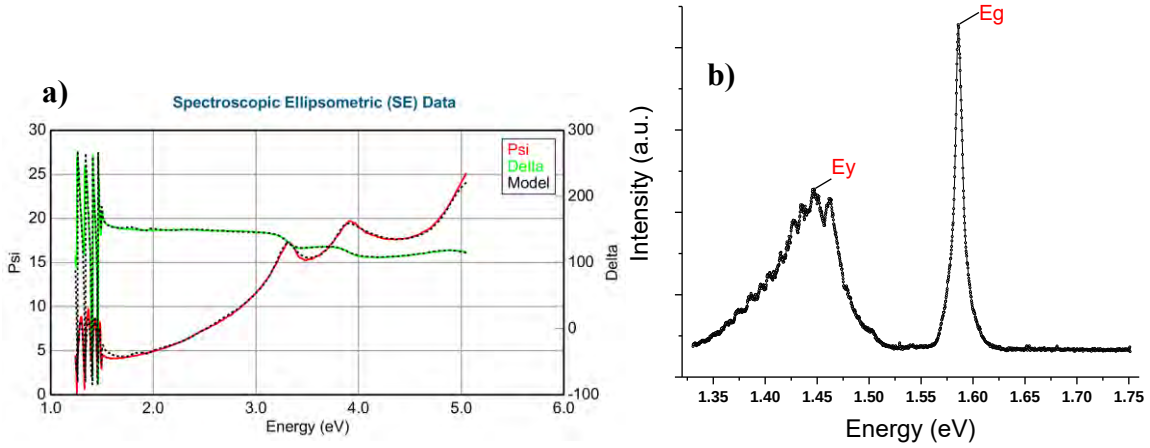

Figure 1 (a) SE measurement data and fit with CdTe oscillator model. (b) PL spectrum of CdTe sample.

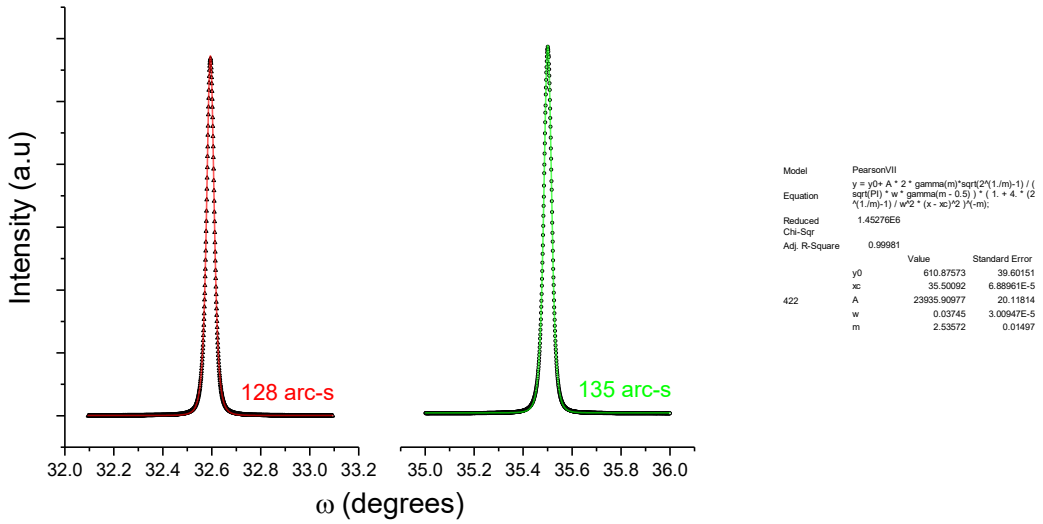

Figure 2 HRXRD CdTe(422) rocking curve (RC) measurements and fit with PearsonVII function from both [-111] (left) and [0-11] (right) azimuths.

In order to understand the defect structure related Y-emission in PL spectra of CdTe layers, correlations between band-edge emission intensity to Y-emission intensity ratio (Eg int./Ey int.), SE E0, E1 and E1+Δ1 critical points, XRD RC FWHM anisotropy, and band edge emission (Eg) from PL (80 K) are investigated. Effect of the annealing temperature to band edge emission, SE E0 CP, and EPD values for CdTe layers grown on GaAs(211)B substrates are given in Figure 3 a. Decrease in EPD value with increasing annealing temperature is related to reduction in dislocation density in CdTe layers. However, SE E0 CP and band gap value from PL data may be related to increase in near gap defects. Figure 3 b. shows Eg int./Ey int., RC FWHM anisotropy and SE E1 and E1+Δ1 CP dependence with annealing temperature. We have observed an increase in Eg int./Ey int. ratio, SE E1 and E1+Δ1 CP with increasing annealing temperature.

Effect of the annealing duration to band edge emission (Eg) from PL spectra and XRD RC FWHM anisotropy value for CdTe layers grown on GaAs(211)A substrates are given in Figure 4 a. Both anisotropy in RC FWHM values and Eg values are decreased with increased annealing duration. On the contrary, increase in Eg int./Ey int, SE E1 and E1+Δ1 CP values are observed with increased annealing duration (Figure 4 b).

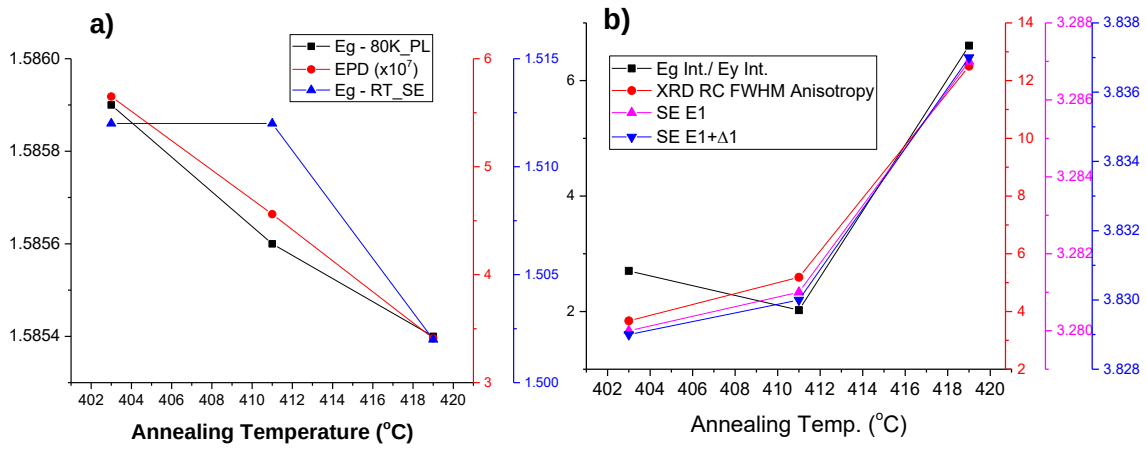

Figure 3 a) Band gap (Eg) value from PL (80K) spectrum and SE (25°C) measurements with EPD for CdTe layers grown on GaAs(211)B substrates which were annealed under different surface temperature values. b) Band gap emission intensity to Y-radiation intensity ratio, XRD RC FWHM anisotropy value with SE E1 and E1+Δ1 critical points for CdTe layers grown on GaAs(211)B substrates which were annealed under different surface temperature values.

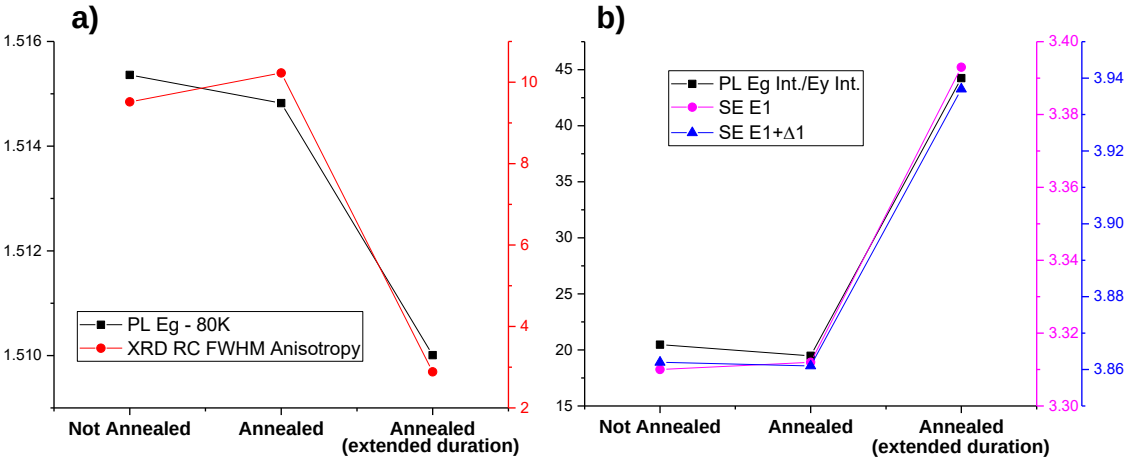

Figure 4 a) Band gap (Eg) value from PL (80K) spectrum with XRD RC FWHM anisotropy value for CdTe layers grown on GaAs(211)A substrates which were annealed under different conditions. b) Band gap emission intensity to Y-radiation intensity ratio, with SE E1 and E1+Δ1 critical points for CdTe layers grown on GaAs(211)A substrates which were annealed under different conditions.

References

1. R. N. Jacobs, C. Nozaki, L. a. Almeida, M. Jaime-Vasquez, C. Lennon, J. K. Markunas, D. Benson, P. Smith, W. F. Zhao, D. J. Smith, C. Billman, J. Arias, and J. Pellegrino, J. Electron. Mater. **41**, 2707 (2012).

2. R. N. Jacobs, L. a. Almeida, J. Markunas, J. Pellegrino, M. Groenert, M. Jaime-Vasquez, N. Mahadik, C. Andrews, S. B. Qadri, T. Lee, and M. Kim, J. Electron. Mater. **37**, 1480 (2008).

3. L. a. Almeida, S. Hirsch, M. Martinka, P. R. Boyd, and J. H. Dinan, J. Electron. Mater. **30**, 608 (2001).

4. S. Seto, A. Tanaka, F. Takeda, and K. Matsuura, J. Cryst. Growth **138**, 346 (1994).

Strain Relaxation and Misfit Dislocations in HgCdTe on Alternative Substrates

I. Madni, W. Lei, J. Antoszewski, R. Gu, L. Faraone

School of Electrical, Electronic and Computer Engineering, University of Western Australia,

35 Stirling Hwy, Crawley, WA 6009, Australia

e-mail: imtiaz.madni@research.uwa.edu.au; Phone: +61-416389414

Abstract:

In this study, high resolution x-ray diffraction was used to observe the strain relaxation in HgCdTe epitaxial layers grown by molecular beam epitaxy on (211)-oriented substrates. Three different substrates, GaSb, GaAs, and CdZnTe, were used in this investigation. The lattice mismatch between epitaxial layers and alternative substrates induces shear strain and deformations in the crystal grown. A thick buffer layer of CdTe was grown on GaAs and GaSb substrates to minimize the lattice mismatch between HgCdTe and substrates. X-ray reciprocal space maps in the symmetric (422) reflections revealed the misfit dislocation densities and strain relaxation characteristics of these materials. Ewald sphere was constructed to visualize the diffraction and the properties of Bragg's law. The samples with lesser mismatched alternative substrate, i.e. HgCdTe/GaSb exhibited fewer shears and the layer relaxed within the buffer. Layers on GaAs were partially relaxed and had strains over wide thickness which caused more misfit dislocations in these layers. When the lattice parameters comparatively matched that of the epitaxial layer, i.e. HgCdTe/CdZnTe, there was negligible strain or shear in any of the reflections and the peak width was much narrower. The analysis of effective buffer layer, strains, and misfit dislocations examined the potential application of GaSb as an alternative substrate. Strain relaxation inside thick layers also demonstrate that the compositions of the grown layers of HgCdTe were highly uniform.

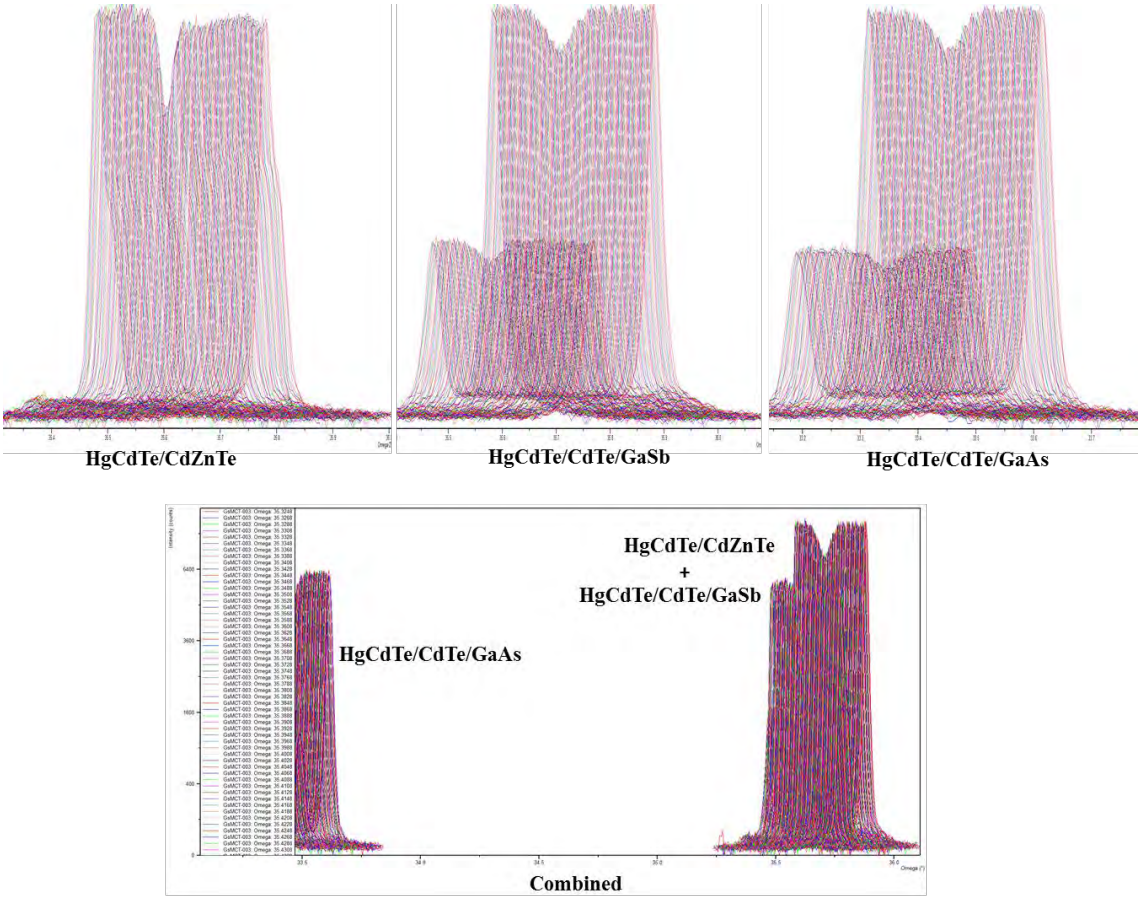

Figure 1. Two-axis measurement curves for the samples.

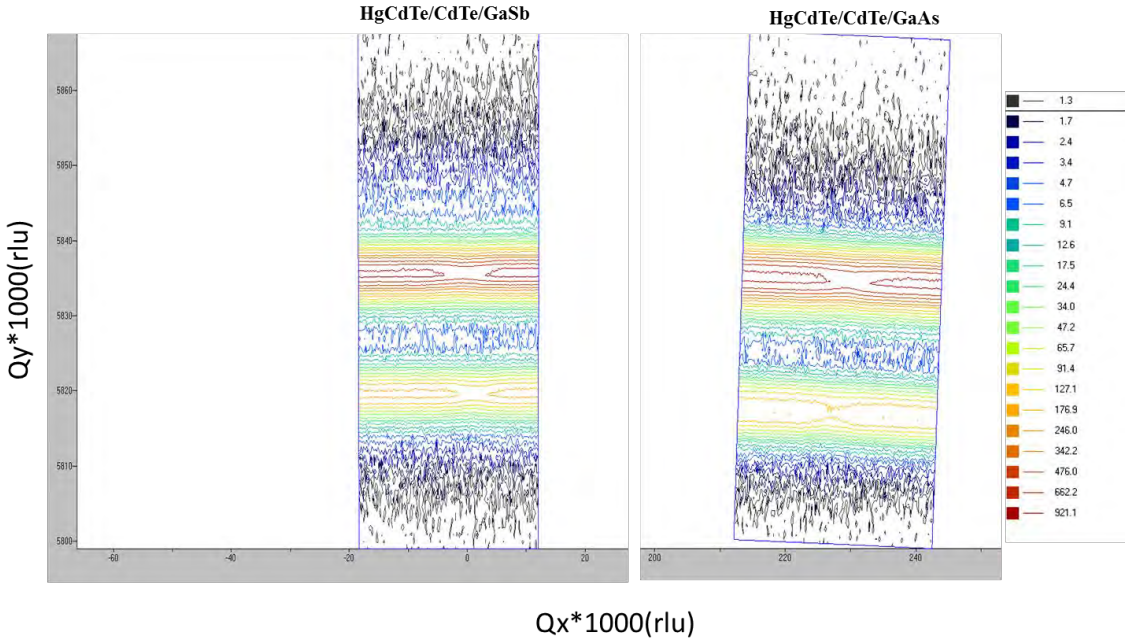

Figure 2. X-ray reciprocal space map of HgCdTe on alternative substrates.

Characterization of *n*-type and *p*-type long-wave InAs/InAsSb superlattices

A.E. Brown[1], N. Baril[1], L.A. Almeida[1], J. Arias[1, 2], and S. Bandara[1].

[1]U. S. Army RDECOM, CERDEC Night Vision and Electronic Sensors Directorate, Fort Belvoir, VA, USA

[2]CACI Technologies, Arlington, VA, USA

InAs/InAsSb type-II superlattice (SL) materials have garnered significant attention for high performance infrared imaging applications. A primary reason for research efforts on Ga-free InAs/InAsSb SLs is the benefit of longer minority carrier lifetimes compared to those measured in competing InAs/GaSb material systems [1, 2]. Despite promising lifetimes and results from devices, little additional characterization work has been done to date exploring the basic transport properties of InAs/InAsSb SL materials. At this time, research has focused primarily on unintentially (uid) doped *n*-type absorber layers suitable for nBn based detector structures. High minority carrier electron mobility is expected in the case of *p*-type absorbers, but the issue of high surface leakage currents remains an ongoing challenge before this architecture can be fully utilized. Therefore, fundamental characterization of both *n*-type and *p*-type materials are necessary to better understand the InAs/InAsSb SL material system.

A series of unintentially doped (*n*-type) and Be-doped (*p*-type) long-wave infrared InAs/InAsSb layers are investigated in this work. Results from photoluminescence, minority carrier lifetime, in-plane mobility, and surface treatment studies will be discussed. Variable-field Hall measurements will be analyzed in order to extract multi-carrier properties [3-6].

The effect of doping on the electron in-plane mobility and carrier concentration as a function of temperature can be seen in Fig. 1. Intrinsic activation of carrier concentration approaching room temperature are similar between the two samples. Low-temperature behavior shows freeze-out of the electron carrier population in the Be-doped sample for T < 77 K. In the uid sample, the background donor level of electrons is approximately 1 x 10^{15} cm^{-3}. The electron mobility of the uid sample closely follows that of bulk InAsSb material, suggesting electron populations are less confined to individual SL layers when electron and hole populations are comparable. Be-doping appears to restrict electron conduction in the InAsSb-layers and the resultant mobility is more InAs-like in value.

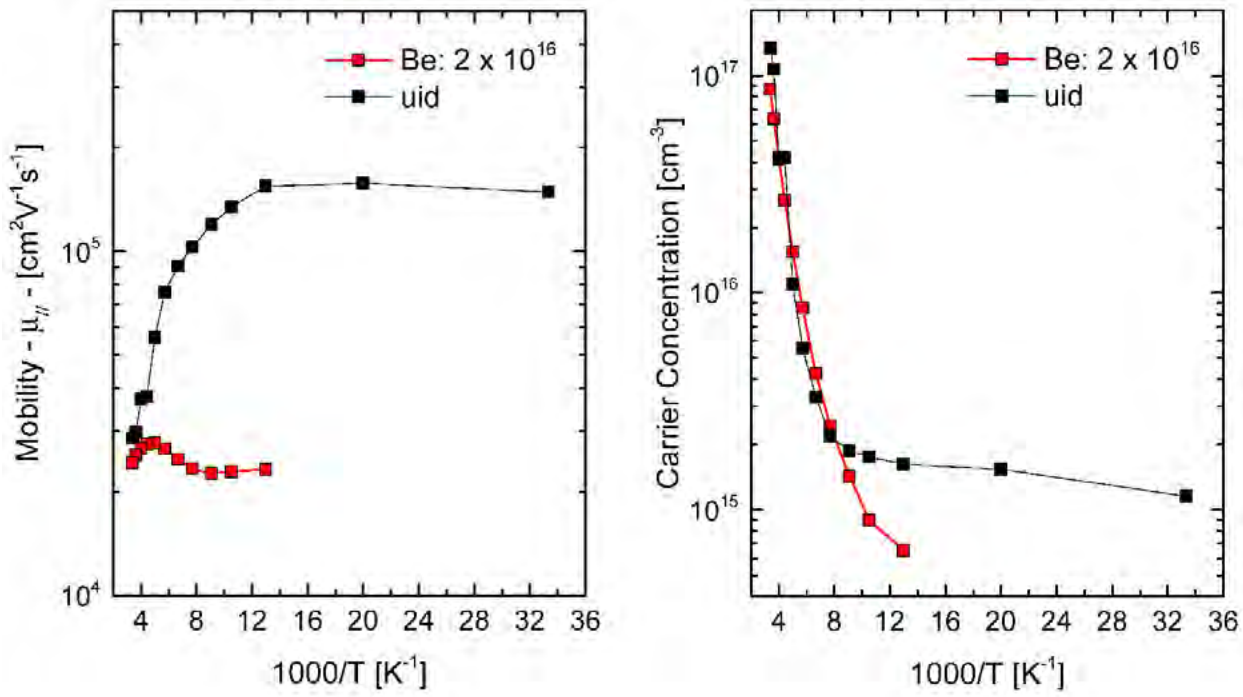

Fig 1. Electron in-plane mobility (left) and carrier concentration (right) versus 1000/T for unintentially doped and Be-doped LW InAs/InAsSb samples.

[1] D. Donetsky, et al. *Appl. Phys. Lett.* 95.21 (2009).

[2] Steenbergen, E. H., et al. *Appl. Phys. Lett.* 99.25 (2011).

[3] W.A. Beck and J.R. Anderson, J. Appl. Phys. **62**, 541 (1987).

[4] Z. Dziuba and M. Gorska, J. Phys. III France **2**, 99 (1992).

[5] J. Antoszewski, D. J. Seymour, L. Faraone, J.R. Meyer, and C.A. Hoffman, J. Electron. Mater. **24**, 1255 (1995).

[6] I. Vurgaftman, J.R. Meer, C.A. Hoffman, D. Redfern, J. Antoszewski, L. Faraone, and J.R. Lindemuth, J. Appl. Phys. **84**, 4966 (1998).

"Effect of photonic annealing on reduction of surface defects on Si(111) and Si(112) measured by changes in the effective surface Debye temperature using LEED"

Surface defects in semiconductors plays very important role in high quality device fabrication and their performance because strong influence on their electrical and optical properties. In this paper we show result of the effect of the photonic annealing using 300 Watt Xe Arc lamp irradiation on the wafer samples of Si(111) and Si(112). The method of characterization employed was Low energy electron diffraction (LEED) and changes of effective surface Debye temperature.

The use of monitoring changes in surface Debye temperature to detect changes in the surface defect concentration is not well established technique but offer several advantages such simplicity and high precision. There is limited literature data which connecting lattice vibrations with defects parameters. The limited nature of the literature resources in this field provides strong motivate experimental investigations. The thermal vibration of the atoms at the surface depends on binding energy, structure and also defects concentration. Most typical surface defects are vacancies, steps, dislocations, boundaries, etc. and they are intrinsic or introduced during surface preparation processes. The defects are influencing the atomic binding energy in the crystal structure which affects the thermal vibration characteristic of the surface. The thermal vibrations characteristic can be characterized by measurements of the surface Debye temperature using LEED. In this method the diffracted beam intensity is measured as a function of the surface temperature. From this plot the surface Debye temperature is calculated. Increasing the primary electron beam energy increases the electron beam penetration to the surface. The diffracted beam close to the normal to the surface give information on thermal vibrations in normal direction. The mean free path for the low energy electrons is in the order of 0.5 nanometers for 100 eV beam energy which ensure the results from the topmost surface layer.

Photonic annealing is applied to reduce surface defects caused by low energy ion bombardment below energy 0.5keV. Photonic annealing of clean Si(111) and Si(112) substrates show LEED pattern changes in the reconstruction of the clean silicon surfaces. It has been demonstrated that photonic annealing is another tool for improving the growth of quality of epitaxial thin films on silicon wafers. The highest temperatures during photonic annealing is at the first surface layer, limiting the restructuring of deeper layers. The variation of the surface Debye temperature using LEED is related to the changes in surface defect densities.

Contact:

CSI2D Inc.

Corporate:

312.282.8407

Steven.kroll@csi2d.com

Author contact:

jozef.ociepa@csi2d.com

dan.zavitz@csi2d.com

Advances and Opportunities in High efficiency CdTe Solar Cells

Gang Xiong

gxiong@firstsolar.com

California Technology Center, First Solar Inc, 1035 Walsh Ave, Santa Clara, CA 95050 USA

In 2015, First Solar has set a new CdTe solar cell efficiency record at 21.1%. Advances in CdTe cell efficiency in the past five years were primary attributed to improvement of Jsc, Voc and FF. Thanks to ZnTe back contact which has higher work function and better chemical affinity with Cu, FF and light soak stability of CdTe devices were significantly improved. The 31.7mA/cm^2 record Jsc was accomplished by elimination of window layer and alloying with Se. Increased V_{oc} has been mostly driven by a nearly two-decade improvement of minority carrier lifetime (from ~1 ns to 100 ns). Our collaboration on DOE fPACE2 program also demonstrated that CdTe as a material is as good as GaAs and 25% device efficiency should be possible.

While 916 mV Voc has been achieved on poly-crystalline CdTe devices with Cu doping and no back surface passivation, further Voc improvement will require some breakthrough on absorber doping and/or reduction of back surface recombination. Recently, we have been able to consistently produce group-V doped CdTe with greater than 10^{16} cm^{-3} hole concentration in poly-crystalline devices. We also demonstrated 810mV devices without Cu addition. Nevertheless SRH recombination in such devices were apparently higher than that of Cu-doped devices, which limits further Voc improvement.

As far as back surface passivation, a few materials such as $Cd_{1-x}Mg_xTe$ showed promise on reduction of CdTe surface recombination velocity. Enhanced Voc was demonstrated on thin absorber devices with back surface passivation layer. However, many back surface passivation materials we investigated exhibited an unfavorable valence band offset hence to block hole transport. Furthermore, some materials may not be manufacturing friendly, for example that $Cd_{1-x}Mg_xTe$ is easy to oxidize in our study.

In summary, we have made great accomplishment in the last couple of years on CdTe solar cell efficiency improvement and understanding of CdTe efficiency entitlement. Significant process and device integration opportunities need to be worked on to further improve device Voc and efficiency. Innovation on material engineering is a must in order to enable future success.

Importance of Target Preparation on Electrical and Optical Properties of ZnTe:Cu Contact Interface Layers

Timothy A. Gessert, Brooke R. Faulkner*, James M. Burst†, Joel N. Duenow†, Craig L. Perkins†, and Bobby To†

EPIR Inc. 590 Territorial Drive, Bolingbrook, IL 60440, USA
**Colorado School of Mines, Physics Department, Golden, CO, 80401 USA*
†National Renewable Energy Laboratory, Golden, CO, 80401 USA
Phone: 720-369-3174, Email: tim.gessert3@gmail.com

Introduction

Developing a low-resistance and stable back contact for both thin-film and epitaxial CdTe photovoltaic (PV) devices is an important goal for the CdTe research community [**1**]. For polycrystalline research devices, studies have have shown that the required contact and device parameters can be achieved by incorporating a Cu-doped ZnTe interface layer between the CdTe absorber and a Ti outer metal contact [**2**]. Moreover, similar contact designs are now used in large-scale commercial module production and have demonstrated both high performance and stability [**3**]. The ZnTe:Cu/metal contact functions by enabling low-resistance tunneling between the ZnTe:Cu and the outer metal (because ZnTe is doped degenerately) [**1,4**], while, the nearly perfect alignment of the CdTe and ZnTe:Cu valence bands allows low resistance hole transport between the CdTe and ZnTe:Cu layers [**1,5**].

Recently, studies have shown that small changes in ZnTe:Cu sputtering target preparation not only affects the compositional and optical properties of the films, but also can produce significant changes in device performance. These changes in performance have been found to be linked to small changes in the amount of Cu, Zn/Te ratio, and oxygen content in the ZnTe:Cu films [**6**,**7**]. Although not yet completely understood, it is tempting to suggest that ZnTe:Cu films containing excessive oxygen may be linked to formation of Cu-O phases that has been previously linked to limiting the amount of Cu that can beneficially diffuse from the ZnTe:Cu into the CdTe [**8**]. Suspecting that the higher oxygen content in the ZnTe:Cu film may be related to changes in film properties and lower device performance, earlier work reduced oxygen in the films by altering both the parameters of the deposition process. [[9]] In this study, we report on controlling oxygen content in the film by altering the amount of oxygen in the targets themselves.

Experimental Details

Superstrate CdS/CdTe materials used in this study were produced at NREL with the structure of glass/SnO_2:F/SnO_2/CdS/CdTe/ZnTe:Cu/Ti as shown in **Fig. 1**. The ZnTe:Cu/Ti contacts were processed in a single multisource vacuum processing chamber at a contact deposition temperatures of 340°C following a 120 min preheat. Prior to ZnTe:Cu deposition, approximately 100 nm of material was removed using ion-beam milling to clean the surface of any process residues, and yield the required interface stoichiometry. The ZnTe:Cu/Ti layer (4 wt.% Cu, ~0.4 µm) was deposited by r.f. magnetron sputtering, and the Ti layer (~0.5 µm) was deposited by d.c. magnetron sputtering. Following a 120 min cool down, the sample was removed from the vacuum

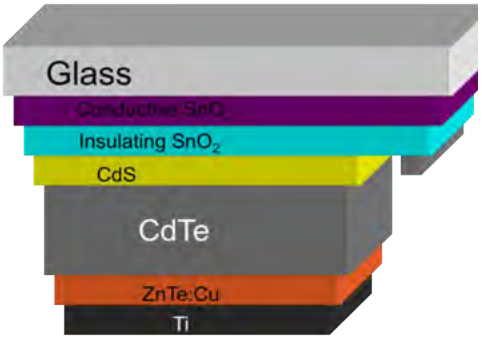

Figure 1. Schematic of CdS/CdTe photovoltaic superstrate device structure.

chamber and a pattern of individual 0.25-cm^2 cells was defined photolithographically and chemically. Contact to the SnO_2:F was a perimeter of ultrasonically soldered indium. Additional experimental parameters are provided elsewhere [8].

ZnTe:Cu films used in this study were deposited from one of three types of sputtering targets onto cleaned soda-lime glass substrates using r.f. magnetron sputtering in a Unifilm Technologies PVD 300, multi-source, planetary-motion sputtering system. Two different recipes were used by the vendor (Materion, Milwaukee, WI) to produce the sputtering targets. The first process (Recipe #1) started with ZnTe powder that was blended with Cu-metal powder, reacted, hot-pressed, and machined to final dimensions. A second recipe (Recipe #2) was developed in attempt to reduce the oxygen concentration in the pressed targets. This recipe used elemental Zn, Cu, and Te as the initial starting powders (instead of ZnTe and Cu). These elemental powders were reacted in a reducing environment to form a mixture of ZnTe and Cu_2Te. This reacted material was re-sized (masticated), and hot-pressed to form the targets with the desired Cu concentrations (2 and 4 wt.%). Recipe #1 targets contained 4 weight percent of Cu, while Recipe #2 was produced with both 2 or 4 weight percent of Cu.

Results and Discussion

Initial materials analysis indicated targets produced from Recipe #2 yielded higher-density targets compared to Recipe #1. Also, for similar sputtering conditions, Recipe #2 produce films that were visually more transparent. The observation of increased visual transparency is consistent with earlier observations that ZnTe:Cu films with lower oxygen content tend to yield a optical band gap values that are more consistent with crystalline ZnTe (i.e., 2.25 eV). **[10]** XPS and EPMA analysis (see **Fig. 2**) confirmed that differences in target synthesis affected also the composition of the films, with Recipe #2 generally resulting in a higher Te/Zn ratio, and less oxygen in the film. Electrical analysis of devices made with the different targets (dark and light current-voltage [IV], see **Fig. 3**) also revealed significant differences in device performance, with the highest performance devices resulting from ZnTe:Cu layers produced from the targets made using Recipe #2.

Although the compositional and electrical results provide compelling evidence regarding the detrimental effect of oxygen in the ZnTe:Cu sputtering target (and possibly equally detrimental effects of lower Te/Zn ratio), earlier studies had also linked oxygen in the ZnTe:Cu film to significant changes in optical band gap.

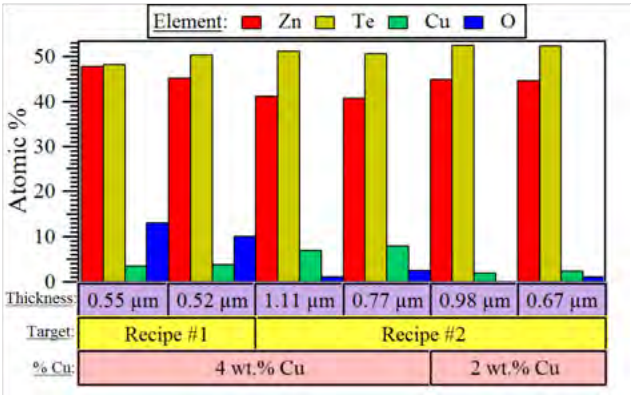

Fig. 2. Compositional data of ZnTe:Cu films deposited from three different target-synthesis recipes. The Zn, Cu, and Te concentrations were determined by EPMA, and oxygen by XPS.

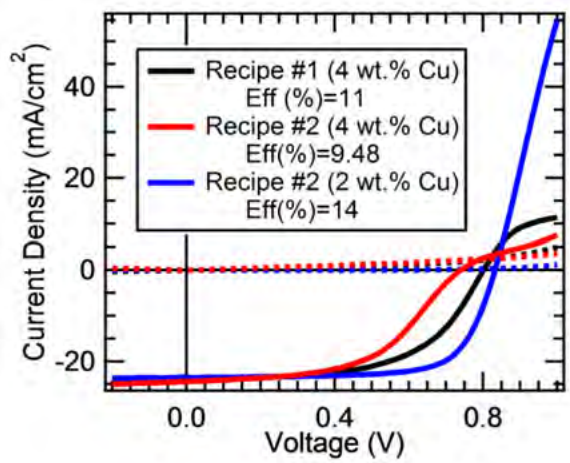

Fig. 3. Light and dark IV measurements of devices made with ZnTe:Cu targets using different target-synthesis recipes.

This study therefore also explored the effect on possible changes in optical properties with variations in target synthesis. Tauc plots shown in **Fig. 4** revealed, as expected from the visual appearance of the films, that films sputtered from Recipe-#2 produced targets demonstrate a higher optical band gap than those sputtered from Recipe #1, with many of the Recipe #2 films demonstrating optical band gap values very near the expected crystalline value of 2.25 eV. At this time, a full analysis of these optical results have not been completed. However, many reports have suggested the presence of an intermediate band gap in ZnTe:O-based materials. We therefore suggest that it is likely a similar intermediate band gap related optical transitions may be occurring here. [**11**] At this time, it is not clear if the the significant differences in device performance are due largely to the oxygen effecting Cu out-diffusion from the ZnTe:Cu, or rather from possible changes in valance-band alignment that could result from the formation of the intermediate band gap.

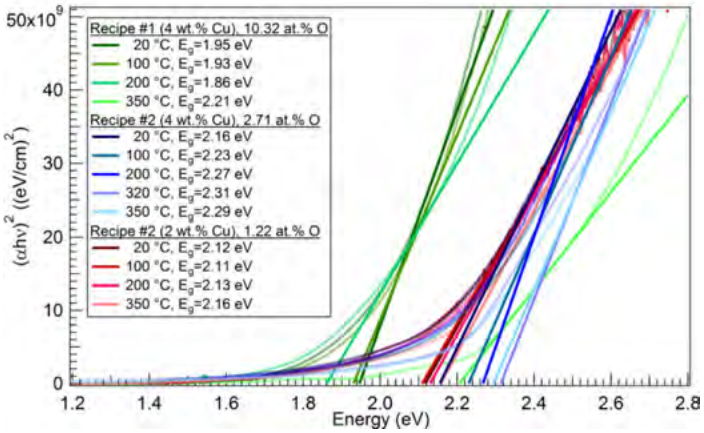

Fig. 4. Tauc plot showing absorption spectra of the ZnTe:Cu films deposited at substrate temperatures ranging 20- 350 °C from each of the three different targets. The optical band gap for each film was determined from the linear fit of each curve and stated in the legend along with the oxygen concentrations.

Acknowledgements

This work was partially facilitated through an Alliance Partnership University Program (APUP) between the National Renewable Energy Laboratory and Colorado School of Mines under Contract No. UGA-0-41025-57, and partially funded by the U.S. Department of Energy under Contract No. DE-AC36-08-GO28308 with the National Renewable Energy Laboratory

References

[1] T.A. Gessert, C.L. Perkins, S.E. Asher, A. Duda, and M.R. Young, "Study of ZnTe:Cu/Metal Interfaces in CdS/CdTe Photovoltaic Solar Cells," *Mat. Res. Soc. Proc.* **796**, pp. 79-84 (2004).

[2] T.A. Gessert, A. Duda, S.E. Asher, C. Narayanswamy, and D. Rose, "Effects of Cu from ZnTe:Cu Contacts in CdS/CdTe Cells,"Proc. 28th IEEE PVSC (IEEE, Piscataway, NJ, 2000), pp. 654-657.

[3] N. Strevel, L. Trippel, C. Kotarba, and I. Khan, "Improvement in CdTe Module and Long Term Degradation Through Advances in Construction and Device Innovation," Photovoltaics International, Vol. 22, pp. 66-74. Dec. 2013 .

[4] T.A. Gessert, S. Asher, S. Johnston, A. Duda, and M.R. Young, "Formation of ZnTe:Cu/Ti Contacts at High Temperature for CdS/CdTe Devices," Proc. 4th WCPVEC, 2006, pp. 432-435.

[5] D. Rioux, D.W. Niles, and H. Hochst, "ZnTe: A Potential Interlayer to Form Low Resistance Back Contacts in CdS/CdTE Solar Cells," J. Appl. Phys. **73** 8381 (1993).

[6] B.R. Faulkner, J.M. Burst, T.R. Ohno, C.L. Perkins, B. To, T.A. Gessert, "ZnTe:Cu Film Properties and Their Impact on CdS/CdTe Devices," Proc. 40th IEEE PVSC (IEEE, Piscataway, NJ, 2014).

[7] T. A. Gessert, J. M. Burst and J. N. Duenow, "Variation of ZnTe:Cu Source and Film Properties and Impacts on CdS/CdTe Solar Cell Performance," in Workshop on Physics and Chemistry of II-VI Materials and Devices, Oct. 1-3, 2013.
[8] T.A. Gessert, S. Asher, S. Johnston, M. Young, P. Dippo, and C. Corwine, "Analysis of CdS/CdTe Devices Incorporating a ZnTe:Cu/Ti Contact," Thin Film Solids, **515**, pp. 6103-6106 (2007).
[9] T.A. Gessert, J.M. Burst, J.N. Duenow, C.L. Perkins, B. To, and B.R. Faulkner, "Variation of ZnTe:Cu Source and Film Properties and Impacts on CdS/CdTe Solar Cell Performance," in Proc. 2013 Workshop on the Physics and Chemistry of II-VI Materials, (2013).
[10] T.A. Gessert, "A Fundamental Study of the Electrical and Optical Properties of Thin-Film r.f.-Sputter-Deposited, Cu-Doped ZnTe," Ph.D. Thesis, University of Wales, College of Cardiff, pp. 134-135 (1996).
[11] W. Wang, S. Lin, and J.D. Phillips, "Intermediate-Band Solar Cells Based on ZnTeO," in Proc. Of 2008 Workshop on the Physics and Chemistry of II-VI Materials," (2008).

High quality $AgGaTe_2$ layers formed from Ga_2Te_3/Ag_2Te two layer structures

A. Uruno[1]*, Y. Sakurakawa[1], and M. Kobayashi[1,2]

a.uruno@fuji.waseda.jp +81-3-5286-1684

[1] *Dept. of Elec. Eng. & Biosci., Waseda Univ., Shinjuku, Tokyo, Japan.*

[2] *Kagami Mem. Res. Inst. for Mat. Sci. & Technol. Waseda Univ., Shinjuku, Tokyo, Japan.*

Abstract: In this paper, $AgGaTe_2$ layer was prepared from successive deposition of Ga_2Te_3/Ag_2Te by the CSS method. The XRD pattern for the as deposited Ga_2Te_3 layer on the Ag_2Te layer exhibited peaks originating from only $AgGaTe_2$. This indicated that the recrystallization of Ga_2Te_3 and Ag_2Te was occurred during Ga_2Te_3 deposition, and resulted in the formation of $AgGaTe_2$.

Keywords: solar cell, chalcopyrite, closed space sublimation

1. INTRODUCTION

I-III-Te_2 compounds are materials which replace Cd of CdTe by group I and III elements. The growth of crystalline $AgGaTe_2$, $AgAlTe_2$ and $Ag(Ga,Al)Te_2$ layers by the closed space sublimation (CSS) method on Si and sapphire substrates has been successfully achieved[1]. In particular, it was revealed that the uniform $AgGaTe_2$ layer on the n-Si substrate without melt-back etching was realized when the $AgGaTe_2$ layer was prepared on the top of the Ag_2Te buffer layer using the mixed source of Ag_2Te and Ga_2Te[2]. This p-$AgGaTe_2$/n-Si structure was applied to the solar cell and a conversion efficiency of 3.0% was achieved[2]. However, Ag_2Te and $AgGa_5Te_8$ were often observed as by-products in those experiments. It was confirmed the stoichiometry control was relatively difficult, because the Ag_2Te buffer layer was an additional supply source for the growth of $AgGaTe_2$. Therefore, $AgGaTe_2$ layer was attempted to prepare from successive deposition of Ga_2Te_3/Ag_2Te (two layer structure). The mole ratio control would

be relatively simplified since it could be realized by the thickness control of two independent layers. In this study, the Ag_2Te and Ga_2Te_3 single layer were deposited directly on the Si substrate respectively, and the characteristic of layers was investigated. Then, the preparation of Ga_2Te_3/Ag_2Te two layer structure was performed.

2. EXPERIMANTAL

The Ag_2Te layers and the Ga_2Te_3 layers were deposited on (001) n-Si substrate under various condition by the CSS method. The Ag_2Te and Ga_2Te_3 source temperatures were varied from 750°C to 850°C and 680°C to 700°C, respectively. The temperature difference between the source and substrate was set to approximately 40°C constant. The crystallographic properties were evaluated by θ-2θ profiles of X-ray diffraction (XRD), and cross-sectional scanning electron microscopy (SEM) was used to characterize the layered structure.

3. RESULTS AND DISCUSSION

SEM images of Ag_2Te and Ga_2Te_3 single layers on Si substrates are shown in Fig.1. The source temperature of Ag_2Te and Ga_2Te_3 were approximately 840°C and 700°C, respectively. It was revealed that the Ag_2Te layer surface exhibited a membrane filter structure. On the other hand, the Ga_2Te_3 layer exhibited smooth surface layer with flat grains. The Ga_2Te_3/Ag_2Te two layer structure was prepared using similar parameters; designed Ag_2Te layer and the Ga_2Te_3 layer thickness were approximately 2 μm by tuning the deposition time. Figure 2 shows the XRD pattern for the as deposited Ga_2Te_3 layer on the Ag_2Te layer. The pattern exhibited peaks originating only from $AgGaTe_2$. This fact probably indicated that the recrystallization of the layer was occurred during the Ga_2Te_3 deposition, which resulted in the formation of the $AgGaTe_2$ layer. SEM of the obtained layer also confirmed the formation of homogeneous layer on the Si substrate (Fig. 3.). From these results, it was cleared that high quality $AgGaTe_2$ layers could be

grown on Si substrate from Ga_2Te_3/Ag_2Te two layer structure through the recrystallization. It was considered that Ag_2Te layer acted as an effective layer for elimination of the melt-back etching problem, and the membrane filter structure surface includes numerous kinks acted as the effective nucleation site of Ga_2Te_3.

4. CONCLUSION

Ag_2Te and Ga_2Te_3 single layers were deposited on the (001) Si substrate. It was confirmed that the Ag_2Te layer surface exhibited a membrane filter structure, while the Ga_2Te_3 layer surface exhibited smooth layer with flat grains. $AgGaTe_2$ layer was prepared from successive deposition of Ga_2Te_3 on Ag_2Te/Si. The XRD pattern of the Ga_2Te_3/Ag_2Te layer exhibited peaks originating only from $AgGaTe_2$. This indicated that the recrystallization of Ga_2Te_3 and Ag_2Te was occurred during the Ga_2Te_3 deposition, and resulted in the formation of $AgGaTe_2$.

ACKNOWLEDGMENTS

This work was supported in part by Waseda Univ. Research Initiatives, Waseda Univ. Grant for Special Research, and Project and JSPS Research Fellowships for Young Scientists.

REFERENCE

[1] A. Uruno, A. Usui, T. Inoue, Y. Takeda, and M. Kobayashi, J. Electron. Mater. **44**, 3013 (2015).

[2] A. Uruno, and M. Kobayashi, J. Electron. Mater. **45**, 4692 (2016).

FIGURES

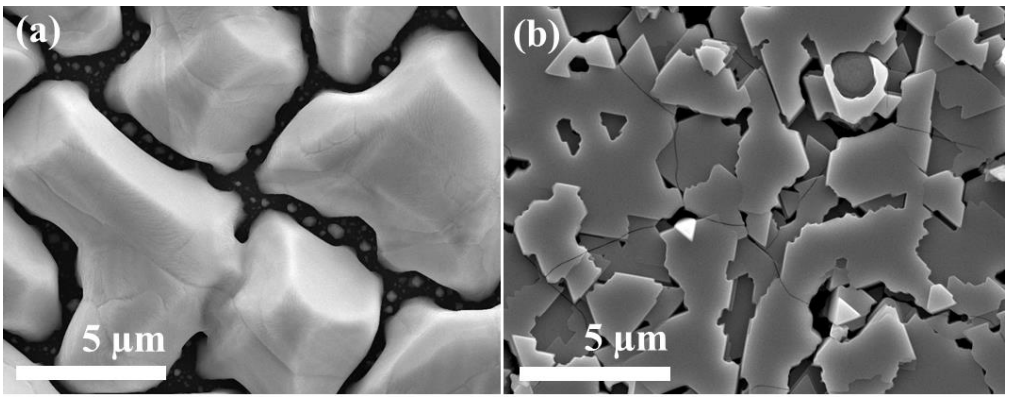

Figure 1. (a) The SEM surface image of (a) Ag_2Te layer and (b) Ga_2Te_3 layer.

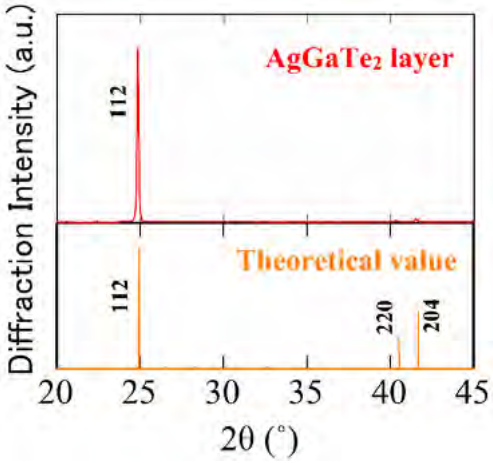

Figure 2. XRD θ-2θ scans of the as deposited Ga_2Te_3/Ag_2Te bilayer and the theoretical value of $AgGaTe_2$.

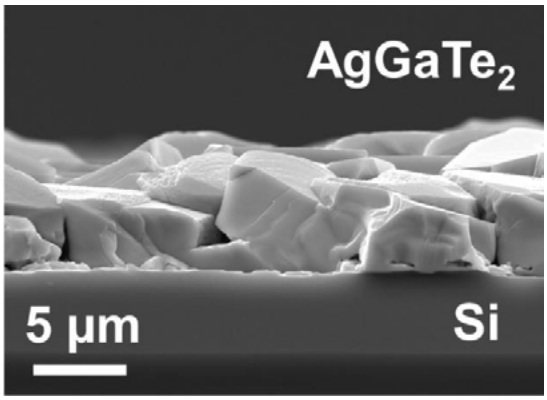

Figure 3. The cross-sectional SEM image of the $AgGaTe_2$ layer obtained from Ga_2Te_3/Ag_2Te substrate.

Iodine doping of CdTe and CdMgTe for Photovoltaic Applications

O.S. Ogedengbe,[1] P.A.R.D. Jayathilaka,[1] J.E. Petersen,[1] S. Sohal,[1] E.G LeBlanc,[1] M. Edirisooriya,[1] C.H. Swartz, [1] K.N. Zaunbrecher,[2] A. Wang,[3] T.M. Barnes[2] T.H. Myers,[1]
oso6@txstate.edu – *512 245 1839*

[1]Materials Science, Engineering, & Commercialization Program, Texas State University, San Marcos, TX 78666, USA
[2]National Renewable Energy Laboratory, 15013 Denver West Parkway MS RSF200, Golden, CO 80401, USA
[3] EAG, Inc. (Evans Analytical Group), 810 Kifer Road, Sunnyvale, CA 94086, USA

CdTe solar cells continue to improve in device performance and market share, but its current solar conversion efficiency of 21%[1] remains more than ten absolute percent below the predicted Shockley–Queisser limit. Since the short-circuit current density is near the theoretical limit, efforts are focusing on improving open-circuit voltage (V_{OC}) and fill factor, which are currently below 900 mV and 80%, respectively, for most devices[2]. The use of extrinsic dopants are expected to improve the V_{OC} dramatically. Several research efforts have demonstrated long carrier lifetimes and low interface state density, other important criteria, in both epitaxial CdTe and bulk CdTe along with a single crystal CdTe device with *Voc* of 1017 mV[3]. CdTe-based solar cells typically rely on the n-side to be heavily doped at levels which have been shown to be problematic for doping with Indium (In)[4], which is currently the n-type dopant of choice. The other n-type dopants that have been used successfully in CdTe are chlorine (Cl), bromine (Br), and iodine (I). Cl and Br appear to be very similar to In in terms of maximum N_D (2×10^{18} cm^{-3}) and compensation[5, 6]. I-doping of CdTe grown on (100)-oriented CdZnTe[7], (100)-oriented CdTe and (211)B-oriented GaAs[8] substrates resulted in N_D of mid-10^{18} cm^{-3} without apparent compensation. I-doped CdTe samples made with ethyliodide yielded extremely bright excitonic PL at 300 K, suggesting that these samples had fewer non-radiative defects[8]. Thus, we have investigated I as a n-type dopant for CdTe layers to determine N_D, τ, and process compatibility in the typical PV device stack.

Iodine has been shown to easily and reliably produce heavy doping in CdTe at levels up to $7.4\text{x}10^{18}$ cm^{-3} as shown in Figure 1. While not demonstrated in this study, it might be possible to achieve a slightly higher level, but it is clear that heavy compensation occurs much above this concentration of I. Based on calibrated SIMS measurements, the highest doped sample had an activation of greater than 80%. Consistent with this, temperature-dependent Hall measurements indicated a very low activation energy, < 10meV for heavily doped samples as indicated in Figure 3. Room temperature mobility was good at 800 $cm^2V^{-1}s^{-1}$, and increased with decreasing temperature as shown in Fig. 2. We have n-type doping of $Cd_{0.65}Mg_{0.35}Te$ up to $2\text{x}10^{17}$ cm^{-3} with iodine without observation of structural degradation. Fig. 4 shows the temperature dependence of carrier concentration for a layer with I at $6\text{x}10^{16}$ cm^{-3}. We note that little temperature dependence was observed for n-type carrier concentration in CdTe at doping levels above $5\text{x}10^{17}$ cm^{-3} or in CdMgTe above $1\text{x}10^{17}$ cm^{-3}.

We have produced molecular beam epitaxy (MBE) grown double heterostructures (DH) with variable n-type iodine doping and shown surface recombination well below 200 cm/s. The iodine-doped samples show long lifetimes with evidence of photon recycling effects and no evidence of PL degradation with doping as high as $2x10^{18}cm^{-3}$, in contrast to In which exhibits significant non-radiative recombination at levels above $5x10^{16}cm^{-3}$ [4]. This suggests that iodine may be the preferred dopant for highly doped n-type CdTe.

The appropriate relationship for low-injection TRPL lifetimes in the case of doping is as follows:

$$\frac{1}{\tau_{eff}} = \frac{1}{\tau_{rad}} + \frac{1}{\tau_{SRH}} + \frac{2S}{d}$$

where S is the surface recombination velocity and d is absorber thickness in the last term which represents the effect of surface recombination. The radiative lifetime is given by

$$\tau_{rad} = \frac{1}{B_{rad} n \varphi}$$

where n is the carrier concentration and B is the radiative parameter. Previous studies analyzing the PL dependence on excitation intensity coupled with TRPL on undoped DH strongly support a value of B_{rad} = 1×10^{-10} cm^3s^{-1}, which is consisted with the Van Roosbroeck-Shockley (VRS) relationship between absorption and recombination[9] that yields a similar value obtained solely from the absorption spectrum of CdTe[10, 11]. The parameter φ is the so-called "photon recycling factor" which recognizes that in high quality material, especially in a thick DH configuration, photons emitted in the radiative recombination process can be reabsorbed to create another electron-hole pair, effectively recycling the original pair.

Figure 5 contains a plot of the TRPL lifetimes measured for three iodine doping levels at various absorber thicknesses in CdTe/ $Cd_{0.65}Mg_{0.35}Te$ DHs. Based on prior work, this CdMgTe barrier composition results in a SRV of 160 cm/s with nominally undoped material grown at Texas State. The red line in the graph illustrates the expected upper limit on TRPL lifetime expected due to surface recombination based on this value. From the results for TRPL shown, it is clear that several values exceed this limit, suggesting that SRV in these doped samples is actually less than 160 cm/s. Assuming that the three highest values for the $n\sim1x10^{16}$ cm^{-3} DHs are due primarily to surface recombination and radiative recombination with φ ~1, the measured lifetimes indicate a SRV on the order of 25 cm/s.

The radiative lifetimes indicated for a given doping level assuming φ ~1 and B_{rad} = 1×10^{-10} cm^3s^{-1} are shown color-coded along with the TRPL measured for the associated doping levels. The $n\sim1x10^{16}$ cm^{-3} DHs seem to be reasonably explained without invoking photon recycling (with the above caveat on actual SRV). In contrast, the majority of the TRPL lifetimes measured for the $n\sim1x10^{17}$ cm^{-3} and $n\sim1x10^{18}$ cm^{-3} DHs exceed the radiative limit by factors of three to six. This effect is consistent with what is observed for doped GaAs/AlGaAs DHs, again underscoring that once surface recombination is controlled the electronic properties of CdTe are comparable to

those of GaAs, with the potential benefits of a slightly lower radiative recombination parameter and a higher tolerance to dislocations.

Fig. 6 illustrates that the PL intensity increases with increasing I concentration similar to that observed with In doping. However, for I levels as high as $2x10^{18}cm^{-3}$ (the highest in a DH grown to date) the PL intensity does not show degradation. This result, coupled with the longer lifetimes observed for I-doping compared to equivalent In-doping levels, suggest that iodine may be the preferred dopant for highly doped n-type CdTe. Iodine has proven to be thermally stable in CdTe device structures grown by MBE at anneal conditions of 500 °C for 12 hours and 600 °C for 4 hours in sealed ampoules under Cd over pressure. The results of these thermal anneals, as shown in Figure 7, indicate that there is no significant change in the concentration-depth profile of the annealed samples when compared to that of the unannealed sample, which are pieces from the same epilayer, as characterized by SIMS. This result suggests that iodine is not a fast diffusing dopant in CdTe, which makes an additional case for the use of iodine as the preferred n-type dopant.

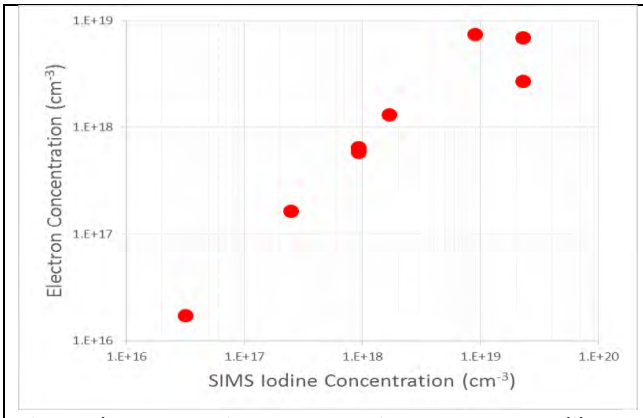

Fig 1. Electron carrier concentration at 300K vs. calibrated SIMS iodine concentration, illustrating the high level of activation and wide range of electron concentration

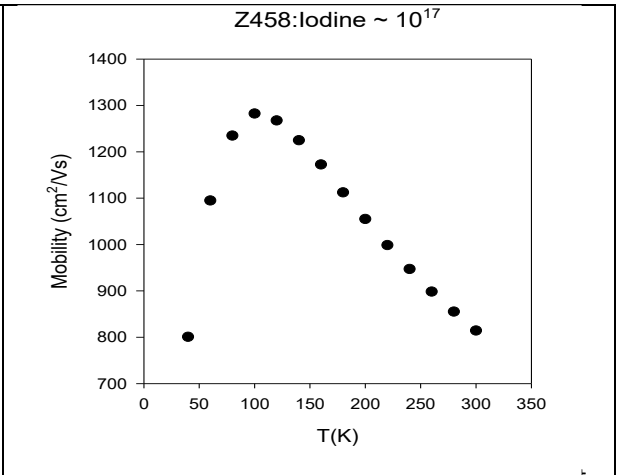

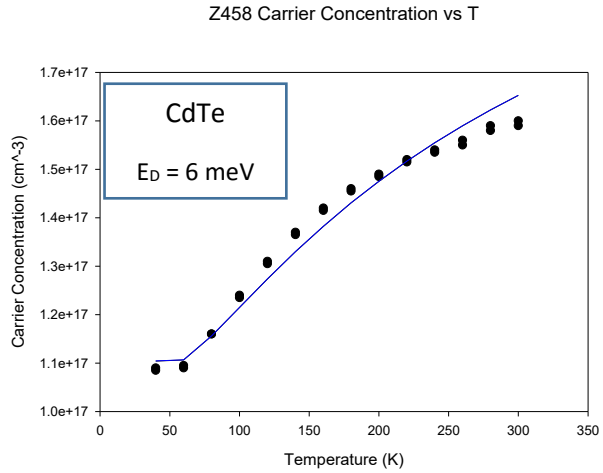

Fig 3. Temperature dependence of carrier concentration with I at $1.6x10^{17}$ cm^{-3}

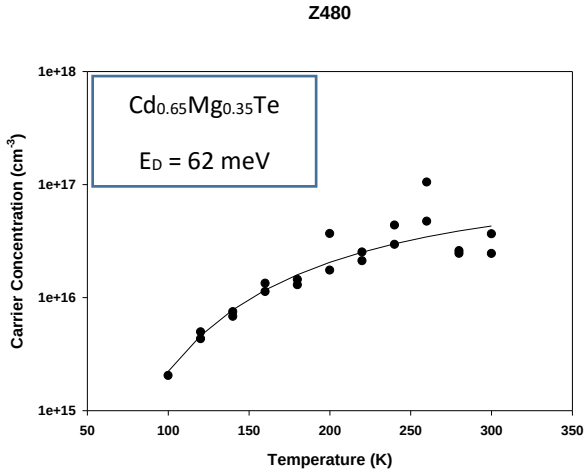

Fig 4. Temperature dependence of carrier concentration with I at $6x10^{16}$ cm^{-3}

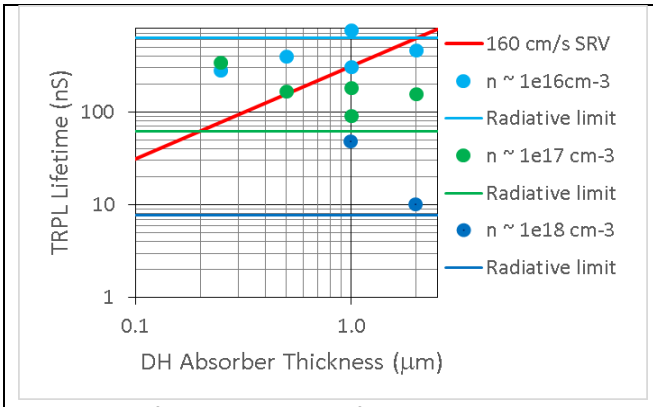

Fig. 5 TRPL lifetimes measured for three doping levels at various absorber thicknesses in CdTe/$Cd_{0.65}Mg_{0.35}Te$ DHs

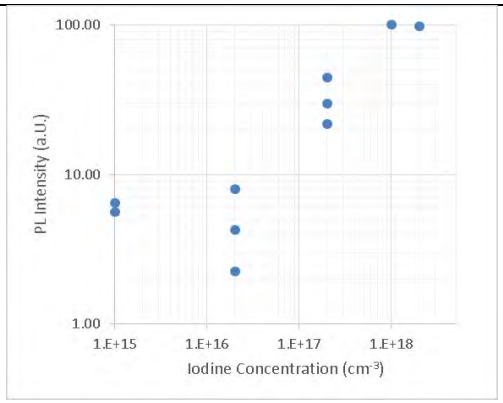

Fig 6. Integrated PL intensity vs. Iodine concentration in I-doped CdTe/CdMgTe DHs

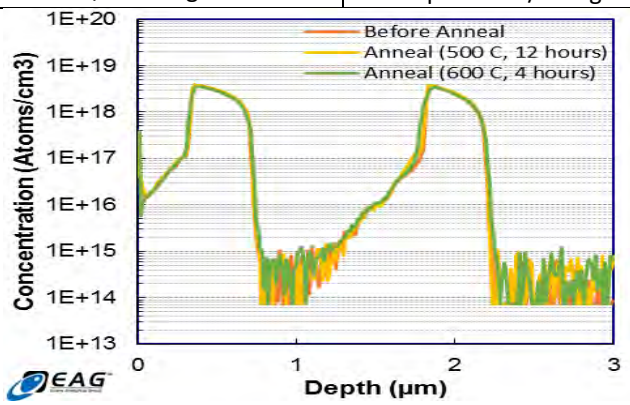

Fig 7. SIMS profile of an un-annealed and annealed Iodine step-doped CdTe samples for anneal conditions of 500 °C, 12 hours and 600 °C, 4 hours under Cd over pressure

1. M. A. Green, K. Emery, Y. Hishikawa, W. Warta and E. D. Dunlop, Progress in Photovoltaics: Research and Applications **24** (NREL/JA-5J00-65643) (2016).
2. T. Gessert, S.-H. Wei, J. Ma, D. Albin, R. Dhere, J. Duenow, D. Kuciauskas, A. Kanevce, T. Barnes and J. Burst, Solar Energy Materials and Solar Cells **119**, 149-155 (2013).
3. J. M. Burst, J. N. Duenow, D. S. Albin, E. Colegrove, M. O. Reese, J. A. Aguiar, C.-S. Jiang, M. Patel, M. M. Al-Jassim and D. Kuciauskas, Nature Energy **1**, 16015 (2016).
4. X.-H. Zhao, S. Liu, Y. Zhao, C. M. Campbell, M. B. Lassise, Y.-S. Kuo and Y.-H. Zhang, presented at the Photovoltaic Specialist Conference (PVSC), 2015 IEEE 42nd, 2015 (unpublished).
5. A. Waag, T. Litz, F. Fischer, H. Heinke, S. Scholl, D. Hommel, G. Landwehr and G. Bilger, Journal of crystal growth **138** (1), 437-442 (1994).
6. F. Bassani, S. Tatarenko, K. Kheng, P. Jouneau, K. Saminadayar, N. Magnea and R. Cox, Applied physics letters **63** (15), 2106-2108 (1993).
7. D. Brun-Le-Cunff, T. Baron, B. Daudin, S. Tatarenko and B. Blanchard, Applied physics letters **67** (7), 965-967 (1995).
8. N. Giles, J. Lee, T. Myers, Z. Yu, B. Wagner, R. Benz and C. Summers, Journal of electronic materials **24** (5), 691-696 (1995).
9. W. Van Roosbroeck and W. Shockley, Physical Review **94** (6), 1558 (1954).
10. A. P. Kirk, M. J. DiNezza, S. Liu, X.-H. Zhao and Y.-H. Zhang, presented at the 2013 IEEE 39th Photovoltaic Specialists Conference (PVSC), 2013 (unpublished).
11. A. Rakhshani, Journal of applied physics **81** (12), 7988-7993 (1997).

Preparation and photoelectric properties of n-TiO_2/p-$Cd_{1-x}Zn_xTe$ heterojunction films

Kai Xu, Yue Shen*, Zongkun Zhang, Jian Huang, Meng Cao, Feng Gu, Linjun Wang
School of Materials Science and Engineering, Shanghai University, Shanghai 200072, China
E-mail address : yueshen@shu.edu.cn

Abstract

In this paper, we adopt chemical and physical methods to preparing n-TiO_2 and p-$Cd_{1-x}Zn_xTe$ films, respectively. In order to improve interlayer introduction and enhance the efficiency of the solar cell, the TiO_2 film is prepared as mesoporous layer by doctor blade method. And the p-$Cd_{1-x}Zn_xTe$ layer is coated by near space sublimation method. Their electrical properties were investigated at forward and reverse biases. The I-V characteristics of heterojunction n-TiO_2/p-$Cd_{1-x}Zn_xTe$ and the main photoelectric parameters were measured under AM 1.5 illumination with an incident light intensity of 100 mW/cm^2 at room temperature. The diffuse reflectance spectroscopy show n-TiO_2/p-$Cd_{1-x}Zn_xTe$ heterojunctions have strong absorption from 300~800 nm, almost including the whole visible light.

1. INTRODUCTION

CdTe is one of the most prospective materials for highly efficient photovoltaic conversion. Comparing with CdTe, $Cd_{1-x}Zn_xTe$ possess better structural perfection, because the addition of Zn atoms to CdTe leads to the reduction of the dislocation density and prevents the cellular structure of their arrangement due to the strengthening of the CdTe lattice. And titanium dioxide (TiO_2) is normally used as a transparent conductive oxide in solar cells applications because it has a high transparency for visible light, large value of the refractive index, controllable specific resistance, good adhesion, high chemical resistance, and is environment friendly. These properties make n-TiO_2/p-$Cd_{1-x}Zn_xTe$ heterojunctions an ideal material for application in photovoltaics [1-3].

2. FIGURES

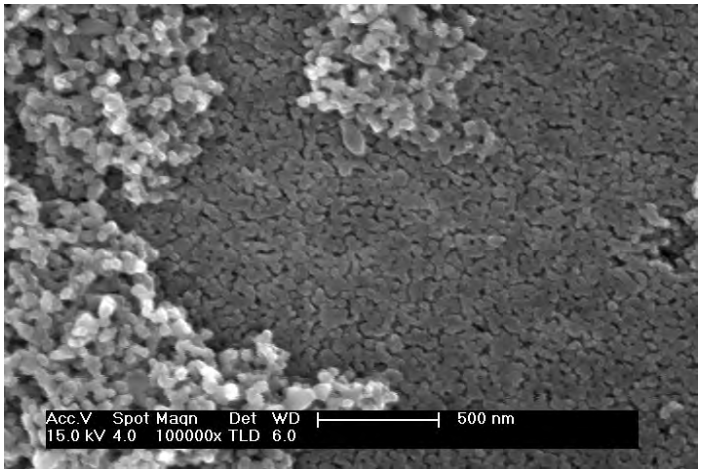

Figure 1 SEM of TiO_2 compact layer on FTO.

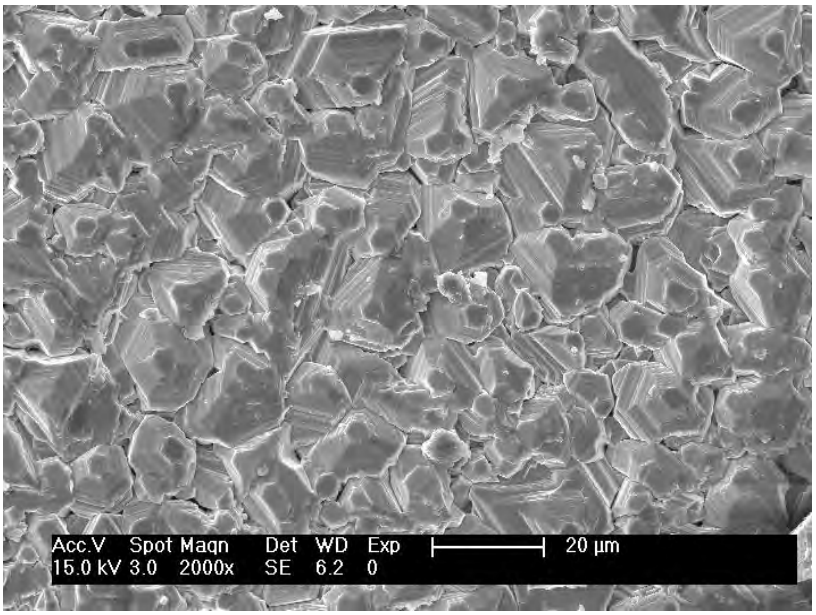

Figure 1 SEM of CZT film.

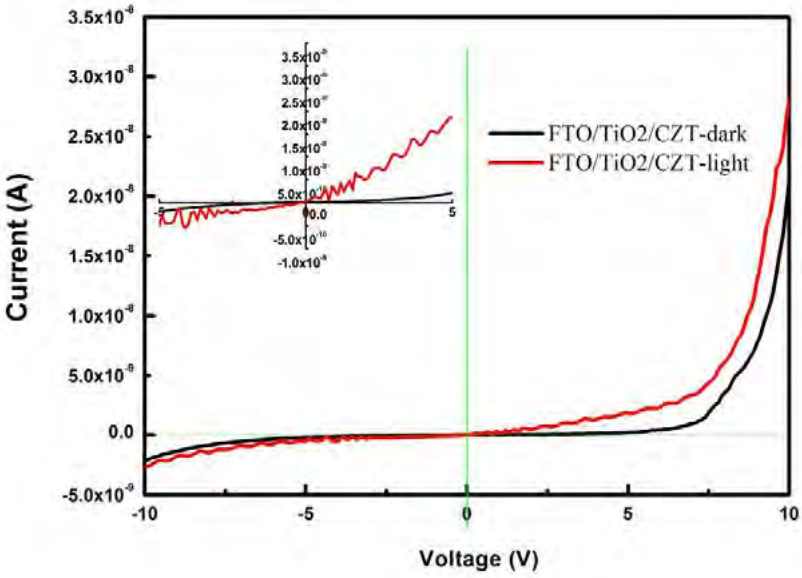

Figure 3 the I-V characteristics of heterojunction n-TiO_2/p-Cd1-xZnxTe under different condition.

3. REFERENCES

1. M. Houshmand, H. Esmaili, M. Hossein Zandi and N. E. Gorji, *Materials Letters*, 2015, **157**, 123-126.
2. V. V. Brus, M. I. Ilashchuk, Z. D. Kovalyuk, P. D. Maryanchuk and O. A. Parfenyuk, *Semiconductor Science and Technology*, 2013, **28**, 015014.
3. V. V. Brus, M. I. Ilashchuk, Z. D. Kovalyuk and P. D. Maryanchuk, *Semiconductor Science and Technology*, 2012, **27**, 055008.

MOVPE-grown HgCdTe heterostructure development at Leonardo (formally Selex-ES)

C.D.Maxey, J.W.Wilson I.Baker, L.Hipwood,

Leonardo, First Avenue, Millbrook Ind Est, Southampton, Hants, SO15 0LG, UK

* Tel: 023 80316711
Fax: 023 80316777
E-mail: chris.maxey@leonardocompany.com

Abstract

This presentation will describe the progress in development of IR detectors based on MOVPE growth of fully doped heterostructures. By careful control of the heterostructure design and processing many device architectures can be achieved that allow the production of IR detectors with spectral response ranging from 0.8 – 17μm. Focal plane arrays have been developed with a range of pixel pitch, formats sizes and operating temperature from megapixel MW or SW arrays with 8 – 17 μm pitch for conventional imaging to smaller arrays for specific applications , including electron avalanche photodiode (eAPD) with spectral response from 0.8 to 2.5μm for spectroscopy, interferometry, single photon detection and wavefront sensing.

Keywords: eAPD, HgCdTe, IRFPA, MOVPE, megapixel

GEOMETRICAL CHARACTERISTIC OF CD-RICH INCLUSION DEFECTS IN CDZNTE MATERIALS

Chao Xu, Fengfeng Sheng and Jianrong Yang

charlesxu@mail.sitp.ac.cn +86-15201918400

Key Laboratory of Infrared Imaging Materials and Devices, Shanghai Institute of Technical Physics, Chinese Academy of Sciences, 500 Yu Tian Road, Shanghai, 200083, People's Republic of China.

Abstract: The geometrical characteristic of Cd-rich inclusion detects in CdZnTe crystals were investigated by infrared transmission (IRT) microscopy and chemical etching methods. Based on the experimental results, the orientation and shape of dislocation extension belts were determined. The results show that the dislocation extension belts situate inside both {110} and {113} planes and the extension directions in 3-D space is <211> crystal orientation. To explain the IRT images of Cd-rich inclusion observed in the experiments, a 3D model with plate-shaped structure was proposed. And the gray level of the dislocation extension belt on IRT image depend on the thickness of the belt that the light passes through. The IRT images of the Cd-rich inclusion defect can be well explained by the 3-D defect model if assuming that the defect can be discriminated from IRT microscope only when its absorption layer thicknesses is larger than twice the thickness of the dislocation extension belts.

Key words*:* Compound；Semiconductors; Defects; Dislocation; Inclusions

1. INTRODUCTION

CdZnTe (CZT) is one of the most promising materials for the fabrications of HgCdTe infrared focal plane arrays (IRFPAs) and χ-ray or γ-ray detectors [1, 2]. But the yield of the detectors is often limited by the high density defects relative with the inclusion/precipitates defects in CZT

materials. Now the inclusions/precipitates have become the main defects to degrade the detectors [3-5]. In CdZnTe material, there are two kinds of inclusions: Te-rich and Cd-rich inclusions. Based on the IRT images and surface morphologies of inclusions, the geometrical shapes of the Te-rich precipitates and evolution rule during the growth process were revealed [6-9]. Different from Te-rich inclusion, Cd-rich inclusion will induce large quantities of dislocations in the materials around the inclusion during growth process. But up to now, the geometrical structure of Cd-rich inclusion defect has not been revealed in the details. By measuring the angles between the radial extension belts and cleavage edges of CdZnTe samples, the orientations of the radial extension belts were determined. By studying the structures of IRT images of Cd-inclusion defects along <111>, <110>, <112> and <100> directions, a 3-D model to describe the spatial structure of the Cd-rich inclusion defect was obtained.

2. CHARACTERIZATION OF CD-RICH DEFECTS

Fig.1 shows IRT images of Cd-rich inclusion defects observed along 4 different crystal orientations. The projections of Cd-rich inclusion defects present the images of six-pointed stars on (111), (110) and (112) planes and a cross-shaped image on (100) plane. The micro-structures of Cd-rich inclusion defects on (111) B surface were revealed by the Everson etch [10] in Fig.2. The pole figure in Fig.3 shows that the plane both perpendicular to {110} plane and parallel to <211> orientation is {113} plane. Assuming that the dislocation belts have a simple cylindrical structure, the sketch of Cd-rich inclusion defects projected on (111) plane can be obtained by simple calculation. The result is shown in Fig.4. The dislocation extension belts with 3-fold symmetrical in the central part were observed in the experiments by continuously etching Cd-rich inclusion defects situated on (111) B surface. The results were shown in Fig.5.

3. MODELING OF THE CD-RICH DEFECTS

In order to explain the experimental results, the model is improved by assuming that the dislocation extension belts have plate-shaped structures parallel to {110} planes. Some characteristic parameters, such as length l, width w and thickness d are used to describe the basic properties of the plate-shaped extension belts. As the extension length increases, the width w and thickness d will decrease gradually. Based on such consideration, a 3-D model for Cd-rich inclusion defect is proposed in Fig.6.

4. VERIFICATION OF THE 3-D DEFECT MODEL

If assuming that the dislocation extension belts with absorption layer thicknesses larger than 2d can be discriminated from IRT image, the IRT images of the Cd-rich defects can be extracted from the 3-D models in Fig.6. The results are shown in Fig.7. Based on such assumption, six dislocation extension planes can be observed by IRT microscope along <111> direction, as shown in Fig.7 (a). It can be seen that the defect model based on plate-shaped extension belts proposed in this paper can reasonably explain the IRT images of the Cd-rich inclusion defects.

5. FIGURES

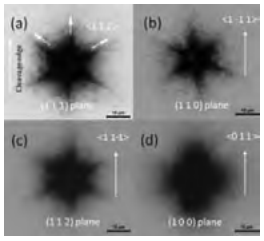

Fig. 1 IRT images of Cd-rich inclusion defects observed along (a) <111>, (b) <110>, (c) <112> and (d) <100> crystal orientations.

Fig.2 Morphology of etch pit profile of Cd-rich inclusion defect exposed on (111) B surface of CdZnTe sample.

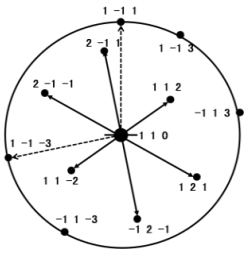

Fig.3 Pole figure of (110) plane.

Fig.4 Sketch of Cd-rich inclusion defects projected on (111) plane. The right figure is the projection along opposite direction.

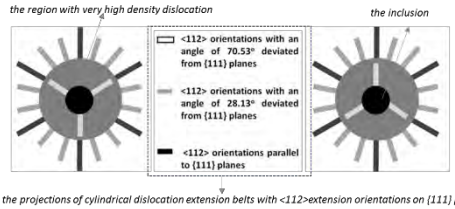

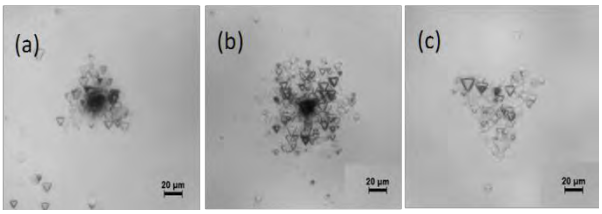

Fig.5 Etch pit morphologies of Cd-rich inclusion defect on (111) B surface observed by IRT microscopy. (a) Beneath the surface. (b) Revealed on the surface. (c) Removed from the surface.

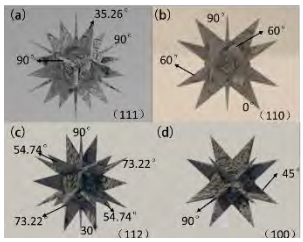

Fig.6 3-D model of the Cd-rich inclusion observed along different directions. (a) <111> direction. (b) <110> direction. (c) <112> direction. (d) <100> direction

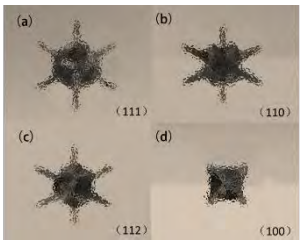

Fig.7. The simulated IRT images of the Cd-rich defects derived from the 3-D models: (a) IRT image toward <111> direction. (b) IRT image toward <110> direction. (c) IRT image toward <112> direction. (d) IRT image toward <100> direction.

REFERENCES

[1] M. Reddy, J.M. Peterson, D.D. Lofgreen, T. Vang, E.A. Patten, W.A. Radford, S.M. Johnson, Journal of Electronic Materials 39 (2010) 974-980.

[2] L.M. Andrea Zappettini, Mingzheng Zha, Giacomo Benassi, Nicola Zambelli, Davide Calestani,Lucio Zanotti, Enos Gombia, Roberto Mosca, Massimiliano Zanichelli, Maura Pavesi, Natalia Auricchio, and Ezio Caroli, Growth and Characterization of CZT Crystals by the Vertical Bridgman Method for X-Ray Detector Applications, IEEE TRANSACTIONS ON NUCLEAR SCIENCE, 2011.

[3] F.F. Sheng, C.H. Zhou, S.W. Sun, J.R. Yang, Journal of Electronic Materials 43 (2014) 1397-1402.

[4] V. Lordi, Journal of Crystal Growth 379 (2013) 84-92.

[5] A.E. Bolotnikov, G.S. Camarda, Y. Cui, G. Yang, A. Hossain, K. Kim, R.B. James, Journal of Crystal Growth 379 (2013) 46-56.

[6] P.F. Yu, W.Q. Jie, Journal of Crystal Growth 381 (2013) 57-60.

[7] Y. He, W. Jie, Y. Xu, T. Wang, G. Zha, P. Yu, X. Zheng, Y. Zhou, H. Liu, Scripta Materialia 67 (2012) 5-8.

[8] X.P. Cui, W.Z. Fang, S.W. Sun, C.J. Zhang, H.L. Xu, J.R. Yang, Journal of Crystal Growth 321 (2011) 40-44.

[9] T. Wang, W. Jie, D. Zeng, Materials Science and Engineering: A 472 (2008) 227-230.

[10] W.J. Everson, C.K. Sepich, J.L. Sepich, B.E. Dean, G. Neugebauer, H.F. Schaake, Journal of Electronic Materials 24 (1995) 505-510.

Characterization of (211) and (100) CdTe layers grown on Si substrates by metalorganic vapor phase epitaxy.

K. Yasuda*, M. Niraula, M. Kojima, S. Kitagawa, S. Tsubota, T. Yamaguchi,
J. Ozawa, and Y. Agata
Graduate School of Engineering, Nagoya Institute of Technology
Gokiso, Showa, Nagoya 466-8555, Japan
E-mail: yasuda@nitech.ac.jp

Dependence of electrical properties and crystal qualities on the thickness of CdTe layers were studied for (211) and (100) single crystal CdTe layers grown on Si substrates.

CdTe layers were grown on (211) and (100) Si substrates by metalorganic vapor phase epitaxy at growth temperature of 450 ^{0}C. Before the CdTe growths, Si substrates of both orientations were pretreated in the similar manner at the same time. (211) and (100) CdTe layers were also grown in the same growth run. Thickness of CdTe layers were changed from 5 to 45 μm.

Double crystal X-ray rocking curve (DCRC) and 4.2 K photoluminescence (PL) measurements were used for characterizations.

(211) CdTe layers showed a monotonic decrease of FWHM values of DCRC from 1200 to 143 arc-sec. with increase of CdTe layer thickness. For (100) layers, on the other hand, FWHM values distributed randomly from 400 to 1600 arc-sec. PL spectra of (211) CdTe layers also showed emission energy of neutral acceptor bound exciton lines (A^0, X) increased with thickness of CdTe layers. This indicates that the tensile stress in (211) CdTe layers decrease with increase of CdTe thickness. The tensile stress is caused by the difference of thermal expansion coefficients between CdTe and Si substrates. Such a spectral energy shift of exciton region were not observed clearly for (100) layers, but they were in higher energy region than those for (211) layers. These results suggest that tensile stress in (100) CdTe layers have decreased by generation of dislocation.

SIMULATION OF MBE SEMICONDUCTOR FILM GROWTH

II-VI paper 5-4

C.H. Grein and A. Ciani

312-996-6753, grein@uic.edu

University of Illinois at Chicago, Chicago IL 60607

Molecular beam epitaxy (MBE) is a major tool for the growth of high quality semiconductor heterostructures. Its modeling has potential benefits in identifying optimal growth conditions and predicting atomic-scale defects that may form in actual growth. We describe the use of simulation software to conduct realistic atomic-scale MBE growth simulations to explore the parameter space of actual growths, such as substrate surface preparation, growth temperatures, material fluxes, and choices of interfacial layers. Density functional theory (DFT) has become one of the most widely used theoretical tools for investigating the physical properties of structurally and chemically complex materials from first principles. The computational load of DFT is too great to be practical to model such growth. Instead, we utilize DFT to calculate the two and three body coefficients of modified Stillinger-Weber potentials to be used in large-scale molecular dynamics (MD) simulations. The overall objective is to predict the specific structures that emerge from the growth process for specific values of such experimentally controllable parameters as effusion fluxes, flux compositions (atomic vs. molecular), and deposition substrate temperatures. Analysis of the simulations for defect formation and layer interdiffusion assist in recognizing the structural, optical and electronic characteristics of non-optimal growth

parameters. We have utilized the method to simulate the growth on ZnSe on GaAs, InGaN on GaN, CdTe on ZnTe, ZnTe on Si, and InAs/InAsSb superlattices on GaSb (see Figs. 1 and 2).

To simulate epitaxial growth at relatively slow deposition rates, the arrivals of individual atoms or molecules at the substrate are treated as isolated events. MD involves computing the trajectory of each atom during every time step (~1 fs) by integrating Newton's equation of motion. A typical simulated growth starts with a layer of buffer deposited on the substrate. The atoms impinging on the surface will either remain on the surface or be reflected back. If an impinging atom remains on the surface, it may diffuse. The system is then relaxed for a few thousand MD time steps to accommodate incorporation. Then the functional epilayer is deposited, with periodic anneals. The stress energy profiles can be mapped before and after the onset of dislocations. If dislocations are generated in the growth layers due to lattice mismatch, then the stress field maps will indicate their presence. Additionally, a microscopic description of dislocation formation will be revealed that may help in designing novel layer architectures that reduce dislocation densities. Other defects are also readily identified due to the microscopic nature of the simulations. The performance of MD on massively parallel computers makes the treatment of large systems feasible and desirable to study long-range effects. MD readily lends itself to parallel processing because the elements of the force vectors can be independently calculated.

Acknowledgements

We are grateful to the US Government for supporting this effort.

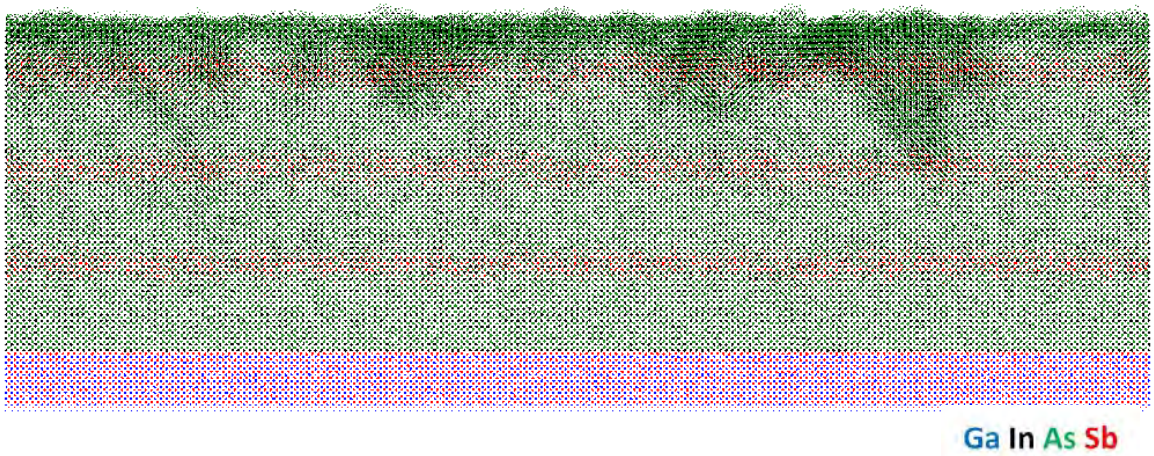

Figure 1. View of simulated 39.45 Å InAs/9.11 Å $InAs_{0.5}Sb_{0.5}$ superlattice grown on a GaSb substrate at 420°C. The vertical direction is the growth direction, [001], and the lateral direction is [100]. Atomic positions along the [010] direction are projected onto the plane of the figure, hence the view is along atomic columns, analogous to transmission electron micrographs. The atomic species are color coded according to the legend. The simulation initiated with just the GaSb substrate. Three periods so the superlattice were grown, and the simulation ended with 2.3 million atoms.

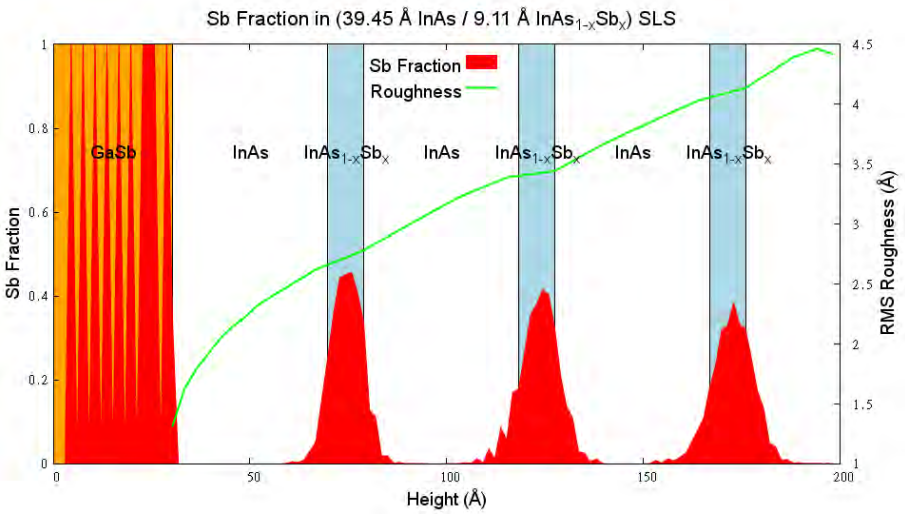

Figure 2. MD simulations of the 39.45 Å InAs/9.11 Å $InAs_{0.5}Sb_{0.5}$ superlattice show Gaussian-like Sb distributions centered about the ideal InAsSb layers. Their width correlates with growth front roughness at the time of deposition.

Chalcogenide Perovskites as Ionic Semiconductors for Photovoltaics

Yi-Yang Sun[1], Michael L. Agiorgousis[1], Peihong Zhang[2], Hao Zeng[2], and S. B. Zhang[*1]

[1] Department of Physics, Applied Physics and Astronomy, Rensselaer Polytechnic Institute, Troy, New York, 12180, USA
[2] Department of Physics, University at Buffalo, State University of New York, Buffalo, New York 14260, USA
*e-mail : zhangs9@rpi.edu

Chalcogenide perovskites ABX_3, where A and B represent (2+) and (4+) cations, respectively, and X represents either S or Se, could be an emerging class of promising solar-cell materials, according to first-principles calculations [1]. For example, $CaZrSe_3$ is predicted to have a direct band gap of 1.35 eV, which would be an ideal band gap for solar cells. Importantly, such materials could potentially have superior optical absorption properties compared to other well-known and mature solar-cell materials as can be seen in Fig. 1. Replacing the A cations by molecular cations as in the halide perovskites preserves these desirable properties. Among other known phases of ABX_3 chalcogenides, we show that the hexagonal phase has too small a band gap to be useful for solar cells. The needle-like phase, on the other hand, has a pseudo-direct band gap, which suggests that it can only be used as bulk, instead of thin-film, materials for photovoltaics. We have experimentally synthesized several of the chalcongenide perovskites and made optical measurements [2], which confirm the theoretical prediction. In particular, the combined optical absorption and PL measurements suggest that $BaZrS_3$ is a direct gap material with a band gap of about 1.7 eV (Fig. 2). We further showed that the band gap can be tuned by anion alloying. Recent results on split-anion organic-inorganic hybrid perovskites (to group-VI + group-VII elements) [3] will also be presented.

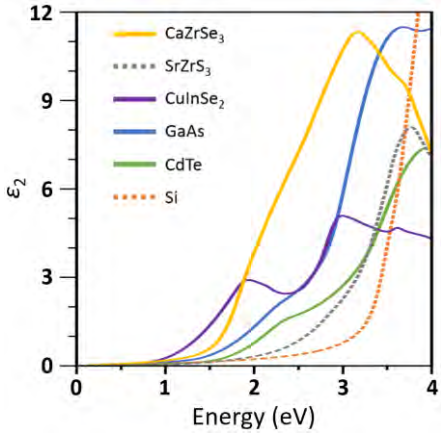

Fig. 1. Imaginary dielectric constants for $CaZrSe_3$ in the perovskite phase and $SrZrS_3$ in the needle-like phase compared to $CuInSe_2$, GaAs, CdTe, Si.

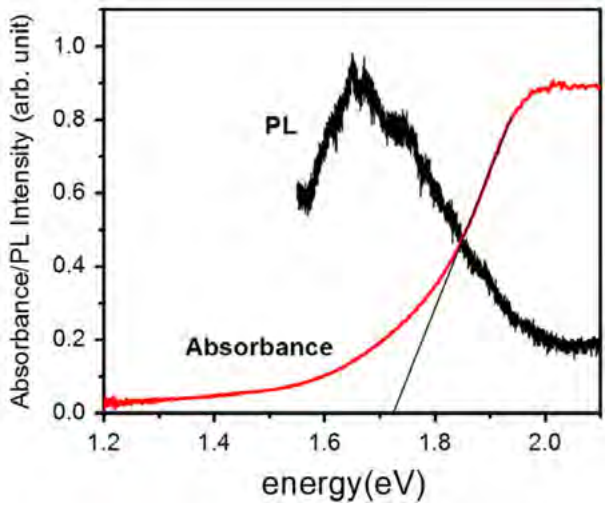

Fig. 2. The UV–vis absorption spectrum and PL spectrum of BaZrS3.

[1] Y. Y. Sun, M. L. Agiorgousis, P. Zhang, and S. B. Zhang, *Nano Lett.* **15**, 581 (2015).
[2] S. Pereraa, et al., *Nano Energy* **22**, 129 (2016).
[3] Y.-Y. Sun, J. Shi, J. Lian, W. Gao, M. L. Agiorgousis, P. Zhang, and S. Zhang, *Nanoscale* **8**, 6284 (2016).

CARRIER LIFETIME STUDY of UNDOPED and IODINE DOPED CdMgTe/CdSeTe DOUBLE HETEROSTRUCTURES GROWN by MOLECULAR BEAM EPITAXY

S. Sohal,[1,2,*] M. Edirisooriya,[1] O. S. Ogedengbe,[1] J. E. Petersen[1], C. H. Swartz,[1] E. G. LeBlanc,[1] T. H. Myers,[1,2] J. V. Li[1,2], M. Holtz[1,2]

[1] Materials Science, Engineering, and Commercialization Program, Texas State University, San Marcos, Texas 78666 [2] Department of Physics, Texas State University, San Marcos, Texas 78666 *Email:sandeep.sohal@txstate.edu

Abstract: Time-resolved photoluminescence (PL) studies are reported for undoped and doped CdMgTe/CdSeTe double heterostructures (DHs) grown by molecular beam epitaxy. Undoped and iodine doped DHs are studied with absorber layer thickness in range from 0.5 to 2.5 μm. The *n*-type free-carrier concentration is varied ~7×10^{15}, 8.4×10^{16}, and 8.4×10^{17} cm^{-3}. Optical injection is varied from 1×10^{10} to 3×10^{11} photons/pulse/cm^2, corresponding to initial injection of photo-carriers up to ~8×10^{15} cm^{-3}, to examine the effects of excess carrier concentration on the PL lifetimes. Undoped DHs exhibit an initial rapid decay followed by a slower dependence with carrier lifetimes up to ~485 ns. The observed dependence of carrier lifetimes in undoped DHs with different absorber layer thickness results in interface recombination velocities (v_{int}) ~1279 and 238 cm/s in the initial and later decay times, respectively, corresponding to high and low optical injection conditions. The lifetimes of doped DHs show a consistent trend with thickness. The values of v_{int} ~80 to 190 cm/s are estimated for doping *n*~7×10^{15} cm^{-3} and 200 to 410 cm/s for *n* ~8.4×10^{16} cm^{-3}. The observed decrease in lifetime with increasing *n* is consistent with growing importance of the radiative recombination rate due to the excess carrier concentration.

Keywords: CdTe, photoluminescence, heterostructures, lifetime

INTRODUCTION

Carrier lifetimes in single crystalline CdTe are reported as very short.[1] This effect is attributed to the presence of surface states which have a deleterious effect on photovoltaic efficiency. Molecular beam epitaxy (MBE) has recently been used to develop CdMgTe/CdTe double heterostructures (DHs) on InSb substrates to demonstrate unprecedented long minority carrier lifetimes.[2,3] This improvement in lifetime was attributed to significant reduction of the interface defect states owing to the presence of the high-quality interface with the CdMgTe capping layer.[2]

We report the behavior of carrier lifetimes in undoped and iodine doped CdMgTe/CdSeTe (DHs) with optical injection, and free-carrier concentration. From undoped samples with different absorber layer thicknesses, the interface recombination velocity (v_{int}) is determined and its behavior with optical injection investigated. Dependence of time-resolved photoluminescence (TRPL) characteristics on *n*-type doping show the competition between radiative and non-radiative processes, and dominance of radiative processes at doping ~8.4×10^{17} cm^{-3}, suggesting high quality DHs can be achieved even at high doping.

EXPERIMENTAL DETAIL

Doped and undoped CdMgTe/CdSeTe DH structures were grown by MBE technique on (100)-oriented InSb substrates. Nominally undoped $Cd_{0.96}Se_{0.04}Te$ absorber layers are grown with thickness varied from 0.5 to 2.5 μm. For the iodine doped

DHs, different absorber thicknesses are grown at particular doping: (a) 0.25-2.0-μm absorber layers thicknesses with carrier concentration 7×10^{15} cm^{-3}, (b) 1-2 μm layers with 8.4×10^{16} cm^{-3}, and (c) 2 μm absorber layer with 8.4×10^{17} cm^{-3}. The TRPL measurements at 430 nm excitation wavelength are performed using the time-correlated single photon counting technique with detection by a fast photomultiplier tube.

RESULTS AND DISCUSSION

The PL carrier decay curves of the undoped samples are shown in Fig. 1. Samples are excited with an optical injection (3×10^{11} photons/pulse/cm^2) which corresponds to initial excess carrier density δp~ 8×10^{15} cm^{-3} at time t = 0 of the laser pulse. The initial carrier density is estimated from the laser power and spot size, both at the sample, reflection coefficient, and absorption (α) for CdTe [4] at excitation wavelength 430 nm. Each curve exhibits initial faster decay followed by a slower dependence at later times, with a dependence on thickness of absorber layer d. The measured PL lifetimes τ_{PL}can be described using [5]

$$\frac{1}{\tau_{PL}} = \frac{1}{\tau_{SRH(Bulk)}} + \frac{2\,v_{int}}{d} + \frac{\mathrm{B}}{}(n+\delta p) \qquad (1)$$

where is the photon recycling factor and depends on thickness, n is the background carrier density, and B is the radiative coefficient. The form of Eq. (1) is valid as long as $d<<L_D$, where L_D is the diffusion length of minority carriers. The first two terms describe non radiative decay to be solely from interface and bulk Shockley-Read Hall (SRH) processes. The last term in Eq. (1) is related to the radiative lifetime. Auger recombination is negligible in CdTe [2] and therefore not included in the above equation. The inset to Fig. 1 summarizes the dependence of $1/\tau$ from initial and later measured lifetimes on absorber layer thickness. The background carrier density in samples is estimated ~ 4×10^{14} cm^{-3} based on secondary ion mass spectroscopy (SIMS) measurements of residual In content in similar DHs. Fitting the data using Eq. (1) and published [2,6] B ~1×10^{-10} cm^{-3}/s we obtain v_{int} ~1279±26 cm/s and $\tau_{SRH(Bulk)}$ ≥ 2.5μs.The fit to later lifetimes generated v_{int} ~ 238±7 cm/s with the values of $\tau_{SRH(Bulk)}$~2.5 μs and B held constant. The v_{int} value indicates effective surface passivation by the CdMgTe barrier layers and reduction in the interface defect states. The identification of high and low injection regions in decay curves has been done according to approach adopted by Luke et al.[7] The dashed lines represent the predicted decay curves in the low injection regime with v_{int} ~ 238 cm/s. The simulations do not adequately describe the early part of decay curves, suggesting that the initial lifetimes may be influenced by the optical injection processes under our measurement conditions. The interpretation of the observed optical injection dependence of v_{int} is complicated by factors such as unknown type of traps at interface, their occupation and interaction with different carrier types, and the abruptness of the interface with neighboring layers, e.g., band bending effects near the interface.[8]

The PL decay curves of iodine-doped samples of different thicknesses (0.25-2.0 μm) in the doping range 7×10^{15}-8.4×10^{17} cm^{-3} are shown in Fig. 2 (a-b). Figure 2(a) presents the effect of thickness on carrier lifetimes at n ~7×10^{15} cm^{-3}. Each decay curve exhibits an initial fast decay followed by long lifetime with a dependence on thickness of absorber layer.

By comparing data in Fig. 2(a), for absorber layer thickness 2 μm, with data in panel 2(b) for higher doping concentration 8.4×10^{16} cm^{-3}, we see the initial and later carrier lifetimes both decrease as *n* increases. With further increase in dopant level to *n* ~ 8.4×10^{17} cm^{-3} the carrier lifetime further decreases and a single exponential decay curve is observed. The inset of Fig. 2(b) represents the effect of optical injection to initial decay curve of 1 μm sample of *n* ~ 8.4×10^{17} cm^{-3}. Factors such as occupation of traps, and asymmetric capture cross sections of carriers at traps may affect the initial decay.[8]

Figure 2(c) summarizes initial and later carrier lifetimes with thickness at injection 3×10^{11} photons/pulse/cm^2. To investigate the influence of interface on later lifetimes, which are relevant for low injection conditions, we estimated the interface recombination velocity considering the last two terms of Eq. (1). The photon recycling factor ( ) is considered and is illustrated in the inset of Fig.2(c).[9] The estimated bulk-SRH lifetime ≥ 2.5 μs, from undoped CdTe DHs discussed above, has an insignificant effect on carrier lifetime in the *n* ~7×10^{15}-8.4×10^{17} cm^{-3} range. The solid curves in Fig. 2(c) represent the combined effect of radiative and interface recombination in Eq. (1), taking into account the photon recycling. To illustrate the impact of v_{int}, we include calculations varying this quantity from 80 to 190 cm/s at *n* ~7×10^{15} cm^{-3}. For carrier concentration 8.4×10^{16} cm^{-3} we include curves calculated using v_{int} ranging from 200 to 410 cm/s. These v_{int} ranges, chosen to span the available data points at these two doping levels, are consistent with what is obtained from analysis of the undoped CdTe DH samples. We attribute the range needed to describe the data as arising from different concentrations of defects responsible for the interface recombination which is sensitive to growth factors. Overall, in the low injection regime the decreased carrier lifetimes with increase in *n* suggests that radiative recombination becomes the dominant factor at higher *n*.

FIGURES

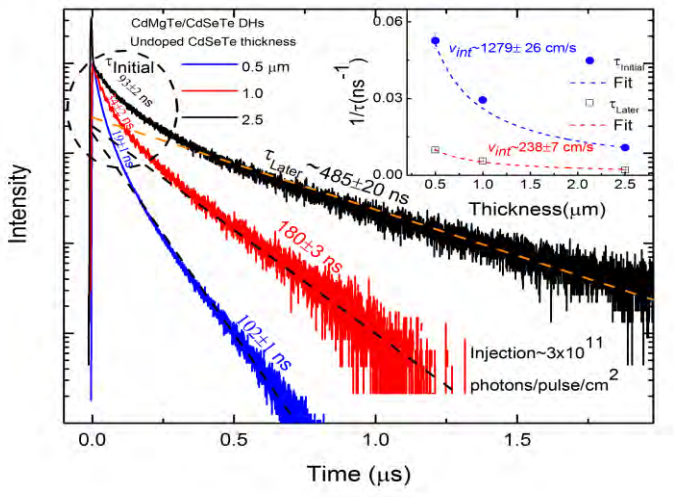

Fig.1 represents the decay curves of undoped CdMgTe/CdSeTe DHs at injection ~ 3×10^{11} photons/pulse/cm^2. The dashed lines represent simulated decay curves in the low injection regime based on Luke *et al.* work.[7] The inset represents the 1/τ (ns^{-1}) versus thickness for early and later times. The dashed lines (blue & red) represent the fit according to Eq.(1) using respective v_{int} values.

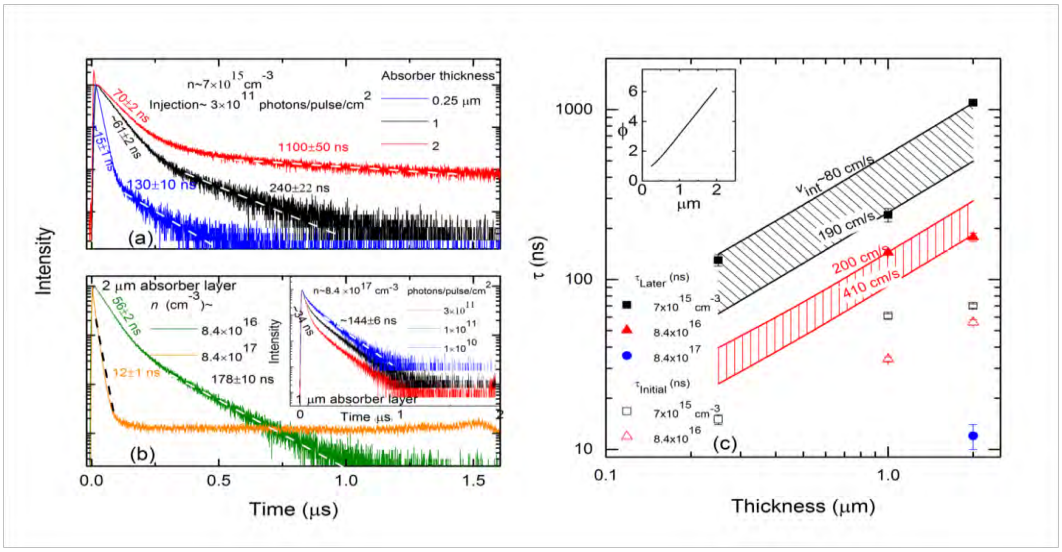

Fig. 2 (a) represents the carrier lifetimes of iodine doped CdMgTe/CdSeTe DHs of different absorber layer thicknesses (0.25 – 2 μm) at n ~ 7×10^{15} cm^{-3}. (b) represents the decay curve for 2 μm absorber layer thickness at n ~ 8.4 $\times(10^{16}$-$10^{17})$ cm^{-3}. The inset of panel (b) represents the effect of optical injection on early part of the decay curve in 1 μm sample. (c) represents the summary of later lifetimes with thickness at different *n*. The inset in panel (c) is the photon recycling factor with thickness.

REFERENCES

[1] D. Kuciauskas, A. Kanevce, P. Dippo, S. Seyedmohammadi, and R. Malik, IEEE J. Photovoltaics **5**, 366 (2015).

[2] C.H. Swartz, M. Edirisooriya, E.G. LeBlanc, O.C. Noriega, P. a. R.D. Jayathilaka, O.S. Ogedengbe, B.L. Hancock, M. Holtz, T.H. Myers, and K.N. Zaunbrecher, Appl. Phys. Lett. **105**, 222107 (2014).

[3] X. Zhao, M.J. Dinezza, S. Liu, C.M. Campbell, and Y. Zhao, Appl. Phys. Lett. **105**, 252101 (2014).

[4] S. Adachi, T. Kimura, and N. Suzuki, J. Appl. Phys. **74**, 3435 (1993).

[5] R.K. Ahrenkiel, in edited by R.K. Ahrenkiel and M.S. Lundstrom (Academic Press, New York, 1993, n.d.), pp. 39–150.

[6] J.M. Burst, J.N. Duenow, D.S. Albin, E. Colegrove, M.O. Reese, J.A. Aguiar, C. Jiang, M.K. Patel, D. Kuciauskas, S. Swain, T. Ablekim, K.G. Lynn, and W.K. Metzger, Nat. Energy **1**, 16015 (2016).

[7] K.L. Luke and L.-J. Cheng, J. Appl. Phys. **61**, 2282 (1987).

[8] S. Sohal, M. Edirisooriya, O.S. Ogedengbe, J. Petersen, C.H. Swartz, E.G. Leblanc, T.H. Myers, J.V. Li, and M. Holtz, Unpublished work (2016).

[9] . . Steiner, . . eis , . arc a, D.J. Friedman, A. Duda, and S.R. Kurtz, J. Appl. Phys. **113**, 123109 (2013).

CONTROLLING THE MAGNESIUM COMPOSITION IN CDTE/CDMGTE HETEROSTRUCTURES

E.G. LeBlanc,[1,] M. Edirisooriya,[1] O.S. Ogedengbe,[1] O.C. Noriega,[1] P.A.R.D. Jayathilaka,[1] S. Rab,[1] C.H. Swartz,[1] D. Diercks,[2] G. Burton,[2] B. Gorman,[2] A. Wang,[4] T.M. Barnes[3] and T.H. Myers[1]

[1]*Materials Science, Engineering, & Commercialization Program, Texas State University, 601 University Drive, San Marcos, TX 78666, USA*

[2]*Colorado School of Mines, 1500 Illinois Street, Golden, CO 80401, USA*

[3]*National Renewable Energy Laboratory, 15013 Denver West Parkway, MS RSF200, Golden, CO 80401, USA*

[4] *EAG Laboratories (Evans Analytical Group), 810 Kifer Road, Sunnyvale, CA 94086, USA*

The wide band gap alloy $Cd_{1-x}Mg_xTe$ forms a type I heterojunction with CdTe, and it has the potential to serve as an electron-reflective buffer layer in CdTe-based solar cells. Barriers made from this material are highly effective at preventing the loss of photocarriers to the strong non-radiative recombination rates of bare CdTe surfaces. Double Heterostructures (DH), which enclose a CdTe film between two $Cd_{1-x}Mg_xTe$ barriers, can even serve as a model system for the study of the optical properties of CdTe, in much the same fashion as GaAs/AlGaAs heterostructures. The effectiveness of the barrier hinges upon establishing a sufficient band offset through control of the Mg composition (x).

The determination of x is typically carried out by high-resolution X-ray diffraction (HR-XRD). The measured growth axis lattice spacing is a consequence of both alloy mole fraction and in-plane strain from the mismatched substrate. To determine the effect of substrate-induced strain, prior reports used the elastic constants resulting from linear interpolation between CdTe and MgTe. However, detailed calculations suggest that such an interpolation is inaccurate. Furthermore, a number of mutually inconsistent relationships between x and band gap (E_g) exist in the literature for $Cd_{1-x}Mg_xTe$.[1,2] Therefore an improved method of estimating x and E_g is

desirable. We demonstrate that spectroscopic ellipsometry (SE) provides a convenient and reliable way to determine these quantities in thin, subsurface layers.

In the CdMgTe films, x was measured by energy dispersive X-ray spectroscopy (EDS) and E_g was measured by cathodoluminescence (CL). From these measurements, a linear correlation between the Mg x value and the E_g was determined as shown in Fig. 2. This correlation agreed well with others found in literature.[1,2,3,4] In double heterostructures, the thin CdMgTe barriers had their E_g measured by variable angle SE in the range of 250-800 nm, at incident angles of 65°, 70°, and 75°. The model used for the CdMgTe DH structure was an approximation of the sample structure, assuming a 10 nm cap layer of CdTe, followed by 30 nm of CdMgTe, and the rest of the structure was approximated as a CdTe substrate. This provides an accurate model since the penetration of light in the material is limited by the absorption coefficient and the absorption depth (α^{-1}). With the spectral range mentioned above used, this means that the furthest light could penetrate the sample was about 0.48 μm, well before the second layer of CdMgTe, typically 1 μm below the first layer of CdMgTe. The measured quantity at each wavelength is the complex reflectance ratio, expressed as amplitude (Ψ) and phase (Δ). The optical properties used for the CdTe layers were available with the accompanying software, so that the complex reflectance ratio is enough to determine the top barrier's real (n) and imaginary (k) indices of refraction as the only free parameters, as shown in Fig. 1.

Using this characterization technique, the E_g of the CdMgTe layer was identified as a maximum in the real refractive index, shown in Fig. 1, which occurs near the band gap energy of the material.[5,6] Because this peak occurs *near* the band gap, the calculation of the Mg x value as identified with ellipsometry was compared with the Mg concentration as determined by Atom

Probe Tomography (APT). Measurements of the Mg concentration via APT resulted in the same *x*-value as SE as shown in Fig. 3 and Fig. 4. Using SE in this way provides a quick, non-destructive means of giving timely feedback to layer growers on Mg incorporation control in CdMgTe layers.

We will also present results concerning interdiffusion of Mg into the surrounding CdTe, which sets processing temperature limits for structures containing CdMgTe.

Funding from the Alliance for Sustainable Energy, LLC, the manager and operator of the National Renewable Energy Laboratory for the U.S. Department of Energy. Contract No. DEAC36-08GO28308 FPACE II: Approaching the S-Q Limit with Epitaxial CdTe, Subcontract ZEJ- 4-42007-0.

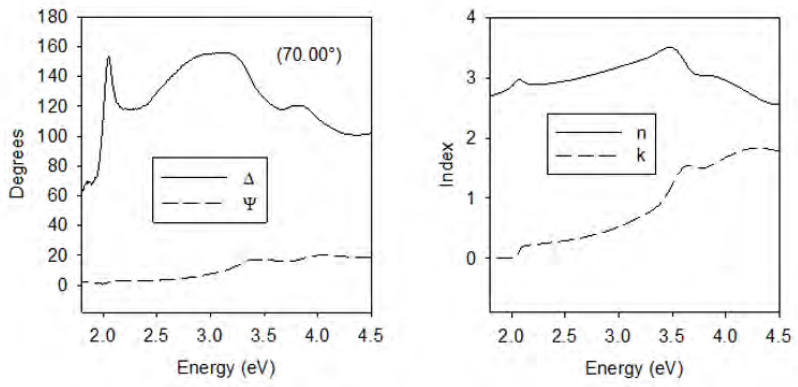

FIG. 1. Typical spectroscopic ellipsometry results, yielding 2.09 eV for the band gap of this particular CdMgTe barrier. The particular model used here specifies a three layer structure - a 10nm cap layer of CdTe, a 30 nm top barrier of CdMgTe, and a CdTe substrate which is treated as semi-infinite, since the absorption coefficient of CdTe prevents light from penetrating through the 0.5-5 micron absorber layer to the bottom CdMgTe barrier. The complex index of refraction of CdTe at each wavelength is fixed at values taken from the literature.

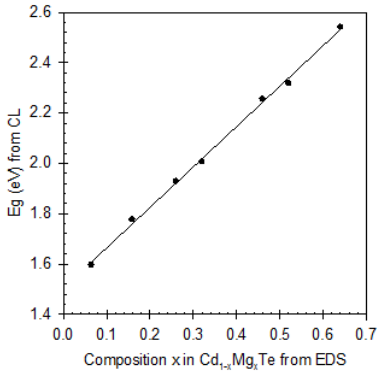

FIG. 2. The cathodoluminescence peak from CdMgTe films is compared to the Mg composition from energy dispersive spectroscopy. The line represents $E_g = (1.60 \pm 0.03)\ x + (1.50 \pm 0.01)$

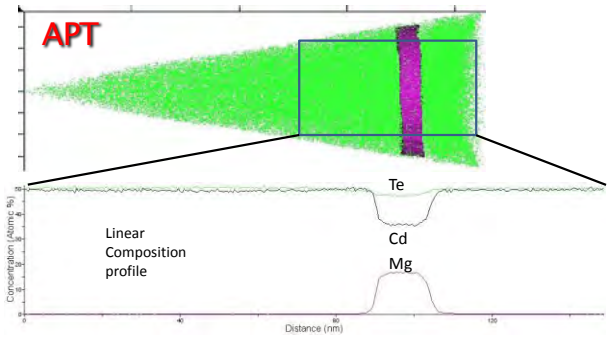

Fig. 3 Atom Probe Tomography (APT) of CdMgTe barrier composition.

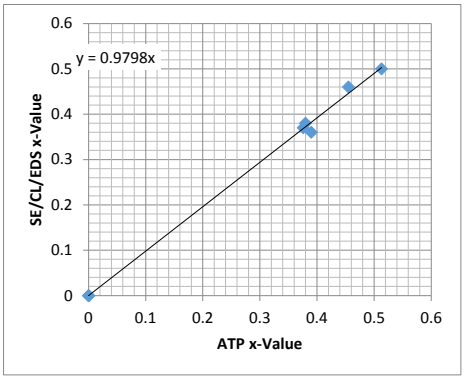

Fig. 4 Comparison between APT and SE

References:

[1] A. Waag, H. Heinke, S. Scholl, C.R. Becker, and G. Landwehr, J. Cryst. Growth **131**, 607 (1993).

[2] O. Martinez, Mater. Chem. Phys. **132**, 559 (2012).

[3] C. Betthausen, Spin Effects in High- and Low-Field Magnetotransport Experiments in Semimagnetic $Cd_{1-x}Mn_xTe$ Heterostructures, University of Regensburg, 2012.

[4] S. Adachi, *Properties of Group-IV, III-V and II-VI Semiconductors* (John Wiley & Sons, 2005).

[5] D. Poelman and J. Vennik, J. Phys. D. Appl. Phys. **21**, 1004 (1988).

[6] J. Chu and A. Sher, *Physics and Properties of Narrow Gap Semiconductors* (Springer Science & Business Media, 2007).

van der Waals epitaxy of CdTe thin film using graphene as buffer layer

Dibyajyoti Mohanty[1*], Weiyu Xie[2], Yiping Wang[3], Zonghuan Lu[2], Jian Shi[3], Shengbai Zhang[2], Gwo-Ching Wang[2], Toh-Ming Lu[2] and Ishwara B. Bhat[1]

[1]Electrical, Computer and Systems Engineering Department,

[2]Physics, Applied Physics and Astronomy Department,

[3]Department of Materials Science and Engineering,

Rensselaer Polytechnic Institute, Troy, NY 12180

Phone: 518 512 7396, Email: mohand@rpi.edu

Conventional heteroepitaxy requires well matched crystalline symmetry, lattice constant, and thermal expansion coefficient between the grown film and the substrate to minimize the strain and defect in the film [1]. In order to overcome this constraint, van der Waals epitaxy (vdWE) technique has garnered significant interest in recent times. Unlike the covalent epitaxy, the bonding between the overlayer and substrate is due to weak van der Waals forces instead of covalent bonds. As a result, not only the lattice matching requirement is relaxed, but also significantly less defects are present in the grown film, due to the dangling bond free interface [2,3]. Traditionally, layered materials, owing to its existing van der Waals forces between layers, have been successfully used as substrates to grow other layered materials epitaxially (2D on 2D) [4]. But the growth of 3D materials on layered materials has proved to be very challenging, with very few materials successfully grown [5]. Among II-VI semiconductor materials CdTe has invoked intense interest in recent years due to its applicability in photovoltaics, aerospace, and radiation detection related applications. Hence, it is highly desirable to produce low cost, epitaxially grown CdTe films on various substrates, which can be fulfilled by vdWE. We have studied 3D CdTe film on graphene buffer layer owing to graphene's inherent advantages such as

high thermal stability, high decomposition temperature, ease of producing high quality graphene and transferring to any substrate of interest.

Single layer graphene deposited via chemical vapor deposition (CVD) process and transferred to SiO_2 (285 nm)/Si(100) substrate was purchased from a vendor (Graphene Supermarket) and used for the study. CdTe thin film (~3 μm thick) was grown on this commercial graphene sample and a reference sample of SiO_2/Si(100) without graphene using a vertical cold wall metalorganic CVD system (MOCVD) using dimethylcadmium (DMCd) and diisopropyltelluride (DIPTe) as precursors and hydrogen as a carrier gas. The XRD θ-2θ scans of the graphene sample and the reference sample are shown in Figs. 1(a) and 1(b), respectively. The preferred orientation of CdTe thin film is along {111} directions. The intensity of CdTe (111) peak from the graphene sample is more than 10 times higher than that of the reference sample indicating a stronger out-of-plane alignment of CdTe grains. Also, the XRD rocking curves of both the samples are shown in Figs. 1(c) and 1(d). The FWHM (0.73°) of the rocking curve measured from the CdTe(111) film on a graphene buffer layer is about 10 times narrower and sharper than the FWHM (7.73°) of the reference sample without a graphene buffer layer suggesting a clear improvement in crystallinity.

The X-ray pole figures for CdTe(111) film grown without and with graphene buffer layer are shown in Figs. 2 (a) and (b), respectively. Pole figures for both the samples have the (111) center pole and a ring at a tilt angle ($\chi \sim 70^o$). In the case of CdTe film grown on SiO_2/Si, the ring at $\chi \sim 70^o$ has a large dispersion indicating the presence of a polycrystalline CdTe film with a fiber texture. On the other hand, the CdTe film grown on graphene buffer layer has 12 visible poles with a narrow ring present at $\chi \sim 70^o$. Graphene has a six-fold symmetry and CdTe film has a three-fold symmetry. When the CdTe film was grown on a graphene layer, it results in three

CdTe poles with their corresponding twins, a total of 6 poles separated by 60° apart from each other. But the graphene grown on a Cu substrate has been found to have more than one orientation [6]. Hence a graphene layer with two different orientations results in 12 CdTe poles shown in the figure. From Density functional theory (DFT) calculations the parallel epitaxial relationship between CdTe and graphene was found to be CdTe $[1\bar{1}0]$ || graphene $[2\bar{1}\bar{1}0]$. Further evidences of epitaxial growth of CdTe film on graphene buffer layer will be revealed and discussed at the conference.

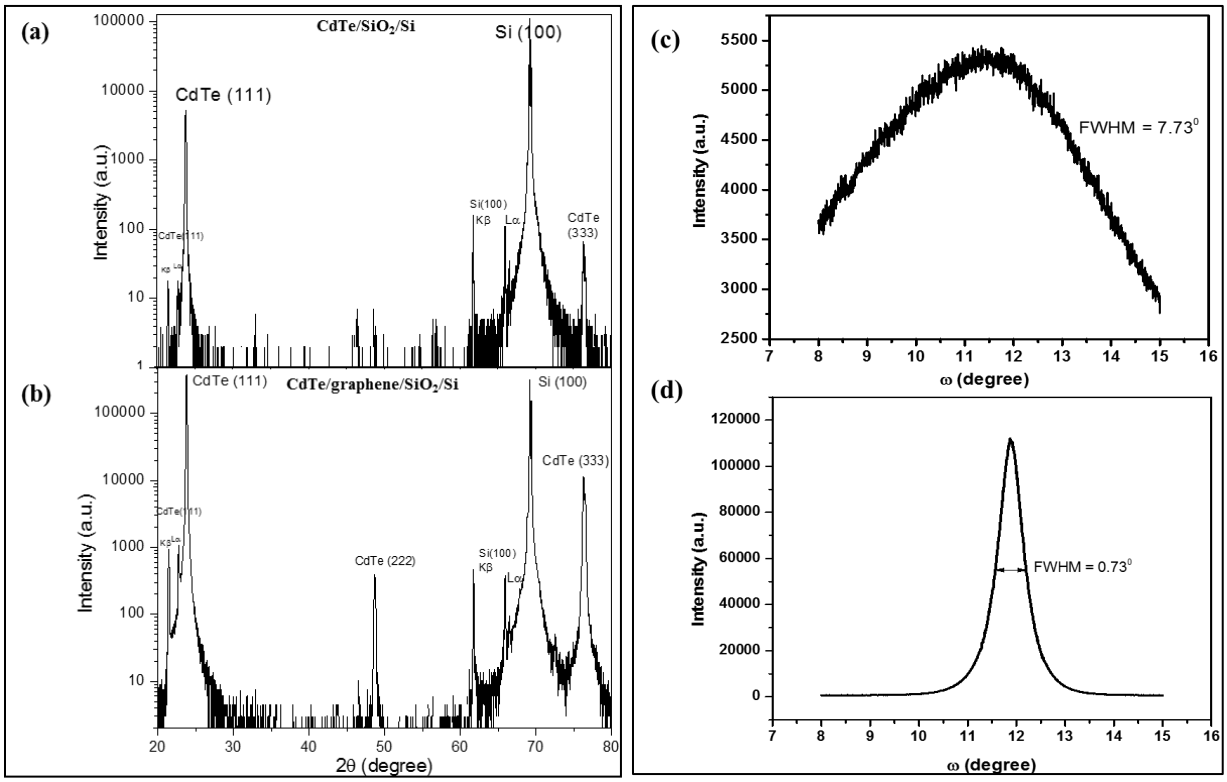

Fig. 1. XRD θ-2θ scans measured from CdTe films grown on (a) SiO_2/Si and (b) graphene/SiO_2/Si with the intensity plotted in a log scale. XRD rocking curves of CdTe(111) planes measured from (c) CdTe/SiO_2/Si and (d) CdTe/graphene/SiO_2/Si samples.

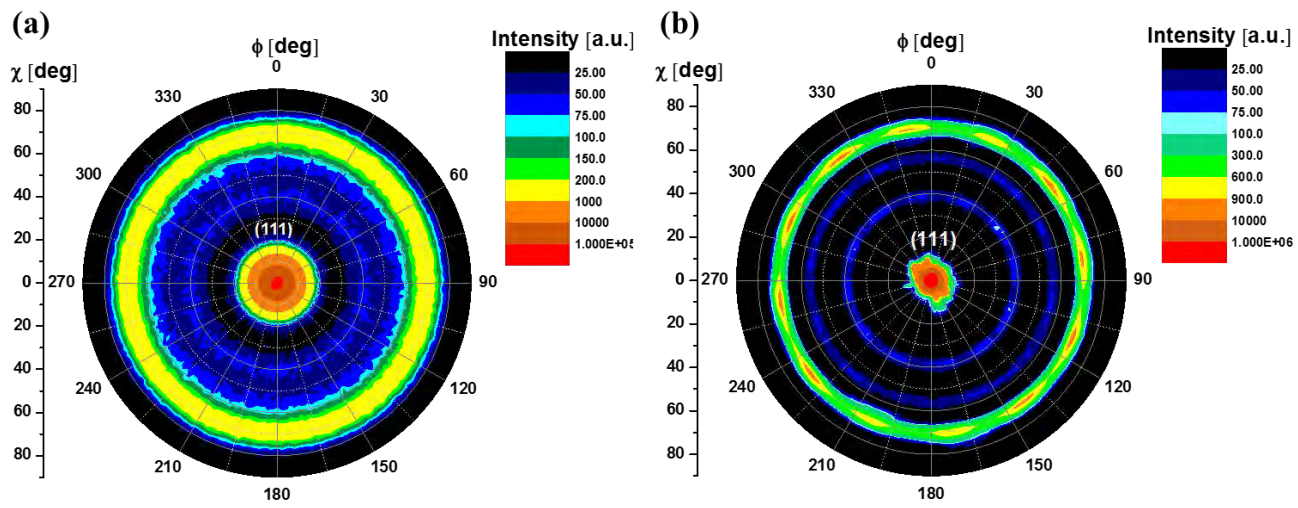

Fig. 2. X-ray pole figures measured from CdTe(111) films grown on (a) SiO_2/Si and (b) graphene/SiO_2/Si.

Acknowledgement:

This project is supported by the National Science Foundation Award # DMR-1305293.

References:

[1] J.W. Matthews, A.E. Blakeslee, Defects in epitaxial multilayers: I. Misfit dislocations, J. Cryst. Growth. 27 (1974) 118–125.

[2] F.S. Ohuchi, B.A. Parkinson, K. Ueno, A. Koma, Van der Waals epitaxial growth and characterization of $MoSe_2$ thin films on SnS_2, J. Appl. Phys. 68 (1990) 2168–2175. doi:10.1063/1.346574.

[3] A. Koma, Van der Waals epitaxy-a new epitaxial growth method for a highly lattice-mismatched system, Thin Solid Films. 216 (1992) 72–76. doi:10.1016/0040-6090(92)90872-9.

[4] K.K. Leung, W. Wang, H. Shu, Y.Y. Hui, S. Wang, P.W.K. Fong, et al., Theoretical and experimental investigations on the growth of SnS van der Waals epitaxies on graphene buffer layer, Cryst. Growth Des. 13 (2013) 4755–4759. doi:10.1021/cg400916h.

[5] J. Kim, C. Bayram, H. Park, C.-W. Cheng, C. Dimitrakopoulos, J.A. Ott, et al., Principle of direct van der Waals epitaxy of single-crystalline films on epitaxial graphene, Nat. Commun. 5 (2014) 4836. doi:10.1038/ncomms5836.

[6] P.Y. Huang, C.S. Ruiz-Vargas, A.M. van der Zande, W.S. Whitney, M.P. Levendorf, J.W. Kevek, et al., Grains and grain boundaries in single-layer graphene atomic patchwork quilts., Nature. 469 (2011) 389–92. doi:10.1038/nature09718.

Monocrystalline CdTe/MgCdTe double-heterostructure solar cells with V_{oc} over 1.1 V and efficiency over 18%

Yong-Hang Zhang

Center for Photonics Innovation & School of Electrical, Computer and Energy Engineering,

Arizona State University, Tempe, AZ 85287

***Abstract* — This talk reports monocrystalline CdTe/MgCdTe double-heterostructure solar cells with hole-selective p-type a-Si:H contacts, achieving a V_{oc} of 1.1 V and a total area efficiency over 18%.**

Cadmium telluride (CdTe) is an excellent photovoltaic material with a high absorption coefficient near the band-edge and a near-optimum bandgap with respect to the detailed balance efficiency for single-junction solar cells. Although these material properties provide great potential for high-efficiency CdTe cells, monocrystalline II-VI material based solar cells still have lower efficiency in comparison with III-V material based ones. This talk reports recent substantial improvement of device performance of CdTe/MgCdTe double heterostructure materials and solar cells.

The cell structure, shown in Fig. 1, consists of an MBE grown CdTe/MgCdTe DH on an InSb substrate, a PECVD (Plasma-enhanced chemical vapor deposition) deposited p-type hydrogenated amorphous silicon (a-Si:H) contact layer, and an Indium Tin Oxide (ITO) top electrode. The CdTe absorber is sandwiched between two lattice-matched MgCdTe barrier layers which provide excellent passivation and supports ample quasi-Fermi-level separation in the CdTe absorber. A 15-nm-thick intrinsic $Mg_{0.4}Cd_{0.6}Te$ layer separates the n-type CdTe absorber and the p-type a-Si:H hole-selective contact. The band-diagram of the solar cell is presented in a previous publication [1].

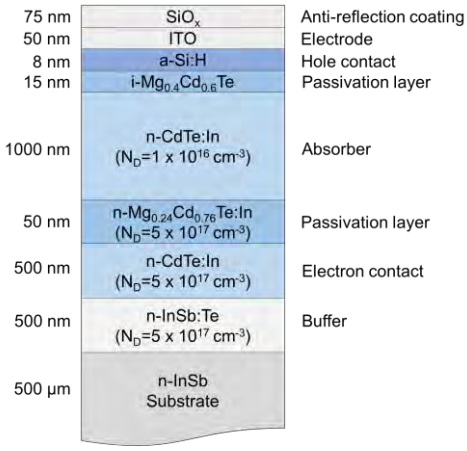

Fig. 1 Layer structure of the CdTe/MgCdTe double-heterostructure solar cell with a p-type a-Si:H as the hole-contact layer.

Fig. 2 shows the a) J-V characteristic and b) external quantum efficiency (EQE) curves for an a-Si:H/CdTe solar cell. The best tested device has a V_{oc} of 1.096 V, a J_{sc} (as measured by the weighted integration of the EQE) of 24.5 mA/cm^2, a Fill Factor of 75.6%, and an active area power conversion efficiency of 20.3%. While the ITO itself serves as an excellent single-layer anti-reflection coating, the addition of Silicon Oxide serves to both improve the conductivity of the ITO as well as provide a dual layer ARC.

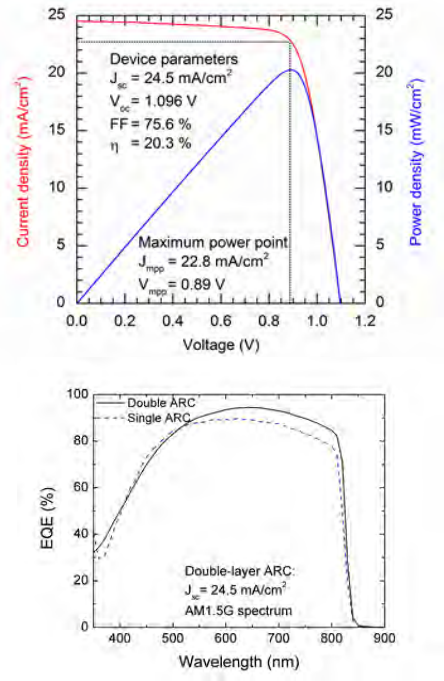

Fig. 2 a) J-V characteristic and b) external quantum efficiency (EQE) curves for an a-Si:H/CdTe solar cell. The best tested device has a V_{oc} of 1.096 V, a J_{sc} (as measured by the weighted integration of the EQE) of 24.5 mA/cm2, a Fill Factor of 75.6%, and an active area power conversion efficiency of 20.3%; the total area efficiency is over 18%.

REFERENCES

[1] Y. Zhao, et al., "*Monocrystalline CdTe solar cells with open-circuit voltage over 1V and efficiency of 17%*", Nature Energy **1**, 16067 (2016).

Analytical and Numerical Analysis of Depletion Region Currents in Extrinsic and Intrinsic VLWIR HgCdTe Detectors

Jonathan Schuster,[1,†] Roger. E. DeWames[2] and Priyalal S. Wijewarnasuriya[1]

[1]U.S. Army Research Laboratory, 2800 Powder Mill Road, Adelphi, MD 20783
[2]Manufacturing Techniques, MTEQ, 10440 Furnace Road, Suite 204, Lorton, VA 22079
[†]jonathan.schuster2.civ@mail.mil

In their seminal paper, Evans and Landsberg [1] derived an analytical formalism that yielded an unavoidable depletion region dark current that depends on the carrier recombination coefficients of both radiative and Auger processes. Note that this is separate from the usual generation-recombination (G-R) depletion region current due to transitions via band gap states. The unavoidable current, discussed by Evans and Landsberg, herein referred to as G-R unavoidable ($J_{GR-unav}$), is given by [1]:

$$J_{GR-unav} = qn_i^2 \left\{ B_0 + \left(B_1 n_{p0} + B_2 p_{n0}\right) \frac{\sinh\left(\eta_D - \eta_j\right)}{\eta_D - \eta_j} \exp\left(\eta_D + \eta_j\right) \right\} W_{dep} \left[\exp\left(\frac{qV_j}{kT}\right) - 1 \right],$$

where $\eta_D = \frac{qV_D}{2kT}$, $\eta_j = \frac{qV_j}{2kT}$, V_D is built in voltage, V_j is the applied bias, B_0 is the radiative recombination coefficient (cm^3/s), and B_1 and B_2 $(= B_1/\Gamma_{\mathrm{Auger-7}})$ are the Auger coefficients for electrons and holes respectively in (cm^6/s), where $\Gamma_{\mathrm{Auger-7}}$ is the Auger-7 multiplier. At small reverse bias the voltage dependent factor: $\sinh(\eta_D - \eta_j)\exp(\eta_D + \eta_j)/(\eta_D - \eta_j)$ is the dominant term, leading to Auger recombination being the primary contributor to $J_{GR-unav}$. For large reverse biases: $\sinh(\eta_D - \eta_j)\exp(\eta_D + \eta_j)/(\eta_D - \eta_j) \rightarrow 0$ leading to the Auger term approaching zero and the expression reduces to $J_{GR-unav} = -qn_i^2 B_0 W_{dep}$. In this large reverse bias regime the current is due entirely to radiative recombination. The only other major current contribution, assuming an ideal diode, is the diffusion current (J_{Diff}):

$$J_{Diff} = q \left[n_{p0} \frac{W_p}{\tau_n} + p_{no} \frac{W_n}{\tau_p} \right] \left[\exp\left(\frac{qV_j}{kT}\right) - 1 \right],$$

where $\tau_{n,p}$ is the carrier lifetime for electrons and holes respectively and $W_{n,p}$ is the width of the quasi-neutral region on the n and p sides respectively ($W_{n,p} = d_{n,p} - W_{dep-n,p}$ where $d_{n,p}$ is the total layer thickness and $W_{dep-n,p}$ is the width of the depletion region in that layer).

Conventional infrared photodiode designs are shallow p^+n homojunctions and in this situation the above diffusion expression reduces to:

$$J_{Diff} = qp_{no}\frac{W_n}{\tau_p}\left[\exp\left(\frac{qV_j}{kT}\right) - 1\right],$$

which is the dark current generated by diffusion of holes in the *n*-type absorber layer. To assure high quantum efficiency the *n*-side thickness is taken to be the cut-off wavelength ~ 10-12 μm for LWIR-VLWIR and the focal plane array operating condition is ~ 50-100 mV reverse bias. Under these conditions the dominant current is the diffusion current. However, as the depletion region expands, whether due to larger biases or lower doping, J_{Diff} will decrease and $J_{GR-unav}$ will increase. For a fully depleted diode the dark current may then be given by $J_{GR-unav}$.

Historically, $J_{GR-unav}$ was usually omitted from device analysis since its contribution was very small due to the relatively high doping used ($\geq 10^{15}$ cm^{-3}) and correspondingly small depletion regions. However, the advent of extremely low doping (low 10^{13} cm^{-3}) [2] has led to much larger depletion regions and this term can no longer be ignored. For example, consider in Figure 1 the dark current *versus* voltage of a VLWIR HgCdTe photodiode with a low doped (5×10^{14} cm^{-3}) absorber layer (still an order of magnitude above the value quoted above, but still less than most current devices). Plotted separately is the diffusion current from the quasi-neutral region (J_{Diff}), the unavoidable current from the depletion region ($J_{GR-unav}$), and the total current. Clearly seen is that as the depletion region expands (increasing voltage), the diffusion current continually decreases such that for very large depletion regions the total current will be primarily due to $J_{GR-unav}$.

Figure 1 is for a device in the extrinsic regime where $N_D >> n_i$. As the doping decreases and/or the temperature increases the device enters the intrinsic regime ($n_i > N_D$). In this regime, the Evans and Landsberg expressions are no longer valid (neither are most other analytical expressions). As such, a

numerical model [3] is now required. The authors will use the numerical model to map the parameter space from where the analytical formulas are valid in the extrinsic regime to the intrinsic regime, quantifying the dark current and quantum efficiency. Initially, this will be performed for a homojunction device [4, 5]. We will then explore the effect of transitioning to a heterojunction device.

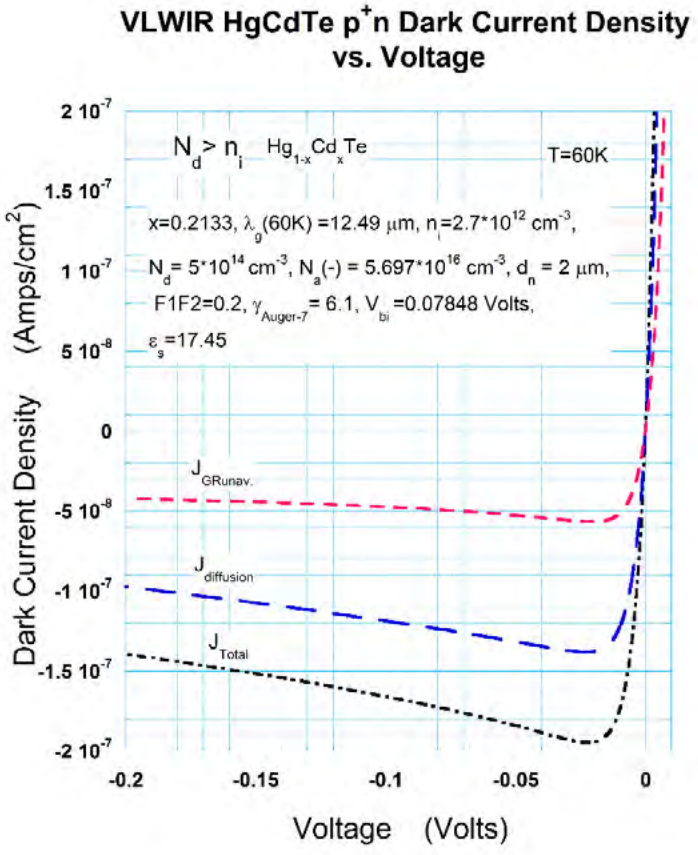

Figure 1. Analytical calculation of the dark current *versus* voltage.

[1] Evans, D. A. a. Landsberg and P. T., "Recombination statistics for Auger effects with applications to p-n junctions," *Solid-State Electronics,* vol. 6, pp. 169-181, 1963.

[2] D. Lee, M. Carmody, E. Piquette, P. Dreiske, A. Chen, A. Yulius, D. Edwall, S. Bhargava, M. Zandian and W. E. Tennant, "High-operating temperature HgCdTe: a vision for the near future," *Journal of Electronic Materials,* vol. Published Online, pp. 1-9, 2016.

[3] J. Schuster, B. Pinkie, S. Tobin, C. Keasler, D. D'Orsogna and E. Bellotti, "Numerical simulation of third-generation HgCdTe detector pixel arrays," *IEEE J. Select. Topics Quantum Electron.,* vol. 19, no. 5, p. 3800415, 2013.

[4] J. Schuster, R. E. DeWames, E. A. DeCuir Jr., E. Bellotti, N. Dhar and P. S. Wijewarnasuriya, "Junction optimization in HgCdTe: Shockley-Read-Hall generation-recombination suppression," *Applied Physics Letters,* vol. 107, p. 023502, 2015.

[5] J. Schuster, R. E. DeWames, E. A. DeCuir Jr., E. Bellotti, N. Dhar and P. S. Wijewarnasuriya, "Heterojunction Depth in P+-on-n eSWIR HgCdTe Infrared Detectors: Generation-Recombination Suppression," *Proccedings of SPIE,* p. 960904, 2015.

Auger and Radiative Lifetimes in ESWIR Materials: HgCdTe, InGaAs, and GeSn

Andreu Glasmann, Stefano Dominici, Hanqing Wen, and Enrico Bellotti[1]
[1] Boston University; bellotti@bu.edu; (617) 358-1576

$Hg_{1-x}Cd_xTe$ has been the material of choice for MWIR, and LWIR infrared sensing due to its highly tunable band gap and favorable material properties. However, $Hg_{1-x}Cd_xTe$ growth and processing for the ESWIR spectral region is less developed, so alternative materials are actively researched. It is important to compare the fundamental limitations of each material to determine which offers optimal device performance. In this article, we investigate the intrinsic recombination mechanisms of ESWIR materials—$In_xGa_{1-x}As$, $Ge_{1-x}Sn_x$, and $Hg_{1-x}Cd_xTe$—with cutoff wavelength near 2.7μm. First, using an empirical pseudo-potential model, we calculate the full band structure of each alloy using the virtual crystal approximation, modified to include disorder effects and spin-orbit coupling. We then evaluate the Auger and radiative recombination rates using a Green's function based model, applied to the full material band structure, yielding intrinsic carrier lifetimes for each given temperature, carrier injection, doping density, and cutoff wavelength. For example, we show that $Hg_{1-x}Cd_xTe$ has longer carrier lifetimes than $In_xGa_{1-x}As$ when strained or relaxed near room temperature, which is advantageous for high operating temperature photodetectors. We perform similar analyses for varying composition $Ge_{1-}Sn_x$ by comparing the calculated lifetimes with $In_xGa_{1-x}As$ and $Hg_{1-x}Cd_xTe$.

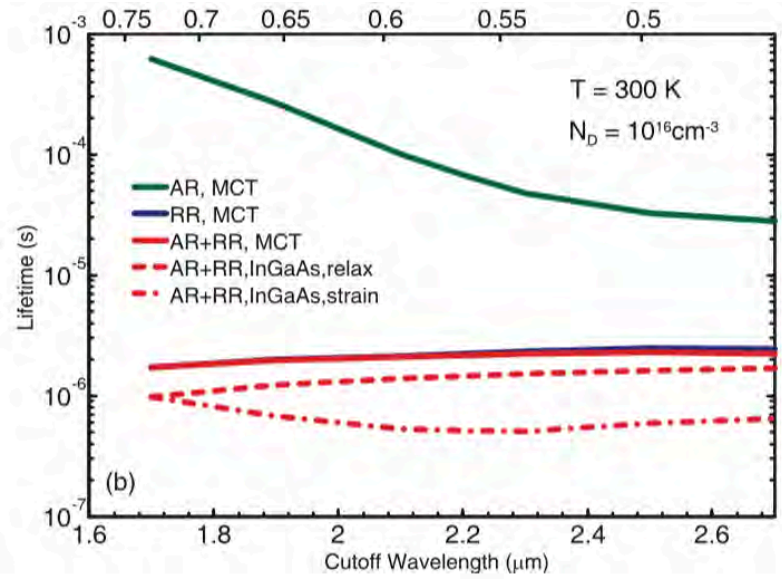

Figure 1: Auger and radiative lifetimes for HgCdTe, InGaAs strained on InP, and relaxed InGaAs as a function of cutoff wavelength.

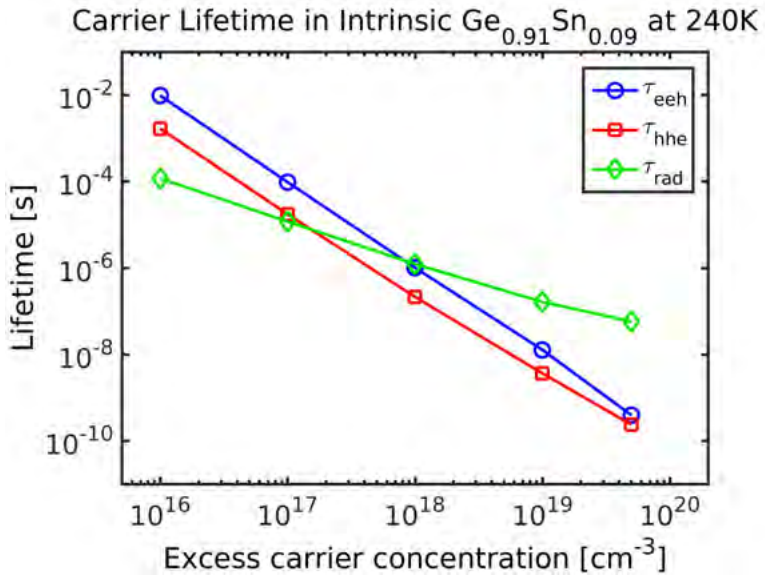

Figure 2: Auger and radiative lifetimes for GeSn with a 2.7 μm cutoff at 240K.

Native point defect levels in strained layer superlattices*

Srini Krishnamurthy[1] and Zhi Gang Yu[2]

[1]SRI International, Menlo Park, CA 94015, [2] Washington State University, Spokane, WA 99202

We use a hybrid method which is a combination of tight-binding (TB) Hamiltonian, first-principles Hamiltonian, and (3) Green's function (GF) for studying native point defects (NPDs). Our TB Hamiltonian ensures accurate band structure and wave function, the sp^3 orbitals basis ensures compatibility for using defect potentials from first-principles approach given by SIESTA [1], and GF approach ensures reliable NPD energy levels from isolated defects. Previously we had successfully applied this method for the calculations NPDs in bulk GaAs, InAs, GaSb, and InSb [2]. We have now extended and applied this approach to obtain band structure and study NPDs in InAs/GaSb strained layer superlattice (SLS) system, lattice-matched to GaSb. This extension required an appropriate (a) averaging for interatomic interactions across the interface to yield band gaps in good agreement with measured values and (b) Brillouin zone integration.

We have studied eight defects—vacancy and anti-site—(V_{In}, As_{In} V_{As}, In_{As}, V_{Ga}, Sb_{Ga}, V_{Sb}, and Ga_{Sb}) in seven SLS systems differing in the number of bilayers (BLs) made of one anion and one cation. The SLS systems studied are InAs (8BL)/GaSb (8BL), InAs (8BL)/GaSb (16BL), InAs (6BL)/GaSb (4BL), InAs (16BL)/GaSb (8BL), InAs (24BL) /GaSb (4BL), InAs (18BL)/GaSb (8BL), and InAs (17BL)/GaSb (8BL). In this study, we evaluated the effect of (a) band gaps in mid-wave IR (MWIR) and long-wave IR (LWIR) bands, (b) relaxation of the sites around the defect, (c) location of the defects in the bulk regions or at interface layers, and (d) inter-diffusion of Sb and As across the interface on the NPD states. The preliminary conclusions include: (1) the defect levels move from the band gap towards the bands when the sites around the defects are relaxed, (2) defects relax more near the interface than in the bulk regions, (3) most mid-gap states have origin in GaSb and their number increases with GaSb layer thickness, and (4) the number of defect states is larger in MWIR systems than in LWIR systems. At least for one abrupt SLS system with the gap in LWIR region— InAs (18BL)/GaSb (8BL)—our calculations did not find defect states near mid gap, suggesting that the limitation to photo-carrier lifetimes may not arise from neutral NPDs in this system. However, the reduction of 1 BL of InAs is calculated to introduce near mid gap states without a noticeable change in the band gap.

* This work is funded by USAF Contract FA8650-11-D-5800 through Universal Technology Corporation.

[1] www.icmab.es/**siesta**/

[2] S. Krishnamurthy, D. Von Orden, and Z.-G. Yu, *J. Elec. Mater.* (2016)

The Evolution of Kinetically-Limited Lattice Relaxation and Threading Dislocation in Temperature-Graded ZnSe/GaAs (001) Metamorphic Heterostructures

T. Kujofsa and J. E. Ayers[†], Electrical and Computer Engineering Department, University of Connecticut, Storrs, CT 06269-4157.

I. Abstract

Metamorphic buffer layers allow tremendous flexibility to design novel semiconductor heterostructures for application in various microelectronic and optical devices. However, device fabrication, reliability and performance are limited by dislocation defects associated with the growth of highly mismatched systems such as ZnSe on GaAs substrate. Thus, understanding kinetically-limited lattice relaxation and development of a plastic flow model applicable to multilayered and compositionally graded heterostructure is desirable to provide guidance in designing ZnSe/GaAs devices. Previously, we reported a plastic flow model for ZnS_ySe_{1-y}/GaAs (001) heterostructures which predicts the non-equilibrium strain relaxation as well as misfit dislocation and threading dislocation densities by accounting for (i) the time evolution of kinetically-limited and equilibrium strain relaxation, (ii) thermal activation of glide, and (iii) misfit-threading dislocation interactions. In this work, we have studied the evolution of kinetically-limited in-plane strain and threading dislocation densities in ZnSe/GaAs (001) metamorphic buffer layers with arbitrary temperature grading profile. In addition, we have investigated the effect of forward versus reverse temperature grading cases on the relaxation mechanism. For each structure, we have studied the temperature grading coefficient dependence on the average and surface kinetically-limited in-plane strain and threading dislocation density. Moreover we show that the use of temperature graded buffer layers

[†] Tel: (617)-383-1514. FAX: (860)-486-2447. e-mail: tedi.kujofsa@gmail.com.

enables the design of ZnSe/GaAs (001) heterostructures with high surface strain values which enhance the sweeping of threading defects and therefore yielding device structures with lower defect densities.

II. Kinetically-Limited Lattice Relaxation and Dislocation Dynamics Model

The foundation for the kinetic model used in this work is derived in [1]. The model predicts lattice relaxation and threading dislocation behavior in (001) zinc blende heteroepitaxial layers of arbitrary thickness and compositional profile. In a general semiconductor heterostructure with lattice mismatch profile $f(z)$, the rate of lattice relaxation at a distance z from the interface is determined by the glide of dislocations in the underlying material, and is given by

$$\frac{d\gamma(z)}{dt} = KBb\sin\alpha\cos\lambda\tau_{eff}^{2}(z)\exp\left(-\frac{U}{kT}\right)\int_{0}^{z}\left[\rho_{A}(\zeta)+\rho_{0}\right]d\zeta\,, \tag{1.}$$

where K and B are constants, b is the length of the Burgers vector, α is the angle between the Burgers vector and line vector, λ is the angle between the Burgers vector and the direction in the interface which is perpendicular to the intersection of the glide plane and the interface, τ_{eff} is the effective stress which is determined by the difference of actual and equilibrium strain, U is the activation energy for dislocation glide, k is the Boltzmann constant, T is the temperature, ρ_A is the areal density of misfit dislocations, ρ_0 is a constant which represents the initial sources of dislocations, and ζ is the variable of integration. The effective stress is determined by the difference of the actual and equilibrium strain profiles in the material above, given by

$$\tau_{eff}(z) = \left[\frac{2\cos\psi\cos\lambda}{h-z}\right]\int_{z}^{h}\left\{\frac{\mu(1-\nu)\left[\varepsilon_{||}(\zeta)-\varepsilon_{eq}(\zeta)\right]}{(1+\nu)}\right\}d\zeta\,, \tag{2.}$$

where h is the layer thickness, ψ is the angle between the surface normal and the slip plane, μ is the shear modulus, ν is the Poisson ratio, $\varepsilon_{||}$ is the in-plane strain, and ε_{eq} is the

equilibrium in-plane strain. Embedded within the kinetic model we have included minimum energy calculations to determine the equilibrium structure after the deposition of each sublayer.

Complementing the lattice relaxation model we have also included dislocation interactions: the basic types of dislocation interactions are (i) introduction of half loops, (ii) bending over of existing dislocations, (iii) annihilation, and (iv) coalescence. Therefore the resulting differential equation for the threading dislocation density is

$$\frac{dD(z)}{dz} = \frac{4\rho_A(z)}{L_{MD}(z)sign\int_0^z \rho_A(\zeta)d\zeta} - C_2 D^2(z), \qquad (3.)$$

where $L_{MD}(z)$ is the length of misfit dislocation segments, and C_2 is a constant. The first term in (3) accounts for the interactions between misfit and threading dislocations. Considering mechanism (i), new misfit dislocations are introduced via half loops if the new misfit dislocations have the same sense (relax the same sign of lattice mismatch) as the underlying misfit segments. This corresponds to the case of $sign(\rho_A(z)) = sign\int_0^z \rho_A(\zeta)d\zeta$ and results in positive $dD(z)/dz$. With respect to mechanism (ii), misfit dislocations are produced by the bending of existing threading dislocations if these misfit dislocations have the opposite sense (relax the opposite sign of mismatch) compared to the underlying misfit segments).

III. In-plane Strain and Threading Dislocations

Lattice relaxation in II-VI devices exhibits a three regime (sluggish, rapid, saturation) behavior as observed in many experimental studies. More importantly, strain relaxation of ZnSe/GaAs (001) occurs much more gradually than predicted by the Matthews and Blakeslee equilibrium theory. In addition, at around 400^{o}C growth of ZnSe layers will exhibit a transition from compressive to tensile strain as the thickness is increased; this is expected on the basis of the differential thermal expansion and is observed experimentally in this material system. Therefore, controlling the defect density is crucial in designing devices with fewer threading dislocations. Moreover, the kinetic model predicts a two regime behavior for the evolution of

the threading dislocation density; first, there exists an initial build-up of the threading dislocation density associated with layers which are beyond the critical layer thickness and as the layer epilayer thickness is further increased, D is inversely proportion to thickness. In this work, we will show how varying the temperature grading coefficient and grading direction effects the kinetically-limited in-plane strain and the surface threading dislocation density. Moreover, we will show how controlling the temperature grading period could lead to lower threading densities.

IV. References

[1] T. Kujofsa, W.Yu, S. Cheruku, B. Outlaw, F. Obst, D. Sidoti, B. Bertoli, P. B. Rago, E. N. Suarez, F. C. Jain and J. E. Ayers, J. Electron. Mater. 41, 2993 (2012).

Scattering in HgCdTe nBn detector with superlattice barrier

N.D. Akhavan*, G. Umana-Membreno, J. Antoszewski, L. Faraone

M018, University of Western Australia, 35 Stirling Hwy, Crawley, WA, 6009

**phone: +61864883748 , Fax: +61864881095 , email: nima.dehdashti@uwa.edu.au*

Abstract

HgCdTe-based unipolar barrier infrared detector incorporating CdTe/HgTe superlattice as a barrier layer has gained interests recently [1,2]. Utilizing CdTe/HgTe superlattice as a barrier layer allows controlling of the energy band alignment between barrier layer and absorber layer and therefore reducing the valence band offset which impedes the flow minority carriers (holes) [3,4]. However, the presence of defects, dislocations and other impurities can affect the superlattice induced energy levels and consequently the current density in the nBn detector. Here, we present a theoretical study on the influence of scattering in the superlattice layer of mercury cadmium telluride (HgCdTe) unipolar *n*-type/Barrier/*n*-type (*n*B*n*) infrared detectors for the midwave IR applications. We will use non-equilibrium Green's function (NEGF) formalism and dephasing scattering model within the NEGF formalism to study the carrier transport under non-equilibrium conditions. Figure 1, Shows bulks barrier and superlattice barrier detector design. In bulk barrier detector, the valence band discontinuity blocks the flow of minority carriers. Figure 2 shows the local density of states (LDOS) and energy-position resolved current density under ballistic condition (no scattering). Including any source of scattering as mentioned above, will disturb the coherent carrier transport and therefore the current.

References

[1]M. Kopytko, J. Wróbel, K. Jóźwikowski, A. Rogalski, J. Antoszewski, N. D. Akhavan, et al., "Engineering the Bandgap of Unipolar HgCdTe-Based nBn Infrared Photodetectors," Journal of Electronic Materials, vol. 44, pp. 158-166, 2015..

[2]D. Benyahia, P. Martyniuk, M. Kopytko, J. Antoszewski, W. Gawron, P. Madejczyk, et al., "nBn HgCdTe infrared detector with HgTe(HgCdTe)/CdTe SLs barrier," Optical and Quantum Electronics, vol. 48, pp. 1-8, 2016.

[3]N. D. Akhavan, G. Umana-Membreno, J. Antoszewski, and L. Faraone, "Design of HgCdTe nBn detector with superlattice barrier layer for IR applications," International Conference on Nanoscience and Nanotechnology (ICONN 2016), 7-11 February 2016, Canberra.

[4] . D. Akhavan, A. Markowska, G. Umana-Membreno, J. Antoszewski, and L. Faraone, "Optimization of HgCdTe nBn detectors with superlattice barrier for IR application," in 2015 U.S. Workshop on the PHYSICS and CHEMISTRY of II-VI MATERIALS, 2015.

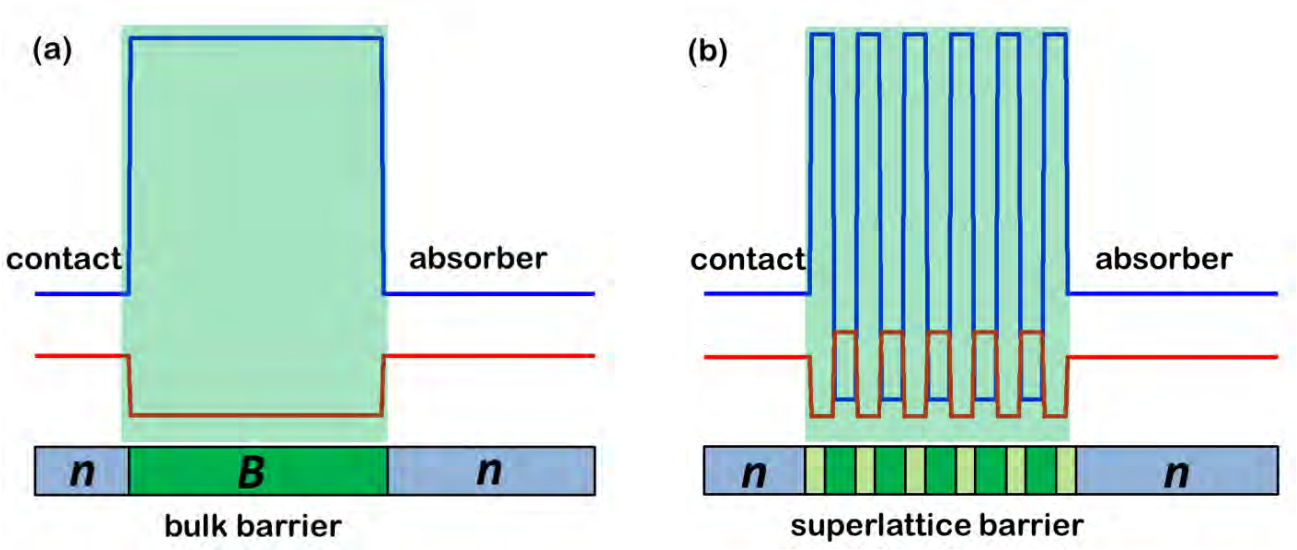

Figure 1. Schematically representation of unipolar HgCdTe-based nBn detector with (a) bulk barrier, and, (b) with superlattice barrier material of CdTe/HgTe.

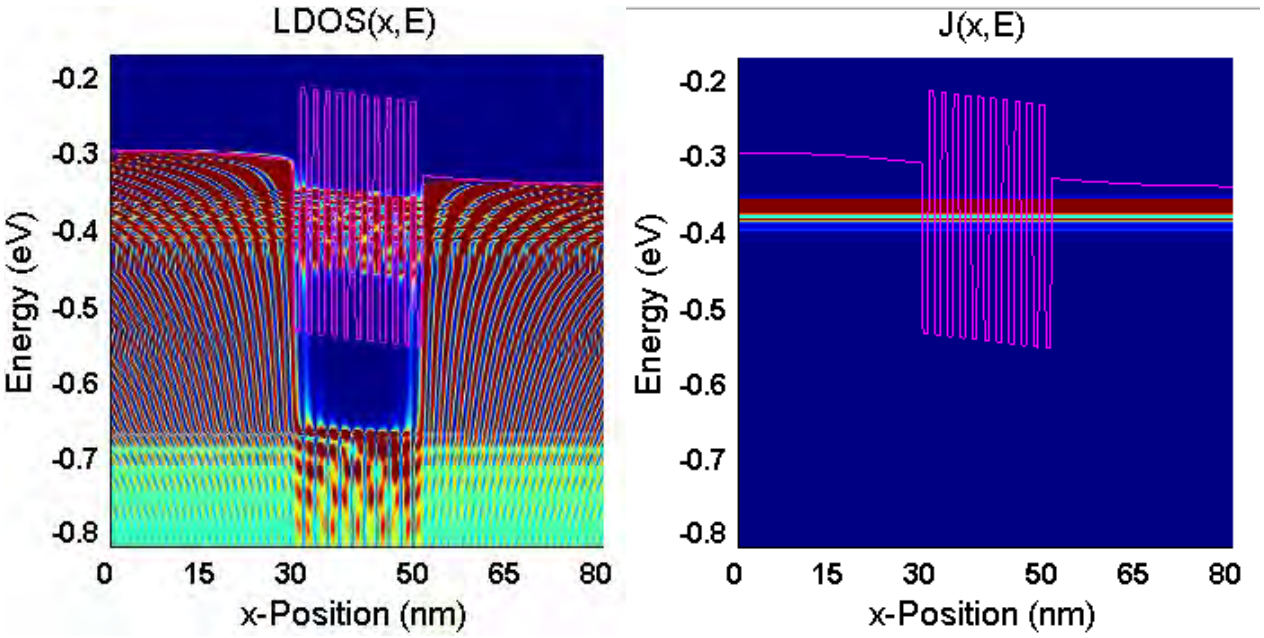

Figure 2. (left) LDOS spectrum in HgCdTe nBn detector, the superlattice induced stets are visible at around -0.35 meV, and, (right) current density spectrum under ballistic carrier transport. It is evident that the minority carrier current flow in the valence band due to availability of LDOS in the valence band.

Development and production of array barrier detectors at SCD

Philip Klipstein
Semiconductor Devices, P.O. Box 2250, Haifa 31021, Israel

SCD has developed a range of advanced IR detectors based on III-V semiconductor heterostructures grown by MBE on GaSb. The XB*n*/XB*p* family of barrier detectors enables diffusion limited dark currents comparable with MCT Rule-07 and high quantum efficiencies.

In 2011, SCD introduced "HOT Pelican D", a 640 × 512 format 15 μm pitch InAsSb/AlSbAs XB*n* detector for the MWIR, with an operating temperature of ~150K. Its low power (~3W), high pixel operability (>99.5%) and long Mean Time to Failure make HOT Pelican D a highly reliable integrated detector-cooler product with a lower Size, Weight and Power and a reduced cost of ownership compared with other MWIR detectors. The second product from this family is the "HOT Hercules", with a 1280 × 1024/15μm format and similar advantages. These detectors are now manufactured on SCD's production line and integrated into various electro-optical systems.

SCD is currently developing a 10 μm pitch XB*n* technology with performance similar to the 15 μm version. An XB*n* Focal Plane Array (FPA) flip-chip bonded to a custom designed readout integrated circuit (ROIC) exhibits a pixel dark current of <200fA, a quantum efficiency (QE) of greater than 70%, excellent array uniformity, and an operability of better than 99.5%.

For Long Wave applications, SCD's 15 μm pitch "Pelican-D LW" XB*p* type II superlattice (T2SL) detector was designed with a ~9.5 μm cut-off wavelength. The detector contains InAs/GaSb and InAs/AlSb T2SLs, and is fabricated into FPA detectors using standard production processes. The Pelican-D LW FPA has a QE of ~50%, and operates at 77K. The pixel operability of the FPA is above 99% and it exhibits a stable residual non uniformity of better than 0.04% of the dynamic range. A new digital ROIC, is used and the complete detector closely follows the interfaces of SCD's MWIR Pelican-D detector family. The T2SL technology is now in the process of qualification and transfer to production.

Variations around p-on-n HgCdTe with Liquid Phase Epitaxy

BAIER Nicolas*, GRAVRAND Olivier, CERVERA Cyril, LOBRE Clément, ROCHETTE Florent
CEA-LETI, 17 rue des Martyrs, 38054 Grenoble Cedex 9, FRANCE
* nicolas.baier@cea.fr

In the scope of the DEFIR joint laboratory with SOFRADIR, many developments have been performed on the p-on-n technology based on liquid phase epitaxy. These developments were introduced to improve the detector performances from short to very long wavelength, for high operating temperatures needs to high end performances with low dark current. Gains in operability, in bias voltage plateau and in dark current have been obtained.

HgTe QUANTUM DOTS FOR NEAR-, MID-, AND LONG WAVELENGTH IR DEVICES

Witold Palosz[1], Sudhir Trivedi[1], Dajie Zhang[1], George Meissner[2], Kimberley Olver[2], Eric DeCuir[2], Priyalal S.Wijewarnasuriya[2]. and Janet L. Jensen[3]

[1]Brimrose Corporation of America, Sparks, Md; [2]Army Research Laboratory, Adelphi, Md, [3]Edgewood Chemical Biological Center, Aberdeen Proving Ground, Md

Abstract

Mercury Telluride Quantum Dots (QDs) offer a potential for fabricating IR devices operating in the range from Near-, thru Mid-, to Long-Wavelength Infrared. We synthesized a variety of colloidal HgTe QDs using the wet technique in non-coordinating environment. Those QDs were used to fabricate devices and measure their photoresponse. We will present the synthesis techniques used in this work, and device fabrication and characterization.

HgTe QDs Synthesis and Characterization

The synthesis of HgTe Quantum Dots was performed using typical chemistry in non-coordinating environment, usually Oleyamine, at temperatures from 80 °C to well over 100 °C. The reaction products were quenched in a solution of Dodecanethiol in Tetrachloroethylene to stabilize the QD suspension, then purified by precipitation and centrifugation [1]. The simple synthesis technique was extended by adopting the SILAR (Successive Ion Layer Adsorption and Reaction) modification used previously for synthesis of CdSe QDs [2]. In a standard procedure, after the injection of one precursor into the other, and then after the initial growth the size of crystals levels off due to depletion of the precursors in the reactor. In the SILAR technique, after the initial period a controlled injection of additional portions of precursors, such as not to allow for formation of new nuclei, allows further growth of already existing grains. The automated injection system used for this technique is shown in Fig. 1. The development of the grain size (reflected by the position of the first exitonic peak) in each technique is demonstrated in Fig. 2: in

traditional technique the size of the QDs levels off after about 10 minutes, but keeps increasing when SILAR technique is employed. The increase in the size of the grains is shown in TEM images in Fig. 3.

Device Fabrication and Characterization

Photoconductive devices were fabricated by drop-casting a suspension of HgTe QDs on interdigitated electrodes (20 μm wide and spaced 20 μm apart) and the deposited layer solid ligand exchanged using a solution of 2% Ethanedithiol and 2% HCl in Ethanol [3]. Three consecutive layers of HgTe QDs were being deposited, with ligand exchange process being done after each deposition. The ligand exchange has a profound effect on the properties of the devices and needs to be well controlled. In the case of a sample shown in Fig. 4, only after 5 minutes of ligand exchange process the sample is virtually free of ligands. Also, ligand exchange process flattens/broadens the peaks and red shifts the position of the first excitonic absorption by about 0.1 μm, as also shown in Fig. 4. Removal of ligands decreases, as intended, the ohmic resistance in the samples, but an excessive "cleaning" the devices off ligands usually led to high currents and prevented measurements of photoresponse of the devices.

For photoresponse measurements the devices are mounted on a 68-pin leadless chip carrier (LCC), wire bonded, and tested for spectral response using the following techniques. Devices are loaded into a continuous flow or pour-fill Lakeshore modular test dewar (MTD150 or MTD125, respectively) with individual BNC break-outs for each wire-bonded device. The dewar is equipped with a window yielding transmission over the spectral range of interest (typically 1-12 μm). A Nicolet 8700 Fourier transform infrared (FTIR) spectrometer in conjunction with a low-noise Keithley 428 transimpedance preamplifier and a FTIR calibration technique is used to provide the accurate relative spectral shape for the device under test (DUT). Radiometric measurements are performed with a cold narrow band-pass filter with a suitable center wavelength which is adequately removed from the DUT cut-off. The calibrated flux density is delivered by a chopped, apertured, cavity blackbody mounted at a fixed distance from the DUT. The chopped DUT signal is fed into a low-noise Keithley 428 transimpedance preamplifier which transforms this current into a proportionally gained voltage output (Volts/Amp). This voltage signal is

then fed into a Standford Research Systems SRS SR830 digital lock-in amplifier to determine the root-mean square (rms) device output which is proportional to the available chopped flux density to the DUT. Given that the gain, modulation form factor, blackbody flux, solid angle, window/filter transmission, and device area are known, one can back out the number of electrons/photon collected, i.e., the external quantum efficiency (for internal Q.E. accurate knowledge of the reflective losses need to be known). This Q.E. is then assigned to the center wavelength of the narrowband filter. From this, the relative spectral response collected via FTIR may be corrected to absolute spectral response.

An example of absorption spectra of a HgTe QD sample and photoresponse of the device fabricated with this material is shown in Fig. 5. The effect of the magnitude of dark current on the photoresponse is illustrated in Fig. 6. Devices with the dark current on the order of a fraction of mA cause a lot of noise, while the photocurrent measured at the total current of about 20 μA shows quite a smooth curve, the photocurrent in both cases being of similar magnitude. The results of our Quantum Efficiency measurements for the material shown in Fig. 5 are given in Fig. 7.

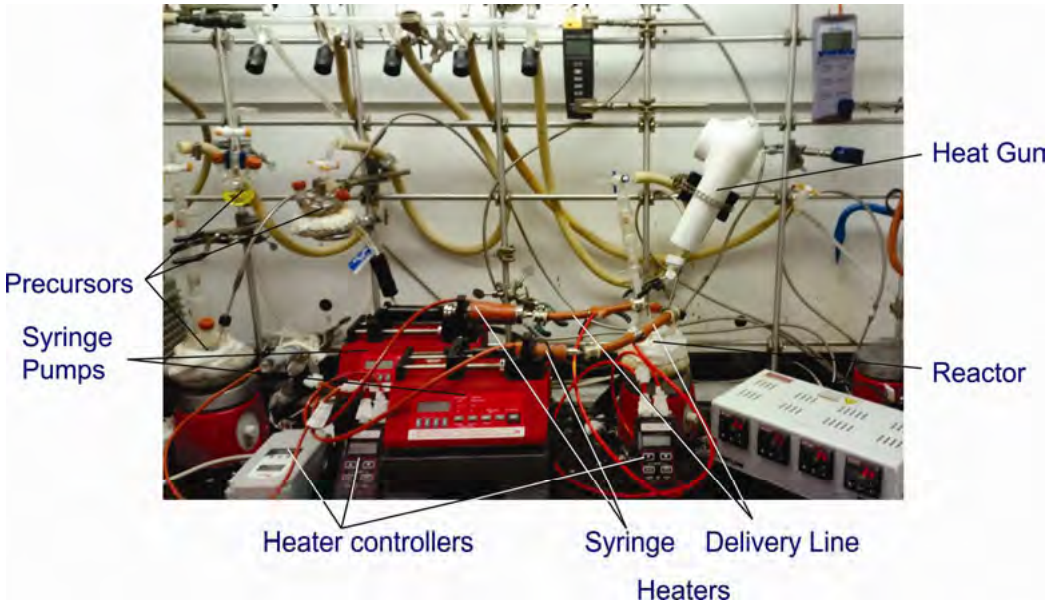

Figure 1. Automated syringe system used in SILAR synthesis procedure.

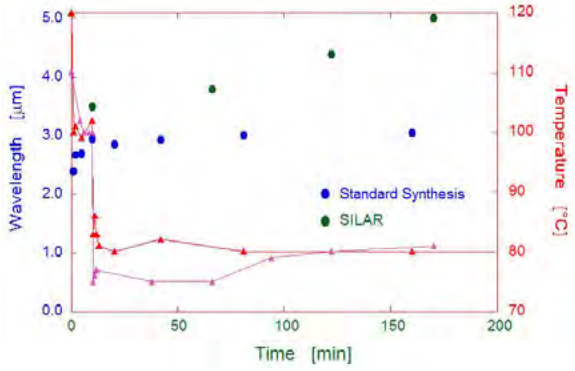

Figure 2. Development of HgTe QDs (reflected by the positions of the absorption peaks) with time.

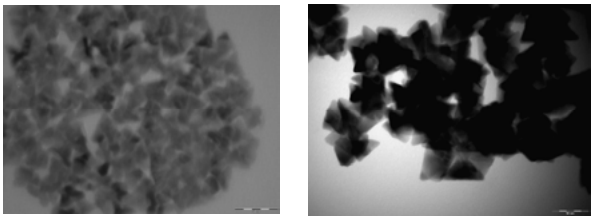

Figure 3. TEM images of the grains obtained at 100 °C using the SILAR technique. The left micrograps is of the grain obtained in 20', the right one after 100' of subsequent intermittent injections of extra precursors. The total length of the marker in the micrographs is 50 nm.

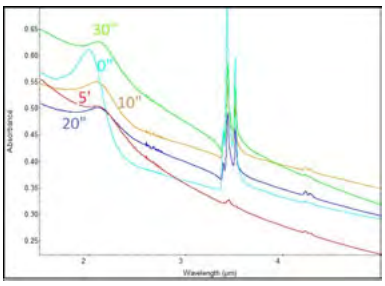

Figure 4. Absorption spectra of a sample after ligand exchange (the exchange time as shown).

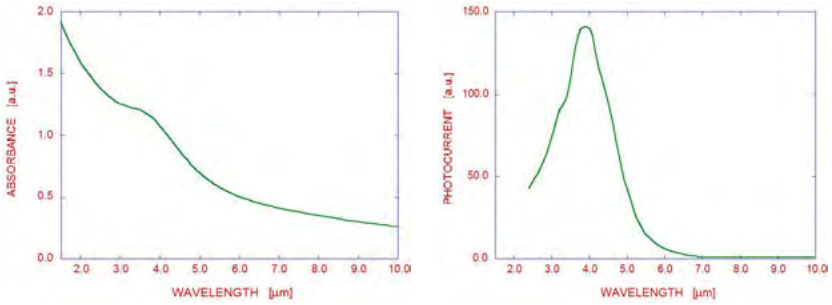

Figure 5. Absorption spectra (left) and photoresponse (right) of our device.

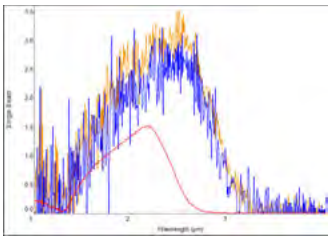

Figure 6. Photoresponse of the devices with low (red curve) and high currents.

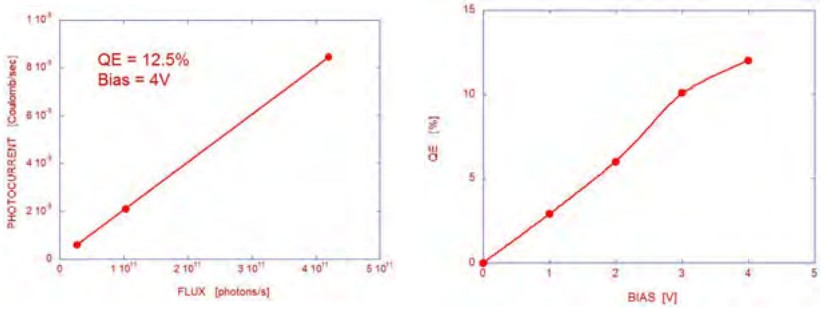

Figure 7. The current vs. photon flux, and the dependence of the QE on the applied bias.

References

1. S. Keuleyan, E. Lhuillier, and P. Guyot-Sionnest, J. Am. Chem. Soc. 133 (2011) 16422–16424.
2. J.J. Li, Y.A. Wang, W. Guo, J.C. Keay, T.D. Mishima, M.B. Johnson, and X. Peng, J. Am. Chem. Soc. 125 (2003), 12567-12575.
3. S.E. Keuleyan, P. Guyot-Sionnest, C. Delerue, and G. Allan, ACS Nano 8 (2014) 8676–8682.

Advances in HgTe Colloidal Quantum Dots for Infrared Detectors

Anthony J. Ciani, Richard E. Pimpinella, and Christoph H. Grein

Sivananthan Laboratories, 590 Territorial Dr. Ste H, Bolingbrook, Illinois 60440

Philippe Guyot-Sionnest

James Franck Institute, 929 East 57th Street, Chicago, Illinois 60637

Via quantum confinement, HgTe colloidal quantum dots (CQD) of sizes between 10 and 20 nm readily lead to infrared gaps between 3 and 12 microns, respectively. Infrared photodetection using dried films of these CQDs has been demonstrated up to a wavelength of 12 microns, and imaging in the MWIR has been reported. Further improvements in the CQD synthesis and film deposition chemistries and techniques may raise the specific detectivity of CQD films and potentially create a new paradigm in infrared photon imaging technology. The photoconductive and optical properties of HgTe CQD films will be discussed relative to infrared imaging, along with recent advancements in CQD detector technology and the feasibility of achieving background-limited detection.

Keywords: HgTe, colloidal quantum dots, infrared, photon detector

OPTICAL AMPLIFICATION IN A SINGLE CdSe–NANOWIRE–BASED LIGHT–EFFECT TRANSISTOR (LET) FOR HIGH SENSITIVITY AND RESPONSIVITY PHOTO-DETECTION

Jason K. Marmon[1,2], Satish C. Rai[3], Kai Wang[3], Weilie Zhou[3], and Yong Zhang[1,2,*]

[1]Nanoscale Science Program, [2]Department of Electrical and Computer Engineering, University of North Carolina at Charlotte, Charlotte, NC 28223, USA. [3]Advanced Materials Research Institute, University of New Orleans, New Orleans, LA 70148, USA. * yong.zhang@uncc.edu

Abstract: A CdSe–nanowire–based, light–effect transistor (LET) demonstrated a high gain *G* of 1130 under 0.47 nW of actually absorbed (532 nm) power or a 503.5 A W^{-1} responsivity when the bias was ~5 V. When gated with multiple light beams, a LET can be used to realize either optical *AND* logic or optical amplification. For the latter application, the photo-current of a weak optical signal at 532 nm was enhanced by a factor of 48, when the device was gated by a white light illumination. These results highlight a novel method for weak optical signal detection that could be extended to any wavelength of light and detection mechanism.

Keywords: Light–effect transistor (LET), high sensitivity and responsivity photodetection, CdSe nanowire, metal–semiconductor, optical amplification, optical logic

Introduction

The light–effect transistor (LET)[1] employs a metal–semiconductor–metal architecture with a single nanowire (e.g., CdSe) serving as the conducting channel, and uses light to control the channel conductivity. A LET's optical gate is structurally simpler than a FET's dielectric gate, which, remarkably, reduces the switch energy by eliminating the capacitive delay found in FETs[2,3], and could enable nanoscale M–S–M detectors to reach THz responses[4]. A LET is capable of offering not only high sensitivity and responsivity photo–detection, which offers an alternative to FETs for high speed and low energy computing applications, a LET also provides optical amplification and optical logic, where the former is of great interest for photo–detection.

Output and Transfer Characteristics

The CdSe–nanowire–based LET in Figure 1, which possesses a diameter/length of ~80 nm/5.5 μm, was demonstrated[1] to have pA–level dark current, ~1.0 μA light current under 86 nW effective (532 nm) illumination power with a bias of 1.4 V, and an on/off ratio of ~1.0×10^6. LET operation occurs under forward bias, where rectification is indicative of asymmetric In/CdSe contacts, where one M–S junction is close to ohmic and the other forms a Schottky contact[5]. Large asymmetric contacts are desired as they drastically reduce the dark or off state current and thereby improve the on/off ratio. For instance, the device in Figure 1A shows nearly resistive behavior up to V_{ds} = 21 V with I_{ds} reaching only ~15 pA. Optical gating with 532 nm light displays a first current plateau at ~2 V with power–dependent, second plateaus at ~6–7.5 V, where increasing the laser power also increases the source–drain current. Figure 1B displays the transfer characteristics (source–drain current vs. optical power), which demonstrate a super–linear current increase over very small laser powers. This region produces high sensitivity and responsivity to optical sources.

High Sensitivity and Responsivity

The device, following Figure 2, possesses a high gain G (defined as output electrons to input photons ratio) of 1130 under 0.47 nW of actually absorbed power or a 503.5 A W^{-1} responsivity when the bias was ~5 V. The G increases ~1.5 orders in magnitude by increasing the effective illumination from one to a few hundred picowatts of effective power, which is then reduced by a similar amount upon increasing the power to ~100 nW. This behavior is consistent with the transfer characteristics, which demonstrate current saturation at higher optical powers. The device's sensitivity (defined as the source–drain current divided by the effective illumination power) follows an identical pattern but with lower magnitude values than the quantum efficiency. Both high sensitivity and responsivity are observed at very low optical powers (e.g., < 1 nW).

Optical Amplification and Optical Logic

When operating in the "subthreshold" region, the LET's transfer characteristics exhibited a super–linear relationship between source–drain current and optical–gate power. This LET feature can be used to realize either optical *AND* logic or optical amplification when gated with multiple light beams. For example, two weak illumination beams, designated as signal *A* (viewed as an optical signal to be detected) and *B* (referred to as an amplification beam) independently produce source–drain currents of 11 nA (532 nm) and 37 nA (halogen light) respectively. When illuminated simultaneously, the current was amplified to 535 nA, which represents an amplification of signal *A* by a factor of 48 (Figure 3). These results highlight a novel method for weak optical signal detection that could be extended to any wavelength of light and detection mechanism, and could find application in, for instance, night vision products.

Figures

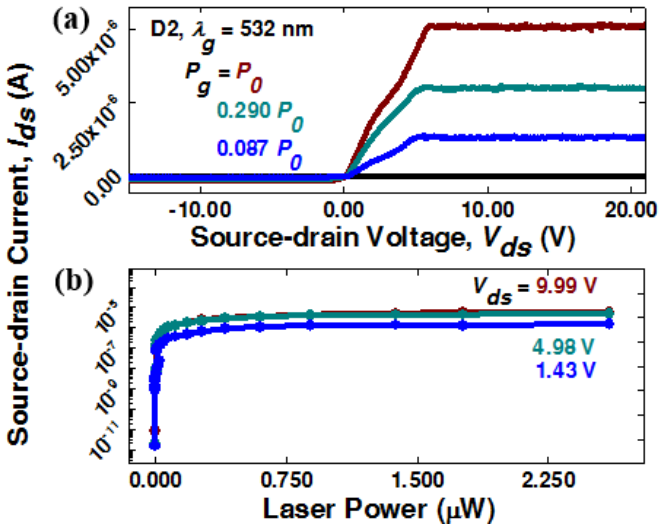

Figure 1 Output and transfer characteristics for a CdSe–nanowire–based LET. **(a)** Output characteristics under different gate power P_g's of 532 nm light. The black curve is the dark current. **(b)** Transfer characteristics collected with bias of 1.43, 4.98, and 9.99 V. An on/off ratio of ~1.0x10^6 was achieved under $P_g = P_0 = 86$ nW, where P_0 is the actually absorbed optical power (estimated using the projected area).

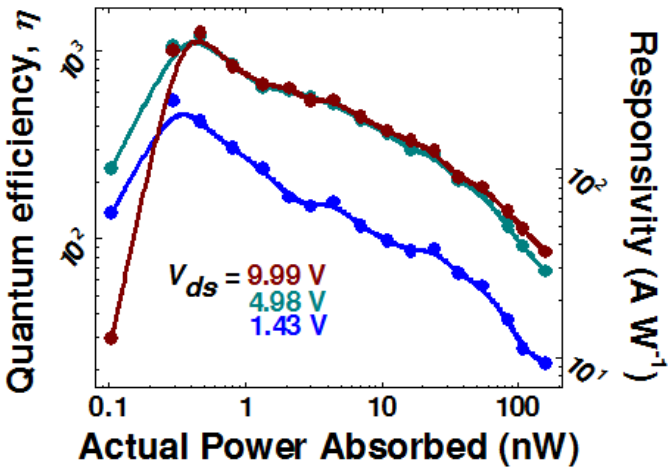

Figure 2 Quantum efficiency (or optical gain) and sensitivity as a function of illumination power (actually absorbed power). A maximum gain of 1130 was achieved under 0.46 nW (red line) of 532 nm light, which corresponds to a responsivity of 503.5 A W^{-1}.

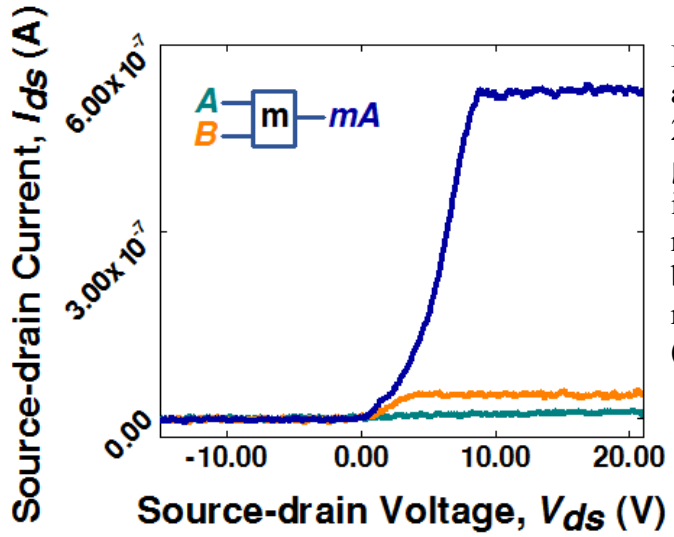

Figure 3 Typical example of optical amplification using signal $A = P_{g1}(532nm) =$ 2 nW and signal $B = P_{g2}(halogen) = 1.57$ μW of actually absorbed power. Individual illumination yields 11 nA (532 nm) and 37 nA (halogen light) of current, while two–beam illumination results in a current of 535 nA, which implies an enhancement factor (m) of ~48 for signal A.

References

1 Marmon, J. K., Rai, S. C., Wang, K., Zhou, W. & Zhang, Y. Light-effect transistor (LET) with multiple independent gating controls for optical logic gates and optical amplification. *Frontiers in Physics* **4**, 1-10 (2016).

2 ITRS. International Technology Roadmap for Semiconductors (ITRS). (2013).

3 Kyung, C.-M. *Nano devices and circuit techniques for low-energy applications and energy harvesting*. (Springer, 2015).

4 Marks, Z. & Van Zeghbroeck, B. High-speed nanoscale metal-semiconductor-metal photodetectors with terahertz bandwidth. *Optical and Quantum Electronics* **42**, 771-776 (2011).

5 Shockley, W. & Pearson, G. L. Modulation of conductance of thin films of semi-conductors by surface charges. *Physical Review* **74**, 232-233 (1948).

Performance of Science Grade HgCdTe H4RG-15 Image Sensors

Majid Zandian[1], Mark Farris[1], William McLevige[1], Dennis Edwall[1], Erdem Arkun[1], Eric Holland[1], James E Gunn[2], Stephen Smee[4], Donald N. B. Hall[3], Klaus W. Hodapp[3], Atsushi Shimon[5], Naoyuki Tamura[5], Michael Carmody[1], John Auyeung[1], and James W. Beletic[1]

[1]Teledyne Imaging Sensors, 5212 Verdugo Way, Camarillo, CA 93012, USA
[2]Princeton University, 23 Payton Hall, Princeton, NJ 08544, USA
[3]University of Hawaii, Institute for Astronomy, 640 North A'ohoku Place, Hilo, HI 96720, USA
[4]John Hopkins University, 3400 N. Charles Street, Baltimore, MD 21218, USA
[5]Kavli Institute for the Physics and Mathematics of the Universe, 5-1-5 Kashiwanoha, Kashiwa, 277-8583, Japan

ABSTRACT

In this paper we present the test results of science grade substrate-removed 4K×4K HgCdTe H4RG-15 NIR 1.7 µm and SWIR 2.5 µm sensor chip assemblies (SCAs). Teledyne's 4K×4K, 15 µm pixel pitch infrared array, which was developed for the era of Extremely Large Telescopes, is first being used in new instrumentation on existing telescopes. We report the data on H4RG-15 arrays that have achieved science grade performance: very low dark current (<0.01 e^-/pixel/sec), high quantum efficiency (70-90%), single CDS readout noise of 18 e^-, operability >97%, total crosstalk <1.5%, well capacity >70 ke^-, and power dissipation less than 4 mW. These SCAs are substrate-removed HgCdTe which simultaneously detect visible and infrared light, enabling spectrographs to use a single SCA for Visible-IR sensitivity. Larger focal plane arrays can be constructed by assembling mosaics of individual arrays.

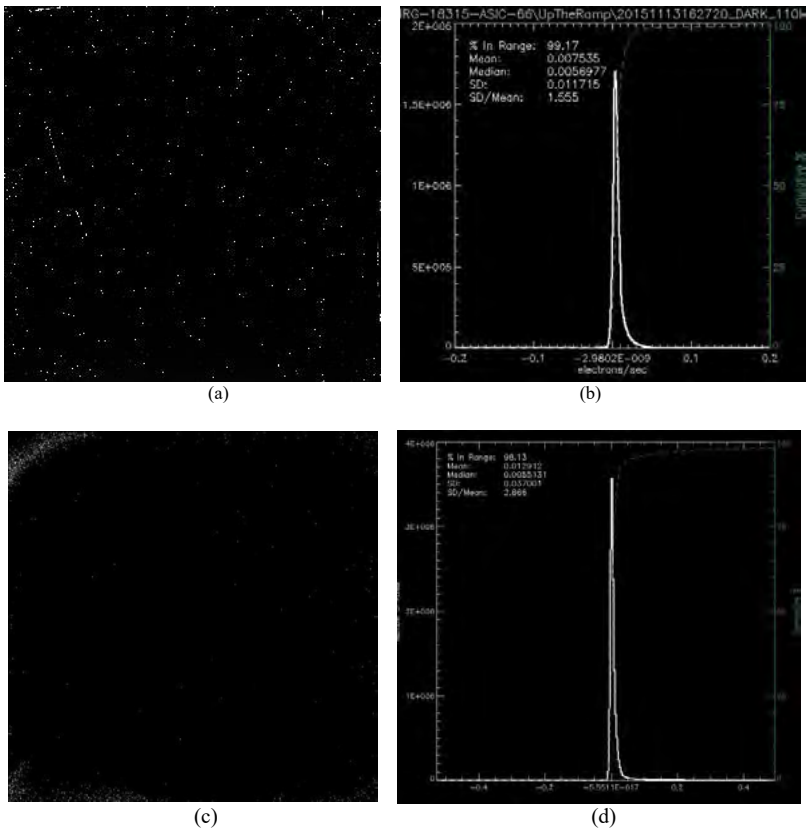

Figure 1. (a) Dark current map and (b) histograms for H4RG-15 1.7 µm S/N 18315 at 110K. Dark current map and (c) histograms for H4RG-15 2.5 µm S/N 18575 at 80K. Plots represent a median dark current less than 0.006 e-/second for both NIR and SWIR SCAs.

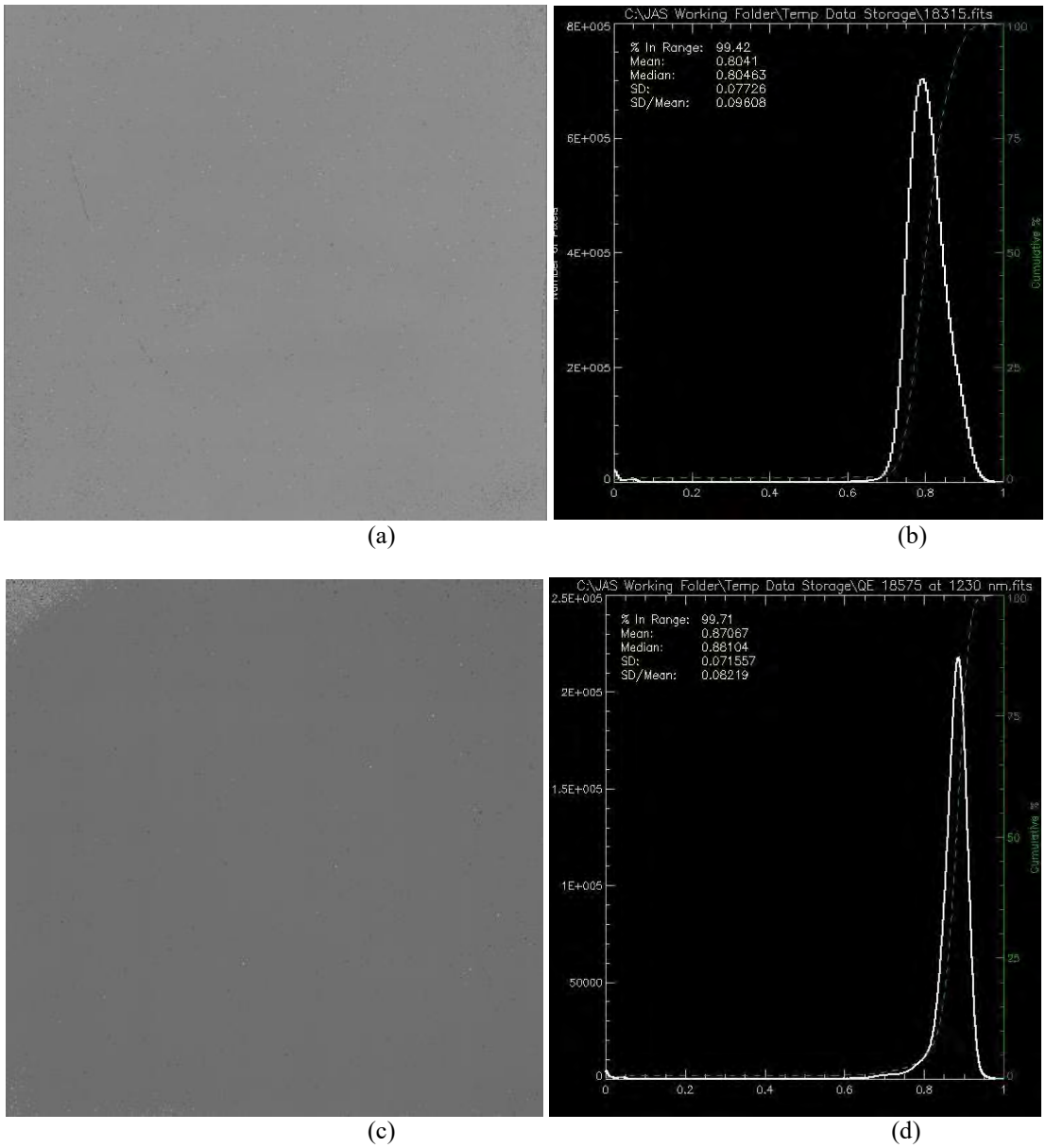

Figure 2. QE (a) Gray-scale map, and (b) histogram of H4RG-15 1.7 μm S/N 18315 with good uniformity across the array. Data was taken at 1230 nm at 120 K. The histogram of the same array shows the tight distribution with median QE at 80.4%. QE (c) Gray-scale map, and (d) histogram of H4RG-15 2.5 μm S/N 18575 with good uniformity across the array. Data was taken at 1230 nm at 80K. The histogram of the same array shows the tight distribution with median QE at 88.1%.

Table 1. SCA performance for NIR 1.7 μm and SWIR 2.5 μm

Parameter	Unit	SCA 18315 NIR 1.7 μm	SCA 18321 NIR 1.7 μm	SCA 18575 SWIR 2.5 μm	Comments
Array format [I]		4096 x 4096	4096 x 4096	4096 x 4096	Measured
Read-out integrated circuit (ROIC)		H4RG-15	H4RG-15	H4RG-15	Measured
Power Dissipation [II]	mW	3.04	3.53	3.01	Measured
Detector Material		HgCdTe	HgCdTe	HgCdTe	Measured
Detector Substrate		CdZnTe, removed	CdZnTe, removed	CdZnTe, removed	Measured
Cutoff wavelength (50% of peak QE)	μm	1.79	1.78	2.45	Measured
Mean Quantum Efficiency (QE) at 800 nm	%	55	65	60.5	Measured
Mean Quantum Efficiency (QE) at 1,000 nm	%	72	70	84.6	spectral curve and AR coating witness
Mean Quantum Efficiency (QE) at 1,230 nm	%	80	70	88.1	Measured
Mean Quantum Efficiency (QE) at 1,500 nm	%	86	71	93.1	spectral curve and AR coating witness
Mean Quantum Efficiency (QE) at 2,000 nm	%	N/A	N/A	85.2	Measured
Median Dark current: 1.7μm: @ 0.25 and 0.35 V bias @ 110-130K 2.5μm: @ 0.25 V bias @ 80K	e^-/s	0.023 @ 130K at 250 mV 0.019 @ 120K at 250 mV 0.006 @ 110K at 250 mV 0.032 @ 120K at 350 mV	0.047 @ 130K at 250 mV 0.009 @ 120K at 250 mV 0.008 @ 110K at 250 mV 0.068 @ 120K at 500 mV	0.0055 @ 80K at 250 mV	Measured
Median Readout Noise, correlated double sampling (CDS) at 100 kHz pixel readout rate	e^-	18.1	20.8	17.5	Measured
Well Capacity at 0.25 and 0.35 V bias	e^-	≥ 61549 @250 mV ≥ 79185 @350 mV	≥ 68045 @250 mV ≥ 90676@500 mV	≥ 141376 @250 mV	Measured
Crosstalk [III]	%	1.1	0.8	1.0	Measured
Operability [IV]	%	97.4	97.2	93.5	Measured
Cluster: 50 or more contiguous inoperable pixels	%	0.11	1.1	0.2	Measured
SCA Flatness [V]	μm	13.9	13.6	19.6	Measured

I. There are 4088 x 4088 pixels for light detection plus 4 rows and columns of reference pixels on each side for a total of 4096 x 4096

II. At 100 kHz pixel read-out rate, un-buffered, 32 outputs. Does not include external current source; power has to be optimized by the user with respect to the system in which the device is used

III. Crosstalk includes optical (charge diffusion) and electrical (inter-pixel capacitance) components

IV. A pixel is considered operable if QE ≥ 30% at 1500 nm, dark current ≤ 0.5 e^-/sec for SWIR and ≤ 0.1 e^-/sec for NIR , and single correlated double sample (CDS) noise is ≤35 e^-

V. Maximum variation (peak-to-valley) to best fit plane. Note: The flatness of each SCA was measured using white light interferometry and entire SCA surface was imaged and analyzed.

An Empirical Study of the Disparity in Radiation Tolerance of the Minority Carrier Lifetime between II-VI and III-V Space Detector Technologies in the MWIR

Geoffrey D. Jenkins, Christian P. Morath, Vincent M. Cowan
Space Vehicles Directorate, Air Force Research Laboratory, Albuquerque NM, USA

Abstract: Presented here is a comparison of empirically determined radiation tolerance metrics and room temperature thermal annealing behavior between II-VI and III-V space infrared detector materials. The metric considered herein is the degradation rate of the inverse minority carrier recombination lifetime, or *recombination rate,* of samples held at 120 Kelvin and exposed to stepwise 63 MeV proton irradiation up to doses of 100 to 200 kRad[Si]. Lifetimes were determined using the time-resolved-photoluminescence (TRPL) technique. It is shown that, of the detector wafer structures characterized to date, the best HgCdTe sample had an order of magnitude lower degradation rate than the best InAs/InAsSb unipolar barrier detector. Additionally, HgCdTe samples exhibited near 100% recovery of their minority carrier lifetime following thermal annealing at room temperature, whereas InAsSb/InAsSb samples typically only recovered much less than 50% under similar conditions. The implications of these results as far as comparing defect introduction rates and how this impacts detector performance is then described.

Keywords: radiation tolerance, proton, InAs, HgCdTe, lifetime, MWIR

Introduction

As many research and development efforts in the infrared (IR) space detector community continue to focus on physically achieving the theoretical performance potential of III-V-based detector technology[1-2], the Air Force Research Laboratory (AFRL) continues to provide iterative characterization feedback[3-4] on supplied detector prototype materials. Although several metrics are provided overall, of concern herein is radiation tolerance, specifically the changes in the minority carrier lifetimes of mid-wave-infrared (MWIR) prototype detectors with increases in cumulative proton irradiation. The significance of these changes, relative to those seen in II-VI detector technology (HgCdTe), is discussed.

Experiment

The detector metric of interest here is the minority carrier lifetime, which is a key factor in determining detector performance[5]. Here, it was empirically determined via the contactless method of time-resolved-photoluminescence (TRPL), where post-injection PL transients (see Figure 1) are fitted to extract carrier lifetimes. The details of this experiment, including irradiation protocol, may be found elsewhere[4]. Changes in minority carrier recombination rates (proportional to inverse carrier lifetime) with proton irradiation have been shown to be linear when material lifetimes are limited by Shockley-Read-Hall (SRH) recombination, as increases in defect trap densities are directly proportional to proton fluence[4,6]. The slopes of these changes are recorded as the minority carrier lifetime damage factors and become radiation tolerance metrics for comparing detector material prototypes, as shown in Figure 2.

Results

Although many detector prototypes have been characterized, only a few high quality III-V and II-VI performers characterized to date are compared here for the sake of clarity. In addition to differences in lifetime radiation tolerance, a disparity in lifetime recoveries after thermal annealing is discussed, as these differences have been consistent throughout several characterizations of each material type and varied designs, hinting that lifetime radiation tolerance may be largely agnostic to detector structure and more dependent on bulk material properties.

Radiation Tolerance

Data on recombination rates vs proton fluence, and the fitted lifetime damage factors, are shown in Figure 2 for comparison of III-V and II-VI lifetime radiation tolerance. The slopes with smaller magnitudes are more radiation-hard than the others. Most III-V characterizations to date are more in family with sample III-V (a) than with III-V (b). Compared to HgCdTe, these III-V samples are approximately 11 to 39 times more susceptible to lifetime degradation with proton irradiation.

Annealing Behavior

After in-situ lifetime characterizations with stepwise proton irradiation with samples held at 120 Kelvin, samples are warmed up and then cooled and re-characterized at 120K to see if there is any healing, i.e. recovery in minority carrier lifetimes. In samples characterized to date, lifetime recoveries exhibited in HgCdTe (Figure 3) have been significant while those in III-V materials have not (Figure 4). In performing consecutive anneals, first at 220K and then 295K, it has been shown that damage healing in HgCdTe also occurs at lower temperatures.

Figures

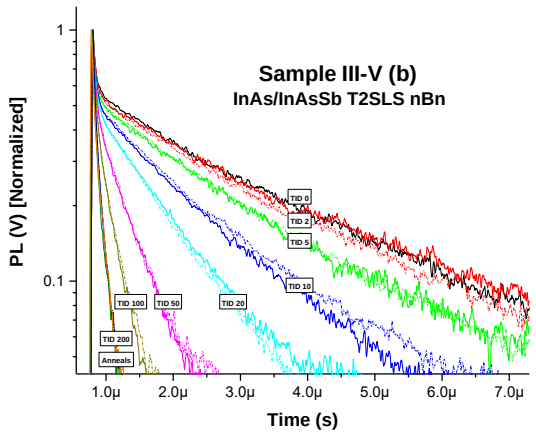

Figure 1: Photoluminescence transients

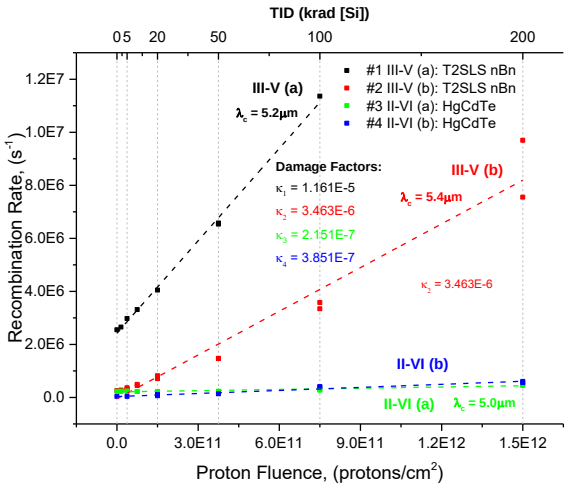

Figure 2: Lifetime damage factors

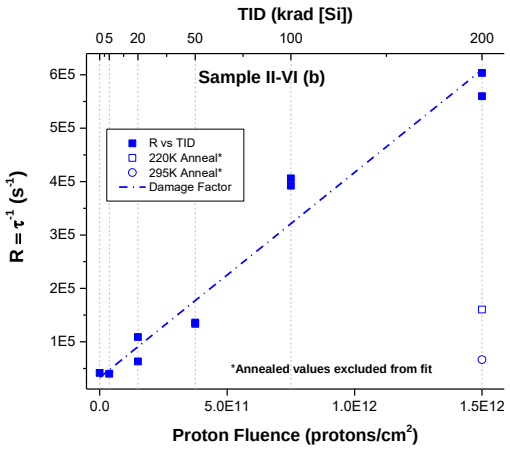

Figure 3: II-VI post-anneal lifetime recovery

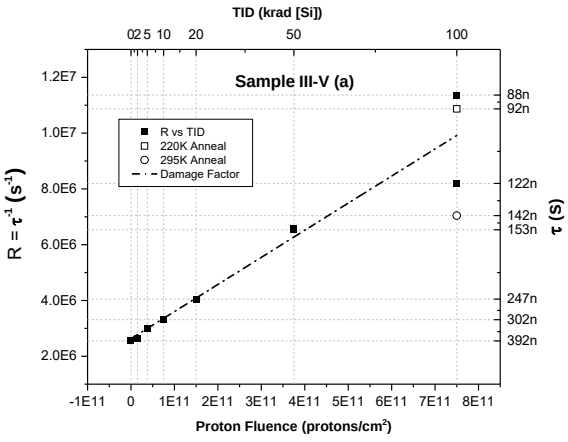

Figure 4: III-V post-anneal lifetime recovery

References

[1] Gamini Ariyawansa, Charles J. Reyner, Elizabeth H. Steenbergen, et al, "InGaAs/InAsSb strained layer superlattices for mid-wave infrared detectors," Appl. Phys. Lett. 108, 022106 (2016)

[2] Rhiger, D.R., "Performance Comparison of Long-Wavelength Infrared Type II Superlattice Devices with HgCdTe," Journal of Elec Materials (2011) 40: 1815

[3] C. P. Morath, E. A. Garduno, V. M. Cowan, and G. D. Jenkins, "More accurate quantum efficiency damage factor for proton-irradiated, III-V-based unipolar barrier infrared detectors," IEEE trans on nuclear science, 2016

[4] Jenkins, G., D., Morath, C., P., et al, "Empirical trends of minority carrier recombination lifetime vs proton radiation for rad-hard IR detector materials", Proc. SPIE. 9616, Nanophotonics and Macrophotonics for Space Environments IX, 96160G (2015)

[5] Connelly, B., C., Metcalfe, G., D., et al, "Direct minority carrier lifetime measurements and recombination mechanisms in long-wave infrared type II superlattices using time-resolved photoluminescence," Proc. of SPIE (2013).

[6] L. Höglund, D. Z. Ting, A. Khoshakhlagh, et al, "Influence of proton radiation on the minority carrier lifetime in midwave infrared InAs/InAsSb superlattices," Applied Physics Letters 108, 263504 (2016)

Novel Applications and New Physical Phenomena Based on Heterovalent and Heterocrystalline Nanostructures

Maria Tamargo
The City College of New York
New York, NY 10031

Over the last several years our group has extensively investigated the growth of II-VI compounds on III-V substrates and has developed the techniques and the understanding to achieve heteroepitaxy of comparable quality to that of isovalent (III-VI/III-V) systems. More recently, we have begun to investigate the growth of multilayered structures of materials having dissimilar crystal structures, such structures of "layered" Bi_2Se_3 combined with three-dimensional II-VI semiconductors. Recent results along these directions will be presented.

Intersubband devices such as quantum cascade (QC) lasers, quantum well infrared photodetectors (QWIPs), and quantum cascade detectors (QCDs) have been grown and investigated based on wide bandgap II-VI structures grown on InP substrates. Devices with properties that rival those of III-V based devices and that provide additional new and unique capabilities have been reported.[1]

Ultra-small quantum dots of ZnTe embedded in ZnCdSe grown on InP substrates have also been investigated. The type-II band alignment of these nanostructures and their materials parameters make them attractive as candidates for intermediate band solar cells (IBSC).[2]

Finally, the growth of Bi_2Se_3/ZnCdSe superlattices has recently been reported. High crystalline quality layers with abrupt interfaces that can be tailored to enhance the topological properties of the Bi_2Se_3 materials have been obtained.[3]

1. J. De Jesus, G. Chen, L. C. Hernandez-Mainet, A. Shen and M. C. Tamargo, Strain compensated CdSe/ZnSe/ZnCdMgSe quantum wells as building blocks for near to mid-IR intersubband devices, J. Crystal Growth **425**, 207 (2015)
2. S. Dhomkar, U. Manna, L. Peng, R. Moug, I. C. Noyan, M. C. Tamargo and I. L. Kuskovsky, Feasibility of submonolayer ZnTe/ZnCdSe quantum dots as intermediate band solar cell material system, Sol. Energ. Mat. Sol. C **117**, 604–609 (2013).
3. Z. Chen, L. Zhao, K. Park, T. A. Garcia, M. C. Tamargo, and L. Krusin-Elbaum, Robust Topological Interfaces and Charge Transfer in Epitaxial Bi_2Se_3/II−VI Semiconductor Superlattices, Nano Letters 15, 6365-6370 (2015)

CHEMICAL ETCHING AND CHEMOMECHANICAL POLISHING OF CADMIUM ZINC TELLURIDE X-RAYS AND GAMMA-RAYS DETECTORS

Stephen U. Egarievwe[1,2,4], Eric D. Lukosi[2], Ezekiel O. Agbalagba[3], Anwar Hossain[4], Rubi Gul[1,4], Utpal N. Roy[4], Aleksey E. Bolotnikov[4], and Ralph B. James[5]

stephen.egarievwe@aamu.edu

[1]*Nuclear Engineering and Radiological Science Center, Alabama A&M University, Normal, AL, USA*

[2]*Nuclear Engineering Department, University of Tennessee, Knoxville, TN, USA*

[3]*Department of Physics, Federal University of Petroleum Resources, Effurun, Delta State, Nigeria*

[4]*Dept. of Nonproliferation and National Security, Brookhaven National Laboratory, Upton, NY, USA*

[5]*Savannah River National Laboratory, Science & Technology, Aiken, SC, USA*

Abstract: In this paper we compare the effects of chemical etching and chemomechanical polishing on CdZnTe detectors using bromine-methanol-ethylene glycol. The measured bulk resistivity of the wafers were of the order of 10^{10} ohms-cm. The chemo-mechanically polishing removed scratches from the wafer surface better than the chemical etching. X-ray photoelectron spectroscopy showed chemical etching increased tellurium oxide peaks while chemomechanical polishing decreased them. Chemomechanical polishing decreased the mobility-lifetime product by 10.2% compared to 3.7% for chemical etching.

Keywords: Chemomechanical polishing, CdZnTe, Etching, Gamma-rays, Nuclear detectors, X-rays.

Introduction

Chemical etching and chemomechanical polishing are important processes in the fabrication of cadmium zinc telluride (CdZnTe) X-rays and gamma-rays detectors[1,2]. These processes are two techniques used separately to further smoothen the surfaces of CdZnTe wafers after mechanical polishing. Chemomechanical polishing has been observed to result in less surface leakage current compared to chemical etching. However, many reported works compared these two processes using different

chemicals. There is lack of reporting on the use of the same chemical solution to study these two processing techniques. The present study reports on comparing the effects of chemical etching and chemomechanical polishing on CdZnTe detectors using the same chemical solution: bromine-methanol-ethylene glycol.

Experiment

Two samples cut from the same region of the CdZnTe ingot were used to study the two surface processing techniques: chemical etching and chemomechanical polishing. Sample 1 has dimensions of 5.4 mm x 5.3 mm x 1.6 mm, and sample 2 has dimensions of 5.8 mm x 6.0 mm x 1.7 mm. The two samples were mechanically polished with 800-grit and 1200-grit silicon carbide abrasive papers, followed by polishing on MultiTex pads with decreasing size alumina powder to 0.1 μm. The following measurements were made on the two samples:

1. X-ray photoelectron spectroscopy (XPS) using an RHK Technology UHV 7500 system in an ultrahigh-vacuum setup at pressure below 8 x 10^{-10} Pa was undertaken to scan for peaks of cadmium (Cd), tellurium (Te) and tellurium oxide (TeO_2) on the surfaces of the samples.
2. Current-voltage measurements were made after the deposition of electrical contacts using a 5% gold chloride ($AuCl_3$) solution on the center of the two opposite planar surfaces of each CdZnTe wafer.
3. Charge-carrier mobility-lifetime products for the samples were measured using Am-241 at an applied voltage of 150 V.

After the above three measurements, the gold contacts were removed using a 1200-grit silicon carbide abrasive paper. The mechanical polishing process was repeated for both samples. Next, sample 1 was chemically etched in bromine-methanol-ethylene (BME) glycol solution, and sample 2 was chemo-mechanically polished using BME glycol solution. The chemical etching was done by dipping the CdZnTe sample in the BME glycol solution. The chemo-mechanical polishing was accomplished by polishing the wafer on a felt pad using BME glycol solution. Optical images of the wafer surfaces were taken using a microscope fitted with a CCD camera. The three measurements (XPS, current-voltage, and charge-carrier mobility-lifetime products) were then repeated on the two samples.

Results

The measured bulk resistivity of the wafers is of the order of 10^{10} ohms-cm. Optical images of the surfaces in Figure 1 showed that the chemo-mechanical polishing process removed scratches better than chemical etching. X-ray photoelectron spectroscopy results showed that chemical etching increased the tellurium oxide peaks of mechanically polished CdZnTe wafer while chemomechanical polishing decreased these peaks. Charge-carrier mobility-lifetime product measurements using Am-241 (see Figures 2 and 3) showed a decrease by 10.2% for chemomechanical polishing (from 1.56 x 10^{10} cm^{-3}/V to 1.40 x 10^{10} cm^{-3}/V) compared to 3.7% for chemical etching (from 1.08 x 10^{10} cm^{-3}/V to 1.04 x 10^{10} cm^{-3}/V).

Acknowledgements

This work has been supported by the U.S. Department of Homeland Security, Domestic Nuclear Detection Office, under competitively awarded contract/IAA award number 2012-DN-077-ARI065-05. Alabama A&M University researchers were also supported by the U.S. Nuclear Regulatory Commission through award number NRC-27-10-514, and BNL scientists received support from the U.S. Department of Energy Office of Defense Nuclear Nonproliferation R&D. These supports do not constitute an expressed or implied endorsement by the U.S. Government.

Figures

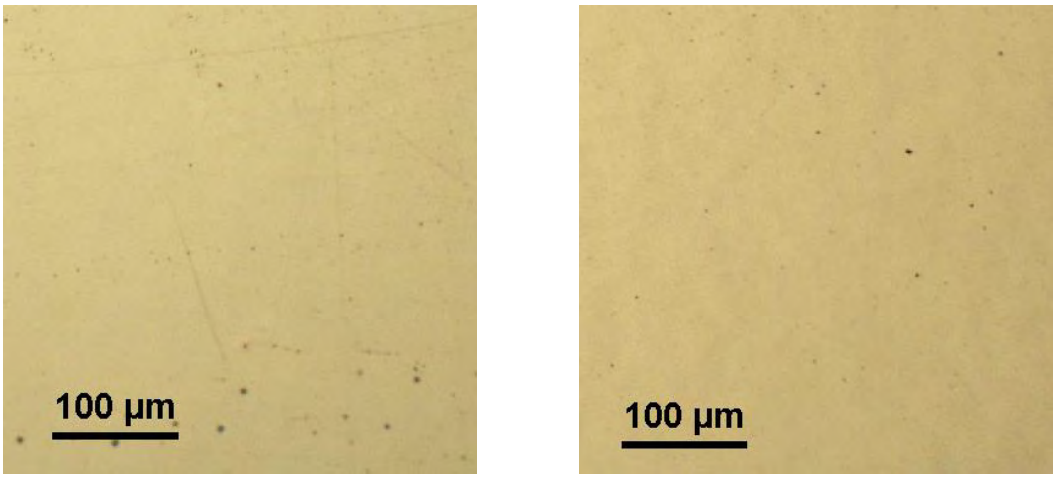

(a) Chemically etched surface. (b) Chemo-mechanically polished surface.

Figure 1. Optical images of the wafer surfaces taken using a microscope fitted with a CCD camera.

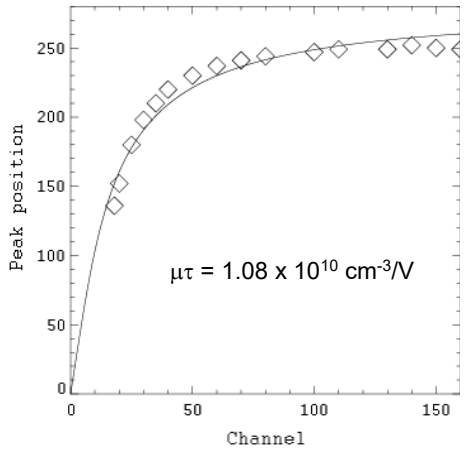

(a) Before chemical etching.

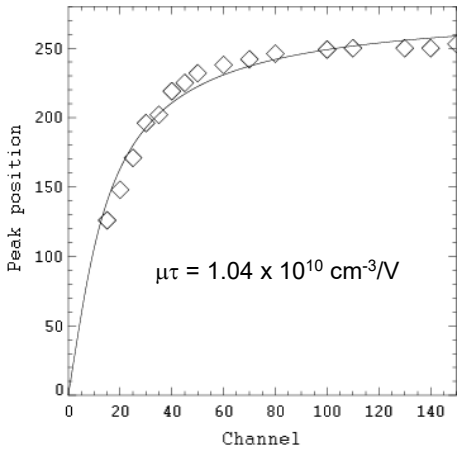

(b) After chemical etching.

Figure 2. Charge-carrier mobility-lifetime product of sample 1.

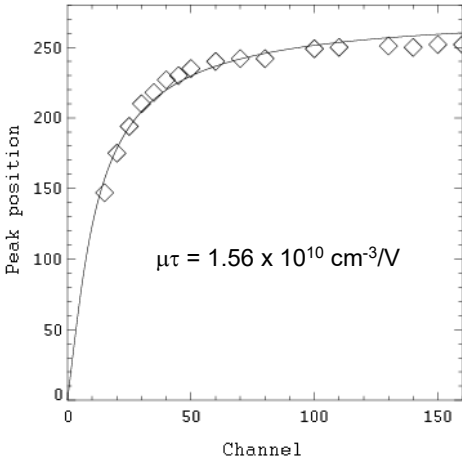

(a) Before chemomechanical polishing.

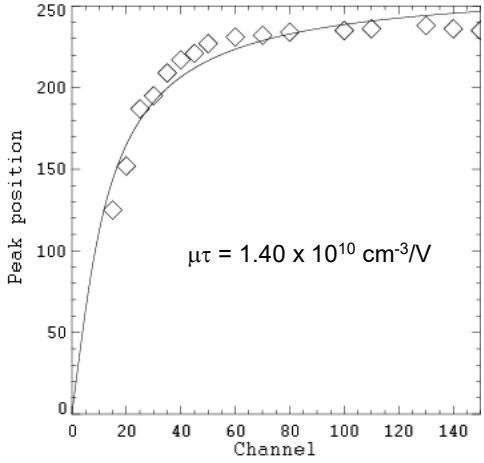

(b) After chemomechanical polishing.

Figure 3. Charge-carrier mobility-lifetime products of sample 2.

References

[1] S. U. Egarievwe, A. Hossain, I. O. Okwechime, R. Gul, and R. B. James. “Effects of Chemo-Mechanical Polishing on CdZnTe X-Ray and Gamma-Ray Detectors,” *Journal of Electronic Materials*, vol. 44, Issue 9, pp. 3194–3201, Sept. 2015.

[2] S. U. Egarievwe, A. Hossain, I. O. Okwechime, A. A. Egarievwe, D. E. Jones, U. N. Roy, R. B. James. “Effects of Chemical Treatments on CdZnTe X-Ray and Gamma-Ray Detectors,” *IEEE Transactions on Nuclear Science*, Vol. 63, No. 2, pp. 1091–1098, 2016.

Effects of electrode contacts on the performance of CdZnTe film UV detectors

Linjun Wang, Jian Huang, Ke Tang, Yue Shen

School of Materials Science and Engineering, Shanghai University, Shanghai 200444, China

Cadmium zinc telluride (CdZnTe) is one of the promising materials for high-energy radiation and photon detectors compared to conventional silicon, germanium and gallium arsenide, due to its high average atomic number, excellent carrier transport property and a large band-gap [1]. CdZnTe detectors are being developed to be used in environmental monitoring, nuclear medicine, industrial non-destructive testing, security checks, space science, nuclear weapons and other nuclear technology penetration [2,3]. Owing to the high cost and the difficulty of CdZnTe bulk crystal growth, polycrystalline CdZnTe film begins to be considered for large-area radiation detector applications [4,5].

Previous work on polycrystalline CdZnTe devices indicated that the performance of the devices depended not only on the film quality but also on electrode contacts [6,7]. So far it is not an easy way to form a well ohmic or quasi-ohmic contact for high-resistivity CdZnTe films by directly depositing metal such as Au, Ti or Al [8,9]. Recently, to solve this problem, multilayer metal electrode structure (such as Pt/Au, Cr/Au, Ti/Pt/Au) or low resistance intermediate layer (such as graphene intermediate layer) was used to improve the contact electrical properties [2]. ZnTe，which has similar structure with CdZnTe and low resistivity after doping, is a potential candidate for such an intermediate layer [10,11].

In this paper, low resistivity ZnTe:Cu films were used as an interlayer between Au electrodes and CdZnTe films to reduce the contact resistance. The Cu-doped ZnTe was sputtered by RF magnetron sputtering on CdZnTe films. The effects of Cu-doped ZnTe intermediate layer on the contact properties of Au/ZnTe:Cu/CdZnTe structure and CdZnTe UV detectors were discussed.

CdZnTe films were deposited by close space sublimation (CSS) method. High-purity $Cd_{0.9}Zn_{0.1}Te$ powder (purity 99.99%) was used as sublimation source material. The thickness of CdZnTe films were about 300 μm. The as-deposited CdZnTe samples were polished by mechanical polishing (MP) process by mechanical polisher. Then interdigitated Cu-doped ZnTe films (5 at% Cu) and Au electrodes were deposited on the surface of the CdZnTe film respectively, as shown in Fig.1.

Fig.2 shows the XRD pattern of as-deposited CdZnTe films. The CdZnTe film exhibit zinc blends structure with strong preferential (111) orientation and no other peaks can be observed except CdZnTe (111), (422) and (333). The experimental lattice constant (a) for CdZnTe film is 6.4 **Å**, which can be obtained from Bragg's relation [12]: $2d\sin\theta = \lambda$ and $a = d_{111}\sqrt{h^2 + k^2 + l^2}$. According to the a=6.4**Å**, the content of Zn (at%) and E_g can also be calculated by Vegard's law:a=6.48-0.37x and E_g=1.51+0.606x-0.139x^2 which was proposed by Reon and Jone [13]. The values of Zn content (at%) and E_g are 22% and 1.64 eV, respectively.

Fig.3 is the cross-section image of the ZnTe: Cu/CdZnTe structure. As the fig.3 shown, the thickness of CdZnTe and ZnTe:Cu layer is about 300 μm and 100 nm, respectively. It can be observed that the ZnTe:Cu layer is well coalesced with the

CdZnTe film. The Hall effect measurement shows that the ZnTe:Cu film is p-type conduction with low resistivity of about 0.015 Ω·cm.

Fig.4 shows the *I-V* characteristic of Au and Au/ZnTe:Cu contacts on the polished CdZnTe film. From the linear dependence of the *I-V* characteristics, the ohmic contacts between Au/ZnTe:Cu contacts and polished CdZnTe films are confirmed. The approximate linear *I-V* curves of Au contacts on polished CdZnTe films were also observed in the figure. To evaluate the effect of ZnTe:Cu layer and polishing treatment on the contact characteristics, the *I-V* curves were fitted using the non-linear function: $I(V) = aV^b$, where a is constant, b is an ohmic resistance coefficient [14]. If b=1, the contact is ohmic. We can find that the b value of Au/ZnTe:Cu/polished-CdZnTe is 0.99, which is more close to 1, while the Au/polished-CdZnTe is 0.67. This result indicates ZnTe:Cu intermediate layer is favored to the formation of good ohmic contact.

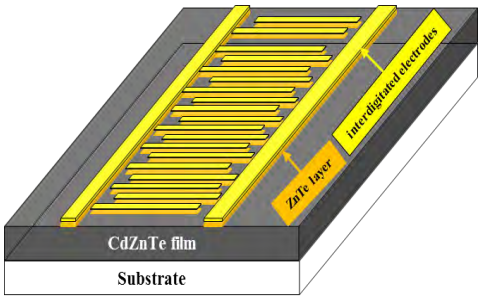

Fig.1 The structure of the CdZnTe films and interdigitated electrodes.

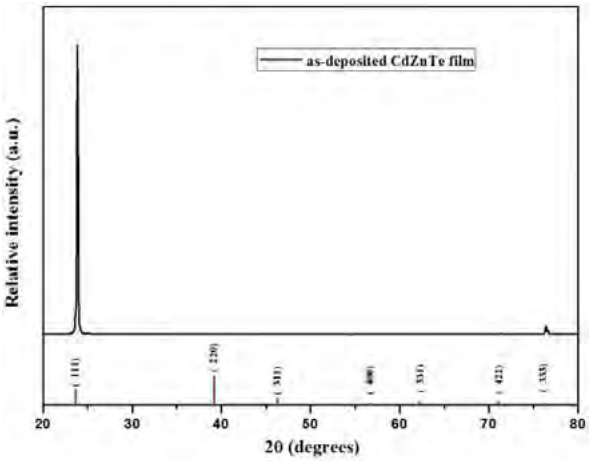

Fig.2 The XRD pattern of as-deposited CdZnTe films

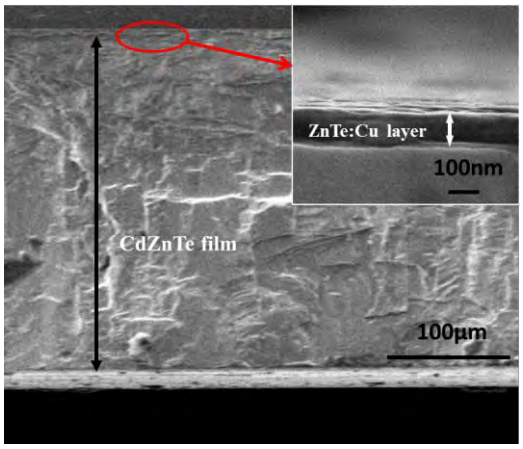

Fig.3 The cross-section SEM images of the ZnTe: Cu/CdZnTe, the insert is the interface enlargement image of ZnTe:Cu layer

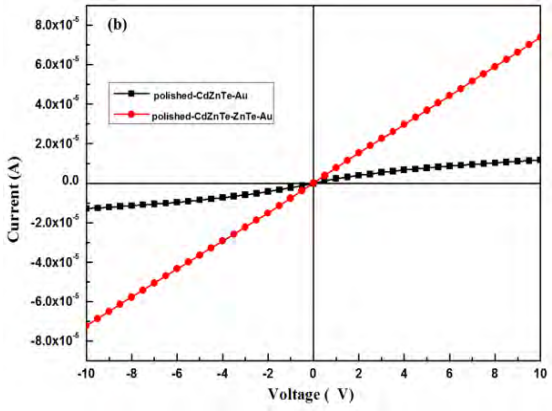

Fig.4 Current-voltage (*I-V*) characteristic of Au and Au/ZnTe:Cu contacts on polished CdZnTe films

References

[1] S.H. Cho, J.H. Suh, J.H. Won, K.H. Kim, K.H. Jin, U.K. Sun, Nuclear Instruments & Methods in Physics Research, 591 (2008) 203-205.

[2]T.E. Schlesinger, J.E. Toney, H. Yoon, E.Y. Lee, B.A. Brunett, L. Franks, R.B. James, Materials Science & Engineering R Reports, 32 (2001) 103-189.

[3] J. Gutowski, Physica Status Solidi, 240 (2003) 269-271.

[4] K.H. Kim, S.H. Cho, J.H. Suh, J.H. Won, J.K. Hong, S.U. Kim, Current Applied Physics, 9 (2009) 306-310.

[5] H. Xu, R. Xu, J. Huang, J. Zhang, K. Tang, L. Wang, Applied Surface Science, 305 (2014) 477-480.

[6] K.F. Qin, L.J. Wang, J.J. Zhang, J.H. Min, X.Y. Liang, J. Huang, K. Tang, Y.B. Xia, Materials Science Forum, 663-665 (2010) 1298-1301.

[7] J. Sun, L. Fu, Z. Nie, Y. Shi, Y. Li, Applied Physics A, 115 (2014) 1309-1316.

[8] A.E. Bolotnikov, S.E. Boggs, C.M.H. Chen, W.R. Cook, F.A. Harrison, S.M. Schindler, Nuclear Instruments & Methods in Physics Research, 482 (2001) 395-407.

[9] A. Makhtari, F. La Via, V. Raineri, L. Calcagno, F. Frisina, Microelectronic Engineering, 55 (2001) 375-381.

[10] K. Sato, S. Adachi, Journal of Applied Physics, 23 (1991) 9569-9577.

[11] D. Rioux, D.W. Niles, H. Hochst, Journal of Applied Physics, 73 (1993) 8381-8385.

[12] J. Park, M. Jo, J. Lee, S. Jung, W. Lee, S. Kim, S. Park, J. Shin, H. Hwang, Microelectronic Engineering, 88 (2011) 935-938.

[13]W. Sang, Y. Qian, W. Shi, L. Wang, J. Yang, D. Liu, Journal of Crystal Growth, s 214–215 (2000) 30-34.

[14] B.W. Choi, H.N.G. Wadley, Journal of Crystal Growth, 208 (2000) 219-230.

Dry Etching Characteristics of MOVPE Grown CdTe Epilayers in CH_4, H_2, Ar ECR Plasmas

K. Yasuda*, M. Niraula, N. Araki, M. Miyata, S. Kitagawa, M. Kojima, J. Ozawa, S. Tsubota, T. Yamaguchi, and Y. Agata

Nagoya Institute of Technology, Graduate School of Engineering

Gokiso, Showa, Nagoya 466-8555, Japan

*Tel: 81-52-735-5435, Email: yasuda@nitech.ac.jp

Dry etching of single crystal CdTe epitaxial layers was studied in H_2/Ar and CH_4/H_2/Ar electron cyclotron resonance plasmas for its application in fine pixel x-ray gamma ray imaging array development. Here we report on the etching rate, compositional properties of the etched surface as well as the effect of the etching on electrical properties of the crystals.

MOVPE grown (100) oriented single crystal CdTe epilayers on GaAs substrate were used. The etching was performed in reactor equipped with an ECR plasma source (2.45 GHz) and permanent magnets. The plasma was generated at 600W microwave power, 2 mTorr pressure, using a mixture of CH_4, H_2, and Ar gases. The crystals were placed on a water cooled substrate holder at room temperature with no DC bias applied. X-ray photoelectron spectroscopy (XPS), 4.2 K photoluminescence and the Hall measurement (300K) were used to evaluate the sample.

The etching rate remained almost constant at 120 nm/min for low CH_4 flow rates up to 2 ccm, however, it decreased to zero when the flow rate was increased to 5 ccm, keeping the H_2 and Ar flow rates constant at 1.9 and 1.5 ccm, respectively. XPS results confirmed that no hydrocarbon polymer film was formed on the crystal surface. On the other hand, etching was observed when using only H_2 and Ar as the plasma gases, but no etching in the absence of H_2. These results indicate that H_2 is essential for the etching, and the etching occurs due to the chemical reaction of hydrogen species and not due to the sputtering of the Ar^+-ions. Smooth surface with low under-cut was obtained. The PL and the Hall data confirmed that there was no deterioration in electrical properties of the crystals due to the etching. Details on etching mechanism and properties of the etched crystals will be presented.

OVERCOMING ETCH CHALLENGES ON A 6” MBE $Hg_{1-X}Cd_XTe$/Si WAFER

Palash Apte, Elyse Norton, Solomon Robinson

Raytheon Vision Systems, 75 Coromar Drive, Goleta CA 93117.

ABSTRACT

The effect of increasing Photoresist (PR) thickness on the dry etched characteristics of a 6” MBE $Hg_{1-x}Cd_xTe$/Si wafer is investigated. It is determined that the $Hg_{1-x}Cd_xTe$ etch rate (ER) does not vary with a change in the PR thickness. Also, the vertical ER of the PR is seen to be independent of the PR thickness but the lateral ER is seen to reduce significantly with increased PR thickness. Indeed, very little reduction in the pixel mesa area post dry etch is seen for the thicker PR. Consequently, the trench sidewall angle is also seen to vary as a function of the PR thickness.

INTRODUCTION

Fabrication of next gen infrared (IR) $Hg_{1-x}Cd_xTe$ /CZT detectors requires the dry etching of deep mesa trenches to delineate the pixels. However, to reduce costs and increase yield, it is desirable to use 6” Si substrates. Unfortunately, these larger wafers when dry etched, suffer from the macroloading effect[1,2,3] which causes the vertical PR ER to increase as the exposed $Hg_{1-x}Cd_xTe$ area increases. Since the selectivity of $Hg_{1-x}Cd_xTe$ to PR is low for our process[4], this prevents us from etching deep trenches without etching through the PR. Also, since the lateral PR ER is large and the etched trenches are deep, the X,Y mesa dimensions of the pixel are substantially reduced which is not conducive for subsequent downstream processes. Although there are a few different ways of addressing this problem[5-9], unfortunately, none of these solutions work for us. A simple

method would be to just increase the thickness of the PR. Results from such an experiment are described here. It is seen that the lateral PR ER decreased with increased PR thickness while the $Hg_{1-x}Cd_xTe$ ER did not change with PR thickness. Moreover, substantial PR was left on the wafer post etch which allowed for deeper trenches. Also, the trench sidewall angle was seen to vary with PR thickness.

EXPERIMENTAL

Three 6" and one 4" Si wafers with LWIR MBE $Hg_{1-x}Cd_xTe$ grown on them were acquired. One 6" wafer was coated with 11.3um of PR whereas the rest of the wafers were all coated with the same PR thickness (<6um). All of the wafers were patterned with a standard pattern and developed. All wafers were processed in a similar fashion prior to dry etching and then dry etched in an ICP process chamber using a hydrogen based process gas chemistry. Mesa dimensions were measured using a microscope. A confocal laser microscope was used to measure the trench depths. A nanoscope was used to measure the PR thickness.

RESULTS AND DISCUSSIONS

As can be seen from figure 1, the mesa top dimension loss for the wafer with the thicker PR is significantly less than for the other three wafers with the thinner PR implying that the thicker PR wafer has the slowest lateral PR ER[10]. The thicker PR wafer had >7um of PR remaining after the dry etch (as compared to the other 3 wafers which had less than 2um of PR remaining after the dry etch) which allows for more process margin. Thus, the thicker PR wafer allows us the option of wet etching the wafer after the dry etch while allowing for enough mesa top area for downstream processes. It would also allow for dry etching deeper trenches for the next

generation of IR detectors. Also, from figure 1, it appears that the $Hg_{1-x}Cd_xTe$ ER is independent of the PR thickness. Figure 2 shows a Focused Ion Beam/Scanning Electron Microscopy (FIB/SEM) for the 6" wafer with the 6" pattern with 11.3um of PR whereas figure 3 shows a FIB/SEM for the 6" wafer with the 6" pattern with PR<6um. The trench sidewall angle is much steeper with 1 slope for the wafer with the thicker PR as compared to the wafer with the thinner PR which has a shallower angle with 2 slopes. This leads to the possibility of creating tailor made trench sidewalls. Less dry etch induced damage on the thicker PR wafer is expected[4,9].

CONCLUSIONS

A simple and easy to implement method to etch deep trenches with reduced lateral PR ER in a 6" MBE/Si $Hg_{1-x}Cd_xTe$ wafer is described. Increased PR thickness allows for more mesa top area post dry etch, allows for the creation of tailor made trench sidewalls and allows for the use of wet etch at the end of the dry etch to reduce/remove any damage caused by the dry etch.

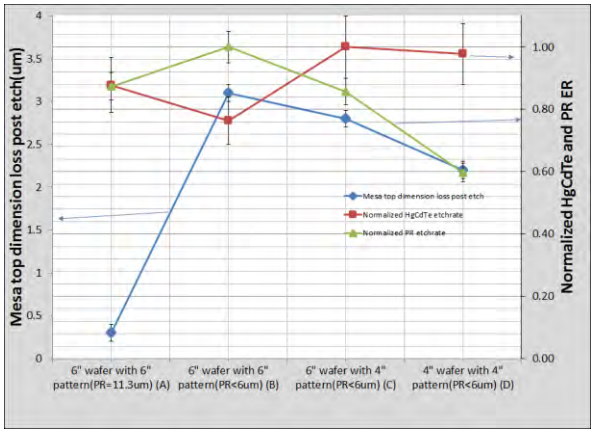

Figure 1

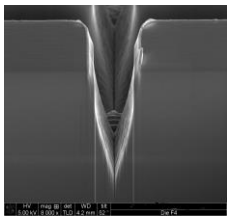

Figure 2

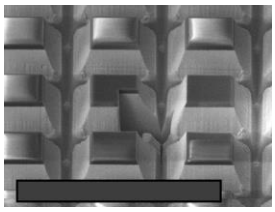

Figure 3

ACKNOWLEDGEMENTS

The authors would like to acknowledge and thank Night Vision and Electronic Sensors Directorate (NVESD) for the use of data and FIB/SEM for this paper.

REFERENCES

1. Stoltz et al., Journal of Electronic Materials, Vol 33, No.6, 2004
2. Apte et al., Journal of Electronic Materials, Vol. 45, No. 9, 2016
3. C.J.Mogab, Journal of Electrochemical Society : Solid State Science and Technology, Vol 124, No. 8, August 1977
4. Wenting et al., Proceedings of SPIE, Vol. 7658, 76584A-2
5. Stoltz et al., Journal of Electronic Materials, Vol. 39, No.7, 2010
6. Stoltz et al., Journal of Electronic Materials, Vol. 36, No. 8, 2007
7. Stoltz et al., Journal of Electronic Materials, Vol. 31, No. 7, 2002
8. Ye et al., Proceedings of SPIE, Vol. 8353, 83532T-2
9. Ye et al., Journal of Electronic Materials, Vol. 40, No. 8, 2011
10. Benson et al., Journal of electronic Materials, Vol. 32, No. 7, 2003

DEFECT- AND CHEMICAL-INDUCED TUNING OF EXCITON–PHONON COUPLING IN BULK AND THIN FILM ZnTe FOR OPTICALLY DRIVEN SENSOR APPLICATIONS

Jason K. Marmon[1-2], Yuanping Chen[3], Priyalal S. Wijewarnasuriya[3], Tao Sheng[4], Haitao Zhang[5], and Yong Zhang[1-2,*]

[1]Nanoscale Science Program, [2]Department of Electrical and Computer Engineering, University of North Carolina at Charlotte, Charlotte, NC 28223, USA. [3]U.S. Army Research Laboratory, Adelphi, MD 20783, USA. [4]Optical Science and Engineering Program, [5]Department of Mechanical Engineering and Engineering Science, University of North Carolina at Charlotte, Charlotte, NC 28223, USA. *yong.zhang@uncc.edu

Abstract: Continuous–wave, resonant Raman spectroscopy is used to accurately probe extrinsic and intrinsic contributions to electron–phonon coupling (EPC) in bulk and thin film ZnTe. ZnTe's I_{2LO}/I_{1LO}, a common measure of EPC, is very sensitive to the material's defect concentration, thermal perturbation, and chemical environment, and remarkably, were altered by up to an order of magnitude. These findings enable development of novel, dynamically tunable, optoelectronic applications and devices.

Keywords: tunable electron–phonon coupling strength, Huang–Rhys factor, bulk and thin film ZnTe, resonant Raman spectroscopy, optoelectronic sensor

Introduction

Defects and impurities can significantly modify electron–phonon coupling (EPC) in a semiconductor[1-4]. Therefore, it is important to be able to accurately measure the EPC strength and ultimately control it for both fundamental understanding and application. When ZnTe is optically excited with light near resonance to its fundamental bandgap, it typically exhibits multiple–order, resonant Raman peaks at nLO frequencies, with n =1, 2, … The intensity ratio of the second to first order Raman peaks, $R = I_{2LO}/I_{1LO}$, is often used as an indicator for EPC strength, because it is generally believed to be proportional to the Huang–Rhys factor[5] that describes the relative lattice relaxation between the excited and ground states due to EPC. Despite the correlation of the two quantities is far complicated than normally thought to be, the ratio R can nevertheless be used as

a convenient indicator for EPC. The I_{2LO}/I_{1LO} values are not only very sensitive to the material's defect concentration, but that they can be dynamically tuned through thermal perturbation and the chemical environment.

Tunable Electron–phonon Coupling Strength

Varying bulk ZnTe's defect concentration represents a static method for altering the I_{2LO}/I_{1LO}, while changing the chemical environment offers a dynamic route with the latter offering about an order of magnitude change. Figure 1A–B plots bulk photoluminescence (PL) and Raman spectra for high quality bulk material (B1), increasing defect concentrations (B2 and B3), and for ~2.5% cadmium impurities (B4). In bulk material, the presence of defects not only quenches the PL but they also increase the intensity of the 1LO relative to the 2LO. Figures 1C plot the I_{2LO}/I_{1LO} values as a function of each sample's stoichiometric ratio, which were obtained from energy dispersive x–ray measurements. As examples, bulk I_{2LO}/I_{1LO} values changed from 7.7±0.6 (B1) to 2.0±0.2 (B3) as the stoichiometric ratio went from near unity to 0.94 (Zn:Te). Defect concentration and the presence of impurities significantly altered the coupling strength.

Figure 2 is the equivalent for four of eight thin film samples. The thin films are numbered from TF1 to TF3 in order of increasing coupling strength, which does not correlate with the PL intensity in Figure 2A, while the vertically offset Raman spectra show a modest change in LO intensities. These samples were grown by varying the nucleation temperature while the growth or substrate temperature was held constant at 300ºC (wine circles), while sample TF4 represents three other samples where the growth temperature was varied while the nucleation temperature was held constant at 300ºC (dark cyan circles). Figure 2C plots the coupling strength as a function of nucleation or growth temperature as thin films did not display a strong dependence on stoichiometry. As examples, the thin film I_{2LO}/I_{1LO} values changed from 7.5±0.7 to 8.4±1.2 as the

x-ray diffraction full width at half maximum increased from 74.0º to 86.0º (with corresponding stoichiometric ratios of 0.96 and 0.94, which respectively show the relatively smaller defect concentration range than in the bulk samples).

PL and Raman spectra were measured for high quality bulk ZnTe before and after methanol exposure (Figures 3A–B respectively), which: (1) quenched PL emission (without inducing a peak energy shift); (2) blue-shifted the first three LO peak (e.g., the 1LO by 0.4 cm^{-1}, 2LO and 3LO by 1.2 cm^{-1}); and (3) the I_{2LO}/I_{1LO} was drastically reduced from 9.6 to 1.9 (using a different sample than in Figure 1), while the higher order ratios experienced negligible change. These findings highlight the ability to tune EPC strengths at material interfaces and surfaces, which have tangible applications in, for instance, optical bar code and sensor applications respectively.

Figures

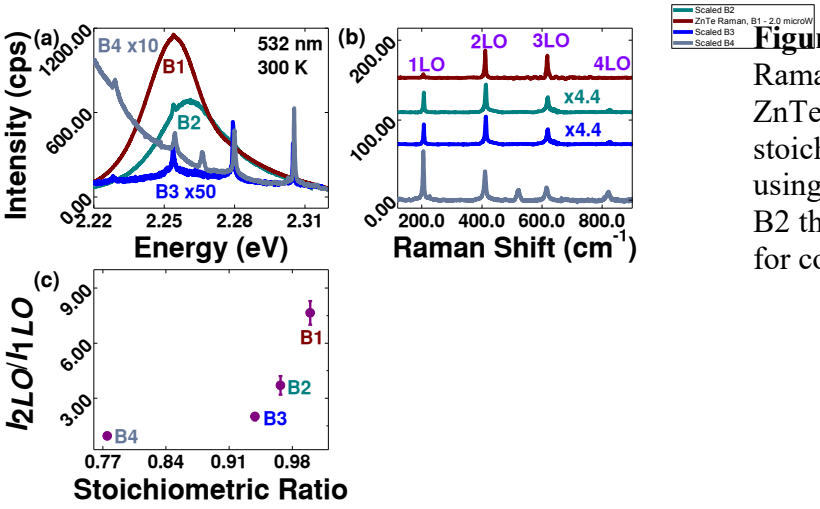

Figure 1 (a–b) Photoluminescence and Raman spectra of representative bulk ZnTe samples. **(c)** ZnTe's stoichiometric dependence on I_{2LO}/I_{1LO} using 1.62–2.26 μW (although samples B2 through B4 were scaled to 2.00 μW for comparison with B1).

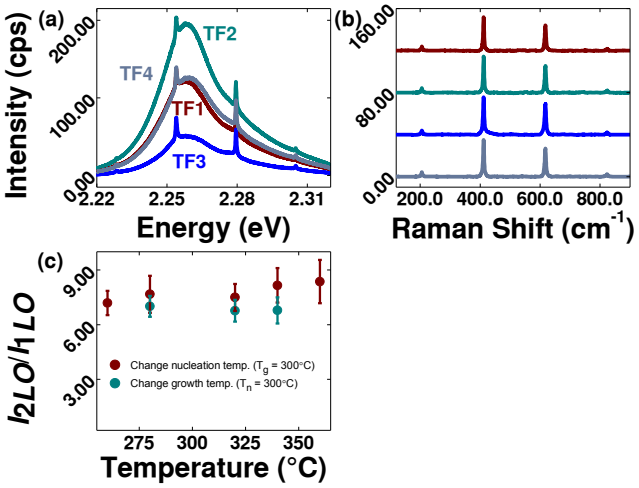

Figure 2 (a–b) Photoluminescence and Raman spectra of representative ZnTe thin film samples. **(c)** ZnTe's stoichiometric dependence on I_{2LO}/I_{1LO} using 2.06 μW (but scaled to 2.00 μW for comparison with B1). **(d)** Thin film I_{2LO}/I_{1LO} when the nucleation temperature (wine) or growth temperature (dark cyan) was varied while the other temperature parameter was held constant at 300ºC.

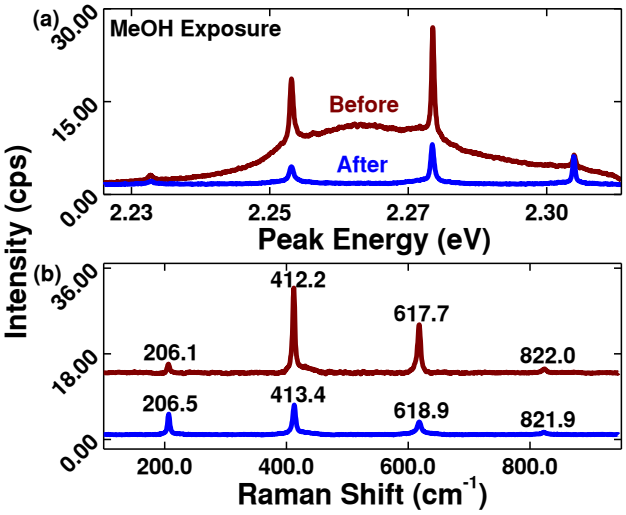

Figure 3 Impact of methanol exposure on EPC strength. **(a)** PL and **(b)** Raman spectra before and after exposing high quality bulk ZnTe to methanol (2.31 μW).

References

1 Mazurczyk, V. J. F., H.Y. Effects of optical phonons in the impurity photoconductivity of ZnTe. *Physics Letters* **26A**, 220-221 (1968).

2 Rashba, E. I. Optical spectra of phonons bound to impurity centers. *Zhurnal Eksperimentalnoi I Teoreticheskoi Fiziki* **71**, 319-329 (1976).

3 Gogolin, A. A. & Rashba, E. I. Mechanism of strong resonant 1LO Raman scattering. *Solid State Communications* **19**, 1177-1179, doi:10.1016/0038-1098(76)90813-9 (1976).

4 Permogorov, S. in *Excitons* (eds E.I.; Rashba & M.D.; Struge) 177-203 (North Holland Publishing Company, 1982).

5 Huang, K. & Rhys, A. Theory of light absorption and non-radiative transistions in F-centers. *Proceedings of the Royal Society of London Series a-Mathematical and Physical Sciences* **204**, 406-423, doi:10.1098/rspa.1950.0184 (1950).

Optical, structural and electrical characterization of $Cd_{1-x}Zn_xTe$ thin films deposited by thermal evaporation

Z. Ali[1*], M. Ashraf[1], M. Ali[2], S. Ahmed[2]

[1]*Optics Laboratories, P.O. Box 1021, Islamabad, Pakistan*

[2]*Advanced Electronics Laboratories, International Islamic University, Islamabad, Pakistan*

Zulfiqar1965@yahoo.com

Abstract: High quality polycrystalline $Cd_{1-x}Zn_xTe$ (CZT) thin films with compositions (x = 0, 0.25, 0.5, 0.75, 1) were deposited on glass substrates by thermal evaporation technique. Optical, structural and electrical properties of CZT films were investigated as a function of Zn content. The X-ray diffraction (XRD) results showed that CZT films are polycrystalline in nature with predominant diffraction lines corresponding to (111) plane. Composition has been determined by using SEM. A straight-forward analysis proposed by Swanepoel has been applied to derive the optical constants and the film thickness. It was found that the refractive indices of films increases with the increase of Zn content into the films. Direct optical band gaps were observed and the band gap varied with Zn content from 1.50 to 1.85 eV. Detailed electrical characterizations such as, I-V, C-V, Temperature-varied Hall Effect measurements, Charge based Deep Level Transient Spectroscopy (Q-DLTS) and Photo Stimulated Internal Field Transient Spectroscopy (PIFTS) were performed to study and evaluate the potential of carrier dynamics for versatile applications. It was observed that as the Zn content increased in the matrix, the resistivity of the deposited thin films decreased. The results reported in this paper suggest that the optical properties, lattice constant, resistivity, carrier dynamics and photo-response of CZT films can be tailored for a specific application by selecting suitable Zn content.

Keywords: $Cd_{1-x}Zn_xTe$ thin film, Thermal evaporation, Optical constants, Electrical resistivity, Hall Effect, Q-DLTS, PIFTS.

1. INTRODUCTION

$Cd_{1-x}Zn_xTe$ (CZT) is one of the most promising II – VI ternary material for wide range of applications in optoelectronic devices, gamma- ray and X-ray detectors[1-3]. The CZT thin films are also good candidates for high efficiency tandem solar cell because of band gap variation from 1.45 eV (CdTe) to 2.26 eV [4]. The growth of CZT by thin film technology is simple and cost effective process as compared to single crystal growth techniques[5-8]. Previously, CZT thin films have been grown by variety of techniques which includes chemical vapor deposition[9], sputtering [10], closed space sublimation[1], molecular beam epitaxy[11] metal-organic chemical vapor deposition[12], electrodeposition[13] and thermal evaporation[11]. Thermal evaporation is relatively simple,

cost-effective and films on large sizes of substrates can be grown. It is reported in the literature that the optical properties of thin films can be tailored with the variation of composition[14,15]. The properties of thin films also depend on the deposition parameters such as preconditions, substrate temperature, evaporation rate etc[16]. Therefore, in this study, we have deposited CZT thin films by some carefully optimized parameters using thermal evaporation technique. We have also systematically investigated the effect of Zinc content ($0 \leq x \leq 1$) on the physical properties of CZT thin films for diverse device applications in perspective.

2. EXPERIMENTAL SETUP

The $Cd_{1-x}Zn_xTe$ ($0 \leq x \leq 1$) target material was prepared by mixing CdTe and ZnTe (99.99%) in pure powdered form with different concentration (x = 0.00, 0.25, 0.50, 0.75, 1.00). The desired material for various values of 'x' was prepared as: Weight of CdTe = *(112.41+127.60) × (1-x) gm = (240.01) (1-x) gm*, and Weight of ZnTe= *(65.39+127.60) × 'x' gm = (192.99) × 'x' gm*. Resistive heating was used during the thermal evaporation to deposit the desired thin films. The vacuum coating system for preparing these films was Edward 610 with vacuum better than 1×10^{-5} mbar maintained in the chamber. Pre-deposition heating of substrate at 200 ^{o}C for 10 minutes was done in order to degas the samples. Film thickness and deposition rate (~0.50 nm/s) was monitored by quartz crystal thickness monitor FTM7. Five sets of films were deposited with different compositions in five independent runs. The structure of CZT films was determined by X-ray diffraction (XRD) at room temperature by Bruker D8 diffractometer using CuK_{α} radiation in the scanning mode. The Transmittance of deposited films was measured in the range of 500 – 1500 nm using Perkin Elmer Lambda 19 UV/VIS/NIR spectrophotometer. Rapid Thermal Annealing of the selected samples was carried for 60s dwell in the temperature ranges 100-400 ^{o}C. Hall measurements were performed using SWIN Hall Effect system with 1 mA electric current, 5300 G magnetic field and 1 cm^2 of the sample cross sectional area. ASMEC was utilized for the Charge-Deep Level Transient Spectroscopy (Q-DLTS) for detailed electrical characterization of the samples performed at 2.5 V forward bias pulses.

3. RESULTS AND DISCUSSION

The XRD spectra of CZT films revealed that the films are polycrystalline in nature with preferred orientation along (111) together with other planes (220) and (311) in very minute quantity[17]. It has been reported that CdTe and ZnTe films grown by thermal evaporation are mostly cubic[17]. Our deposited films are also cubic Zincblende[18,19]. We observe a linear variation of lattice constant with the increase of Zn content into the films. This shows that our results are within good agreement with Vegard's law. The transmission of films increases

with the increase of Zn content. Our results show that the refractive indices of the deposited films increase with the increase of Zn content. As the value of Zn content increases, the band gap of films increases. This variation of band gap is due the difference in band gaps of ZnTe (2.26 eV) and that of CdTe (1.5eV)[20,21]. It is observed that the band gap of $Cd_{1-x}Zn_xTe$ films lies in the range 1.5–1.85 eV (Figures will be included in the paper).

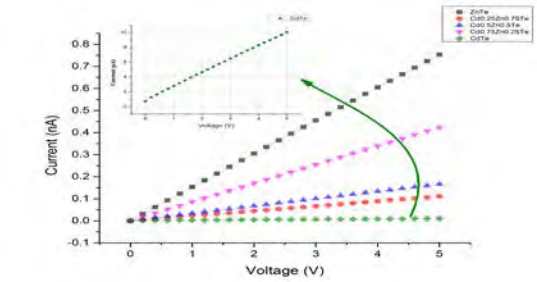

Figure 1: I-V curves for $Cd_{1-x}Zn_xTe$Thin films.

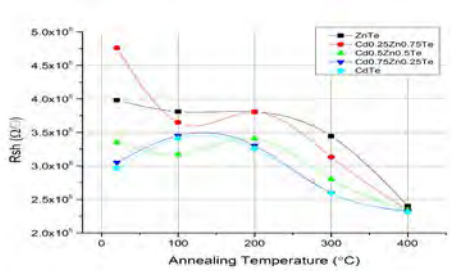

Figure 2: Sheet Resistance for $Cd_{1-x}Zn_xTe$Thin films.

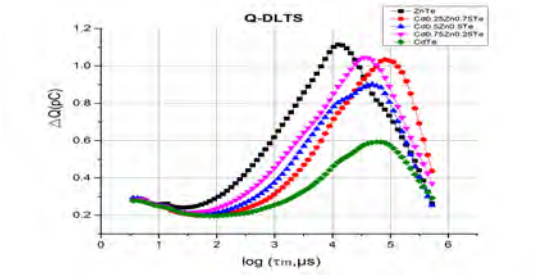

Figure 3: Q-DLTS spectra for $Cd_{1-x}Zn_xTe$Thin films.

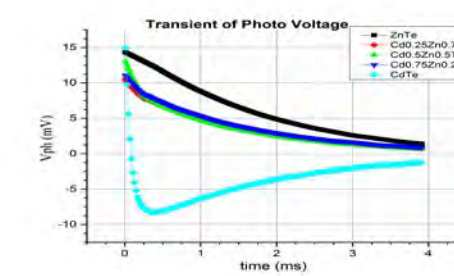

Figure 4: PIETS spectra for Cd$_{1-x}$Zn$_x$TeThin films

Fig. 1 shows the current-voltage[22] (I-V) characteristics of as-deposited $Cd_{1-x}Zn_xTe$ samples. ZnTe shows a maximum conductivity whereas CdTe shows the minimum conductivity. It is observed that by decreasing Zn and Increasing Cd content into the matrix, conductivity of the deposited samples increases. Magnitude of electric current (<1nA to few pA) and profile (shape of the curve) as a function of applied bias provides an insight to the formation of almost uniformly doped films using the optimized parameters during the thermal evaporation process. Evolution of Sheet resistance as a function of post-deposited annealing temperatures is presented in Fig. 2 which provides a hint on the presence of possible defect (trap) centers in the deposited matrix. Q-DLTS, a charge relaxation technique based on the measurements of transients of trapped charges upon the specific electric field[23], is also suitable for detecting small concentration of impurities and defects and to measure their properties. Measured spectra between rate window 'τ' and the change of charge value ΔQ, at an applied voltage of 2.5V is shown in Fig. 3. Rate window 'τ' is actually; $\tau = t_1(\alpha-1)/\ln(\alpha)$, where $\alpha = t_2/t_1 = 2$ and

t_1,t_2 are the periods from the beginning of the discharge. Maximum of the measured charge "ΔQ_{max}" is located at "τ_{max}" and $\tau_{max} = 1/e$; and '*e*' is the emission rate. Thus the emission rates of samples with distinct (or no) doping can be observed directly by glancing 'ΔQ' vs 'τ' spectra (Fig. 3), relevant to the efficiency of prospective optoelectronic/solar devices. Photo stimulated internal field transient spectroscopy (PIFTS) uses kinetics of photo voltages and photo current. In this technique carriers are generated only by a very short and sharp pulse of light onto the sample and then decay of the carriers are observed with the function of time. PIFTS spectra for $Cd_{1-x}Zn_xTe$ samples are shown in Fig. 4. Compared to the other samples, it is observed that CdTe contains sufficient amount of charge carriers which can easily be energized with a rather little energy flux of the incident light.

4. REFERENCES

[1] J. Huang, L. J. Wang, K. Tang, Run Xu, J. J. Zhang, Y. B. Xia and X. G. Lu, Physics Procedia **32**, 161 (2012).
[2] G. N. Panin, C. Diaz-Guerra and J. Piqueras, Semicond. Sci. Technol. **13**, 576 (1998).
[3] Y. Eisen, A. Shor and I. Mardor, IEEE Trans. Nucl. Sci. **51,** (2004) 1191.
[4] A. Arbaoui, A. Outzourhit, N. Achargui, L. Bellakhder, H. E. Ameziane, and J. C. Bernede, Solar Energy Materials and Solar Cells, Elsevier **90**, 1364 (2006).
[5] T. J. Coutts, K. Emery and J.S. Ward, Prog Photovolt: Res Appl. **10**, 195 (2002).
[6] M. Dammak, S. Alaya, A. Zerrai, G. Bremond and R. Triboulet, Semicond. Sci. Technol., 13 (1998) 762.
[7] J. S. Kwon, D. Y. Shin, I. S. Choi, H. S. Kim, K. H. Kim, S. U. Kim and M. J. Park, Phys. Stat. Sol. B **229**, 1097 (2002).
[8] K. H. Kim, Y. H. Na, Y. J. Park, T. R. Jung, S. U. Kim and J. K. Hong, IEEE Trans. Nucl. Sci. **51**, 3094 (2004).
[9] M. Sridharan, M. Mekaladevi, S. Narayandass, D. Mangalaraj and H. C. Lee, Cryst Res Technol. **39**, 328 (2004).
[10] T. L. Chu, S. S. Chu and C. Ferekides, J. Britt, J. Appl. Phys. **71**, 5635 (1992).
[11] J. H. Dinan and S. B. Qadri, J. Vac. Sci. Technol. A **3**, 851 (1985).
[12] K. H. Kim, Y. H. Na, Y. J. Park, T. R. Jung, S. U. Kim and J. K. Hong, IEEE Trans. Nucl. Sci. **51**, 3094 (2004).
[13] M. Basol, V. K. Kapur and M. L. Ferris, J. Appl. Phys. **66**, 1816 (1989).
[14] M. Ashraf, S.M.J. Akhtar, M. Mehmood and A. Qayyum, Eur. Phys. J. Appl. Phys. **48**, 10501 (2009).
[15] M. Ashraf, S.M.J. Akhtar and A. Qayyum, Materials Science in Semiconductor Processing 15 (2012) 251.
[16] G.G. Rusu, M. Rusu, M. Girtan, Vacuum **81**, 1476 (2007).
[17] R. G. Solanki, Indian Journal of Pure & Applied Physics **48**, 133 (2010).
[18] H. S. Soliman, F. M. Allam, A. A. El- Shazly, Journal of Material Science: Material in Electronics **7**, 233 (1996).
[19] S. M. Johnson, S. Sen, W. H. Konkel and M. H. Kalisher, Journal of Vacuum Science and Technology B **9**, 1897 (1991).
[20] Umeshkumar P. Khairnar, Sulakshana S. Behere, Panjabrao H. Pawar, Journal of Surface Engineered Materials and Advanced Technology **1**, 51 (2011).
[21] A. Rohatgi, S. A. Ringel, R. Sudharsanan, P. V. Meyears, C. H. Liu and V. Ramanathan, Solar Cells **27**, 219 (1989).
[22] Kerr, Lei L., Sheng S. Li, S. W. Johnston, T. J. Anderson, O. D. Crisalle, W. K. Kim, J. Abushama, and R. N. Noufi, Solid-State Electronics **48**, 1579 (2004).
[23] Rothenberger, Jason B., Daniel E. Montenegro, Mark A. Prelas, Tushar K. Ghosh, Robert V. Tompson, and Sudarshan K. Loyalka, Journal of Materials Research **27**, 1198 (2012).

Characterization of thermally treated MgZnO nanowire alloys synthesized by vapor-transport technique for deep UV detection

Authors: Ebraheem Ali Azhar, Jignesh Vanjaria, Seungho Ahn, Tom Salagaj, Nick Sbrockey, Gary Tompa, Hongbin Yu

Alloying Mg with ZnO has been described as a way toward engineering the bandgap of MgZnO to as high as a 5.8 eV for various electronic and optoelectronic applications, including solar blind detectors for communication systems. Mg-ZnO alloy systems have also shown to phase segregate for large Mg content. These factors, enhanced optical combined have made nanostructred MgZnO a promising solution for achieving the stated goals of such alloyed systems. In this study, MgZnO nanowires were synthesized via a high temperature vapor transport technique, in which Mg was incorporated by the tandem disassociation of Mg_3N_2 powder, along with ZnO powder in the same reaction tube furnace. These structures were grown on a Si substrate with a thin, sputtered ZnO seed to catalyze growth. The resulting nanowires were highly ordered and tended toward vertical orientation [1,2]. The nanowire arrays were then subject to a combination of annealing conditions, varying temperature and ambient gas environments. Scanning electron microscopy, as well as EDX mapping confirmed the presence of Mg clustered formations along the ZnO nanowires. Photoluminescence measurements revealed the presence of a small tail peak at a higher energy than the band edge of ZnO. Additionally, it was found that the peaks consistent with the 1LO and 2LO (longitudinal optical) phonon modes had blue-shifted from approximately 585 cm-1 to 605 cm-1 averaged across several positions among the samples. These results indicate a greater composition and better registration of Mg in the ZnO nanowire lattice, as compared to the unnannealed case [3]. Additional electrical and optoelectronic measurements were conducted, and enhanced conduction in the presence of UV light was confirmed. The relative photodetection metrics (responsivity, photoconductive gain, detectivity, noise equivilant product) were also compared in all cases.

References

[1]H. Yu, E. A. Azhar, T. Belagodu, S. Lim, and S. Dey, “ZnO nanowire based visible-transparent ultraviolet detectors on polymer substrates,” Journal of Applied Physics, vol. 111, no. 10, p. 102806, May 2012.

[2]T. Belagodu, E. A. Azhar, and H. Yu, “Modulation of charge conduction in ZnO nanowires through selective surface molecular functionalization,” Nanoscale, vol. 4, no. 23, pp. 7330–7333, Nov. 2012.

[3]J. Huso, H. Che, D. Thapa, A. Canul, M. D. McCluskey, and L. Bergman, “Phonon dynamics and Urbach energy studies of MgZnO alloys,” Journal of Applied Physics, vol. 117, no. 12, p. 125702, Mar. 2015.

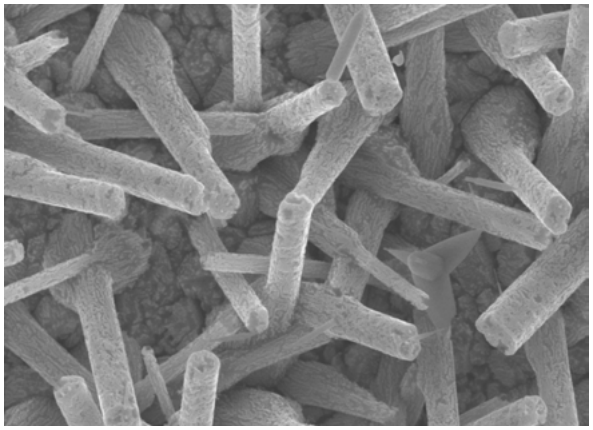

Fig. 1. SEM Micrograph of as-grown wires inset: zoomed view of single wire

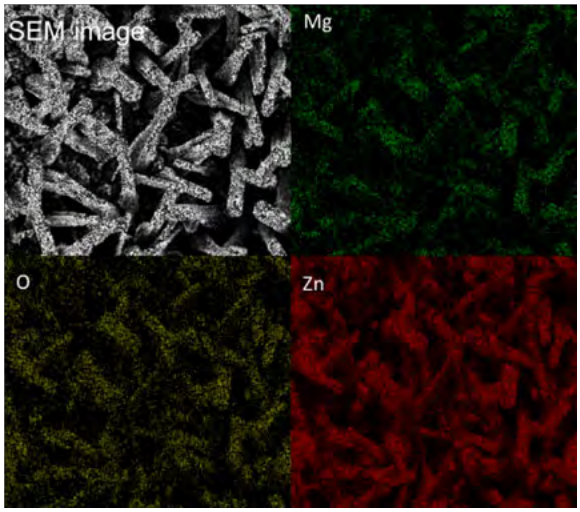

Fig. 2. EDX Map revealing presence of Mg on wire surface

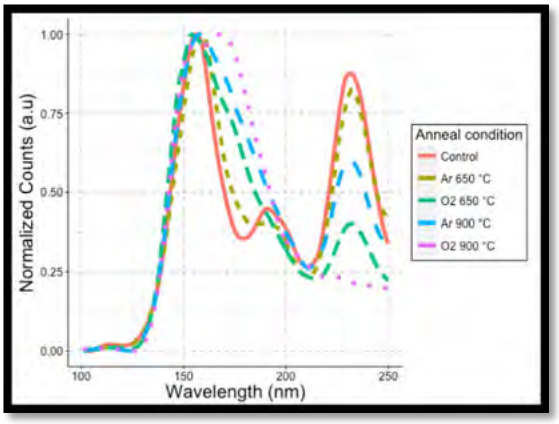

Fig. 3. Cathodoluminesence of MgZnO wires showing deep UV emission.

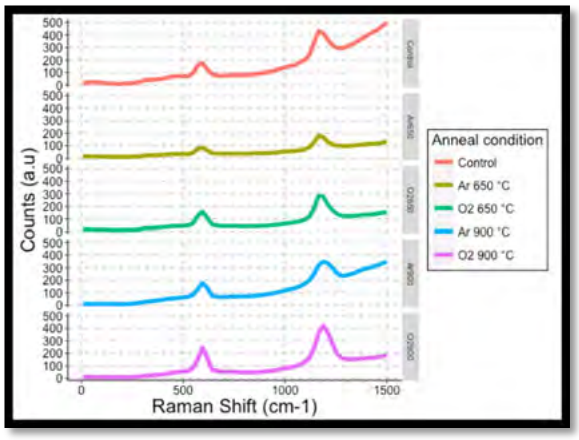

Fig. 4. Resonant Raman scattering measurement indicating the presence of MgZnO with various composition under different annealing

Micro-diffraction investigation of localized strain in mesa-etched HgCdTe photodiodes

A. Tuaz[1], P. Ballet[1], X. Biquard[2], F. Rieutord[2]
[1]Univ. Grenoble Alpes, CEA, LETI, MINATEC campus, F38054 Grenoble, France
[2]Univ. Grenoble Alpes, CEA, INAC-SP2M, NRS, 17 rue des Martyrs, 38000 Grenoble, France
aymeric.tuaz@cea.fr
Student paper, advisors: P. Ballet and X. Biquard

Abstract: We present an X-ray diffraction investigation of localized strain and lattice disorientation in HgCdTe layers with a submicronic resolution using a synchrotron white beam in Laue configuration. Diffraction peak displacement mapping evidences bending of the crystal planes around mesa-etched photodiodes, with strong dependence upon the processing steps.

Keywords: HgCdTe, Micro-diffraction, Strain, Orientation tilt

Introduction:

Within the general goal of reaching high operating temperature while maintaining strong requirements on IR photodetector performance, the pressure on HgCdTe material quality is increasingly growing. In particular, careful attention is now being paid to strain and strain relaxation within HgCdTe photodiodes. While recent studies [1, 2] have focused on the lattice mismatch induced strain over areas in the order of the wafer, no experimental investigation has been able to resolve the strain at the micrometer level. Processing steps such as etching or passivation effects on strain generation and lattice relaxation need to be investigated to guarantee optimal material quality throughout the detector fabrication process.

The resolution scale restriction can be solved using a focused synchrotron X-ray white beam. Indeed, by performing Laue diffraction measurements we can access micrometer scale mapping of both the local deviatoric strain as well as the local lattice orientation [3, 4].

Experimental procedure:

In this work, we develop experimental access to strain and lattice disorientation of our layers with a submicronic resolution thanks to the micro-diffraction setup of the French beamline BM32 at the European Synchrotron Radiation Facility [5]. We have conducted Laue experiments with a ø300nm white beam probe: the spot contains all energies in the 5-23keV range, a CCD camera placed above the sample simultaneously intercepts all diffraction peaks for each point of the mapping. From the displacement of these peaks, we are able to map both strain and lattice orientation tilt inside an etched photodiode, with emphasis on the neighborhood of the etching.

The samples consist in an $Hg_{1-x}Cd_xTe$ layer, with 30% cadmium fraction, deposited on a CdZnTe substrate either by molecular beam epitaxy, [211] orientation, or liquid phase epitaxy, [111] orientation. Given

the varying thickness of our HgCdTe layers between 5 and 6.5µm, the etching depth is adjusted to always have a 2.5µm thick layer below the etched area. In order to provide exploitable measurements, the samples were designed taking account the penetration length of the beam which goes from 20 to 150µm, depending on the energy and the material (HgCdTe layer or CdZnTe substrate). Trenches of several millimeter long have been etched, using an ion beam, to ensure that we are not biased by this phenomenon. The samples are then passivated using two different parameters leading to a hard and a soft passivation. Half of the samples are annealed to look at the respective effect of processing steps on strain. Samples are finally cleaved perpendicularly to the trenches, to allow for a cross-section micro-diffraction mapping (see figure 1).

Results:

The study of the diffraction peak displacement, perpendicular to the trench, reveals the same pattern for all samples: the edges of the trenches are tilted. Indeed, average diffraction peak position indicates an orientation tilt of the lattice in the few microns around the etching (see figure 2 and 3). This tilt is at its maximum at the top edge of the trench, and an inversion seems to occur at the bottom edge. Furthermore, this observation seems to very much depend on process parameters. The passivation itself leads to various values of tilt (see figure 2.a and 2.c). The sample of figure 2.a represents the process resulting in a hard passivation, and the soft one is shown on figure 2.c. The deformation pattern is similar but the value of the tilt is stronger in the first case. As expected, it is found that the annealing tends to reduce the overall strain in the layer (compare figures 2.a and 2.b, as well as 2.c and 2.d). The opposite behavior of the positive displacement at the bottom edge in figure 2.d is not understood yet. And even after annealing, we still observe a difference between the hard and soft passivation.

In either case, the maximum tilt remains below 170 arcsecs. Comparing this to the 50 arcsecs full width at half maximum of the diffraction peaks, the order of magnitude is the same. Then the orientation tilt does not result in a plastic deformation.

On the other hand, the sample presented in figure 3 has a distinct behavior. Although we found the same overall shape of the displacement, the values do not match. Using the same scale as before, we may appreciate the evolution far from the top edges. We found a maximum displacement around 1000 arcsecs, which is incoherent with the value of the previous samples. Here, we assume a plastic deformation in the saturated region. If we take a look at the shape of the diffraction peaks in this area (see figure 3.b), we observe the peak breaking-up, which is a clear evidence of a plastic deformation, while the same peak has a normal shape away from the edge (see figure 3.c). Moreover, this huge deformation is propagating down to several microns, even into the substrate.

Thus, the study on the peak displacement highlights the lattice orientation tilt after etching, passivation and annealing. In order to link this tilt to the strain within the layer, we have to take into account the relative peak movement one from another, not an average displacement. Due to the very low values of strain expected (between 3 and 5.10^{-4}) [2], the position measurement of the peaks is critical for the strain mapping. In addition, while the analysis of the displacement in the x axis (perpendicular to the trench) is easily done, in the y axis (along the trench) some phenomenon must be considered that considerably complicate the analysis. In particular, modelling of the penetration length, retro-diffracted peaks contribution and tilt of the sample has been investigated. The strain mapping is still underway.

Figures:

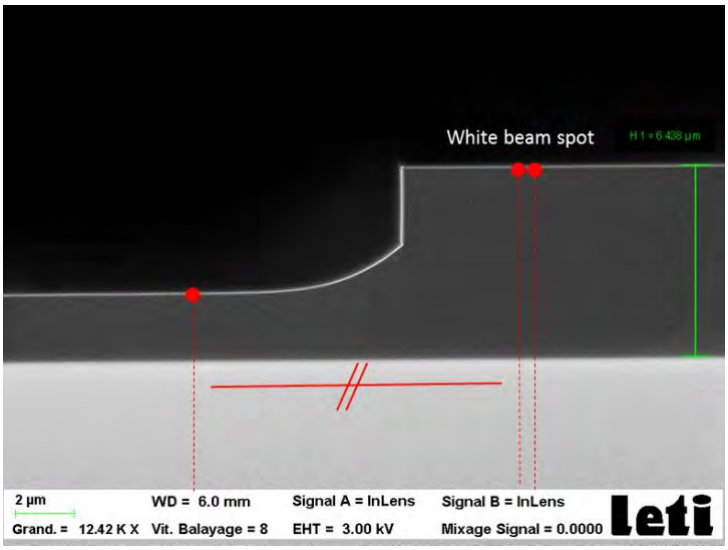

Figure 1: Side view of an etched trench inside a 6.5µm thick HgCdTe layer on a CdZnTe substrate. The red dots represent the size of the X-beam penetrating the sample.

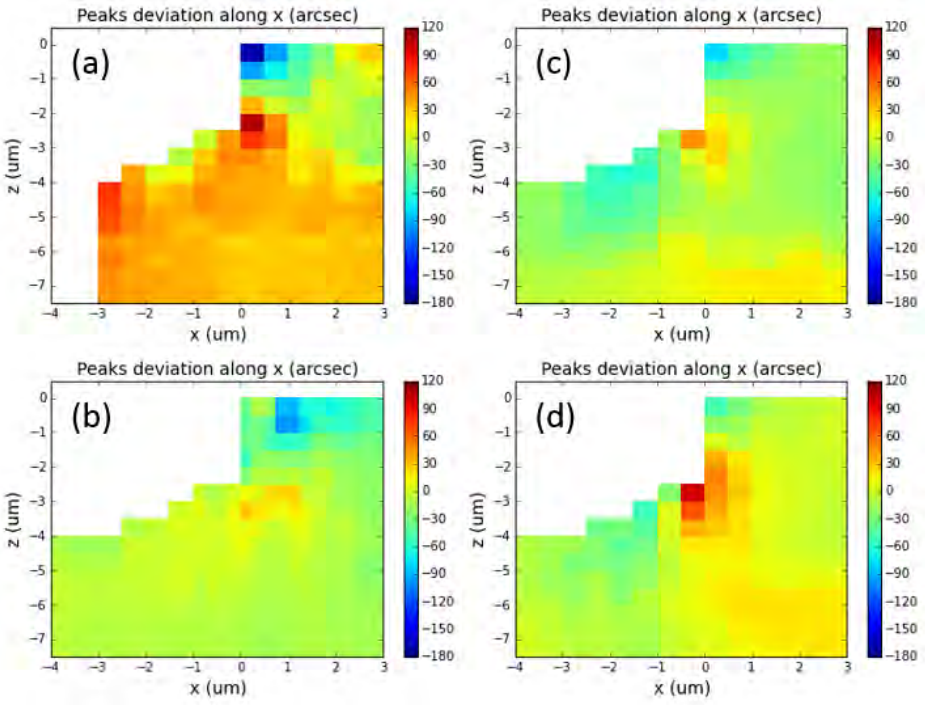

Figure 2: X-section mapping, showing the evolution of the orientation tilt of the material, given by the average lateral displacement of the diffraction peak center. The orientation tilt which is associated to strain is clearly visible all around the etching. The samples have seen different process: hard passivation with (b) or without (a) annealing, and soft passivation with (d) or without (c) annealing.

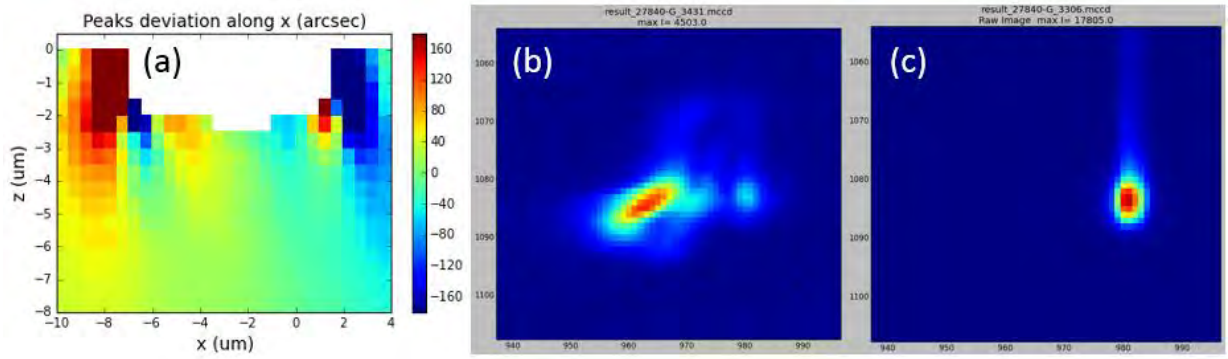

Figure 3: X-section mapping (a), showing the symmetrical effect of the trench. The saturated edges are sign of a plastic relaxation. The shape of the same diffraction peak (b) at the top edge of the trench and (c) 4µm away from the edge is a clear evidence of plastic deformation.

References:

[1] T. Colin, T. Skauli, and S. Lovold, *J. Crystal Growth* 175/176, 670 (1997)
[2] P. Ballet, X. Baudry, B. Polge, D. Brellier, J. Merlin, and P. Gergaud, *J. Electron. Mater.* 42, 3133 (2013)
[3] N. Tamura, A.A. MacDowell, R. Spolenak, B.C. Valek, J.C. Bravman, W.L. Brown, R.S. Celestre, H.A. Padmore, B.V. Batterman, and J.R. Patel, *J. Synchrotron Rad.* 10, 137 (2003)
[4] M. Kunz, K. Chen, N. Tamura, and H.R. Wenk, *Am. Mineral.* 94, 1059 (2009)
[5] O. Ulrich, X. Biquard, P. Bleuet, O. Geaymond, P. Gergaud, J.S. Micha, O. Robach, and F. Rieutord, *Rev. Sci. Instrum.* 82, 033908 (2011)

Temperature and injection dependence of Photo Luminescence Decay in MWIR HgCdTe

[1]B.Delacourt, [1]P.Ballet, [1]F.Boulard, [1]A.Ferron, [1]L.Bonnefond, [1]T.Pellerin, [2]A.Kerlain, [2]V.Destefanis, [1]J.Rothman (*)

[1]Univ. Grenoble Alpes, CEA, LETI, MINATEC Campus, F38054 Grenoble, France

[2]SOFRADIR – Development and Production center, Actipole – 364 Route de Valence, CS – 10021 – 38113 Veurey-Voroize, France

(*) corresponding author's e-mail address: johan.rothman@cea.fr

Abstract:

The minority carrier lifetime is a key parameter in semiconductor physics and its value is involved in many devices figures of merit such as the photodiode dark current and the quantum efficiency. To study this carrier recombination kinetics, a Photo Luminescence Decay (PLD) set-up has been developed where the time-resolved signal is measured using a single element large area HgCdTe Avalanche Photo Diode (APD). The high APD gain (M= 20 to 50) and the low noise factor (F=1.2) of the APD increase the sensitivity of the set-up and allow the study of the recombination kinetics in a broad range of signal levels. The three main generation/recombination mechanisms that contribute to the value of the carrier lifetime (Auger, radiative and Shockley-Read-Hall (SRH)) cannot be directly distinguished in a standard low level of non-equilibrium carrier injection experiment. However, the contribution of each mechanism varies differently as a function of the carrier concentration in the sample. These functions are well-known and can be used to discriminate the different contributions. We present a method that allows to estimate the contributions from the different mechanisms to the minority carrier lifetime from the fitting of the temporal variation of the PLD signal at different levels of photo-injections. The usefulness of the method is illustrated by the exploitation of PLD data measured as a function of sample temperature on Mid-Wave InfraRed (MWIR) extrinsic N-type and intrinsic P-type HgCdTe samples. The temperature evolution of the different contributions to the lifetime are compared with experimental and theoretical values reported in the literature.

Keywords: HgCdTe, PLD, lifetime, MWIR, photo-injection, photon recycling

Note: This is a student paper (advisor: J. Rothman).

DIFFUSION MECHANISM FOR ARSENIC IN INTRINSIC AND EXTRINSIC HgCdTe

T. Grenouilloux[1,2(*)], A. Ferron[3], N. Péré-Laperne[1], D. Mathiot[2]

[1] SOFRADIR, Avenue de la Vauve - CS20018, 91127 Palaiseau, France

[2] Laboratoire ICube, Université de Strasbourg and CNRS, 23 rue de Loess, BP 20, 67037 Strasbourg cedex 2, France

[3] Univ. Grenoble Alpes, CEA, LETI, MINATEC Campus, F38054 Grenoble, France

(*) Corresponding author's e-mail address: thomas.grenouilloux@sofradir.com

Extended abstract:

Due to its low diffusivity and high activation rate, arsenic has become the dopant of choice for the p-doped area in the p/n HgCdTe High Operating Temperature (HOT) technology. Its diffusion mechanism, however, remains imprecise. In this work, arsenic diffusion was studied in MBE HgCdTe structures consisting of alternatively As-doped and intrinsic layers grown on a CdZnTe substrate. Annealings were then performed on these samples, and the resulting As concentration profiles were obtained using Secondary Ion Mass Spectroscopy (SIMS) analysis. Anneal temperatures ranged from 350°C to 450°C and anneal times from few minutes to few hours, as it is commonly encountered in the literature. Two different mercury partial pressures (P_{Hg}) and cadmium atomic fraction (x_{Cd}) were studied.

Each anneal was simulated using a 1D finite element software solving the Fick diffusion equation. This allowed us to determine the corresponding arsenic diffusion coefficient (D_{As}) by adjusting the simulated concentration profile to the experiment.

In Figure 1 is shown a typical arsenic concentration profile obtained by a 450°C anneal under high P_{Hg}. First, this profile exhibits two different diffusion regimes: one at high concentration, typically above a few 10^{18}at.cm^{-3}, one at lower concentration. The former is attributed to a delayed diffusion mechanism of inactive arsenic, due to the high arsenic concentration. On the other hand, the latter corresponds to active arsenic diffusion. Both regimes were studied and simulated, as they are co-dependent. However this paper is focusing on the analysis of active arsenic results. Under these thermodynamic conditions, D_{As} was found to vary with arsenic concentration, indicating a Fermi-level effect on the diffusion. Figure 1 displays the evidence of such an effect and shows the arsenic diffusion profile after a 450°C anneal, compared to two simulated profile, with and without the Fermi-level effect on the arsenic diffusion. From this comparison arises the conclusion that there is a Fermi-level effect on arsenic diffusion at 450°C. In these annealing conditions, arsenic is activated as a p-type dopant, which tells us that the point defect assisting the diffusion is a donor. This eliminates the cation vacancy as the diffusion vector, this defect being widely accepted as an acceptor defect in the literature [1][2].

We found that for temperatures lower than 450°C, arsenic diffused in intrinsic conditions, thus its diffusion coefficient was independent on its concentration. D_{As} was observed to increase with decreasing x_{Cd} and P_{Hg}, as found in the literature [3][4][5]. In Figure 2 is shown a comparison of a diffusion profile under high and low P_{Hg}, which demonstrates the greater diffusion at the lower partial pressure.

To conclude on the diffusion mechanism for As, we propose that As exists on both the II (n-type) and the VI (p-type) sublattices, as suggested in [6][7]. The proportions are determined by the thermodynamic conditions of annealing. Chandra et al. [4][5] showed that D_{As} decreases with increasing P_{Hg} with two regimes, which supports this conclusion. Our new data demonstrates the Fermi-level effect on diffusion at 450°C, which leads us to the conclusion that only the Te interstitial

assists the diffusion of As_{VI}, while the diffusion mechanism of As_{II} is still unknown but the cation vacancy remains a strong candidate.

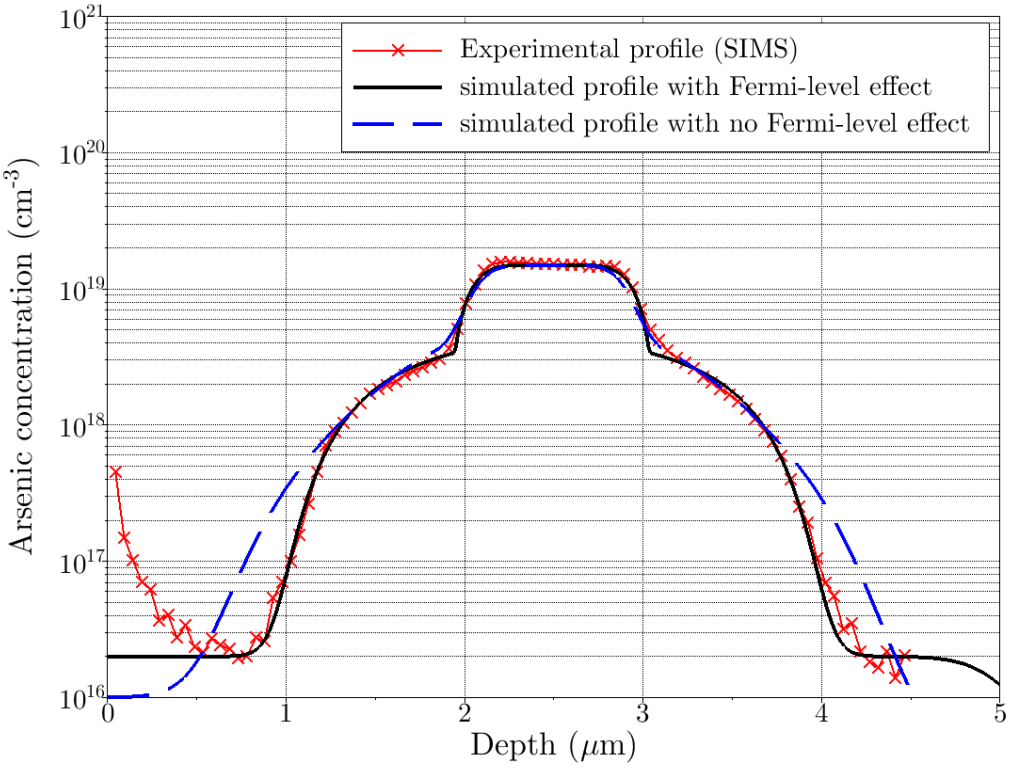

Figure 1 : Concentration profile of arsenic after a 450°C anneal under high P_{Hg} in LWIR HgCdTe. Above a few $10^{18}cm^{-3}$, arsenic diffuses via a retarded diffusion mechanism and is inactive, while at lower concentrations arsenic is active when it diffuses. Comparison with the adjusted simulated profiles taking into account (full line) or not (dashed line) the Fermi-level effect on the arsenic diffusion.

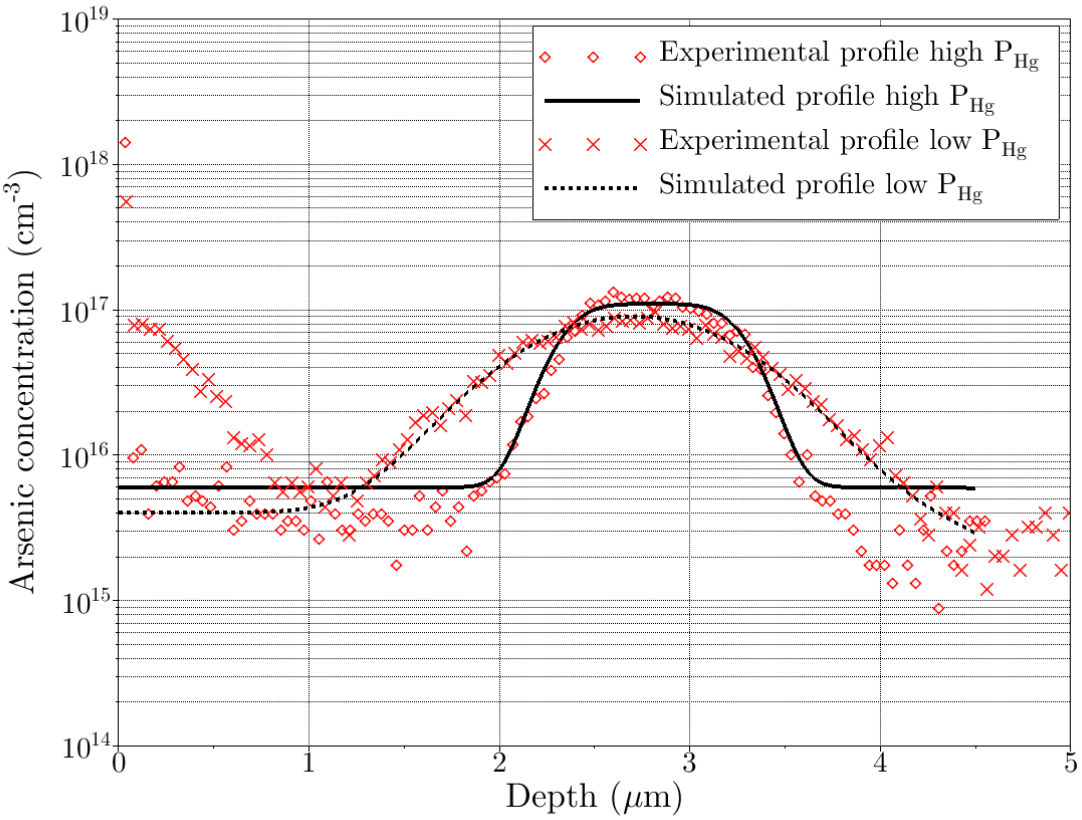

Figure 2 : Concentration profile of arsenic after a 425°C anneal at high (diamonds) and low (crosses) PHg, and their associated simulated diffusion profile (respectively full and dotted line), in MWIR HgCdTe.

References :

[1]. H.G. Robinson, D.H. Mao, B.L. Williams, S. Holander-Gleixner, J.E. Yu and C.R. Helms, *J. Electron. Mater.* **25**, 1336 (1996)

[2]. M.A. Berding, M. Van Schiflgaarde and A. Sher, *Phys. Rev. B* **50**, 1519 (1994)

[3]. A.M. Itsuno, P.Y. Emelie, J.D. Phillips, S; Velicu, C.H. Grein and P.S. Wijewarnasuriya, *J. Electron. Mater.* **39**, 945 (2010)

[4]. D. Chandra, M.W. Goodwin, M.C. Chen and J.A. Dodge, *J. Electron. Mater.* **22**, 1033 (1993)

[5]. D. Chandra, M.W. Goodwin, M.C. Chen and L.K. Magel, *J. Electron. Mater.* **24**, 599 (1995)

[6]. X. Biquard, I. Alliot, P. Ballet, *J. Appl. Phys.* **106**, 103501 (2009)

[7]. P. Capper and D. Shaw, *Proc. Of SPIE* **6294**, 62940M (2006)

Effect of buffer layer on the properties of boron and gallium co-doped ZnO films

Jian Huang, Jin Yang, Lu Yuanxi, Ke Tang, Feng Gu, Yue Shen, Linjun Wang

School of Materials Science and Engineering, Shanghai University, Shanghai 200444, China

Zinc oxide (ZnO) which has a hexagonal wurtzite structure become one of the most important binary II–VI semiconductor compounds because its wide direct band gap of 3.37 eV at room temperature and its large exciton binding energy (~60meV) [1]. In recent years, due to its excellent electrical, optical properties, good adhesion to the substrate, low cost, non-toxicity and stability in hydrogen plasma processes, ZnO-based transparent conducting oxides (TCO) films have been widely studied for application in optoelectronic devices such as microelectronic devices, lasers, light emitting diodes, sensors and solar cells[2-4]. The conductivity of the pure ZnO films can be changed by several orders of magnitude by doping with aluminum (Al)[5], gallium (Ga)[6], boron(B)[7], etc. Among the dopants used for the ZnO TCO films, Ga seems to be one of the most successful and promising candidates because of its ions have a similar ionic radius compared to Zn^{2+}, which should result in only small ZnO lattice deformations even for high Ga concentrations [8]. Furthermore, Ga is less reactive and more resistant to oxidation compared with other impurities [9]. B-doped ZnO, which also get extensively research because it could exhibits higher transparency, higher conductivity and improved thermal stability[10, 11]. Therefore, it is attractive to investigate the properties of B and Ga co-doped ZnO (BGZO) films[12]. The direct growth of doped-ZnO films on substrates, such as glass or Si

may introduce defect and/or large residual stress because of the lattice mismatch and different thermal expansion coefficients, which make the growth of high-quality doped-ZnO films particularly difficult. In this paper, we attempt to grow high-quality boron and gallium co-doped ZnO (BGZO) films with by introducing ZnO buffer layers between BGZO films and substrates. The effects of buffer layer on the properties of BGZO films are investigated in detail.

BGZO films were prepared by using RF magnetron sputtering method with a BGZO ceramic target (98 wt% ZnO with 1.8 wt% Ga_2O_3 and 0.2 wt % B_2O_3, purity 99.99%). Sputtering was performed under an Ar atmosphere with an operating pressure of 6 mTorr. The growth of BGZO films were prepared by a two-step process. Firstly, the ZnO buffer layer with a thickness of 0-50 nm was prepared on quartz glasses substrates at low sputtering power of 60W. Then, BGZO films were deposited with a thickness of 300nm at high sputtering power of 150W on the buffer layers.

In order to investigate the crystalline structure of the BGZO films, XRD patterns were scanned in the 2θ range from $20^o$to 70^o. Fig.1 shows the XRD patterns of BGZO films with different thickness of buffer layers. All the films exhibit hexagonal wurtzite structure and *c*-axis preferential orientation, and no diffraction peaks of B, Ga, Ga_2O_3, B_2O_3, or other impurity phases are detected within the detection limit, which could indicate that Ga^{3+} and B^{3+} ions are substituted into Zn^{2+} ion sites or incorporated into interstitial sites in the ZnO lattice. The intensity of (002) peak of annealed samples enhanced obviously with the increasing of thickness of buffer layers indicating the improved crystalline quality of the films.

Fig.2 shows the full width at half maximum (FWHM) of (002) peaks of BGZO films and calculated grain size with different thickness of buffer layers. The average grain size of the BGZO films was estimated through the Debye–Scherrer formula[13]: $D = {k\lambda}/{B\cos\theta}$, where k is a constant of 0.9, λ is the X-ray wavelength of 0.154056 nm, B is the FWHM value of the (0 0 2) diffraction peak, and θ is the Bragg angle. As shown in Fig.2, the FWHM values decrease and the grain size increase with the increasing of thickness of buffer layers.

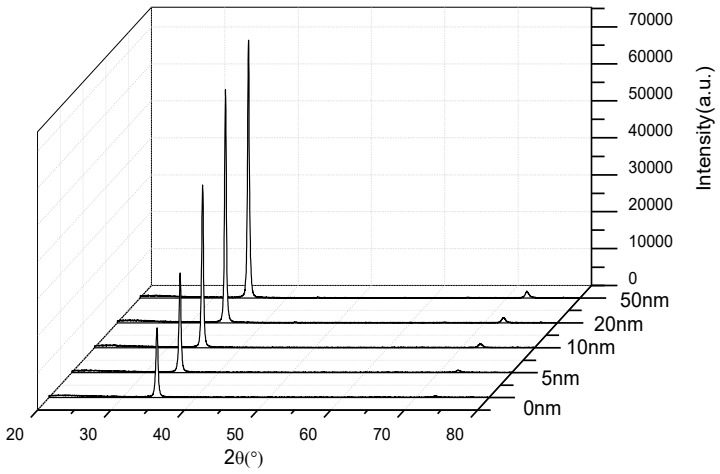

Fig.1 XRD patterns of BGZO films with different thickness of buffer layers

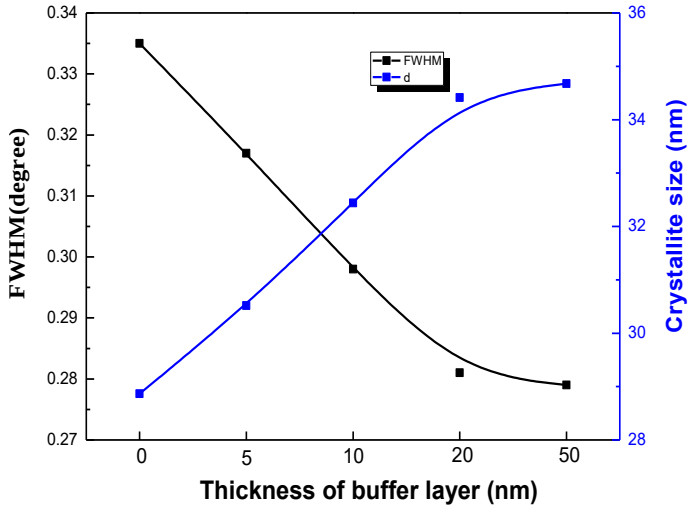

Fig.2 The FWHM of (002) peaks and crystallite size of BGZO films

References

[1] L. Ma, X. Ai, X. Huang, S. Ma, Effects of the substrate and oxygen partial pressure on the microstructures and optical properties of Ti-doped ZnO thin films, Superlattices & Microstructures 50(50) (2011) 703-712.

[2] M. Boujnah, M. Boumadyan, S. Naji, A. Benyoussef, A.E. Kenz, M. Loulidi, High efficiency of transmittance and electrical conductivity of V doped ZnO used in Solar cells Applications, Journal of Alloys and Compounds 671 (2016) 560-565.

[3] K.W. Kim, N.J. Choi, K.B. Kim, M. Kim, S.N. Lee, Growth and characterization of nonpolar (10-10) ZnO transparent conductive oxide on semipolar (11-22) GaN-based light-emitting diodes, Journal of Alloys & Compounds 666 (2016) 88-92.

[4] Y.J. Lee, E.-S. Cho, S.J. Kwon, Pulsed-DC magnetron sputtering of intrinsic ZnO film and its application to CIS solar cell, Vacuum 126 (2016) 91-100.

[5] J.J. Ding, H.X. Chen, S.Y. Ma, The Al-doping and post-annealing treatment effects on the structural and optical properties of ZnO:Al thin films deposited on Si substrate, Applied Surface Science 256(13) (2010) 4304–4309.

[6] X. Bie, J.G. Lu, L. Gong, L. Lin, B.H. Zhao, Z.Z. Ye, Transparent conductive ZnO:Ga films prepared by DC reactive magnetron sputtering at low temperature, Applied Surface Science 256(1) (2009) 289-293.

[7] J. Steinhauser, N. Oliveira, E. Vallatsauvain, C. Ballif, Transition between grain boundary and intragrain scattering transport mechanisms in boron-doped zinc oxide thin films, Applied Physics Letters 90(14) (2007) 142107-142107-3.

[8] S.J. Henley, M.N.R. Ashfold, D. Cherns, The growth of transparent conducting ZnO films by pulsed laser ablation, Surface & Coatings Technology 177 (2004) 271-276.

[9] V. Assunção, E. Fortunato, A. Marques, H. Águas, I. Ferreira, M.E.V. Costa, R. Martins, Influence of the deposition pressure on the properties of transparent and conductive ZnO:Ga thin-film produced by r.f. sputtering at room temperature, Thin Solid Films 427(s 1–2) (2003) 401-405.

[10] C.Y. Tsay, W.T. Hsu, Sol–gel derived undoped and boron-doped ZnO semiconductor thin films: Preparation and characterization, Ceramics International 39(7) (2013) 7425-7432.

[11] H.I. Kang, K.I. Lee, Optical and electrical properties of aluminum and boron co-doped zinc thin films as a function of the substrate temperature, Journal- Korean Physical Society (57) (2010).

[12] L. Zhang, J. Huang, J. Yang, K. Tang, B. Ren, Y. Hu, L. Wang, L. Wang, The effects of thickness on properties of B and Ga co-doped ZnO films grown by magnetron sputtering, Materials Science in Semiconductor Processing 42 (2016) 277-282.

[13] L. Sagalowicz, G.R. Fox, Planar defects in ZnO thin films deposited on optical fibers and flat substrates, Salud Uninorte 14(5) (1999) 1876-1885.

tal Growth 304(1) (2007) 64-68.

Characterization of evolution of implant induced defects in arsenic implanted and annealed HgCdTe epilayers

Changshi Shi, Chun Lin, Yanfeng Wei and Lu Chen

shichangzhi@mail.sitp.ac.cn – +86-021-25051949

Research Center for Advanced Materials and Devices, Shanghai Institute of Technical Physics, Chinese Academy of Sciences, 500 Yutian Road, Shanghai, 200083, China.

Abstract: The evolution of amorphized layer and induced defects near surface of arsenic-implanted HgCdTe was characterized by HRTEM, and the arsenic profiles were measured by SIMS. By XRD analysis, the influences of pre-annealing and ion implantation on lattice structure were studied.

Keywords: Induced defect, HgCdTe, ion implantation, annealing, lattice structure.

1. INTRODUCTION

P-on-n infrared photodiodes have been demonstrated to provide the advantages of low dark current, low series resistance and high operating temperature[1,2]. So it is necessary to study the behaviors of implanted arsenic ions in HgCdTe and their influence on lattice structure. Our previous work has investigated the roles of amorphized layer and induced defects generated in arsenic-implanted HgCdTe on the distribution and diffusion of dopants[3]. The residual point defects deep in arsenic-implanted HgCdTe even after annealing have been measured by Lobre, et al[4]. However, these deep point defects are difficult to characterize. Here, the HgCdTe epilayers were grown on CdZnTe and GaAs substrates by liquid phase epitaxy (LPE) and molecular beam epitaxy (MBE), respectively. The evolution of amorphized layer and induced defects generated in these HgCdTe samples subjected to arsenic ion implantation and Hg overpressure annealing is characterized by high resolution transmission electron microscopy (HRTEM). Then, X-ray diffraction (XRD) analysis was carried out to study the influences of pre-annealing and ion implantation on lattice structure. Additionally, the influences of implant energy on the surface amorphization and induced defects were also studied, as well as the distributions of arsenic dopants.

2. MATERIALS, METHODS AND CHARACTERIZATION

The HgCdTe epilayers (x_{Cd}=0.24) were grown on CdZnTe substrates by LPE and then coated with CdTe as barrier cap layers. Before ion implantation, the LPE samples were pre-annealed at 240ºC for 48 hrs. Sequentially, arsenic ions were implanted into the samples at the energies of 300, 400 and 450keV with the dose of $2\times10^{14}cm^{-3}$. A two-step thermal annealing (420ºC in the first step and 240ºC in the second step) under Hg overpressure was carried out to activate arsenic ions and eliminate implant damage. To compare

the variation of lattice structure, the HgCdTe epilayer (x_{Cd}~0.24) was grown on GaAs substrate by MBE, and the CdTe-coated MBE sample without pre-annealing was implanted by arsenic ions of $2\times10^{14}cm^{-3}$ at 450keV. The amorphized layers and induced defects near the surface of as-implanted HgCdTe were characterized by HRTEM, and the arsenic profiles in the samples before and after Hg overpressure annealing were measured by secondary ion mass spectroscopy (SIMS). Finally, the characteristic diffraction peaks of LPE and MBE samples before and after ion implantation were measured by XRD to describe the variation of lattice structure resulting from ion implantation and annealing.

3. ARSENIC PROFILES AND INDUCED DEFECT EVOLUTION

Figure 1 provides the TEM image of amorphized layer and induced defects in HgCdTe epilayer implanted by arsenic at 400keV. By TEM characterization, it is discovered that the implant damage layer includes an amorphized-MCT (a-MCT) layer and a small defect layer. Moreover, the a-MCT thickness and induced defect depth both increase with improving implant energy. However, the thicknesses of the small defect layers beneath a-MCT were around 200nm for all the samples. The TEM images in Figure 2 indicate that the induced defects contain vacancy clusters, dislocation lines and dislocation loops. For the samples implanted at 300 and 400keV, the amorphous region and induced defects can be eliminated after annealing. When the implant energy is raised to 450keV, a residual point defect belt was observed around the position of the previous amorphous/crystal (a/c) interface in the as-implanted HgCdTe after annealing as shown in Figure 3(a). It implies that the recrystallization occurs from the surface towards the a/c interface. Figure 3(b) provides the TEM image of a residual point defect. It can be discovered that the defect is a cluster of vacancies. The arsenic profiles of as-implanted and annealed samples with different implant energies are shown in Figure 4. It can be seen that the end-of-range (EOR) depth of arsenic ions before and after annealing both increase with elevating implant energy. It implies that the lattice recovery and defect elimination of arsenic-implanted HgCdTe during annealing are more rapid than the indiffusion of arsenic ions, considering the very low diffusion coefficient of arsenic ions in HgCdTe even at high temperature[5].

4. VARIATION OF LATTICE STRUCTURE

For comparison, the XRD characteristic peaks of the GaAs-based MBE HgCdTe sample without pre-annealing and the CdZnTe-based LPE HgCdTe sample with pre-annealing before and after ion implantation were illustrated in Figure 5 and 6. By measuring the FWHMs of diffraction peaks, it is discovered that the arsenic ion implantation not only broadens the FWHM of the characteristic peak from 81arcsec to 101arcsec, but also give arise to the deviation of the peak position towards small angle direction for the

GaAs-based MBE sample without pre-annealing. It indicates that the introduction of atomic stress (lattice distortion, interstitial or substitutional dopants) due to ion implantation increase the lattice constant of HgCdTe, thereby leading to the deviation of the characteristic peak. However, for the CdZnTe-based LPE sample with pre-annealing, the characteristic peak after ion implantation is considered to be split into two peaks utilizing Gauss fitting, and the FWHMs of each fitted peak and the combined peak are both broadened. It is noteworthy that the combined peak deviates towards large angle direction, which is likely due to that the pre-annealing significantly decrease the lattice constant of HgCdTe overwhelming the role of ion implantation.

5. FIGURES

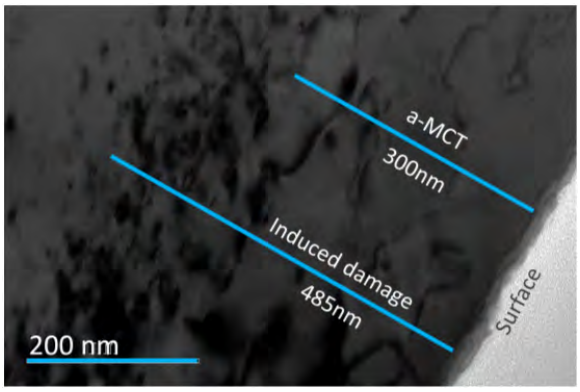

Figure 1 TEM image of amorphous layer and induced defects in HgCdTe epilayer implanted by arsenic at 400keV.

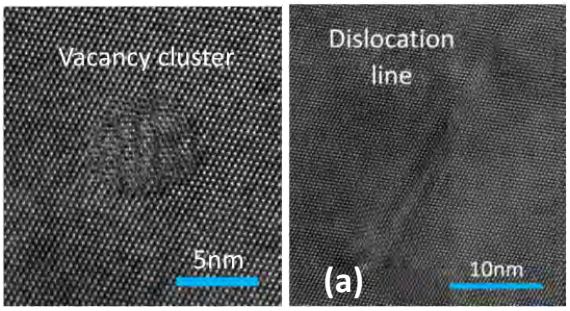

Figure 2 Induced defects generated in small defect layer of arsenic-implanted HgCdTe: (a) Vacancy cluster. (b) Dislocation line.

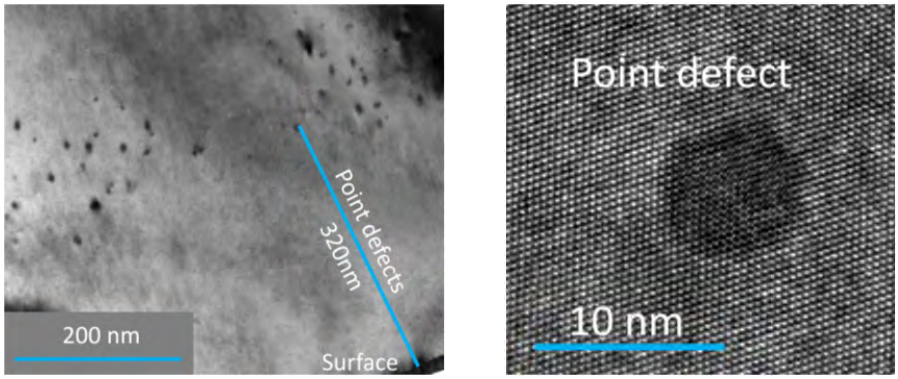

Figure 3 (a) TEM image of residual point defect belt around a/c interface in HgCdTe epilayer implanted by arsenic at 450keV after Hg overpressure annealing. (b) Point defect in HgCdTe epilayer implanted by arsenic at 450keV after Hg overpressure annealing.

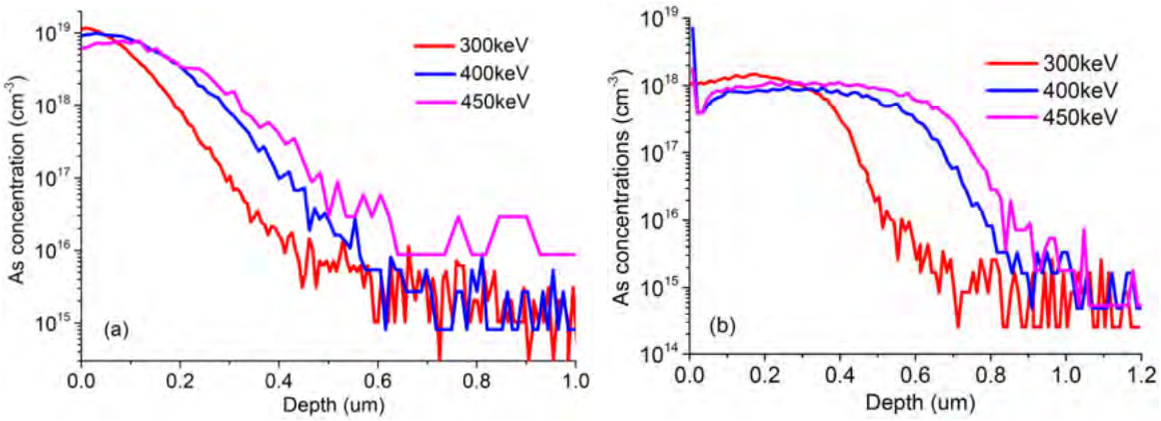

Figure 4 SIMS profiles of arsenic ions in HgCdTe implanted at different energies (300keV, 400keV and 450keV). (a) Before Hg overpressure annealing. (b) After Hg overpressure annealing.

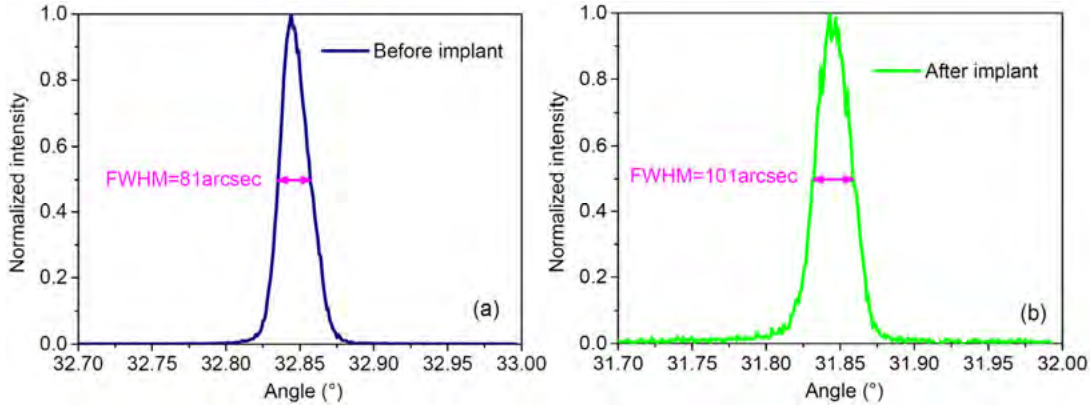

Figure 5 FWHMs of XRD characteristic peaks of GaAs-based MBE HgCdTe epilayers. (a) Before As ion implantation at 450keV, 2×10^{14}cm^{-3}. (b) After As ion implantation at 450keV, 2×10^{14}cm^{-3}.

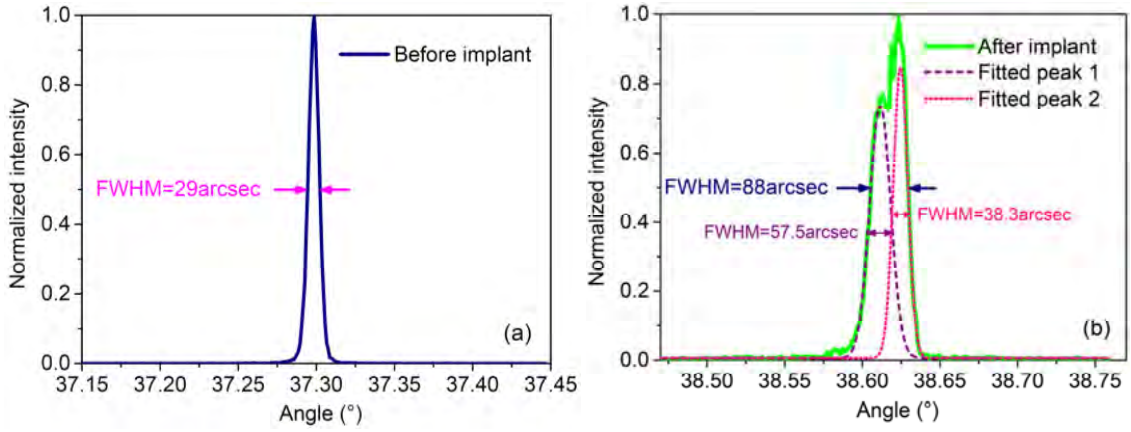

Figure 6 FWHMs of XRD characteristic peaks of CdZnTe-based LPE HgCdTe epilayers. (a) Before As ion implantation at 300keV, 2×10^{14}cm^{-3}. (b) After As ion implantation at 300keV, 2×10^{14}cm^{-3}.

6. REFERENCES

[1] L. Mollard, G. Bourgeois, C. Lobre, et al., Journal of Electronic Materials **43**, 802 (2014).
[2] N. Baier, C. Cervera, O. Gravrand, et al., Journal of Electronic Materials **44**, 3144 (2015).
[3] Changzhi Shi, Chun Lin, Yanfeng Wei, et al., Proc. SPIE 9819, 981923-1 (2016).
[4] C. Lobre, D. Jalabert, I. Vickridge, et al., Nuclear Instruments and Methods in Physics Research B **313**, 76 (2013).
[5] L. Mollard, G. Destefanis, N. Baier, et al., Journal of Electronic Materials **38**, 1805 (2009).

Variable-Field Hall Effect Analysis of HgCdTe Epilayers with Very Low Doping Density

Justin Easley[1], Erdem Arkun[2], Michael Carmody[2], Jamie Phillips[1]

1. Dept. of Elec. Eng. and Comp Science, University of Michigan, Ann Arbor, MI 48109
2. Teledyne Imaging Sensors, Camarillo, CA, 93012

Student Paper

HgCdTe is the most important material used in the production of high performance infrared detectors, due to its versatility across a wide range of wavelengths. HgCdTe continues to be the state of the art for detection in the long wavelength IR (LWIR) regime, based on high quantum efficiency and dark current that approaches theoretical limits governed by fundamental material properties. In order to achieve this level of performance, LWIR devices must be cooled to 77K or below. Further improvements in detector performance may be achieved by lowering the HgCdTe doping concentration in the absorber layer of a conventional p-n heterojunction detector, or by incorporating low doping regions into new device architectures operating under non-equilibrium conditions. These advancements may also help alleviate cooling restrictions, and allow devices to operate at higher temperatures. Characterizing HgCdTe materials with very low doping concentrations, however, poses a challenge. Typical 4-point Hall effect measurements yield an average carrier concentration, making detection of low doped HgCdTe layers very difficult. This study examines HgCdTe epilayers with very low doping concentrations using variable magnetic field Hall effect measurements and multi-carrier fit to examine carrier transport properties in detail. HgCdTe samples were grown by molecular beam epitaxy on CdZnTe substrates at Teledyne Imaging Sensors. The samples were grown to be n-type layers with a target doping levels of $n_1 = 3x10^{15}$ cm^{-3} in the buffer layer and $n_2 = 4x10^{13}$ cm^{-3} in the absorber layer. Hall bar patterns were fabricated using photolithography, wet chemical etching, and metallization for Ti/Au electrical contacts. Experiments were conducted using the Dynacool Physical Property Measurement System (PPMS).

The multi-layered HgCdTe samples were analyzed using the Variable Magnetic Field Hall Effect, and the Multi-Carrier Fitting (MCF) approach[2]. The Hall coefficient, R_H, and the resistivity, ρ, are measured while sweeping the magnetic field from 0-14T. These values are used to compute the conductivity tensor components, σ_{xx} and σ_{xy} and fit to provide numerical values for the carrier density and mobility. Traditional 4-point Hall measurements at 77K give carrier concentration and mobility values of $n = 2.0x10^{15}$ cm^{-3} and $\mu = 23{,}500$ cm^2/Vs. Our data indicates two distinct values, including a lower doped layer with $n = 6.5x10^{13}$ cm^{-3} and $\mu = 275{,}000$ cm^2/Vs. This technique shows promise as a way to analyze layers with significantly lower doping layers, a way to monitor interdiffusion between various

layers, and a starting point to understand and advance the development of HgCdTe epilayers with very low doping concentration.

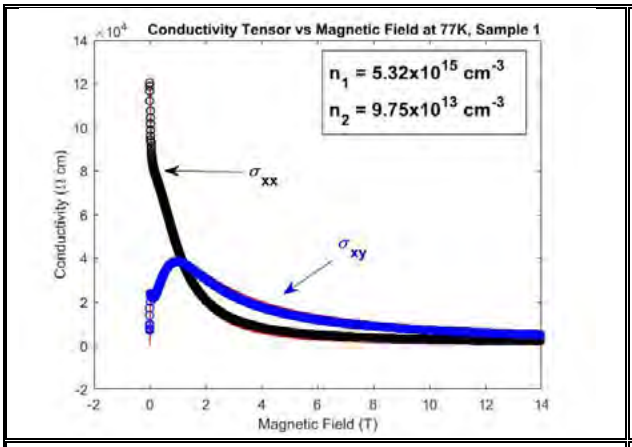

Figure 1: Measured conductivity tensors versus magnetic field at T=77 K and corresponding 2-carrier fit. Sample annealed at 200K.

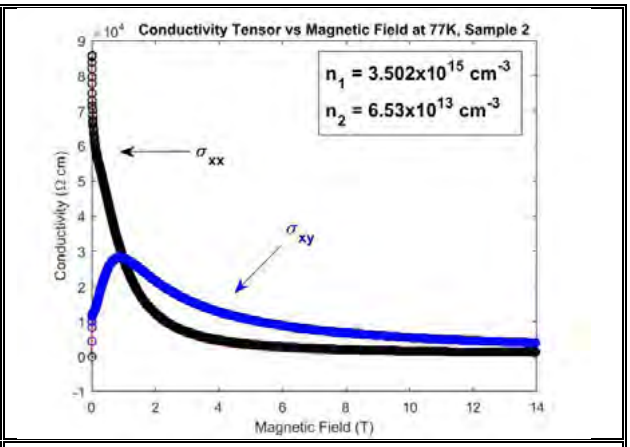

Figure 2: Measured conductivity tensors versus magnetic field at T=77 K and corresponding 2-carrier fit. Sample annealed at 300K.

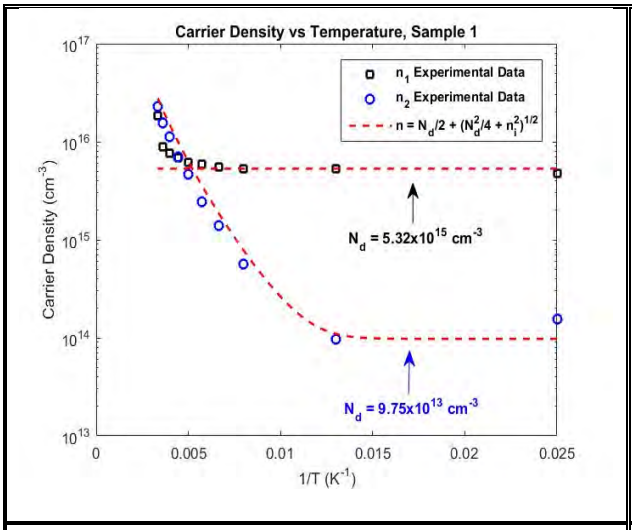

Figure 3: Measured Carrier Density versus Temperature for the absorber layer of Sample 1, compared to intrinsic carrier concentration for x = 0.209, and target doping $N_D = 4x10^{13}$ cm^{-3}.

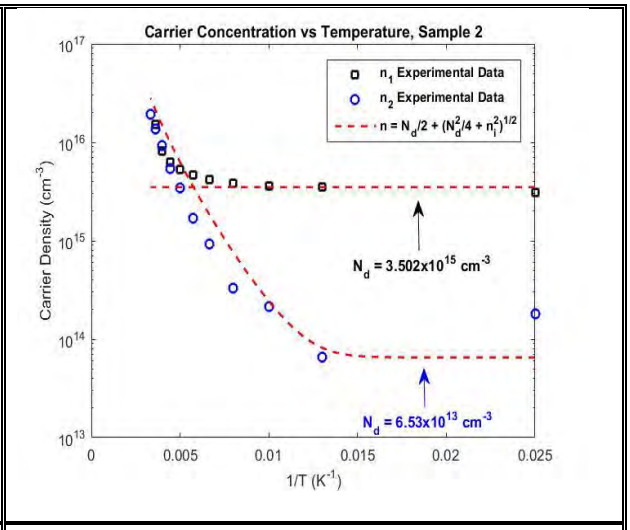

Figure 4: Measured Carrier Density versus Temperature for the absorber layer of Sample 2, compared to intrinsic carrier concentration for x = 0.209, and target doping $N_D = 4x10^{13}$ cm^{-3}.

	4 point Hall (77K)		**Multi Carrier Fit (77K)**			
	n (cm^{-3})	μ (cm^2/Vs)	n_1 (cm^{-3})	μ_1 (cm^2/Vs)	n_2 (cm^{-3})	μ_2 (cm^2/Vs)
Sample 1	$2.0x10^{15}$	23,500	$5.32x10^{15}$	8,806	$9.75x10^{13}$	282,108
Sample 2	$2.0x10^{15}$	23,500	$3.502x10^{15}$	9,817	$6.53x10^{13}$	275,052

Table 1. Comparison between 4 point Hall measurement and Multi Carrier Fit approach

Metamorphic buffers for high absorption long wave infrared superlattices and bulk materials

C. A. Affouda, S. Tomasulo, N. Mahadik, M. Twigg, J. A. Nolde, E. M. Jackson, E. R. Cleveland, E. H. Aifer

chaffra.affouda@nrl.navy.mil, 202-404-2904

U.S. Naval Research Laboratory, 4555 Overlook Ave. Washington, DC 20375, USA

Abstract: The narrow bandgap and varying stagger in band alignment of $InAs_{1-x}Sb_x$ alloys makes it possible to engineer type-II superlattices (T2SL's) for long-wave (LW) infrared sensors operating in the 8-12 µm range. Typically, LW InAs/$InAs_{1-x}Sb_x$ T2SL's that are strain balanced to an underlying GaSb substrate have relatively weak optical absorption due to their large SL period. However, the absorption coefficient of T2SL's with similar bandgap can be greatly improved when growing on metamorphic buffers (MB's) that reduce the lattice mismatch to the $InAs_{1-x}Sb_x$ layers. Here we present results from the growth of LW InAs/$InAs_{1-x}Sb_x$ T2SL's and bulk $InAs_{0.82}Sb_{0.18}$ absorbers on MB's. Material properties of the metamorphic T2SL and bulk absorbers were evaluated using high resolution X-ray diffraction and reciprocal space mapping. Bandgap and lifetime were measured using static and modulated photoluminescence, and absorption was measured using transmission spectroscopy. Our results show that the absorption of the T2SL can be greatly increased by growing on a MB or "virtual substrate" with a larger lattice constant than GaSb without significant minority carrier lifetime degradation.

Keywords: metamorphic buffer, InAsSb, infrared, long wave, type-II, superlattice, lifetime

1. INTRODUCTION

Metamorphic buffers (MB's) can be used to create virtual substrates (VS's) for a targeted material system. Thus by liberating designers from the constraints imposed by the limited set of lattice constants

available in commercial substrates, MB's can enable the realization of electronic devices with improved performance such as multi-junction solar cells[1] and infrared photo-detectors[2]. Here we are using MB's to improve the optical absorption of long wave (LW) InAs/InAsSb type-II superlattices (T2SL's). LW InAs/InAsSb T2SL's that are grown strain balanced to GaSb, suffer from poor optical absorption. It is however possible to increase their optical absorption strength by using MB's. This concept is illustrated in figure 1a where two T2SL's with a similar bandgap of approximately 10 μm are simulated with a K.P solver developed at NRL[3]. The absorber lattice matched to the GaSb substrate is comprised of a 17.6 Å thick $InAs_{0.45}Sb_{0.52}$ layer that must be strained balanced with a 76.9 Å thick InAs layer as shown in figure 1(a). However the absorber grown on a MB with a final lattice constant similar to AlSb only requires a 37.8 Å layer of InAs for strain balancing. Although the same number photons are being absorbed per superlattice period in both cases, the T2SL grown on the MB has a higher absorption coefficient because it has a smaller period. Simulated optical absorptions of InAs/InAsSb T2SL's grown on various substrates are shown in Figure 1b. The simulation clearly shows that the absorption coefficient can be doubled by growing on $In_{0.1}Ga_{0.9}Sb$ (or AlSb) instead of GaSb.

For this experiment the MB was graded in six steps to a final composition of $In_{0.12}Ga_{0.88}Sb$ in order to promote plastic relaxation at each step and optical transparency down to 3 microns. The samples were grown by molecular beam epitaxy in a Varian Mod Gen II using thermally cracked group-V species. Sample-A was strain balanced to the GaSb substrate while Sample-B was grown on the $In_{0.12}Ga_{0.88}Sb$ MB. A description of the T2SL's samples is shown in Figure 2.

2. RESULTS & DISCUSSION

X-ray diffraction rocking curves showed that the samples were perfectly lattice matched to their respective underlying VS. The results of the comparison between the LW T2SL lattice matched to GaSb

(sample-A) and the T2SL lattice matched to an $In_{0.12}Ga_{0.88}Sb$ MB (sample-B) are summarized in figure 3. Continuous wave photoluminescence (PL) spectra of the two samples are shown in figure 3(a) under the same excitation conditions. We clearly see that the PL intensity of the MB T2SL is almost doubled that of sample-A. This suggest that there is no significant degradation of the lifetime when growing on the MB. To confirm this we used the frequency domain PL method[4] to compare the lifetimes of the two samples as shown in figure 3(b). From fits including radiative, Shockley-Read-Hall (SRH) and Auger processes we see that the lifetime of sample-B is SRH limited for low carrier excitations with radiative and Auger contributions at higher injection levels. However the lifetime of sample-A has the peculiar "S" shape suggesting that it is SRH limited over the investigated injection level range. This might explain the increased PL intensity of sample-B.

3. CONCLUSION

We have shown that LW InAs/InAsSb T2SL's can be grown on MB without minority carrier lifetime degradation. Although the T2SL lattice matched to GaSb was expected to have a lifetime higher than the one grown on the MB, we found that its lifetime was limited by SRH traps. For completeness, we are planning to measure the optical absorption of the metamorphic T2SL's in order to assess their performance for LW infrared detection.

4. FIGURES

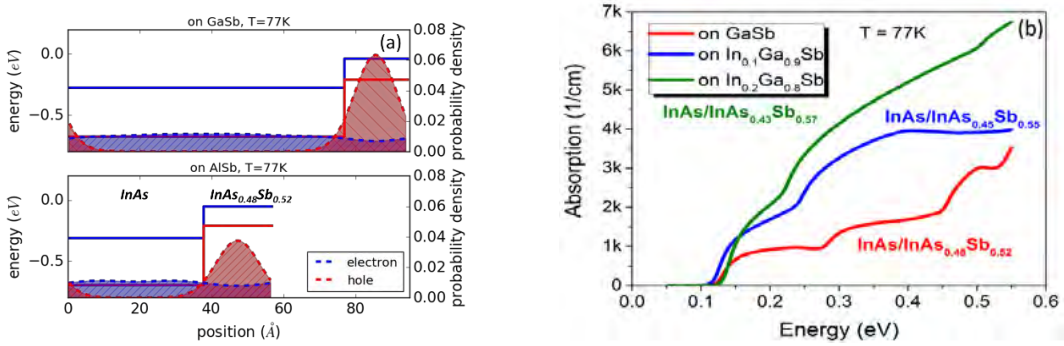

Figure 1: (a) K.P simulation showing electron-hole occupation probabilities in T2SL's. (b) Simulated optical absorption is greatly improved by growing T2SL's on virtual substrates.

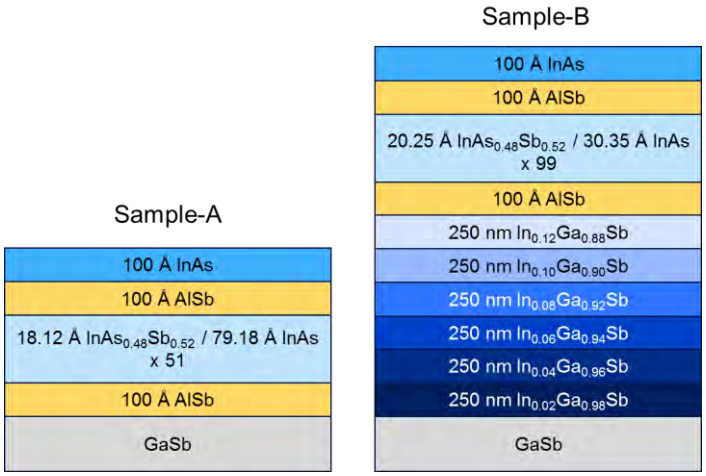

Figure 2: T2SL samples description.

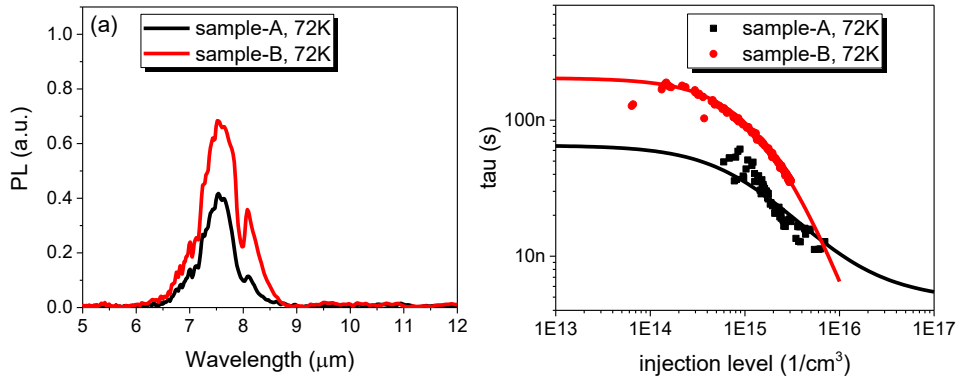

Figure 3: (a) PL intensity comparison of sample-A lattice matched to GaSb and sample-B lattice matched to $In_{0.12}Ga_{0.88}Sb$. (b) Lifetime comparison of the two samples.

5. REFERENCES

[1] W. Guter, J. Schöne, S.P. Philipps, M. Steiner, G. Siefer, A. Wekkeli, E. Welser, E. Oliva, A.W. Bett, and F. Dimroth, Applied Physics Letters **94**, 223504 (2009).

[3] M.P. Lumb, I. Vurgaftman, C.A. Affouda, J.R. Meyer, E.H. Aifer, and R.J. Walters, in *Proc. SPIE* (2012), p. 84710A–84710A–10.

[4] J.R. Lakowicz, editor, in *Principles of Fluorescence Spectroscopy* (Springer US, 2006), pp. 157–204.

[5] D. Wang, Y. Lin, D. Donetsky, L. Shterengas, G. Kipshidze, G. Belenky, W.L. Sarney, H. Hier, and S.P. Svensson, in *Proc. SPIE* (2012), pp. 835312-835312–11.

Plasmonic grating design and optimization for increased operating temperature of MWIR nBn detectors

E. M. Jackson, J. A. Nolde, M. Kim, C. S. Kim, C. T. Ellis, E. R. Cleveland, C. A. Affouda, C. L. Canedy, J. G. Tischler, O. J. Glembocki, I. Vurgaftman, J. R. Meyer, E. H. Aifer
Naval Research Laboratory, Washington, DC 20375

For infrared (IR) imaging applications, it is generally desirable to increase the focal plane array (FPA) operating temperature as much as possible before the signal to noise performance falls below mission requirements. As the operating temperature increases, the required cooling power decreases, affording reductions in the size, weight, and power (SWaP) of the overall imaging system, and thus enabling its use on a wider range of platforms. Here we describe a novel strategy to enable a higher IR FPA operating temperature by using "nBn" device structures with ultra-thin midwave IR (MWIR) absorbers enhanced with metallic gratings. The junction-free "nBn" sensor structure has been shown to operate with bulk diffusion-limited dark current that scales linearly with absorber thickness.[1,2] Here, as we reduce the absorber volume, and thus the dark current, by a factor of 6-10, we compensate for the loss in quantum efficiency (QE) by using a grating to couple incident photons to surface plasmon-polariton (SPP) modes, which increases the effective optical path length within the thin absorber. We have experimentally investigated polarization-independent designs that employ two-dimensional (2D) square gratings, and compare these with numerical simulations.

Gratings were designed using finite element method (FEM) calculations[3] for normally incident light to predict the plasmon resonance wavelength (λ_{spp}), and to determine the values of grating parameters (period, height and duty cycle) that maximize optical absorption in the lattice-matched, bulk InAsSb absorber layer. The device structure is shown schematically in Figure 1. Frequency- and temperature-dependent optical constants for the semiconductor layers were calculated using an 8-band k.p model,[4] while the frequency dependence of the Au film was taken from Rakić, et al.[5] In the simulations, the incident field originates in an infinite GaSb substrate; therefore, the resulting calculations of the InAsSb absorption correspond to the internal QE (IQE) for the structure, assuming

100% carrier collection. Three geometries were considered: 1D linear gratings and 2D gratings consisting of Ge or Au squares in a simple square lattice (Figure 2). The absorber thickness of 0.5 μm was chosen to approximate the decay length of the SPP mode within the InAsSb layer, to enable productive absorption of most of the plasmon energy. The grating period is the primary determinant of λ_{spp}, but has minimal effect on absorption strength. Hence, in our design process, one first choose the period appropriate to the desired wavelength, then optimizes the absorption by adjusting the grating duty cycle and height, and finally makes minor adjustments to the period if necessary to tune the peak position. Figure 3 shows the maximum QE at λ_{spp} (3.3μm) for a 900-nm-period grating as a function of duty cycle, defined here as the percentage of the area of the unit cell in which gold is in direct contact with the InAs layer. While the maximum InAsSb absorption is similar for all three topologies (80-85%), the grating height and duty cycle that maximize the QE vary widely. We note that for both 2D grating geometries the optimum QE occurs when the square covers less than one-half of the area.

The structure of Figure 1 was grown by molecular beam epitaxy (MBE) on a lightly n-doped, transparent GaSb substrate. Ge squares or lines were produced directly on the as-grown wafer by e-beam lithography and a lift-off process using e-beam deposition. The solid lines in Figure 4 represent the measured external QE for a device without a grating (mirror), and for a device with a 2D grating of 900 nm period and Ge thickness of 220nm. These may be compared to the simulated InAsSb absorption (dashed curves), which have been adjusted to account for the initial reflection at the air-GaSb interface. The measured quantum efficiency is reduced by incomplete coverage of the mesa by the grating. To facilitate alignment between the grating region, mesa etch, and metal layer, the grating region had dimensions 150x150 μm^2, with a 140x140 μm^2 metal contact aligned on top of the 160x160 μm^2 mesas. The ratio of the metal coverage to the mesa area resulted in a grating fill factor (FF) of 76%. A simple estimate of the FF effect can be obtained by taking an area weighted average of the grating QE, the QE without backside metal, and the QE for only backside Ge. This calculation suggests that full grating

coverage would increase the external QE (EQE) to about 38%, which corresponds to an IQE of 57% as when an anti-reflection coating (ARC) is employed.

We estimate the minimum plasmon coupling efficiency (η_c) at the resonance peak by attributing the remaining difference in QE to imperfect coupling to plasmons. Assuming 100% carrier collection and a double pass of light in the very thin absorber layer and infinite, non-absorbing substrate, the QE is given by:

$$QE_{meas}/T_1 = [(1 - e^{-\alpha L}) + \eta_c \eta_{abs}\, e^{-\alpha L} + e^{-\alpha L}(1 - e^{-\alpha L}) R_2 (1 - \eta_c)],$$

where T_1 is the transmission of the GaSb-air interface, α is the InAsSb absorption coefficient, L is the absorber thickness, R_2 is the reflection coefficient of the Au grating and η_{abs} is the fraction of the plasmon energy collected in the InAsSb. Since the reflected power in the simulations is less than 1% at the resonance wavelength, we can assume $\eta_c \approx 1$ and then estimate $\eta_{abs} \approx 0.79$. Using this value and the grating QE calculated for 100% FF, we find $\eta_c \approx 0.47$ for the measured devices, which is slightly higher than the coupling observed in ref. 6 for 1D gratings. While this structure has demonstrated strong effective coupling to plasmons, more research will be required to significantly improve upon this value.

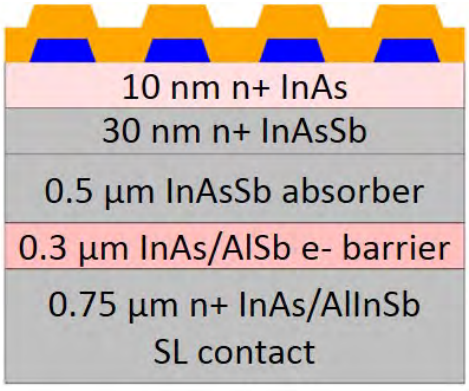

Figure 1: Device structure grown by MBE. The blue and orange regions are germanium and gold. The bandgaps of the contact layer superlattice (SL) and electron barrier SL are approximately 610 and 960 meV, respectively.

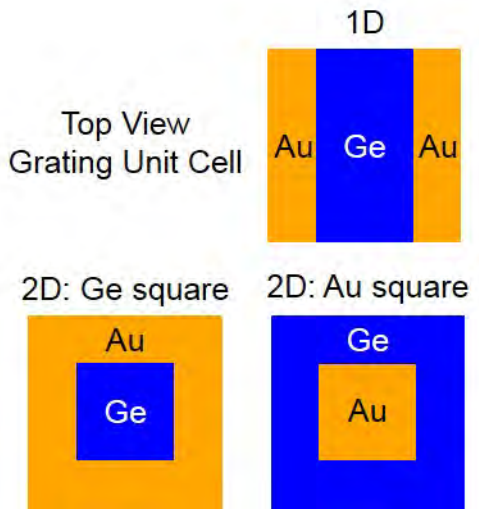

Figure 2: Schematics of the three grating topologies simulated using the FEM software.

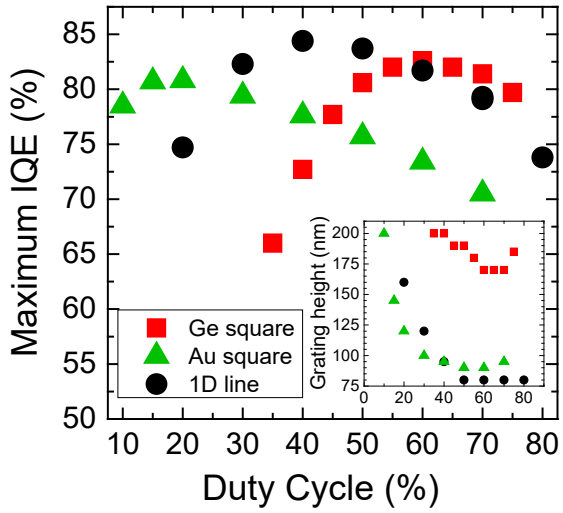

Figure 3: Maximum QE at 3.3 µm vs. duty cycle for three grating topologies: 2D Ge squares (red squares), 2D Au squares (green triangles), and 1D lines (black circles). The QE for the 1D grating assumes incident light polarized perpendicularly to the grating lines. For unpolarized illumination, the QE will be substantially less. The inset shows the optimal height as a function of duty cycle for the three topologies.

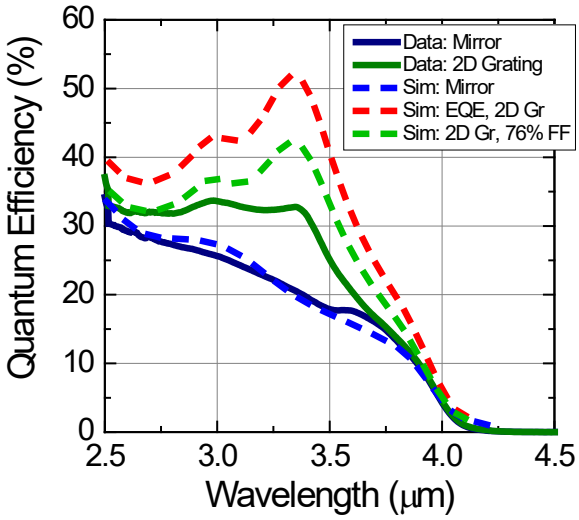

Figure 4: Measured (solid lines) and simulated (dotted lines) QE at 150K with unpolarized illumination for a device without gratings (mirror) and a device with a 2D grating of 900nm period, 75% duty cycle, and 220nm-thick Ge squares.

---

[1] L. Hoglund, D. Z. Ting, A. Soibel, A. Fisher, A. Khoshakhlagh, C. J. Hill, L. Baker, S. Keo, J. Mumolo, and S. D. Gunapala, *IR Phys. & Tech.*, **70**, 62 (2015)

[2] A. Soibel, C. J. Hill, S. A. Keo, L. Hoglund, R. Rosenberg, R. Kowalczyk, A. Khoshakhlagh, A. Fisher, D. Z. Ting, S. D. Gunapala, *IR Phys. & Tech.*, **70**, 121 (2015)

[3] Comsol Multiphysics. Version 5.2. COMSOL, Inc. Burlington, MA (2016)

[4] M. P. Lumb, I. Vurgaftman , C. A. Affouda , J. R. Meyer , E. H. Aifer and R. J. Walters, *Proc. of SPIE*, **8471**, 84710A (2012).

[5] A. D. Rakić, A. B. Djurišic, J. M. Elazar, and M. L. Majewski, *Appl. Opt.* **37**, 5271 (1998)

[6] J. A. Nolde, M. Kim, C. S. Kim, E. M. Jackson, C. T. Ellis, J. Abell, O. J. Glembocki, C. L. Canedy, J. G. Tischler, I. Vurgaftman, J. R. Meyer, and E. H. Aifer, *Appl. Phys. Lett.*, **106**, 261109 (2015)

DEVELOPMENT OF NANOSTRUCTRED ANTIREFLECTION COATINGS FOR INFRARED SENSORS AND OPTICAL APPLICATIONS

Gopal G. Pethuraja, Roger E. Welser, Ashok K. Sood and Yash R. Puri

Gpethuraja@magnoliaoptical.com – 518 618 4200

Magnolia Optical Technologies, Inc.,

52-B Cummings Park, Suite 314, Woburn, MA 01801

251 Fuller Road, CESTM B-250, Albany, NY 12203

Harry Efstathiadis and Pradeep Haldar

College of Nanoscale Science and Engineering, SUNY Polytechnic Institute, Albany, NY 12203

Nibir K. Dhar

U.S. Army Night Vision & Electronic Sensors Directorate, Fort Belvoir, VA 22060

Eric A. DeCuir and Priyalal S. Wijewarnasuriya

U.S. Army Research Laboratory, 2800 Powder Mill Road, Adelphi, MD 20783

ABSTRACT: Reflection loss of a significant portion of the incident infrared (IR) spectrum from IR detector and optical elements limits the performance of Electro-Optical (EO)/IR optical systems. Magnolia has developed and demonstrated ultrahigh performance broadband and omnidirectional antireflection (AR) coatings for visible and near-IR spectral bands. In this paper we present our recent advancements in AR structures for II-VI substrates and devices in various IR spectral bands. The AR structures are fabricated by depositing nanostructured layers using a self-assembly process. AR structure on II-VI substrates were designed and optimized for mid-wavelength IR (MWIR) and long-wavelength IR

(LWIR) spectral bands. The performance of AR coated substrates was tested over the MWIR and LWIR spectral bands.

1. INTRODUCTION

Electro-Optical (EO)/Infrared (IR) optical systems require ultrahigh performance optical coatings that eliminate or minimize optical reflection loss and maximize system sensitivity. II-VI based EO/IR optical systems are being developed for a variety of defense and commercial system applications. Reflection loss of a significant portion of the incident IR spectrum from IR detector and optical elements limits the performance of the EO/IR optical systems. An optical interface layer, i.e., advanced antireflection (AR) coating, can overcome these limitations and significantly enhance the performance of the EO/IR optical systems. Magnolia is working on developing ultrahigh performance AR coatings on various substrates for a wide variety of applications. We have demonstrated ultrahigh performance of our broad AR coatings for visible and near-IR spectral bands. The AR coatings enhance the optical transmission through transparent windows by minimizing broadband reflection losses to less than one percent, a substantial improvement over conventional thin-film AR coating technologies. II-VI infrared substrates, which have moderate to high refractive indices, are used for various IR applications that utilize a wide range of IR spectral bands. AR coatings for these application require thicker and more complex layer structures. Magnolia's nanostructured AR structures show ultrahigh performance at MWIR and LWIR spectral bands.

2. DESIGN OF ANTIREFLECTION STRUCTURES

Nanostructured antireflection coatings have the potential to greatly reduce the reflection of LWIR and MWIR light that is incident on the surface of IR substrates including Cadmium Zinc Telluride (CZT), ZnSe, and Si substrates. The predicted reflectance spectra of single-layer and multi-layer AR structures optimized for 8-10 μm bands on CZT substrate are shown in Figure 1. It shows that the multi-layer structure has the potential to almost eliminate the reflection from the surface of CZT substrates.

Single-layer and Multi-layer AR structures have been optimized for 8-14 um spectral band. Figure 2 compares the predicted performance of the single and multi-layer structures with the

performance of uncoated CZT substrate. The simulated reflectance spectra of the multi-layer structure indicate that the multi-layer structure has the potential to almost eliminate the reflectance loss of signal from the CZT substrates for the 8-14 μm band.

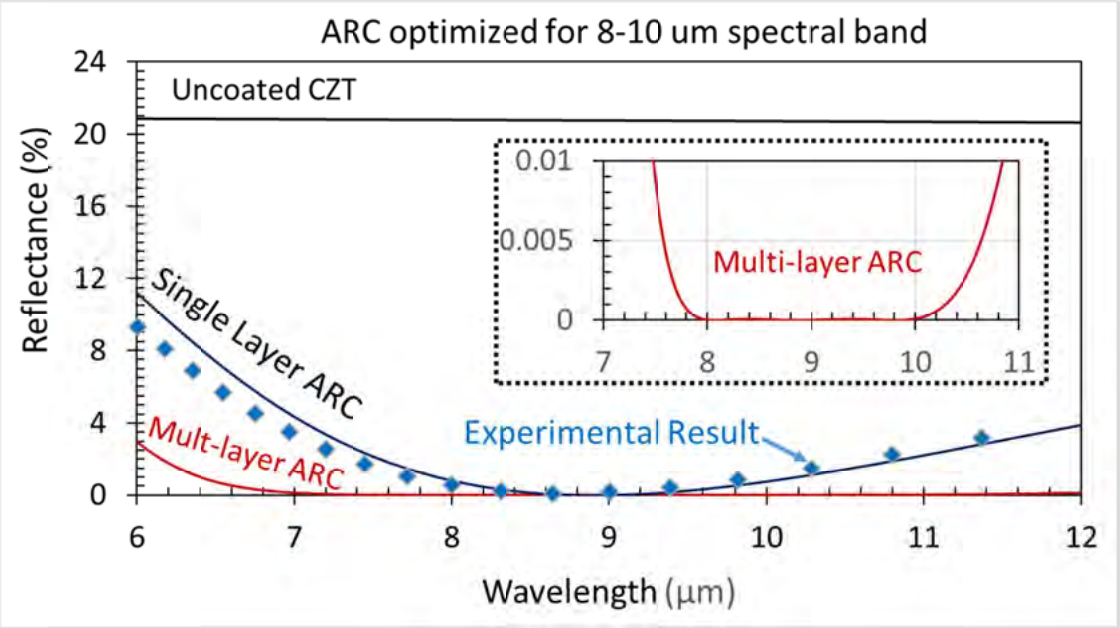

Figure 1: Potential performance of single and multi-layer AR coating structure on CZT substrate optimized for the 8-10 μm band. Comparision of periminaly experimental result with single-layer ARC potential performance. The inset shows that the multi-layer AR coating has the potential to almost eliminate the reflectance for the 8-10 μm spectral band.

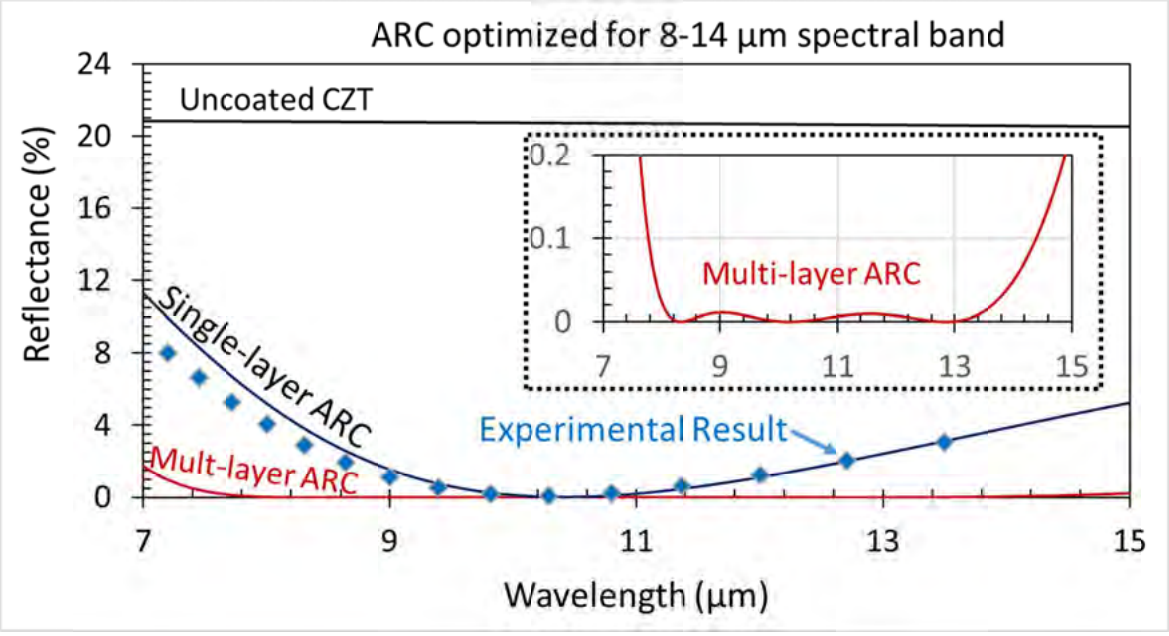

Figure 2: Potential performance of single and multi-layer ARC structure on CZT substrate, optimized for the 8-14 µm band. Comparision of the simulated reflectance spectra of uncoated and AR coated CZT substrates. The inset shows that the multi-layer AR coating has the potential to almost elliminate the reflectance loss from CZT substrate for the 8-14 µm spectral bands.

3. EXPERIMENTAL RESULTS

Preliminary nanostructured AR coatings on CZT substrates have reduced the average reflection in the 8-10 and 8-14 µm bands to less than 0.5% and 1.6%, respectively. The priliminary single-layer AR coatings have been synthesized by growing a nanostructured Si layer with required porosity. The performance of AR coatings have been optimized for 8-10 µm and 8-14 µm by controlling layer thickness and porosity. It clearly demonstrates the ablity of tuning AR performance for a specific spectral band. The preliminary experimental results of single-layer AR coatings are commpred with predicted performance of single-layer AR structures in Figure 1 and Figure 2. The experimental performances are matching closely with the predicted performance of the respective AR structures. Further optimization and implementing multi-layer structure, the reflection loss from the II-VI substrates can be almost elliminated and improved the perfomance of II-VI infra-red devices.

4. REFERENCES

[1] K. Sood, R. A. Richwine, Y. R. Puri, N. K. Dhar, D. L. Polla, and P. S. Wijewarnasuriya, "Multispectral EO/IR Sensor Model for Evaluating UV, Visible, SWIR, MWIR and LWIR System Performance," *Proceedings of SPIE*, Vol. 7300, 2009, pp. 73000H.

[2] K. Sood, Y. R. Puri, L. Becker, M. Z. Tidrow, R. S. Balcerak, G. Brill, P. Wijewarnasuriya, N. Dhar, P. Boieriu, C. Fulk, S. Sivananthan, J. Yehoda, and S. Finke. "Development of High-Performance Radiation-Hardened Antireflection Coatings for LWIR and Multicolor IR Focal Plane Arrays," *Proceedings of SPIE*, Vol. 6206, 2006, pp. 620615.

[3] R. E. Welser, A. W. Sood, G. G. Pethuraja, A. K. Sood, X. Yan, D. J. Poxson, J. Cho, E. Fred Schubert, and J. L. Harvey, "Broadband Nanostructured Antireflection Coating on Glass for Photovoltaic Applications," *38th IEEE Photovoltaic Specialist Conference*, no. 525, June 2012

[4] Gopal G. Pethuraja, Roger E. Welser, John W. Zeller, Yash R. Puri, Ashok K. Sood, Harry Efstathiadis, Pradeep Haldar, Nibir K. Dhar and Priyalal Wijewarnasuriya (2015). "Nanostructured Antireflection Coatings for Optical Detection and Sensing Applications." MRS Proceedings, 1805, mrss15-2137947 doi:10.1557/opl.2015.689.

Epitaxial HgCdTe on Silicon and CdZnTe Substrates: A Performance Comparison

C. Fulk – Invited Talk

Raytheon Vision Systems, 75 Coromar Drive, Goleta, CA

Raytheon has grown and fabricated many thousands of HgCdTe arrays using both silicon and CdZnTe substrates. As such, we have accumulated a large database of both technologies allowing for a statistical and qualitative performance comparison. Metrics such as dark current, cluster defects, noise and their associated distributions are investigated and compared. QE is also illustrated in selected cases. An argument for each technology's advantages and disadvantages are shown for given operating conditions.

We acknowledge the session organizers for arranging prompt review of the papers and thank the authors for choosing this forum for presenting their results. The 2017 U.S. II–VI workshop is going to be held at the Embassy Suites Chicago Downtown-Lakefront Hotel, Chicago, Illinois, USA, on October 31–November 2, 2017.
Workshop website: http://www.II–viworkshop.org/.

S. Sivananthan
Director, Microphysics Laboratory,
University of Illinois at Chicago,
845 W. Taylor St., Chicago, IL 60607
Special Issue Guest Co-Editor

Y. Anter
Sivananthan Laboratories Inc.,
590 Territorial Drive. Unit H.,
Bolingbrook, IL 60440
yanter@sivananthanlabs.us
Special Issue Editorial Coordinator

N.K. Dhar
Chief Scientist, S&T.,
Night Vision and Electronic Sensors Directorate,
10221 Burbeck Road,
Fort Belvoir, VA 22060
Special Issue Guest Co-Editor